

# The molecular structure of selected South African coal-chars to elucidate fundamental principles of coal gasification

**M.J. Roberts**  
**22061452**

Thesis submitted for the degree *Doctor Philosophiae* in  
**Chemical Engineering** at the Potchefstroom Campus of the  
North-West University

Promoter: Prof R.C. Everson (North-West University)  
Co-promoter: Dr G. Domazetis MD Clean Coal Technology  
Pty Ltd (La Trobe University, Australia)

October 2015

## DECLARATION

---

### Declaration

I, Mokone J. Roberts, hereby declare that a thesis with the title:

THE MOLECULAR STRUCTURE OF SELECTED SOUTH AFRICAN COAL-CHARS TO  
ELUCIDATE FUNDAMENTAL PRINCIPLES OF COAL GASIFICATION

is my own work, except where acknowledged, and has not been submitted at any other  
university either in whole or in part.

Signed at Potchefstroom on the ..... day of October 2015

---

Mokone J. Roberts

## ACKNOWLEDGEMENTS

---

### Acknowledgements

First and foremost I acknowledge the sustaining power of faith in God Almighty during the times of uncertainty and testing I experienced in this thesis.

I would like to thank the North-West University, Potchefstroom Campus, for matching me with my PhD study leader and promoter, Professor Raymond Everson, under the directorship of Professor Frans Waanders, for so patiently allowing me an intellectual freedom in the most challenging research I ever experienced. I felt extremely lucky to have Professor Raymond Everson who walked with me and cared so much about my work every step of the way. His calm but enthusiastic and smart demeanour steered my mental abilities to such answers, comprehension and rationale I never thought I could develop. So closely alongside him I would also like to thank my assistant promoter, Professor Hein Neomagus, whose energetic and probing mind would run me around a point until I either captured or knocked it down. A research group meeting would always feel strange and somewhat incomplete if neither of these two Professors were present. The involvement of all my co-promoters was indispensable since the inception of this project. Professor Jonathan Mathews offered me a remote contract from the Penn State University with his curiosity on the atomistic models of coal and dedication to the coal science and technology. Together with one of his protégés, Dr Daniel van Niekerk from SASOL, their fine expertise is gratefully acknowledged. I appreciate and thank the efficient participation of Dr George Domazetis who, despite using different time-zones and programs from as far as the La Trobe University, Melbourne, shared his abundant experiences with the atomistic coal science that involved simulations in both the semi-empirical and high-accuracy density functional theory techniques. I express my gratitude to Dr Cornie Van Sittert, who facilitated the core resources of my thesis throughout in respect with the laboratory for molecular modelling at North-West University. In different combinations, these promoters contributed to the successful publications described chapters 3-5.

## ACKNOWLEDGEMENTS

---

I appreciate the generous collaboration, growing and impressive skills of one of my PhD colleagues, Gregory N. Okolo, with the coal characterisation and experimental work related to coal gasification, including his ability and speed to acquire and interpret results. Okolo's efforts nearly touched all the aspects of my thesis, in particular, the two publications (Chapters 3 and 5), including Chapter 6. Okolo made a phrase I often heard in the streets of Lagos, Nigeria, during my brief visits in the mid-2000s: "I am we", to appear so glaringly in my experiences and memories. The contribution of other junior students like Marie-Louise Visser, Thabiso Moropa, Lebohang Mgano and Thandeka Chaldien in their different years of studies at the North-West University is highly acknowledged. Either in single or joint efforts, high-quality samples for different analyses were produced, at times on 24/7 turnarounds. Coupled with their preparedness to cooperate with other laboratory users, including their ability to acquire support and technical assistance from the Laboratory Manager, the two main engineering technicians and their assistants, these students earned themselves respect among their peers and were empowered with some of the best experiences and practices in coal sample treatment for research purposes.

Most results in this thesis were made possible with support of specialists and sponsors from different divisions, institutions and organisations. In no specific order, I thank SANEDI and ESKOM for supporting this thesis; Mr Aaron Mulaudzi of the Exarro Resources' Grootegeeluk Coal Mine and Mr J.P. Bergh from the Anglo American Corporation's Goedehoop Coal Mine for their dedicated effort to identify and supply me with the desired coal samples used in this thesis; Professor Manie Vosloo of the Chemical Resource Beneficiation faculty of the North-West University for his assistance with the initial layout of my molecular modelling requirements; Professors Rosemary Falcon and Nicola Wagner from the University of the Witwatersrand, Johannesburg, including Ms Vivien Du Cann from Petrographic SA, for offering their resources, guidelines and interesting discussion on coal petrography, which formed part of Chapter 3; Mr Mohamed Jaffer under the instructions of Professor Trevor Sewell at the University of Cape Town for going all the way outside their usual material analyses to

## ACKNOWLEDGEMENTS

---

provide me with the high resolution transmission electron microscopy images of my coal char samples that culminated in chapters 4 and 5; the University of Nottingham's Professor Colin Snape and the Stellenbosch University's Ms Heidi Assumption and Dr Susanne Causemann for their generosity to devote their resources and knowledge of the solid-state nuclear magnetic resonance for my coal chars; the involvement and such steering questions of Professor Jenny Jones from the University of Leeds, UK, which opened my wider understanding of the computational chemistry.

I express gratitude to all of the North-West University faculty members for their help and support towards the accomplishment of my thesis. Professors John Bunt, Quentin Campbell and Christien Strydom, including Dr Rufaro Kaitano strengthened me during my lows and desperations in small but best ways they could despite their busy schedule. I also place on record, my sense of gratitude to everyone else in the campus for having directly or indirectly lent their hand in the daily and final developments of my thesis, including past and present students and research administrators.

I deeply thank my spiritual mother, MaKhabele Elizabeth Mpheqeke, for her unconditional trust in me her devoted responsibility based on her exceptional faith in God, which influenced my voyage enormously when I got troubled and weary. My brothers and sisters from all houses, as well as my in-laws have been so generous with their love and understanding despite extreme differences in our levels of literacy.

Lastly, and most importantly, I wish to thank with abundance of love and warmth my wife MaRoberts and daughters Tiffy, Ratwe, Bontle and Thori Roberts. I shall forever recognise their sacrifice to allow me to pursue these most difficult full-time studies far from home.

*I dedicate this thesis to my parents who did not leave long enough see the first PhD graduate in the family. In so much humble ways, yet against all odds, their love raised me up and gave me strength and values of a winner and survivor I am hitherto.*

## ABSTRACT

---

### Abstract

Advances in the knowledge of chemical structure of coal and development of high performance computational techniques led to more than hundred and thirty four proposed molecular level representations (models) of coal between 1942 and 2010. These models were virtually on the carboniferous coals from the northern hemisphere. There are only two molecular models based on the inertinite- and vitrinite-rich coals from the southern hemisphere. The current investigation is based on the chars derived from the Permian-aged coals in two major South African coalfields, Witbank #4 seam and Waterberg Upper Ecca. The two coals were upgraded to 85 and 93% inertinite- and vitrinite-rich concentrates, on visible mineral matter free basis. The coals were slow heated in inert atmosphere at  $20\text{ }^{\circ}\text{C min}^{-1}$  to 450, 700 and 1000  $^{\circ}\text{C}$  and held at that temperature for an hour. After the HCl-HF treatment technique at ambient temperatures, the characteristics of the coals and chars were examined with proximate, ultimate, helium density, porosity, surface area, petrographic, solid-state  $^{13}\text{C}$  NMR, XRD and HRTEM analytical techniques. The results largely showed that substantial transitions occurred at 700-1000  $^{\circ}\text{C}$ , where the chars became physically different but chemically similar. Consequently, the chars at the highest temperature (1000  $^{\circ}\text{C}$ ) drew attention to the detailed study of the atomistic properties that may give rise to different reactivity behaviours with  $\text{CO}_2$  gas.

The H/C atomic ratios for the inertinite- and vitrinite-rich chars were respectively 0.31 and 0.49 at 450  $^{\circ}\text{C}$  and 0.10 and 0.12 at 1000  $^{\circ}\text{C}$ . The true density was respectively 1.48 and 1.38  $\text{g.cm}^{-3}$  at 450  $^{\circ}\text{C}$  and 1.87 and 1.81  $\text{g.cm}^{-3}$  at 1000  $^{\circ}\text{C}$ . The char form results from the petrographic analysis technique indicated that the 700-1000  $^{\circ}\text{C}$  inertinite-rich chars have lower proportions of thick-walled isotropic coke derived from pure vitrinites (5-8%) compared with the vitrinite-rich chars (91-95%). This property leads to the creation of pores and increases of volume and surface area as the softening walls expand. It was found that the average crystallite diameter,  $L_a$ , and the mean length of the aromatic carbon fringes from the XRD and HRTEM techniques, respectively, were in good agreement and made a definite distinction between the 1000  $^{\circ}\text{C}$  inertinite- and

## ABSTRACT

---

vitritine-rich chars. The crystallite diameter on peak (10) approximations,  $L_a(10)$ , of 37.6Å for the 1000 °C inertinite-rich chars fell within the HRTEM's range of minimum-maximum length boundary of 11x11 aromatic fringes (27-45Å). The  $L_a(10)$  of 30.7Å for the vitritine-rich chars fell nearly on the minimum-maximum length range of 7x7 aromatic fringes (17-28Å.) The HRTEM results showed that the 1000 °C inertinite-rich chars comprised a higher distribution of larger aromatic fringes (11x11 parallelogram catenations) compared with a higher distribution of smaller aromatic fringes (7x7 parallelogram catenations).

The mechanism for the similarity between the 700-1000 °C inertinite- and vitritine-rich chars was the greater transition occurring in the vitritine-rich coal to match the more resistant inertinite-rich coal. This emphasised that the transitions in the properties of vitritine-rich coals were more thermally accelerated than those of the inertinite-rich coals. The similarity between the inertinite- and vitritine-rich chars was shown by the total maceral reflectance, proximate, ultimate, skeletal density and aromaticity results. Evidence for this was the carbon content by mass for the inertinite- and vitritine-rich chars of respectively 90.5 and 85.3% at 450 °C and 95.9 and 94.1% at 1000 °C. The aromaticity from the XRD technique was respectively 87 and 77% at 450 °C and 98 and 96% at 1000 °C. A similar pattern was found in the hydrogen and oxygen contents, the atomic O/C ratios and the aromaticity from the NMR technique.

The subsequent construction of large-scale molecular structures for the 1000 °C inertinite-rich chars comprised 106 molecules constructed from a total of 42929 atoms, while the vitritine-rich char model was made up of 185 molecules consisting of a total of 44315 atoms. The difference between the number of molecules was due to the inertinite-rich char model comprising a higher distribution of larger molecules compared with the vitritine-rich char model, in agreement with the XRD and HRTEM results. These char structures were used to examine the behaviour on the basis of gasification reactivity with CO<sub>2</sub>.

The density functional theory (DFT) was used to evaluate the interactions between CO<sub>2</sub> and the atomistic representations of coal char derived from the inertinite- and vitritine-

---

## ABSTRACT

---

rich South African coals. The construction of char models used the modal aromatic fringes (fringes of highest frequencies in size distributions) from the HRTEM, for the inertinite- and vitrinite-rich chars, respectively (11x11 and 7x7 parallelogram-shaped aromatic carbon rings). The structures were DFT geometrically optimized and used to measure reactivity with the Fukui function,  $f^+(r)$  and to depict a representative reactive carbon edge for the simulations of coal gasification reaction mechanism with  $\text{CO}_2$  gas. The  $f^+(r)$  reactivity indices of the reactive edge follows the sequence: zigzag C remote from the tip C ( $C_{zi} = 0.266$ ) > first armchair C ( $C_{r1} = 0.087$ ) > tip C ( $C_t = 0.075$ ) > second armchair C ( $C_{r2} = 0.029$ ) > zigzag C proximate to the tip C ( $C_z = 0.027$ ). The DFT simulated mean activation energy,  $\Delta E_b$ , for the gasification reaction mechanism (formation of second CO gas molecule) was  $233 \text{ kJ mol}^{-1}$ . The reaction for the formation of second CO molecule is defines gasification in essence. The experimental activation energy determined with the TGA and random pore model to account essentially for the pore variation in addition to the gasification chemical reaction were found to be very similar:  $191 \pm 25 \text{ kJ mol}^{-1}$  and  $210 \pm 8 \text{ kJ mol}^{-1}$ ; and in good agreement with the atomistic results. The investigation gave promise towards the utility of molecular representations of coal char within the context of fundamental coal gasification reaction mechanism with  $\text{CO}_2$ .

## OPSOMMING

---

### Opsomming

Vooruitgang in die kennis van die chemiese struktuur van steenkool en die ontwikkeling van hoëwerkverrigting-rekenaartegniese het gelei meer as honderd vier en dertig voorgestelde molekulêre vlak voorstellings (modelle) van steenkool tussen 1942 en 2010. Hierdie modelle was feitlik almal steenkool van die noordelike halfrond. Daar is net twee molekulêre modelle gebaseer op die inertiniet- en vitrinietryke steenkool uit die suidelike halfrond. Die huidige ondersoek is gebaseer op die sintels afgelei van die Perm-ouderdom van steenkool in twee groot Suid-Afrikaanse steenkoolvelde, Witbank # 4 rif en Waterberg-Bo-Ecca. Die twee steenkole is opgegradeer tot 85 en 93% inertiniet- en vitrinietryke konsentrate, respektiewelik, op 'n sigbare mineraal-vry basis. Die steenkool is stadig verhit in 'n inerte atmosfeer teen  $20^{\circ}\text{C min}^{-1}$  tot  $450$ ,  $700$  en  $1000^{\circ}\text{C}$  en by daardie temperatuur vir een uur gehou. Na toepassing van die HCl/HF-behandelingstegniek by omgewingstemperatuur, is die eienskappe van die steenkool en sintels ondersoek met kort-analise, eind-analise, heliumdigtheid, porositeit, oppervlakte, petrografiese, vastetoestand  $^{13}\text{C}$  KMR-, XSD en HRTEM analitiese tegnieke. Die resultate het getoon dat aansienlike oorgange plaasgevind het by  $700$ - $1000^{\circ}\text{C}$ , waar die sintels fisies verander is, maar chemies soortgelyk was. Gevolglik het die sintels op die hoogste temperatuur ( $1000^{\circ}\text{C}$ ) die aandag gelei na die gedetailleerde studie van die atomiese eienskappe wat aanleiding gee tot verskillende reaktiwiteit-gedrag met  $\text{CO}_2$  gas.

Die H/C atoomverhoudings vir die inertiniet- en vitrinietryke sintels was onderskeidelik  $0.31$  en  $0.49$  by  $450^{\circ}\text{C}$  en  $0.10$  en  $0.12$  by  $1000^{\circ}\text{C}$ . Die ware digtheid was onderskeidelik  $1.48$  en  $1.38 \text{ g cm}^{-3}$  by  $450^{\circ}\text{C}$  en  $1.87$  en  $1.81 \text{ g cm}^{-3}$  by  $1000^{\circ}\text{C}$ . Die sintelvorm-resultate van die petrografiese analisetegniek het aangedui dat die  $700$ - $1000^{\circ}\text{C}$  inertinietryke sintels 'n laer verhouding van dikwandige isotropiese kooks het, afgelei van suiwer vitriniete ( $5$ - $8\%$ ), in vergelyking met die vitrinietryke sintels ( $91$ - $95\%$ ). Hierdie eienskap lei tot die skepping van porieë en verhoog die volume en oppervlakte soos die versagte wande uitsit. Daar is gevind dat die gemiddelde kristallietdeursnee en die gemiddelde lengte van die aromatiese koolstofrande van die XSD- en HRTEM-tegnieke,

## OPSOMMING

---

onderskeidelik, goed ooreengekom het en 'n definitiewe onderskeid tussen die 1000°C inertiniet- en vitrinietryke sintels getref het. Die  $L_a(10)$  van 37.6Å vir die 1000°C inertinietryke sintels het binne die HRTEM reeks van minimum-maksimum lengtegrens van 11x11 aromatiese rande (27-45Å) geval. Die  $L_a(10)$  van 30.7Å vir die vitrinietryke sintels het byna op die minimum-maksimum lengte reeks 7x7 aromatiese rand (17-28Å) geval. Die HRTEM-resultate het getoon dat die 1000 °C inertinietryke sintels bestaan het uit 'n hoër verspreiding van groter aromatiese rande (11x11 parallelogram-aaneenskakelings) in vergelyking met 'n hoër verspreiding van kleiner aromatiese rande (7x7 parallelogram-aaneenskakelings).

Die meganisme vir die ooreenkoms tussen die 700-1000 °C inertiniet- en vitrinietryke sintels was die groter oorgang in die vitrinietryke steenkool om die meer bestande inertiniet-ryke steenkool te ewenaar. Dit beklemtoon dat die oorgange in die eienskappe van vitrinietryke steenkool meer termies geaktiveer is as dié van die inertinietryke steenkool. Die ooreenkoms tussen die inertiniet- en vitrinietryke sintels is getoon deur die resultate van totale maseraalreflektansie, kort-analise, eind-analise, geraamde digtheid en aromatisiteit. Bewyse hiervoor was die koolstofinhoud volgens massa vir die inertiniet- en vitrinietryke sintels van onderskeidelik 90.5 en 85.3% by 450 °C en 95.9 en 94.1% by 1000 °C. Die aromatisiteit volgens die XSD-tegniek was onderskeidelik, 87 en 77% by 450°C en 98 en 96% teen 1000°C. 'n Soortgelyke patroon is vir die waterstof- en suurstofinhoud gevind, die atoom O/C verhoudings en die aromatisiteit dmv die KMR-tegniek.

Die daaropvolgende konstruksie van grootskaalse molekulêre strukture vir die 1000°C inertinietryke sintels bestaan uit 106 molekules wat saamgestel is uit 'n totaal van 42 929 atome, terwyl die vitrinietryke sintelmodel opgemaak is uit 185 molekules wat bestaan uit 'n totaal van 44 315 atome. Die verskil tussen die aantal molekules was te wyte aan die inertinietryke sintelmodel wat bestaan uit 'n groter verspreiding van groter molekules in vergelyking met die vitrinietryke sintelmodel, in ooreenstemming met die XSD- en HRTEM-resultate. Hierdie sintelstrukture is gebruik om die gedrag op grond van vergassingsreaktiwiteit met CO<sub>2</sub> te ondersoek.

## OPSOMMING

---

Die DFT is gebruik om die interaksies tussen CO<sub>2</sub> en die atomiese voorstellings van steenkool sintel, afgelei van die inertiniet- en vitrinietryke Suid-Afrikaanse steenkool, te evalueer. Die konstruksie van sintelmodelle het die aromatiese rande van die HRTEM gebruik, van die hoogste frekwensies vir die inertiniet- en vitrinietryke sintels, onderskeidelik (11x11 en 7x7). Die strukture is DFT-meetskuldig geoptimaliseer en gebruik om reaktiwiteit met die Fukui-funksie,  $f^+(r)$  te meet. Die 3x3 aromatiese steenkoolsintelstrukture is gebruik om 'n verteenwoordigende reaktiewe koolstofrand vir die evaluering van die steenkoolvergassingsreaksiemeganisme met CO<sub>2</sub> gas uit te beeld. Die  $f^+(r)$  reaktiwiteitsindekse van die reaktiewe rand het die volgorde: sigsag C ver van die punt C ( $C_{zi} = 0.266$ ) > eerste stoel C ( $C_{r1} = 0.087$ ) > punt C ( $C_t = 0.075$ ) > tweede stoel C ( $C_{r2} = 0.029$ ) > sigsag C naby die punt C ( $C_z = 0.027$ ). Die DFT-gesimuleerde gemiddelde aktiveringsenergie op die reaktiewe rand was 233 kJ mol<sup>-1</sup>. Die aktiveringsenergie  $E_a$ , bepaal met behulp van die ewekansige poriemodel om die porievariasie bykomend tot die chemiese reaksie in ag te neem, is ook gevind baie soortgelyk te wees vir die ontaste vitriniet- ( $191 \pm 25$  kJ mol<sup>-1</sup>) en inertinietryke sintels ( $210 \pm 8$  kJ mol<sup>-1</sup>). Goeie ooreenkoms is gevind tussen die DFT- en eksperimentele resultate. Die ondersoek hou belofte in vir die nut van molekulêre voorstellings van steenkoolsintel binne die konteks van die fundamentele steenkoolvergassingsreaksiemeganisme met CO<sub>2</sub>.

## KEYWORDS

---

### Keywords

- Advanced coal properties
- Pyrolysis
- Micro-image processing and analyses
- High performance computing
- Computational chemistry
- Molecular modelling
- Density functional theory
- Energy
- Reactivity
- Experimental verification
- Inertinite- and vitrinite-rich chars
- Fukui function
- Transition theory

# TABLE OF CONTENTS

---

## Table of contents

<b>Declaration</b>	<b>i</b>
<b>Acknowledgements</b>	<b>ii</b>
<b>Abstract</b>	<b>v</b>
<b>Opsomming</b>	<b>viii</b>
<b>Keywords</b>	<b>xi</b>
<b>Table of contents</b>	<b>xii</b>
<b>List of figures</b>	<b>xxii</b>
<b>List of tables</b>	<b>xxix</b>
<b>Publications in peer-reviewed journals</b>	<b>xxxii</b>
<b>Peer-reviewed conference proceedings</b>	<b>xxxiii</b>
<b>Chapter 1: General introduction</b>	<b>1</b>
<b>1.1 Background</b>	<b>1</b>
<b>1.2 Motivation</b>	<b>2</b>
<b>1.3 Problem statement</b>	<b>3</b>
<b>1.4 Objective</b>	<b>4</b>
<b>1.4.1 Background</b>	<b>4</b>
<b>1.4.2 Specific objectives</b>	<b>5</b>
<b>1.4.2.1 Characterisation</b>	<b>5</b>
<b>1.4.2.2 Construction of molecular models</b>	<b>5</b>

# TABLE OF CONTENTS

---

1.4.2.3 Perform atomistic reactivity simulations between char models and carbon dioxide gas molecules .....	6
1.4.2.4 Determination of reaction kinetics .....	6
1.5 Scope and outline of the research project .....	6
1.5.1 Background .....	6
1.5.2 Breakdown by chapter .....	7
Nomenclature .....	10
1.6 References .....	11
Chapter 2: Literature overview .....	12
2.1 Introduction .....	12
2.2 Origin and nature of coal deposits.....	12
2.2.1 Global coal deposits .....	13
2.2.2 The South African coal deposits .....	14
2.3 Coal utilisation.....	15
2.3.1 Background .....	15
2.3.2 Coal gasification.....	16
2.4 Reaction phases during gas-solid interactions in gasification.....	19
2.4.1 Devolatilisation of coal .....	19
2.4.2 Coal char gasification reactions.....	20
2.4.3 Gas phase reactions in a coal gasifier .....	22
2.5 Coal and char characterisation .....	22

# TABLE OF CONTENTS

---

2.5.1 Standard analyses.....	23
2.5.1.1 Proximate analyses .....	24
2.5.1.2 Ultimate analyses .....	25
2.5.1.3 Petrographic analysis .....	26
2.5.1.4 Physical structural properties .....	28
2.5.2 Additional structural properties (XRD, HRTEM, NMR).....	30
2.5.2.1 The X-ray diffraction (XRD).....	30
2.5.2.2 High resolution transmission electron microscopy.....	34
2.5.2.3 Solid state <sup>13</sup> C nuclear magnetic resonance spectroscopy.....	37
2.6 Molecular modelling.....	40
2.6.1 Molecular models for bituminous coal .....	41
2.6.2 Atomistic models for the coal char formation.....	44
2.7 Reactivity of coals chars .....	48
2.7.1 Reaction rate regimes .....	48
2.7.1.1 Chemical-reaction rate control.....	49
2.7.1.2 Diffusion-reaction rate control .....	50
2.7.1.3 Gas film bulk-diffusion rate control .....	50
2.7.2 Reaction rate models .....	51
2.7.2.1 Background .....	51
2.7.2.2 Random pore model.....	51
2.8 Molecular reactivity modelling .....	53

---

# TABLE OF CONTENTS

---

2.8.1 The Dmol <sup>3</sup> and density functional theory .....	54
2.8.2 The Fukui function .....	54
2.8.3 Fundamental gasification reaction mechanism .....	56
2.8.4 Application and behaviour of molecular models for coal and char ....	59
2.9 Experimental verification .....	60
Nomenclature .....	61
2.10 References .....	64
<b>Chapter 3: Coal and char characterisation.....</b>	<b>76</b>
3.1 Abstract.....	76
3.2 Introduction and background.....	78
3.3 Experimental methods .....	79
3.3.1 Sample preparation .....	79
3.3.2 Characterisation of coals and chars .....	82
3.3.3 The NMR and XRD techniques .....	84
3.4 Results .....	86
3.4.1 Chemical properties .....	86
3.4.2 Physical properties .....	87
3.4.3 Petrographic properties .....	89
3.4.3.1 Coals .....	89
3.4.3.2 Chars .....	91
3.4.4 Solid-state <sup>13</sup> C nuclear magnetic resonance .....	95

---

# TABLE OF CONTENTS

---

3.4.5 X-ray diffraction.....	98
3.5 Conclusions.....	102
Nomenclature .....	104
3.6 References.....	107
<b>Chapter 4: Large-scale molecular modelling of chars .....</b>	<b>112</b>
4.1 Abstract.....	112
4.2 Introduction and background.....	114
4.3 Experimental methods .....	116
4.3.1 Coal and char characterisation .....	116
4.3.2 High-resolution transmission electron microscopy (HRTEM).....	116
4.3.3 Computational requirements and molecular modelling procedure ..	118
4.4 Results and Discussion .....	120
4.4.1 Petrographic analyses .....	120
4.4.2 Proximate and ultimate analysis .....	121
4.4.3 Skeletal density .....	122
4.4.4 Solid-state <sup>13</sup> C nuclear magnetic resonance (NMR) .....	122
4.4.5 X-ray diffraction (XRD) .....	124
4.4.6 High-resolution transmission electron microscopy .....	125
4.5 Construction of 3D molecular models of chars .....	126
4.5.1 The HRTEM and the aromatic skeleton of chars .....	126
4.5.2 Trimming.....	131

---

# TABLE OF CONTENTS

---

4.5.3 Hydrogen and oxygen functional atoms.....	133
4.5.4 Nitrogen and sulphur functional atoms .....	134
4.6 Evaluation of large-scale molecular models of chars.....	135
4.7 Conclusions.....	139
Nomenclature .....	140
4.8 References.....	141
<b>Chapter 5: Density functional theory molecular modelling and experimental particle kinetics for CO<sub>2</sub>-char gasification. ....</b>	<b>144</b>
5.1 Abstract.....	144
5.2 Introduction .....	145
5.3 Chars and Methodology.....	147
5.3.1 Char molecular models.....	147
5.3.2 The DFT computational methods .....	149
5.3.2.1 The DFT reactivity modelling with the Fukui function .....	151
5.3.2.2 The DFT modelling of char-CO <sub>2</sub> gasification reaction mechanism .....	153
5.3.3 Experimentation: Char-CO <sub>2</sub> reactivity (Particle kinetics).....	155
5.3.3.1 Thermogravimetric analyser.....	155
5.3.3.2 Experimental procedure.....	156
5.3.3.3 Calculation of activation energies.....	156
5.4 Results and Discussion .....	158

# TABLE OF CONTENTS

---

5.4.2 DFT reactivity modelling and the Fukui function .....	159
5.4.3 DFT modelling for char-CO <sub>2</sub> gasification reaction mechanism.....	164
5.4.3.1 The loss of H to form an active site.....	164
5.4.3.2 CO <sub>2</sub> chemisorption on reactive edge.....	168
5.4.3.3 The loss of first CO gas molecule through dissociation of adsorbed CO <sub>2</sub> gas molecule .....	172
5.4.3.4 Formation of the second CO gas molecule .....	175
5.5 Experimental reactivity and parameters (Particle kinetics).....	179
5.5.1 Validation of activation energy.....	181
5.5.2 Mechanisms of Char gasification by CO <sub>2</sub> .....	183
5.6 Conclusions.....	185
Nomenclature .....	187
5.7 References.....	190
<b>Chapter 6: Gasification experiments of 1000 °C chars with CO<sub>2</sub> gas.....</b>	<b>197</b>
6.1 Introduction .....	197
6.2 Reaction rate modelling.....	197
6.2.1 Reaction rate models .....	197
6.2.2 The random pore model.....	198
6.2.3 Evaluation procedure .....	199
6.3 Experimental.....	201
6.3.1 Thermogravimetric analyser.....	201

# TABLE OF CONTENTS

---

6.3.2 Experimental procedure.....	202
6.3.3 Reaction conditions .....	202
6.4 Results and Discussion .....	203
6.5 Modelling and evaluation of associated parameters .....	206
6.5.1 Model evaluation .....	206
6.5.2 Reaction rate parameters (intrinsic reaction rate parameters) .....	207
6.6 Conclusions.....	210
Nomenclature .....	212
6.7 References.....	214
<b>Chapter 7: General conclusions .....</b>	<b>216</b>
7.1 General conclusions .....	216
7.2 Contributions to the knowledge base of coal science and technology .....	219
7.3 Recommendations and future work.....	221
<b>Appendix: .....</b>	<b>222</b>
<b>Appendix A: Petrographic analyses .....</b>	<b>222</b>
A1. Blocks and macerals. (See figure captions for details) .....	222
A2 Repeatability of maceral counting.....	223
A3. Classification system for the coal chars.....	225
<b>Appendix B: The XRD analyses .....</b>	<b>228</b>

# TABLE OF CONTENTS

---

B.1: Changes in diffractogram patterns from parent coals to chars. See figure captions for details. ....	228
B.2. Comparison of XRD structural parameters. See figure captions for details.....	229
B.3: Comparison and reproducibility of selected diffractogram patterns. See Figure captions for details.....	230
Appendix C: The HRTEM image processing procedure.....	231
C1. Steps 1 and 2. Dissect the raw image into suitable areas and start cropping.....	231
C2. Steps 3 and 4. Apply fast Fourier transform filter forward followed by general ideal filter. ....	231
C3. Steps 5 and 6. Apply inverse fast Fourier transform filter followed by a suitable threshold level.....	232
C4. Step 7 and 8. Invert binary image and apply conditional smoothing.....	232
C5. Step 9 and 10. Skeletonise and trim .....	233
C6. Step 11 and 12. Colour by length and calculate all properties of the features (e.g. skeleton length).....	233
C7. Step 13. Conduct scale adjustments by cropping an area containing the scale bar at a size equal to Step 1. Correct the data accordingly. ....	234
C.8 Noise separated during trimming exercises .....	235
Appendix D: Spin states for the molecular structures used in Chapter 5.....	236
Appendix E: Reproducibility of the TGA experimental results .....	237

# TABLE OF CONTENTS

---

Appendix F: Uncertainty limits associated with calculation of activation energies.....238

## LIST OF FIGURES

---

### List of figures

Figure 2-1. The XRD spectra showing the three characteristic peaks (Lu <i>et al.</i> , 2001:1821; Everson <i>et al.</i> , 2013:148).....	31
Figure 2-2. Determination of amorphous fraction of carbon ( $x_A$ ), from Gaussian curve deconvolution (Everson <i>et al.</i> , 2013:148).....	33
Figure 2-3. The conventional ((a)-(f) up to (i)) and the advanced filtration technique ((a)-(h) up to (j)-(k)) (Sharma <i>et al.</i> , 1999:1203).....	36
Figure 2-4. Typical HRTEM microphotograph (left-hand side) with its lattice fringes (right-hand side), after the advanced filtration technique (Sharma <i>et al.</i> , 2002:54; Sharma <i>et al.</i> , 1999:1203).....	36
Figure 2-5. The molecular representations of bituminous coal (Mathews and Chaffee, 2012:1): (a) Fuchs and Sandoff structure (Fuchs and Sandhoff, 1942:567), (b) Given (Given, 1960:147), (c) adapted from Given (Given, 1962:39), (d) Meyers (Meyers, 1981), (e) Cartz and Hirsch (Cartz and Hirsch, 1960:557), (f) Ladner (as printed in Gibson (Mathews and Chaffee, 2012:1)) (Gibson, 1978:67), (g) Solomon (Solomon, 1981:61), (h) Hill and Lyon (Hill and Lyon, 1962:36), (i) adapted from Wisser (Wisser, 1984:325), (j) Shinn (Shinn, 1984:1187). Structures are reprinted with permission of the copyright holders (Mathews and Chaffee, 2012:1). .....	43
Figure 2-6. Selected molecular representations of bituminous coal (Mathews and Chaffee, 2012:1): (a-f) the space-filling representation of Spiro (Spiro, 1981:1121), (a) Wisser model, (b) Given model, (c) Solomon model, (d) Wisser model, (e) Solomon model, (f) Solomon model globular configuration, (g) Lazarov and Marinov (Lazarov and Marinov, 1987:411), (h) Zao Zhuang coal model (Nomura, Artok, Murata, Yamamoto, Hama, Gao, and Kiden) (Nomura <i>et al.</i> , 1998:512), (i) Takanohashi <i>et al.</i> Upper Freeport model (Takanohashi and Kawashima, 2002:379), (j) Narkiewicz and Mathews (Narkiewicz and Mathews, 2008:3104), (k-l) inertinite-rich and vitrinite-rich models of Van	

## LIST OF FIGURES

---

Niekerk and Mathews (Niekerk and Mathews, 2010:73). Structures were reprinted with permission of the copyright holders (Mathews and Chaffee, 2012:1).....	45
Figure 2-7. Structure of coal-to-char transitions derived via molecular modelling approaches (Mathews <i>et al.</i> , 2011:718). ((a), left-hand side) drop-tube reactor temperature profile and SEM of coal and char particles, and molecular models of coal and chars for Lewiston–Stockton vitrinite (Mathews <i>et al.</i> , 1998:136). ((b), right-hand side) Pittsburgh #8 coal to char transitions ((b), right hand side) for wire-mesh generated chars (Jones <i>et al.</i> , 1999:1737). Copyright Elsevier (1999) (Mathews <i>et al.</i> , 2011:718). Reprinted with permission (Mathews <i>et al.</i> , 2011:718). .....	46
Figure 2-8. Coal char structures. ((a), left-hand side) Marzec oligomeric C <sub>173</sub> H <sub>88</sub> O <sub>2</sub> model for low-temperature coal char (Marzec, 1997:837). In ((a), left-hand side), arrows indicate H atoms that are less than 0.1 nm apart; strong repulsive forces between them make the planar conformer unstable (Marzec, 1997:837). ((b), right-hand side) Castro-Marcano Illinois No. 6 coal chars; composed of 7458 atoms (C <sub>5743</sub> H <sub>1511</sub> O <sub>131</sub> N <sub>61</sub> S <sub>12</sub> ) within 66 molecules (Castro-Marcano <i>et al.</i> , 2012:1272), where green = C, white = H, red = O, blue = N and yellow = S.....	47
Figure 2-9. Illustration of four different CO <sub>2</sub> chemisorption orientations on different char models. Zigzag models (z4, z5, z7, z9), armchair models (a3, a5) and tip models (t3, t4). Numbers after the letters represent the number of six-membered carbon rings (Montoya <i>et al.</i> , 2003:29).....	58
Figure 3-1. Schematic representation of char generation equipment.....	80
Figure 3-2. Surface area and porosity transitions of the IR and VR particles with temperature. ....	88
Figure 3-3. Total (Mean random) reflectance scan (Rsc%) for coals and chars.....	92
Figure 3-4. Maceral contents for (a) inertinite-rich coals and chars and (b) vitrinite-rich coals and chars, where mmb = visible mineral matter basis.....	93

## LIST OF FIGURES

---

Figure 3-5. Transformation of inertinites, vitrinites and inerts from (a) coals (left-hand side) to (b) char forms (right-hand side) with increasing temperature, where IR and VR = inertinite- and vitrinite-rich, respectively. ....	95
Figure 3-6. The NMR spectra, where: (a) - (d) = inertinite-rich particles (chars-coal) and (e) – (h) = vitrinite-rich particles (chars - coal); @numbers = temperatures in °C.....	97
Figure 3-7. Baseline corrected and smoothed XRD diffractograms of coals and chars, where: (a) and (b) = inertinite- and vitrinite-rich particles, respectively; (c)–(f) = inertinite- vs vitrinite-rich particles. Numbers in the legends = temperatures in °C.....	99
Figure 4-1. Dissections showing cropped HRTEM images. ....	118
Figure 4-2. The <sup>13</sup> C NMR spectra of the inertinite- and vitrinite-rich chars generated at 1000 °C ((a) and (c), left-hand side) and their corresponding parent coals ((b) and (d), right-hand side). ....	123
Figure 4-3. Baseline corrected and smoothed XRD diffractograms of chars generated at 1000 °C ((a), left-hand side) and parent coals ((b), right-hand side). ....	125
Figure 4-4. HRTEM results. HRTEM results. Cropped image ((a), left-hand side) and skeletonised image after image processing ((b), right-hand side). ....	127
Figure 4-5. A 21x21 parallelogram-shaped aromatic fringe showing maximum (MaxL) and minimum (MinL) lengths.....	128
Figure 4-6. Aromatic fringe length distributions from the HRTEM. ....	131
Figure 4-7. An example of 25 aromatic fringes of length distributions from the HRTEM, used during the model constructions.....	132
Figure 4-8. Example of geometric representations of char molecules after trimming an 11x11 aromatic fringe. ....	133

## LIST OF FIGURES

---

- Figure 4-9. Cross-linked ((a), left-hand side) and individual ((b), right-hand) molecules with their functional atoms. Green = C and white = H..... 134
- Figure 4-10. Geometry optimised and annealed 3D molecular models of inertinite-rich chars ((a), left-hand side) and vitrinite-rich chars ((b, right-hand side). Green = C, white = H, red = O, blue = N and yellow = S. .... 136
- Figure 5-1. HRTEM results. Microphotograph for the inertinite-rich chars ((a), top left) with scale bar = 5 nm. Lattice after image processing ((b), top right). Parallelogram catenations ((c), bottom left). Distributions of aromatic raft lengths ((d), bottom right), where, dark and light bars = inertinite- and vitrinite-rich chars, respectively. .... 159
- Figure 5-2. The PAH char models used to determine the nucleophilic Fukui values of the edge carbon sites, where (a), (b) and (c) = 3x3, 4x4 and 5x5 structures, respectively..... 160
- Figure 5-3. Geometry optimized structures for H-loss from (a) benzene molecule at (b) *para*-, (c) *meta*- and (d) *ortho*-carbon sites..... 165
- Figure 5-4. Geometry optimised structures for H-loss from (a) 3x3 char structure at (b)-(f) =  $C_1^-$ ,  $C_2^-$ ,  $C_{2i}^-$ ,  $C_{r1}$  and  $C_{r2}$ -carbons, respectively..... 166
- Figure 5-5. Structures with free edge carbon sites, where (a) = Benzene (left-hand side) and (b) = 3x3 char (right-hand side)..... 167
- Figure 5-6. Various optimised structures for the CO<sub>2</sub> chemisorption on single active sites in the reactive C\* edge. Top left is 3x3 char model (a), Top right is CO<sub>2</sub> model (b), (c) is the 3x3 char model with free active sites and (d) to (h) the chemisorption structures. Red = oxygen atoms..... 169
- Figure 5-7. Bond bending and elongations of geometry optimised CO<sub>2</sub>-C\* chemisorption structures, where: red = oxygen atoms. .... 172
- Figure 5-8. Ground state reactants (a), (left-hand side) and products (b), (right-hand side) structures used for the computation of CO<sub>2</sub> dissociation on C<sub>zi</sub>. .... 173

## LIST OF FIGURES

---

Figure 5-9. Transition state structure at $C_{zi}$ (a) (left-hand side). Ground state char(C=O) quinone structure (b) (reactants) for the loss of second CO on $C_{zi}$ . Numbers = bond lengths in Å.....	176
Figure 5-10. Transition state structures for the decomposition reactions at respective active sites (i.e. reactive edge), where, (a)-(e) = results at $C_{zi}$ , $C_t$ , $C_z$ , $C_{r1}$ and $C_{r2}$ , respectively. Red = oxygen atoms.....	178
Figure 5-11. Conversion-time plot for inertinite- and vitrinite-rich chars, where, (a), left-hand side = inertinite-rich char and (b), right-hand side = vitrinite-rich chars.....	180
Figure 5-12. Influence of isothermal reaction temperatures on the lumped reaction rates of the chars.....	180
Figure 5-13. Validation of activation energy calculated according to atomistic reaction kinetics with experimental results obtained from thermogravimetric experimentation. ....	181
Figure 5-14. Comparison of experimental and model predictions. ....	182
Figure 5-15. Comparison of activation energies. ....	183
Figure 5-16. Mechanisms of char gasification by $CO_2$ , where (a) = chemisorption of $CO_2$ to active sites in char, (b) = yield of first CO and (c) = yield of second CO. ....	185
Figure 6-1. Raw TGA results of the isothermal char- $CO_2$ gasification at 900 °C.....	204
Figure 6-2. Influence of isothermal gasification reaction temperature on the reactivity of the (a) IR (left-hand side) and (b) VR chars (right-hand side).....	205
Figure 6-3. Comparison of the $CO_2$ gasification reactivity of the IR and VR chars. Conversion-time plot at 900 °C (a), left-hand side and 980 °C (b), right-hand side, respectively. ....	206
Figure 6-4. Fractional carbon conversion vs reduced time plots of (a) Char IR; and (b) Char VR; at all the isothermal reaction temperatures.....	206

## LIST OF FIGURES

---

Figure 6-5. RPM fitting to the experimental data of (a) char IR, and (b) VR.....	208
Figure 6-6. Arrhenius plots of the char-CO <sub>2</sub> gasification reactions of chars IR and VR from RPM data.....	209
Figure A-1. Blocks prepared for petrographic analysis. ....	222
Figure A-2. Mayor macerals found during petrographic analysis. Inertodetrinite with semifusinite ((a), top row left). Semifusinite ((b) top row middle). Micrinite and pyrite in colotellinite ((c), top row right). Colotellinite ((d), bottom row left). Copotellinite between inertinites ((e), bottom row middle). Pseudovitrinite ((f), bottom row right). ....	223
Figure B-1. Diffractograms for inertinite- and vitrinite-rich particles on respective sets of axis. Inertinite-rich particles ((a), top left) and vitrinite-rich particles ((b), top right). Zoomed (002) band for inertinite-rich particles ((c), bottom left) and vitrinite-rich particles ((d), bottom right). IR and VR = inertinite- and vitrinite-rich, respectively.....	228
Figure B-2. Comparison of XRD structural parameters. IR and VR = inertinite- and vitrinite-rich, respectively. Numbers = temperature (°C). From top left to bottom right, (a) $d_{002}$ , (b) $L_c$ , (c) $N_{ave}$ , (d) $L_a$ (10) and $L_a$ (11), (e) $f_a$ , (f) $X_a$ , (g) $IOD$ , (h) $IOD$ compared with $X_a$ .....	229
Figure B-3. Selected diffractogram patterns. Inertinite-rich chars ((a), top left) and vitrinite-rich chars ((b), top right) at 450, 700 and 1000 °C. Reproducibility of diffractogram patterns for vitrinite-rich chars at 450 °C ((c), bottom left) and vitrinite-rich coals ((d), bottom right).....	230
Figure C-1. The HRTEM image for the vitrinite-rich chars generated at 1000 °C. Vitri1.G = area to be cropped ((Step 1), left-hand side) and cropped area ((Step 2), right-hand side).....	231
Figure C-2. Fast Fourier transform forward ((Step 3), left-hand side) followed by a general ideal filter ((Step 4), right-hand side).....	231
Figure C-3. Inverse fast Fourier transform filter ((Step 5), left-hand side) followed by a suitable threshold level ((Step 6), right-hand side).....	232
Figure C-4. Binary image inverted ((Step 7, left-hand side) followed by an ideal conditional smoothing five times at high median ((Step 8, right-hand side).....	232

## LIST OF FIGURES

---

Figure C-5. Skeletonised binary image ((Step 9), left-hand side) followed by trimming ((Step 10, right-hand side).....	233
Figure C-6. Final results of lattice coloured by length ((Step 11), left-hand side) and representation of all selected features properties after a calculation Step.12 (right-hand side).....	233
Figure C-7. Scale adjustment.....	234
Figure C-8. Example of unwanted features extracted during the trimming process.....	235
Figure E-1. Reproducibility results for char at 960 °C.....	237

## LIST OF TABLES

---

### List of tables

Table 1-1. Scope of the research project.....	8
Table 2-1. Main coal gasification reactions.....	21
Table 2-2. Four stages for the change of the micro-texture during carbonization up to 3000 °C (Feng <i>et al.</i> , 2002:481). .....	35
Table 2-3. Typical structural parameters from solid-state <sup>13</sup> C NMR for vitrinite-rich Waterberg and inertinite-rich Highveld coals (Van Niekerk <i>et al.</i> , 2008:290). .....	38
Table 3-1. Proximate and ultimate analysis of parent coals and chars. ....	87
Table 3-2. Major physical and structural parameters of demineralised coals and de-ashed chars.....	88
Table 3-3. Vitrinite random reflectance for the density separated (parent) coals. ....	89
Table 3-4. Maceral compositions for the parent coals (% by volume).....	90
Table 3-5. Microlithotype analysis of the parent coals. ....	91
Table 3-6. Char form analysis and summary of major reflectance properties, following classification published in Everson <i>et al.</i> (Everson <i>et al.</i> , 2008:3082). .....	94
Table 3-7. Structural and lattice parameters for inertinite and vitrinite coals and chars.....	98
Table 3-8. Summary of structural parameters extracted from the XRD diffractograms. ....	101
Table 4-1. Proximate and ultimate analysis of parent coal and char.....	121
Table 4-2. Summary of structural parameters extracted from the XRD diffractograms .....	125
Table 4-3. Allocation of parallelogram-shaped aromatic fringes from the HRTEM fringe results.....	130
Table 4-4. Comparison between the inertinite- and vitrinite-rich char models.....	137

---

## LIST OF TABLES

---

Table 4-5. Model and experimental results for the inertinite- and vitrinite-rich chars with C normalised to 1000 .....	138
Table 5-1. Definition of H-terminated edge carbons, including position and quantity. ....	160
Table 5-2. Reactivity of 3x3 ((a), left-hand side), 4x4 ((b), middle) and 5x5 ((b), right-hand side) coal char models from $f^*(r)$ . ....	162
Table 5-3. Calculated $\Delta E_b$ and $E_{\text{reac}}$ values for the loss of H from the benzene and 3x3 char structures. ....	167
Table 5-4. Distribution of Fukui indices on the 3x3 char model with a reactive edge. ....	169
Table 5-5. Simulation energetics for CO <sub>2</sub> -char chemisorption at the reactive edge. ....	171
Table 5-6. Computed $E_{\text{reac}}$ and $\Delta E_b$ for loss of the first CO gas molecule. ....	174
Table 5-7. Computed $\Delta E_b$ and $E_{\text{reac}}$ for loss of second CO gas molecule. ....	177
Table 5-8. Estimated reaction parameters. ....	182
Table 6-1. Reaction conditions for char-CO <sub>2</sub> gasification experiments. ....	203
Table 6-2. Model parameters. ....	207
Table 6-3. Models used, structural parameter, and kinetic parameters obtained for char-CO <sub>2</sub> gasification reaction by other investigators. ....	210
Table A-1. Theoretical standard deviation and repeatability limit of the percentage of a component, based on counts of 500 points. ....	224
Table A-2. Classification system used in the petrographic analyses of chars. ....	225
Table D-1. Spin states for the molecular structures used in Chapter 5. ....	236
Table F-1. Determination of experimental error from different Arrhenius plots ( $N = 7$ ; $DF = 14$ ; $CI = 95\%$ )*. ....	238

## LIST OF TABLES

---

Table F-2. Summary of estimated activation energies from the gasification experiments with uncertainties.....	238
---	-----

## PUBLICATIONS AND PARTICIPATION IN CONFERENCES

---

### Publications in peer-reviewed journals

This section contains published work in accredited, peer-reviewed journals.

**Publication 1.** Mokone J. Roberts, Raymond C Everson, Hein W.J.P. Neomagus, Gregory N. Okolo, Daniel Van Niekerk, Jonathan P. Mathews. *The characterisation of slow-heated inertinite- and vitrinite-rich pyrolysis chars from selected South African coalfields*. FUEL, 2015. 158: p. 591-601.

**Publication #2.** Mokone J. Roberts, Raymond C. Everson, Hein W.J.P. Neomagus, Daniel Van Niekerk, Jonathan P. Mathews, David J. Branken. *Influence of maceral composition on the structure, properties and behaviour of chars derived from South African coals*. FUEL, 2015. 142: p. 9-20.

**Publication #3.** Mokone J. Roberts, Raymond C. Everson, George Domazetis, Hein W.J.P. Neomagus, Cornelia G.C.E. Van Sittert, Gregory N. Okolo, J.M. Jones, Daniel Van Niekerk, Jonathan P. Mathews. *Density functional theory molecular modelling and experimental particle kinetics for CO<sub>2</sub>-char gasification*. CARBON, 2015. 93: p. 295-314.

**Publication #4.** Gregory N. Okolo, Raymond C. Everson, Hein W.J.P. Neomagus, Mokone J. Roberts, Richard Sakurovs. *Comparing the porosity and surface areas of coal as measured by gas adsorption, mercury intrusion and SAXS techniques*. FUEL, 2015. 141 (0): p. 293-304.

**Publication #5.** Gregory N. Okolo, Raymond C. Everson, Hein W.J.P. Neomagus, Mokone J. Roberts, Richard Sakurovs. *Chemical-structural properties of South African bituminous coals: Insights from wide angle XRD-carbon fraction analysis, ATR-FTIR, solid state <sup>13</sup>C NMR and HRTEM techniques*. FUEL, 2015. 158: p. 779-792.

## PUBLICATIONS AND PARTICIPATION IN CONFERENCES

---

### Peer-reviewed conference proceedings

**Conference #1.** Mokone J. Roberts, Raymond C. Everson, Hein W.J.P. Neomagus. 2012. *The molecular structure of selected South African coal-chars to elucidate fundamental principles of coal gasification*. Centre for High Performance Computing. National Meeting and Conference. International Convention Centre, Durban, KwaZulu-Natal Province, South Africa.

**Conference #2.** Mokone J. Roberts, Raymond C. Everson, Hein W.J.P. Neomagus. 2012. *Advanced characterisation of chars derived from inertinite- and vitrinite-enriched coal towards molecular structures*. The South African Institution of Chemical Engineers. Champagne Sports Resort and Conferencing Venue. Central Drakensberg, KwaZulu-Natal Province, South Africa.

**Conference #3.** Mokone J. Roberts, Raymond C. Everson, Hein W. J. P. Neomagus, Jonathan P. Mathews, George Domazetis, Cornelia G.C.E. van Sittert. 2013. *Molecular mechanics to model coal char structures and DFT to model their reactivity with CO<sub>2</sub> gas for synthetic gas production*. Centre for High Performance Computing. National Meeting and Conference. International Convention Centre, Cape Town, Western Cape Province, South Africa.

**Conference #4.** Mokone J. Roberts, Raymond C. Everson, Cornelia G.C.E. Van Sittert, Hein W.J.P. Neomagus, Daniel Van Niekerk, Jonathan P. Mathews, George Domazetis. 2013. *The molecular structure of selected South African coal-chars to elucidate fundamental principles of the reaction between char and carbon dioxide*. International Conference of Coal Science and Technology. State College City, Pennsylvania State, USA.

## PUBLICATIONS AND PARTICIPATION IN CONFERENCES

---

**Conference #5.** Mokone J. Roberts, Raymond C. Everson, Hein W. J. P. Neomagus, Daniel Van Niekerk, Jonathan P. Mathews, George Domazetis, Cornelia G.C.E. Van Sittert. 2013. *Properties of chars derived from South African inertinite- and vitrinite-rich coals using molecular modelling*. Fossil Fuel Foundation. Stonehenge Conference Centre, Parys, North West Province, South Africa.

# CHAPTER 1: GENERAL INTRODUCTION

---

## Chapter 1: General introduction

This thesis comprises a collection of three papers prepared for publication in accredited journals. The three papers respectively cover the characterisation of coal chars, construction of large-scale molecular representations of coal chars and atomistic reactivity simulation of the reactivity of coal char models with carbon dioxide, including validation of results with experimental work. Chapter 1 gives a brief introductory overview and orientation of this thesis from the beginning, through the execution steps and, finally, the conclusion. Accordingly, the chapter is subdivided into sections 1.2 to 1.6 with specific attention to the background behind the study, attributes of the project motivation, the specific problem in the current knowledge on the topic and opportunities for the research at hand, formulated hypothesis of the central theoretical statement, research objectives and project scope respectively.

### 1.1 Background

Coal plays an important role towards the world's primary sources of energy and is likely to continue for foreseeable time. Coal has spurred the industrial revolutions of many countries because a variety of chemicals and compounds can be derived from coal and it has also been an important contributor to infrastructure for development. For example, in China, coal is the major fossil fuel consumed, facilitating the growing economic development. South Africa makes electricity and liquid transportation fuels from coal (DMR, 2011/2012:201). Many industrialised nations, such as the United States, have for decades selected coal as the fuel of choice (Smith, 1994). Other industrial spin offs by coal is the metallurgical coke, which is vital in the production of steel.

Coal contributed 27.3% of world primary energy in 2012 (EIA, 2012). Total world's coal reserves were estimated at about 860.9 Bt in 2012, according to the mineral economics statistics collated by the South African Department of Mineral Resources (DMR, 2011/2012:201). South Africa holds the world's eighth-largest amount of recoverable

## CHAPTER 1: GENERAL INTRODUCTION

---

coal reserves (30.2 billion tons). This value accounted for 95% of total African coal reserves and nearly 4% of total world reserves. Coal producing countries of the world aggregated about 7695.5 Mt in 2012 and South Africa was a significant participant, accounting for the 7<sup>th</sup> highest production. In the same year, China alone accounted for more than three-quarters of incremental coal production, while domestic consumption was more than three times that of global trade (IEA, 2012). The top six global coal suppliers include Indonesia, Australia, Russia, USA, Colombia and South Africa (DMR, 2011/2012:201).

Coal is highly heterogeneous and requires several analytical techniques for its characterisation to predict its behaviour during conversion processes such as combustion and gasification. Standard analyses such as proximate, ultimate and ash provide only bulk characteristics (Gupta, 2007:451). The utilisation behaviour of coal based on these analyses does not adequately describe the impact of coal quality on conversion efficiencies and plant performance. The heterogeneity of the organic material in the coal arises from maceral constituents, classified in three groups, namely, inertinite, vitrinite, and liptinite (Van Krevelen, 1993; Falcon, 1987:323; Falcon, 1986; Yu *et al.*, 2003:1160). The mineral and volatile matter contents, functional groups and heterogeneity of coal macerals causes wide diversity in coal particle behaviour during pyrolysis, combustion and gasification processes and contributes to the complexity of structure of coal and its chars (Yu *et al.*, 2003:1160). Consequently, in-depth studies are required. A number of analytical techniques, such as XRD, <sup>13</sup>C NMR and HRTEM, are available to provide information on the chemical structure of coal.

### 1.2 Motivation

Advances in the knowledge of chemical structure of coal led to more than one hundred proposed molecular level representations (models) of coal during the past 50-100 years (Mathews and Chaffee, 2012:1). Some of these models were enhanced by the development of high performance computational techniques. The chemical information

---

## CHAPTER 1: GENERAL INTRODUCTION

---

was based almost exclusively on the carboniferous coals from the northern hemisphere. In contrast to this, there are only two molecular models based on the inertinite- and vitrinite-rich coals from the southern hemisphere (Niekerk and Mathews, 2010:73). The most economic utilisation of coal involves combustion and gasification processes, which consist of a char generation step prior to reaction with oxygen/carbon dioxide/steam. The knowledge of char structure and its impact on reactivity is desirable to efficient operation of combustion and gasification processes. Therefore, to supplement the scarce molecular representations of the Gondwana coals published by Van Niekerk *et al.* (Niekerk and Mathews, 2010:73), a project was formulated to construct molecular representations of chars derived from the South African inertinite- and vitrinite-rich coals. The resulting atomistic structures could be used to evaluate gasification reaction mechanisms with CO<sub>2</sub> using molecular modelling techniques.

### 1.3 Problem statement

Several papers exist on the molecular modelling studies to evaluate the reactivity of oxygen and oxygen-carrying gases with carbonaceous material (Montoya *et al.*, 2002:4236; Montoya *et al.*, 2003:29; Sendt and Haynes, 2005:2141; Sendt and Haynes, 2011:1851; Sendt and Haynes, 2005:629; Radovic, 2005:907; Radovic, 2009:17166). The studies include the chemisorption of oxygen-carrying gases on often simplistic representations of carbonaceous surfaces using the DFT modelling techniques (Montoya *et al.*, 2003:29; Sendt and Haynes, 2005:2141; Sendt and Haynes, 2005:629; Radovic, 2005:907). Montoya *et al.* used ab initio methods to model the kinetics of elementary reaction in carbonaceous material (Montoya *et al.*, 2002:4236). Radovic *et al.* used DFT to model the active carbon sites responsible for reaction with the oxygen-carrying gases and to demonstrate a dissociative chemisorption reaction of CO<sub>2</sub> on the active carbon sites (Radovic, 2009:17166; Radović *et al.*, 1983:849; Radovic, 2005:907). However, investigations were often on the chemisorption, dissociation or decomposition reactions on the carbonaceous surfaces, respectively, but not on all three reactions within a single investigation, which may represent a complete

## CHAPTER 1: GENERAL INTRODUCTION

---

gasification reaction mechanism. In addition to this, studies adopted carbon models not necessarily derived from coal. Coal macerals impart structural differences, consequently reactivity differences (Sun *et al.*, 2003:669; Zilm *et al.*, 1981:717). Fletcher *et al.* also highlighted that “the similarity in chemical structure of the chars is in contrast to the general trend in char reactivity (in oxygen)” (Fletcher *et al.*, 1992:643). The authors concluded that the principal causes of differences in de-ashed char reactivity are physical structure (e.g., active surface area/porosity) rather than chemical structure (Fletcher *et al.*, 1992:643).

Therefore, there was an opportunity to consider other properties such as crystallite size or molecular distributions and for the construction of molecular structures of chars derived from the inertinite- and vitrinite-rich coals and to evaluate the structure-reactivity relationship on an atomistic level. This relationship may be based on the char-carbon dioxide gasification reaction mechanism. Standard and other characterisation techniques could provide data, while high performance computing resources could enhance visualisation and accuracy.

### 1.4 Objective

#### 1.4.1 Background

The research objectives essential for the attainment of milestones are outlined here and include the specific objectives.

The objective of this investigation is to construct molecular structures of chars derived from the inertinite- and vitrinite-rich South African coals. An attempt was made to evaluate the structure-reactivity relationship based on the CO<sub>2</sub>-char gasification reaction mechanism at an atomistic level. The structural transformations of chars generated at 450, 700 and 1000 °C were analysed and the 1000 °C chars were targeted for the atomistic studies using high performance computational techniques. Coals with particle size distribution of 300-1000 μm were slowly heated at 20 °C minutes and kept at

---

## CHAPTER 1: GENERAL INTRODUCTION

---

respective temperatures for 60 min. Vapour phase secondary reactions of primary volatiles were minimised by inert gas flow rate of  $1.5 \text{ dm}^3 \text{ min}^{-1}$  (Xu and Tomita, 1987:627; Ahuja *et al.*, 1996:272).

### 1.4.2 Specific objectives

Four specific objectives are outlined below as essential pillars of the investigation.

#### 1.4.2.1 Characterisation

**Standard analyses.** These include chemical and physical parameters by means of petrographic, proximate, ultimate, skeletal density, surface area and porosity analyses of density-separated inertinite- and vitrinite-rich coals and their corresponding chars generated at 450, 700, and 1000 °C.

**Other analyses.** Structural characterisation techniques include the X-ray diffraction (XRD) and solid-state  $^{13}\text{C}$  nuclear magnetic resonance (NMR) for the density separated inertinite- and vitrinite-rich coals and their corresponding chars generated at 450, 700, and 1000 °C. The high resolution transmission electron microscopy (HRTEM) may only be used on the 1000 °C chars for the purposed of atomistic modelling.

#### 1.4.2.2 Construction of molecular models

Analytical data was used to construct molecular models of the de-ashed chars generated from inertinite- and vitrinite-rich coals at 1000 °C using the available high-performance computational resources such as the Material Studio<sup>R</sup>. The results here were a set-up to explore the structure-reactivity relationship.

## CHAPTER 1: GENERAL INTRODUCTION

---

### 1.4.2.3 Perform atomistic reactivity simulations between char models and carbon dioxide gas molecules

Atomistic simulations were conducted with a quantum mechanics technique of high accuracy, the density functional theory (DFT) for geometry optimisations, single-point energy calculations and transition state search calculations centred on proposed CO<sub>2</sub>-char gasification reaction mechanism. This was meant as an attempt to demonstrate the utility of molecular models.

### 1.4.2.4 Determination of reaction kinetics

Reactivity measurements of de-ashed chars generated from inertinite- and vitrinite-rich coals at 1000 °C were carried out using an experimental thermogravimetric analyser with CO<sub>2</sub> as reactant gas at atmospheric pressure. The results here were compared with those from atomistic reactivity simulations.

## 1.5 Scope and outline of the research project

### 1.5.1 Background

The details of project execution including methods, results, conclusions, recommendations and contributions to the knowledge base of coal science and technology, are outlined in chapter dissections (Section 1.5.2), read in conjunction with Table 1-1.

The research commenced with the rationale for the selection of coals. The Permian-aged Gondwana coals in South Africa; of both the inertinite and vitrinite origin, have significant local and global economic impact. However, the volume of research on these coals is far too low compared to their carboniferous counterparts in the northern hemisphere. Therefore, the two coals from the Witbank #4 and the Waterberg Upper Ecca seams were selected. The coal samples were subjected to laboratory density

## CHAPTER 1: GENERAL INTRODUCTION

---

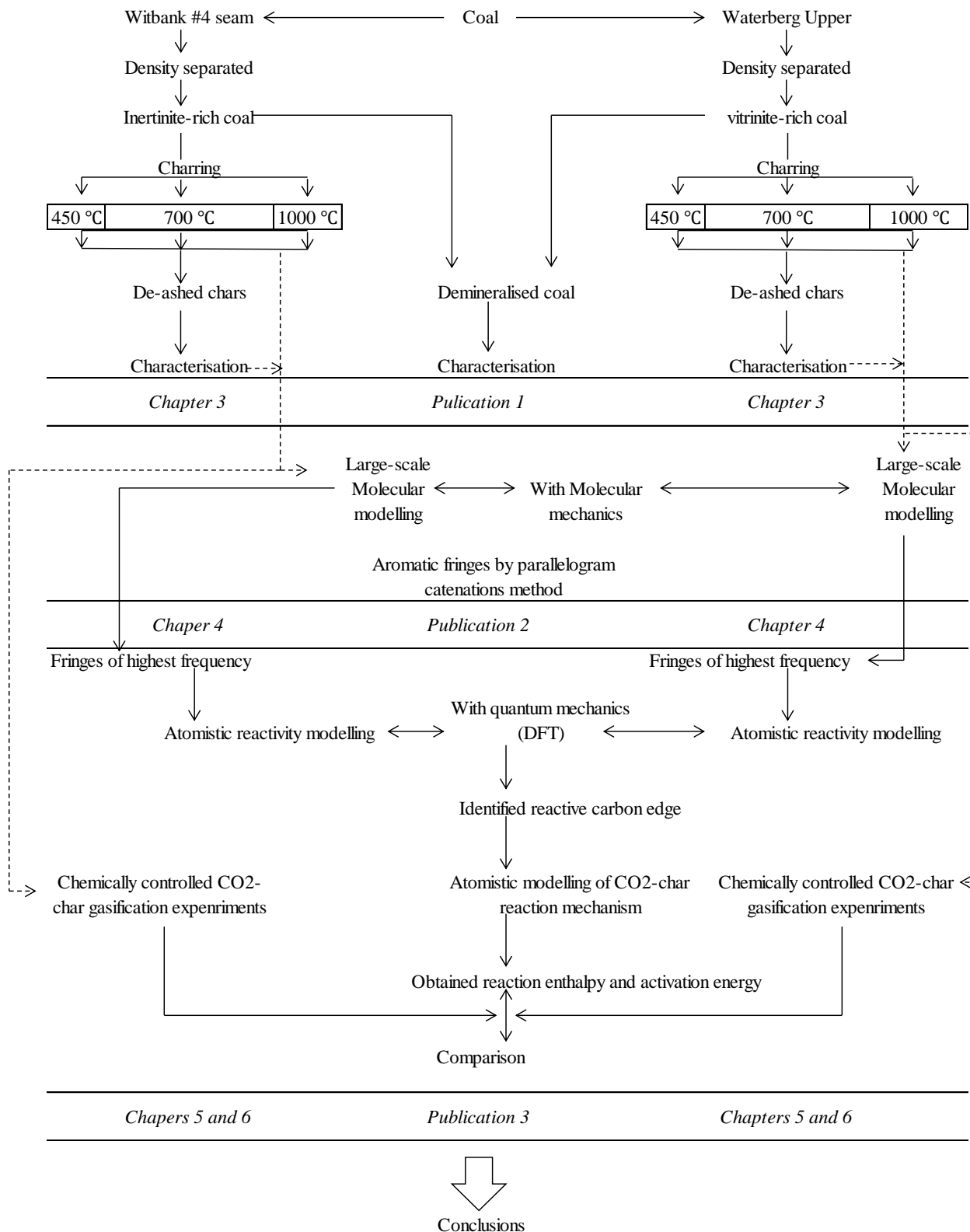
separation techniques to obtain inertinite and vitrinite-rich aliquots, followed by different characterisation techniques. The characterisation was guided by the coal petrography to first verify the suitability of the coals with respect to rank and maceral properties, including their transitions during heating; and to assess opportunities for project expansions. Low (450 °C) and medium-to-high (700-1000 °C) temperatures were selected for this study. The transitions of coal properties at (700-1000 °C) temperatures drew enormous attention and culminated in the study of atomistic properties of the 1000 °C chars that may give hope for a detailed structure-reactivity relationship. The particle size distribution of chars was 300-1000 µm. It is postulated that this particle size distribution and the heat treatment temperatures of 700-1000 °C are typical in fluidised bed processes. Computational techniques of highest accuracy, namely, density functional theory (DFT), were used. Efforts were made to validate the DFT results with experimental methods and valuable inferences were made. Milestones were considered for publication/ presentation in accredited journals/conferences.

### 1.5.2 Breakdown by chapter

**Chapter 1.** Contains the background behind the study, project motivation, the specific problem in the current knowledge on the topic and opportunities for the research at hand, formulated hypothesis of the central theoretical statement, research objectives and project scope. The project scope included the background and project breakdown by chapter.

# CHAPTER 1: GENERAL INTRODUCTION

Table 1-1. Scope of the research project



## CHAPTER 1: GENERAL INTRODUCTION

---

**Chapter 2.** Comprises an overview of the most relevant volume of knowledge in literature citations on the four core research activities, coal/char characterisation, large-scale molecular modelling of coal chars, CO<sub>2</sub>-char gasification and atomistic-scale gasification (reactivity) simulations using DFT. This is to complement literature given in chapters.

**Chapter 3.** This is composed of coal/char characterisation techniques. These entail physical and chemical structural transformations of inertinite- and vitrinite-rich coals at 450, 700, and 1000 °C. Correlations among the results are also highlighted. HRTEM technique only applied to the 1000 °C chars derived from inertinite and vitrinite-rich coals to construct large-scale molecular models and study structure-reactivity relationship.

**Chapter 4.** Detailed construction and evaluation of large-scale molecular models of chars derived from inertinite- and vitrinite-rich coals at 1000 °C is presented in this chapter.

**Chapter 5.** Atomistic/molecular reactivity modelling of CO<sub>2</sub>-char gasification using DFT technique, including the parameters for geometry optimisation, single-point energy calculations and transition state theory.

**Chapter 6.** Description of the experimental apparatus (TGA) used for the gasification experiments, including details of procedures and experimental programme. Special attention here is given to experimental gasification results of chars derived from inertinite- and vitrinite-rich coals at 1000 °C.

**Chapter 7.** General conclusions for this study are drawn and include an account of results from this investigation, contributions to the knowledge base of coal science and technology and recommendations for future research.

**Appendix.** Additional information on petrography, XRD, HRTEM, DFT and particle kinetics is presented in Appendix A-F respectively.

## CHAPTER 1: GENERAL INTRODUCTION

---

### Nomenclature

Acronym	Definition
Bt	Billion tons
DFT	Density functional theory
DMR	Department of Minerals Resources (South Africa)
EIA	Energy Information Administration
HRTEM	High resolution transmission electron microscopy
ss $^{13}\text{C}$ NMR	Solid state nuclear magnetic resonance spectroscopy
XRD	X-ray diffraction

---

# CHAPTER 1: GENERAL INTRODUCTION

---

## 1.6 References

- AHUJA, P.; KUMAR, S. and SINGH, P. C. 1996. A model for primary and heterogeneous secondary reactions of wood pyrolysis. *Chemical engineering & technology*, 19, 272.
- DMR 2011/2012. South Africa's Mineral Industry. Department of Mineral Resources: Mineral Economics Directorate. 29 ed. Pretoria, South Africa.
- EIA 2012. Key world's energy statistics: International Energy Agency (IEA)
- FALCON, L. M. A. F. R. M. S. 1987. The petrographic composition of southern African coals in relation to friability, hardness, and abrasive indices. *Southern African Institute of Mining and Metallurgy*, 87, 323.
- FALCON, R. M. S., SNYMAN, C. P. 1986. *An introduction to coal petrography: Atlas of petrographic constituents in the bituminous coals of southern Africa*, Johannesburg [South Africa], The Geological Society of South Africa.
- FLETCHER, T. H.; SOLUM, M. S.; GRANT, D. M. and PUGMIRE, R. J. 1992. Chemical structure of char in the transition from devolatilization to combustion. *Energy & Fuels*, 6, 643.
- GUPTA, R. 2007. Advanced coal characterization: A review. *Energy & Fuels*, 21, 451.
- IEA 2012. *Medium-Term Coal Market Report*, OECD Publishing.
- MATHEWS, J. P. and CHAFFEE, A. L. 2012. The molecular representations of coal - A review. *Fuel*, 96, 1.
- MONTOYA, A.; MONDRAGÓN, F. and TRUONG, T. N. 2002. First-principles kinetics of CO desorption from oxygen species on carbonaceous surface. *The Journal of Physical Chemistry A*, 106, 4236.
- MONTOYA, A.; MONDRAGÓN, F. and TRUONG, T. N. 2003. CO<sub>2</sub> adsorption on carbonaceous surfaces: a combined experimental and theoretical study. *Carbon*, 41, 29.
- NIEKERK, D. V. and MATHEWS, J. P. 2010. Molecular representations of Permian-aged vitrinite-rich and inertinite-rich South African coals. *Fuel*, 89, 73.
- RADOVIC, L. R. 2005. The mechanism of CO<sub>2</sub> chemisorption on zigzag carbon active sites: A computational chemistry study. *Carbon*, 43, 907.
- RADOVIC, L. R. 2009. Active sites in graphene and the mechanism of CO<sub>2</sub> formation in carbon oxidation. *Journal of the American Chemical Society*, 131, 17166.
- RADOVIĆ, L. R.; WALKER JR, P. L. and JENKINS, R. G. 1983. Importance of carbon active sites in the gasification of coal chars. *Fuel*, 62, 849.
- SENDT, K. and HAYNES, B. S. 2005. Density functional study of the chemisorption of O<sub>2</sub> on the armchair surface of graphite. *Proceedings of the Combustion Institute*, 30, 2141.
- SENDT, K. and HAYNES, B. S. 2005. Density functional study of the chemisorption of O<sub>2</sub> on the zig-zag surface of graphite. *Combustion and Flame*, 143, 629.
- SENDT, K. and HAYNES, B. S. 2011. Density functional study of the reaction of O<sub>2</sub> with a single site on the zigzag edge of graphene. *Proceedings of the Combustion Institute*, 33, 1851.
- SMITH, K. L. 1994. *The structure and reaction processes of coal*, Springer.
- SUN, Q.; LI, W.; CHEN, H. and LI, B. 2003. The variation of structural characteristics of macerals during pyrolysis. *Fuel*, 82, 669.
- VAN KREVELEN, D. W. 1993. *Coal, Typology, Physics, Chemistry, Constitution* Amsterdam, Elsevier.
- XU, W.-C. and TOMITA, A. 1987. Effect of coal type on the flash pyrolysis of various coals. *Fuel*, 66, 627.
- YU, J.; LUCAS, J.; STREZOV, V. and WALL, T. 2003. Swelling and char structures from density fractions of pulverized coal. *Energy & Fuels*, 17, 1160.
- ZILM, K. W.; PUGMIRE, R. J.; LARTER, S. R.; ALLAN, J. and GRANT, D. M. 1981. Carbon-13 CP/MAS spectroscopy of coal macerals. *Fuel*, 60, 717.

## CHAPTER 2: LITERATURE OVERVIEW

---

### Chapter 2: Literature overview

#### 2.1 Introduction

A thorough knowledge of physical and chemical structural features of coal is imperative to understand the behaviour of coal in chemical processes such as gasification and combustion. This chapter provides a literature review on research undertaken on the details of coal origin and nature of coal deposits, coal utilisation processes and the different reaction phases involved, characterisation of coal and char, molecular coal/char structures and their relationship with reactivity. Attention is particularly given to the application of molecular modelling techniques to predict the structures of coal char and understand their relationship with reactivity. Information is in complementary to literature overview given in specific chapters.

#### 2.2 Origin and nature of coal deposits

Coal is a combustible material consisting of lithified plant debris. Large amounts of plant material was originally accumulated and deposited in a swampy environment to form soft, spongy remains known as peat. The peat experienced physical and chemical processes under hot conditions. It was covered by the layers soil and rocks at various depths over periods of up to a number of million years. Extreme compression transformed the peat to coal. This process is called coalification. The heterogeneity the coal occurs from a mixture of different plant material, which underwent a range of biochemical and geological processes, with continued deposition of a wide range of minerals during and after coal deposition (Gibbins *et al.*, 1999:592). Coal has a series of microscopic and macroscopic bands known as lithotypes, which are a variety of maceral proportions and minerals, constituting microlithotypes (Falcon, 1987:323). These microlithotypes and the dissemination, structure and nature of both macerals and minerals are essential for the assessment, processing and utilisation of coal (Falcon, 1987:323). The microscopic units in coal establish its fundamental characteristics. The

## CHAPTER 2: LITERATURE OVERVIEW

---

macerals are divided in three groups, namely, inertinite, vitrinite and liptinite, (Falcon, 1987:323)..

### 2.2.1 Global coal deposits

Major coal deposits occur in the Permian sequences of the countries in the southern hemisphere (South Africa, India, Australia, Madagascar, South America, and the Antarctica); and the Carboniferous strata in the northern hemisphere (Europe and North America) (Suarez-Ruiz, 2008:388). Coal deposition in the southern hemisphere took place during the Permian Age and have common origins in the collapsed continent of Gondwana (Cai and Kandiyoti, 1995:956). These southern hemisphere coals were deposited in subarctic conditions, making the coals distinct from the Carboniferous coals in the northern hemisphere (Cai and Kandiyoti, 1995:956). Most Gondwana coals are bituminous coals with scarce distribution of anthracites and the coal seams are generally thicker when compared with the carboniferous coal deposits in the northern hemisphere (Cai and Kandiyoti, 1995:956). The coals in the southern hemisphere contain clay minerals of much finer distribution and lower amounts of pyritic-type sulphur, compared with their northern hemisphere coals (Cai and Kandiyoti, 1995:956). Petrographic properties of Gondwana coals were found to be widely different from those of carboniferous coals (Cai and Kandiyoti, 1995:956). The vitrinite content is generally 80% at most and occurrences of less than 50% vitrinite can be found (Cai and Kandiyoti, 1995:956). The liptinite group maceral concentrations are usually found to be low (Cai and Kandiyoti, 1995:956). The depositional processes that yielded the coal-bearing sequences were primarily deltaic and fluvial and the shoreline and lacustrine settings were insignificant (Cai and Kandiyoti, 1995:956). A variety of coal ranks occur and have been characterised as high inertinite content and moderate ash content (Cai and Kandiyoti, 1995:956; Cairncross, 2001a:529). The Carboniferous coals are characterised as vitrinite-rich (Hartgers *et al.*, 1994:1055).

## CHAPTER 2: LITERATURE OVERVIEW

---

### 2.2.2 The South African coal deposits

The characteristics of South African coal deposits and their industrial implications are well recognised and published (Fabianska and Kruszewska, 2003:95; Kruszewska, 2003:79; Kruszewska, 1998:1655; Falcon, 1987:323; Falcon, 1986; Holland *et al.*, 1989b:143; Oboirien *et al.*, 2011:735; Snyman, 1989:83; Snyman and Barclay, 1989:375; Snyman and Botha, 1993b:171; Jeffrey, 2005:95). Typical of Gondwana coals, the South African coalfields are poor in liptinite, and generally contains large amounts of inertinite v/v, while Liptinite content is approximately 5% v/v (Kruszewska, 2003:79). Among these coal deposits, specific studies have been made on the two most important, namely, the Witbank (Cairncross, 2001b:529; Cairncross and Cadle, 1988:343; Holland *et al.*, 1989a:143; Cairncross *et al.*, 1990:309; Falcon, 1989:681; Pinetown *et al.*, 2007:166; Pone *et al.*, 2007:124; Mangena *et al.*, 2004:1647) and Waterberg (Faure *et al.*, 1996:147; Jeffrey, 2005:453; Wagner and Tlotleng, 2012:225; Snyman and Botha, 1993a:171; Wagner, 2010; Fourie *et al.*, 2008; Niekerk and Mathews, 2010:73; Van Niekerk and Mathews; Van Niekerk and Mathews, 2010:6393; Van Niekerk *et al.*, 2008:290; Van Niekerk *et al.*, 2010:45; Kruszewska, 1998:1655; Fabianska and Kruszewska, 2003:95) bituminous coalfields.

The Witbank coalfield consists of five coal seams recognised as seam No. 1 to 5. The coals of the Witbank coalfield is generally characterised by high proportions of inertinite maceral group. However, a significant amount of inertinite is semi-reactive and is mainly represented by inertodetrinite, compared with the inertinite maceral group of the northern hemisphere Carboniferous coals (Snyman and Botha, 1993b:171; Falcon, 1986). The No. 4 seam is the most important and accounts for about 26% of the total Witbank coalfield resource and mainly provides the domestic power stations with coal feedstock (Pone *et al.*, 2007:124). The Waterberg coalfield has vast potential to become a replacement coalfield for the Central Basin (Witbank, Highveld and Ermelo coalfields) (Jeffrey, 2005:453). The typical Waterberg coalfield consists of Middle Ecca and Upper Ecca coal seams (Fabianska and Kruszewska, 2003:95). The latter is largely vitrinite-

## CHAPTER 2: LITERATURE OVERVIEW

---

rich coal with a little similarity to the northern hemisphere Carboniferous coals (Kruszewska, 1998:1655).

### 2.3 Coal utilisation

#### 2.3.1 Background

The role of coal as an existing energy resource remains attractive. It is a stable and reliable feedstock to power stations and the cost-effective utilisation of coal is likely to keep it as a vital participant in the energy mix for a number of decades (Irfan *et al.*, 2011:12). There are three main coal utilisation technologies, namely, the direct coal combustion for electrical power generation, coal gasification for synthetic gas production and liquefaction, which involves catalytic synthesis of a variety of hydrocarbons. Mounting population figures, declining oil reserves and an increasing challenges associated with CO<sub>2</sub> emissions are current issues that will urge the transition in the current coal technologies towards better optimisation and ultimately bring more science and technology in the acceptance of new processes (Stanger *et al.*, 2013:764). Indonesia, Australia, Russia, USA and Colombia and South Africa lead the world's coal supply and have a major role to play in ensuring that the properties of these coals are suitable for use in the large number of various processes existing in the current-medium-to-long term and are part of the science and technology development (Stanger *et al.*, 2013:764). Pyrolysis is an important process step in coal utilisation (Zhao *et al.*, 2011:780). The heterogeneity of coal and the complexity of the pyrolysis process have made it imperative to perform experiments of greater degree of certainty to determine the kinetics and mechanisms in coal pyrolysis (Solomon *et al.*, 1993:587). Researchers have studied the pyrolysis products that include evolved gases, volatile matter and formed chars, highlighting coal pyrolysis as a process that essentially involves the C-C bond breakdown, formation of free radicals and rearrangement of bonds to form char, gases and liquids (Guo *et al.*, 2013:23; Van Krevelen, 1993). It is also highlighted that coal pyrolysis occurs by cross-linking reactions, which follow this order: the removal of

## CHAPTER 2: LITERATURE OVERVIEW

---

moisture from coals at about 130 °C, the formation of gases at about 242 °C, the formation of liquids and solid residue or char (Van Krevelen, 1993). In this thesis, special attention is given to coal gasification.

### 2.3.2 Coal gasification

Coal gasification process is likely to experience a wide adoption by the developing countries of the world in the next 20-50 years, because of its greater possibilities to yield better efficiencies than the combustion processes (Cousins *et al.*, 2006:2489). It involves the reaction of coal with air, oxygen, steam, carbon dioxide, or a mixture of these gases at a temperatures exceeding 700 °C, for the recovery of a gaseous product used either as a source of energy or as a feedstock towards the production of chemicals, liquid fuels or other synthetic fuels (Collot, 2006:191; Suarez-Ruiz, 2008:388; Cousins *et al.*, 2006:2489). Gasification converts coal chars into synthesis gas, a mixture of CO and H<sub>2</sub> that is further processed into chemicals and fuel for power generation. This process provides the best fuel alternatives of any of the advanced technologies for the production of electricity (Liu and Niksa, 2004:679). In South Africa, Sasol provides gasification specialisation to convert low grade coal into petroleum products and raw material for the production of chemicals (Van Dyk *et al.*, 2006:243; Collot, 2006:191). This company runs three major coal to liquid (CTL) establishments adapted from the original Lurgi gasification process, which is currently called Sasol-Lurgi bottom gasification process and culminates into Fischer-Trøpsch (FT) products (Collot, 2006:191; Van Dyk *et al.*, 2001).

The reactivity of coal/char with gaseous reactants such as carbon dioxide and steam has a major impact on the design criteria of the gasification reactor. In a typical gasification plant, coal conversion for crude gas production involves steam and oxygen under pressure and at high temperature (Van Dyk *et al.*, 2006:243). Subsequent cooling of evolved gas results in the condensation of co-products such as tar and oils, while other compounds are co-produced and recovered as ammonia, sulphur, cresols and

## CHAPTER 2: LITERATURE OVERVIEW

---

phenols, respectively (Van Dyk *et al.*, 2006:243). The long chain hydrocarbons are generated from the conversion of purified synthesis gas using the Sasol Advanced Synthol (SAS) (Van Dyk *et al.*, 2006:243). Gasifiers are mainly grouped into three categories, namely, moving bed or fixed bed, fluidised bed and entrained flow gasifiers, following the type of reactor bed type used. The type of gasifier is related to the handling and condition of particular feedstock. Other gasifier types are based on rotary kilns, but the commercialisation of such types of gasifiers has not been observed (Collot, 2006:191). Gasification may also be conducted in situ, thus called underground gasification. The flexibility to choose gasification technology is often associated with difficulties of diverse nature. These include coal availability, type and cost; size, reaction kinetics and constraints imposed by international regulations, plant requirements and product utilisation. Coal type may impose limited flexibility for economic, geographical and political reasons and therefore requires extensive experimentation to adapt the gasification technology (Vamvuka, 1999:515; Collot, 2006:191).

**Fixed-bed gasifiers or moving bed gasifiers.** These are characterised by a bed in which the coal moves slowly downward under gravity as it is gasified, usually counter-current to the steam and oxidant feed. Fixed bed gasifiers are suitable for solid feedstock and high-temperature gasification processes (Cousins *et al.*, 2006:2489; Suarez-Ruiz, 2008:388). A moving bed reactor provides relatively simple gasification process where the pyrolysis products are easily separated. It allows easy investigations of the product streams such as solid, liquid and gas (Zhao *et al.*, 2011:780). The secondary reactions caused by primary volatiles are typical during pyrolysis in a fixed bed reactor, in comparison with pyrolysis in the fluidised bed reactor (Zhao *et al.*, 2011:780). This may cause polymerisation or relatively rapid and efficient reactions (Zhao *et al.*, 2011:780). The two examples of commercial fixed bed gasifiers include those originally developed by Lurgi, namely, the Sasol-Lurgi fixed bed dry bottom gasifier and the British Gas Lurgi slagging gasifier (Van Dyk *et al.*, 2006:243; Suarez-Ruiz, 2008:388). The main feature in dry ash version is that temperatures at the bottom of the ash bed are kept below the ash fusion temperature to permit the removal of ash as solid particles (Suarez-Ruiz, 2008:388).

## CHAPTER 2: LITERATURE OVERVIEW

---

**Fluidised bed gasifiers.** These gasifiers are composed of vertical, cylindrical, refractory-lined vessels with recycle cyclones and bottom ash cooling systems (Suarez-Ruiz, 2008:388). Dry coal of fine particle size distribution (<6 mm) is fed through the bottom of the gasifier and fluidised using the oxidant and steam (Suarez-Ruiz, 2008:388). Reaction are accelerated by exceptionally good mixing between the coal particles and oxidant, resulting in efficient heat and mass transfer. The fluidised bed gasifier therefore a low-temperature process (Suarez-Ruiz, 2008:388; Cousins *et al.*, 2006:2489). Fluidised bed gasifiers accepts coals with high sulphur content and reactive feedstock such as low rank coals and biomass (Suarez-Ruiz, 2008:388). This equipment uses steam and oxygen moderately during gasification, usually at ambient temperatures and may, thus, a best choice for a small operator (Suarez-Ruiz, 2008:388). However, the fluidised bed gasifiers can also be suitable for higher throughputs using elevated temperatures (Suarez-Ruiz, 2008:388). The equipment is available in the two main categories, bubbling and circulating types.

**Entrained flow gasifiers.** All feed streams are administered concurrently (Suarez-Ruiz, 2008:388). This reactor is fed with coal of fine particle size distribution or slurry at the same time with the oxygen-carrying gas and steam. The residence time in the reactor is short, therefore the coal is pulverised to provide a high surface area and fast reactions, also the coal and gases flow concurrently at high speed. The coal properties of high importance on the entrained flow gasifier include particle size distribution, equilibrium moisture, fixed carbon, surface carbon/oxygen bonding and free-swelling index (Collot, 2006:191; Suarez-Ruiz, 2008:388). The entrained flow gasifier operation is characterised by uniform reactions zones and reactions at temperatures of 1200 °C and more. This gasifier type may be the most attractive to the world's operators due to its adaptability and suitability for integrated gasification combined cycle (IGCC) operations (Suarez-Ruiz, 2008:388). This equipment also accepts both solid and slurry feeds (Suarez-Ruiz, 2008:388). However, high costs associated with the effect of high operating temperatures on refractory life and difficulty of slag control should be taken into account (Suarez-Ruiz, 2008:388).

## CHAPTER 2: LITERATURE OVERVIEW

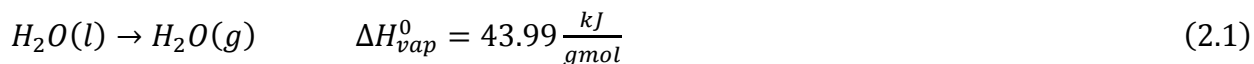
---

### 2.4 Reaction phases during gas-solid interactions in gasification

More efficient power plants that pursue clean coal technologies such as the IGCC are being developed all over the world to use coal (Watanabe and Otaka, 2006:1935). A coal gasifier is the main component of the IGCC plant, and it is imperative to have a detailed understanding of the reaction phases inside the gasifier for its optimum design and characteristic evaluation. The coal reaction scheme in a gasifier consists of four phases: drying, devolatilisation, char gasification and gas phase reactions (Watanabe and Otaka, 2006:1935; Kajitani *et al.*, 2006:163).

#### 2.4.1 Devolatilisation of coal

The first experience of coal when it enters the gasifier is the removal of moisture, according to Equation (2.1).



(Bell *et al.*, 2010).

The terms devolatilisation and pyrolysis are often used as synonyms. The devolatilisation behaviour varies widely according to coals of different types because of different amounts of coalification. The extend of aromatisation in the coal structure is directly related to the rank of the coal (Gupta, 2007:451). The results of petrography on maceral composition of coal play a significant role on the devolatilisation and char conversion reactions. The initial physical changes that take place when coal is heated are influenced by the melting and the manner of decomposition reactions of coal. The loss of water as vapour can have a paramount effect on the whole gasification thermodynamics, especially when gasification involves low grade, wet coal (Bell *et al.*, 2010). However, the impact of loss of water as vapour is relatively small with bituminous coal and dry feed gasifier. The devolatilisation of coal during gasification is not a simple

## CHAPTER 2: LITERATURE OVERVIEW

---

reaction, but the evolution of the volatile matter gives a complex reaction scheme (Liang *et al.*, 2008:435). In addition to this, the reaction chemistry of pyrolysis involves complex free radical reaction mechanisms (Van Dyk *et al.*, 2006:243). The pyrolysis products such as tars, pitches, phenols, etc. are valuable by-products from certain gasification processes (Van Dyk *et al.*, 2006:243). However, there are other processes in which the importance of pyrolysis reactions is negligible since the pyrolysis products are in any event disregarded. The Lurgi fixed bed gasification processes, which became a technology adopted for the Sasol process makes good example here (Van Dyk *et al.*, 2006:243). The pyrolysis product yields are significantly affected by the coal parameters such as petrographic composition, particle size, heating rate, final temperature, pressure; and the atmosphere of gaseous components within which pyrolysis takes place (Van Dyk *et al.*, 2006:243). The gasifier performance sets up a temperature profile for the production and break down of pyrolysis products such as the tars, phenols, oils and low boiling point hydrocarbons in the pyrolysis zone and with the gasifier product gas (Minchener, 2005:2222). It is of vital importance to understand the coal pyrolysis rates as it makes a marked effect on the entire gasification behaviour (Yang *et al.*, 2007:3165).

### 2.4.2 Coal char gasification reactions

The gasification reactions of char after devolatilisation involve steam and carbon dioxide. Gasification can be described as a partial oxidation reaction and the important products are hydrogen and carbon monoxide (Higman and Tam, 2013:1673). In a coal gasifier, CO<sub>2</sub> gasification and H<sub>2</sub>O gasification occur at the same time and are the most important coal gasification reactions (Table 2-1, Equations (2.4) and (2.5)) (Molina and Mondragon, 1998:1831; Higman and Van der Burgt, 2011). These reactions are respectively called the Boudouard reaction and water-gas reaction (Hunt *et al.*, 2013:26871; Higman and Van der Burgt, 2011). Of great essence, the Boudouard reaction represents a means of CO<sub>2</sub> alleviation by converting it to more synthetically flexible CO, which can then be used to produce H<sub>2</sub> according to the water-gas shift

---

## CHAPTER 2: LITERATURE OVERVIEW

---

reaction (Equation (2.7)) or hydrocarbons through the Fischer-Trøpsch process (Ratnasamy and Wagner, 2009:325; Dry, 2002:227). The large positive enthalpy, often estimated at  $172 \text{ kJ mol}^{-1}$  at STP, the equilibrium favours CO production after temperatures  $>700 \text{ }^\circ\text{C}$ , when the entropy ( $-T\Delta S$ ), begins to dictate and the free energy becomes negative (Hunt *et al.*, 2013:26871).

Table 2-1. Main coal gasification reactions

Reaction	Equation No.	Name
$\text{C} + \text{O}_2 \rightleftharpoons \text{CO}_2$	(2.2)	Oxidation
$\text{C} + \frac{1}{2}\text{O}_2 \rightleftharpoons \text{CO}$	(2.3)	Partial oxidation
$\text{C} + \text{CO}_2 \rightleftharpoons 2\text{CO}$	(2.4)	Boudouard
$\text{C} + \text{H}_2\text{O} \rightleftharpoons \text{CO} + \text{H}_2$	(2.5)	Water-gas
$\text{C} + 2\text{H}_2 \rightleftharpoons \text{CH}_4$	(2.6)	Methanation
$\text{CO} + \text{H}_2\text{O} \rightleftharpoons \text{CO}_2 + \text{H}_2$	(2.7)	Water-gas shift
$\text{CH}_4 + \text{H}_2\text{O} \rightleftharpoons \text{CO} + 3\text{H}_2$	(2.8)	Steam reforming

## CHAPTER 2: LITERATURE OVERVIEW

---

### 2.4.3 Gas phase reactions in a coal gasifier

The frequent use of water gas shift reaction (Table 2-1, Equation (2.7)) is in a catalytic reactor downstream of the gasifier to adjust the  $H_2/CO$  ratios and may take place spontaneously because of high reaction temperatures (Bell *et al.*, 2010; Dry, 1996:319). The steam-methane reforming reaction (Equation (2.8)) is used in catalytic reactors to produce CO from  $CH_4$  and may also occur spontaneously because of high reaction temperatures (Bell *et al.*, 2010).

### 2.5 Coal and char characterisation

The determination of much results for coal characterisation is a standard matter often performed by and available from production, supplying and trading sectors of the industry. The coal characterisation results determine the price of the coal by apportionment of production costs as well as to control mining and coal preparation plants and to determine plant efficiency (Speight, 2005). The fast growing use of coal in the 1900s made it essential to devise acceptable methods for coal analysis, with the goal of correlating characterisation results with reactivity. Standard analyses such as proximate analysis, ash analysis, and ash fusion temperatures give only bulk characteristics and performance relationships based on these analytical techniques are unable to describe sufficiently the impact of coal quality on conversion efficiencies and plant performance (Gupta, 2007:451). Several advanced analytical techniques such as the XRD,  $^{13}C$  NMR and HRTEM provide information on the organic structure of coal (Gupta, 2007:451). There are three coal properties related to geological parameters and are determined by some aspect of the origin of coal (Suarez-Ruiz, 2008:388). These properties are briefly defined as follows:

**Rank.** Reflects the extend of metamorphism (maturity or coalification) that the original mass of peat has experienced during its burial history (Falcon, 1987:323; Suarez-Ruiz, 2008:388). This depends in turn on the highest temperature experienced by coal and for

## CHAPTER 2: LITERATURE OVERVIEW

---

how long. Coal rank often reflects the depth to which coal was deposited and maximum and minimum temperature ranges existing at the time of coalification in the basin concerned (Suarez-Ruiz, 2008:388). The most common parameters used to define rank in Europe and North America include volatile matter and carbon content (Falcon, 1987:323). However, these are unsuitable for coals in the southern hemisphere, and the most reliable parameter currently used in South Africa to define rank is the reflectance of vitrinite, which is measured by petrographic technique under oil immersion (Falcon, 1987:323). Rank plays a vital role in coal behaviour. Low rank, brown coals have lower combustion efficiency than high rank, bituminous coals because of their high moisture content. Other effects of coal rank on efficiencies have been reported (Alvarez *et al.*, 1998:849; Gale *et al.*, 1996:766).

**Type.** Coal type is a reflection of the nature of the plant material from which the original peat was derived, such as the combination of plant components (e.g. wood, leaves, algae) involved and the extent of degradation experienced before deposition (Suarez-Ruiz, 2008:388). The individual vegetation (organic matter) existing in coal and, in some cases other parts of material derived from them, are known as macerals.

**Grade.** The grade of a coal indicates the level to which the plant deposits were maintained free from pollution by inorganic material. This includes periods before the deposited plant material was covered (i.e. during peat accumulation), after being buried and during rank development (Suarez-Ruiz, 2008:388). Therefore, a high grade coal is a coal with low overall proportion of inorganic material and, hence, a high amount of organic matter (Suarez-Ruiz, 2008:388).

### 2.5.1 Standard analyses

The standard chemical properties of coal include chemical and physical parameters using the proximate and ultimate analyses, petrographic analysis and helium density measurements.

## CHAPTER 2: LITERATURE OVERVIEW

---

### 2.5.1.1 Proximate analyses

Proximate analysis is one of the conventional techniques composed together with the ultimate analysis. Proximate analysis is constituted by the moisture, ash, volatile matter and fixed carbon contents, respectively. Sample preparation is done according to SABS 0135: Part 1 & 2 (1997). Proximate analysis method follows SABS ISO 1171 (1997) and SABS ISO 566 (1998) for ash yield/content and volatile matter measurements, respectively. Fixed carbon content is determined by difference.

**Moisture.** The properties of the solid carbonaceous residue, char, from the thermal processing of the coals, especially in processes where the coal/char particles experience long residence time can change significantly due to inherent moisture in low-rank coals (Yip *et al.*, 2007:2883). The reaction between char and steam can also lead to profound deactivation of the char at high pyrolysis temperatures. It was found that the effect of inherent moisture decreases as the coal particle size increases (Yip *et al.*, 2007:2883).

**Ash.** It reflects the amount of mineral matter, including the fraction inherent in the coal structure, as well as out of contamination events of the coal seam (Van Dyk *et al.*, 2001). However, it is important to note that there is no ash present in coal, but the mineral matter in coal is expressed in the form of ash (Gupta, 2007:451). The gasification efficiency of a particular coal has intimate dependence on the behaviour of mineral matter in coal char at high-temperatures (BAI *et al.*, 2009:134; Hattingh *et al.*, 2011:2048). Coal gasification process has shown that the mineral matter in the different coal and ash particles may fuse, melt and partially crystallise on cooling to form a number of new phases (e.g. mullite, anorthite, cristobalite, diopside and magnetite) in association with an amorphous or glassy component (Matjie *et al.*, 2011:1426). The high amounts of ash in coal causes a decrease in the maximum temperature and also reduces the higher heating value of product gas (Singh *et al.*, 2013). Ash content can, therefore, be used for predictions in gasification processes. The AFT analysis indicates the softening and melting manner of fuel ash and, therefore, predictions of the variability

## CHAPTER 2: LITERATURE OVERVIEW

---

in fusibility characteristics among different coals (Liu *et al.*, 2013:293). The fusibility of coal minerals is expressed in terms of the amount of the principal oxides existing in the ash, such as  $\text{SiO}_2$ ,  $\text{Al}_2\text{O}_3$ ,  $\text{TiO}_2$ ,  $\text{Fe}_2\text{O}_3$ ,  $\text{CaO}$ ,  $\text{MgO}$ ,  $\text{Na}_2\text{O}$  and  $\text{K}_2\text{O}$  (Suarez-Ruiz, 2008:388; Liu *et al.*, 2013:293; Seggiani, 1999:1121). The AFT measurement provides four temperatures that describes the softening and melting behaviour of ash during heating: initial deformation temperature (IDT), spherical temperature (ST), hemispherical temperature (HT), and fluid temperature (FT) (Liu *et al.*, 2013:293). Ash fusion temperatures also give an indication of the progressive melting of coal ash to slag (Gupta, 2007:451). A few examples of the effect of the major oxides on AFT are: the valence state of iron significantly affect the melting behaviour of ashes, calcium oxide is a fluxing agent which is usually used to reduce the AFTs of coal ashes, as the amount of silica increases, it escapes in the form of amorphous in coal ashes and makes slight contribution to the variety of AFTs; and the decline in the AFTs occurs due to deminishing  $\text{K}_2\text{O}$  content (Gupta, 2007:451).

**Volatile matter.** Large amounts of volatile matter improve the liberation of combustible gases that require a lower process temperature (Vélez *et al.*, 2009:424; Bell *et al.*, 2010). A review of elements influencing gasification showed that the reactivities of low-rank coals (C<80% daf) have unclear correlation with the amount of fixed carbon (coal rank) (Irfan *et al.*, 2011:12).

**Fixed carbon.** After losing moisture and volatiles temperatures up to 900 °C, fixed carbon is burnt in oxygen leaving the ash as a residue, hence determined by difference.

### 2.5.1.2 Ultimate analyses

The analyses for carbon, hydrogen and nitrogen are performed according to ISO standard 12902 (ISO, 2010). Oxygen is determined by difference. Elemental ratios such as hydrogen-to-carbon ratio (H/C) and oxygen-to-carbon ratio (O/C) are determined from the ultimate analysis and may be essential to predict the gasification process.

## CHAPTER 2: LITERATURE OVERVIEW

---

Research done by Van Krevelen found that the elemental composition varies in at least two key phases. The initial one is described by an increase in the O/C ratio and the other one by a similar increase as well as a declining H/C ratio (Krevelen, 1961:828).

The total sulphur and nitrogen contents are also included in the ultimate analysis. An increase in carbon content increases the maximum temperature. The inhibition effect of CO and H<sub>2</sub> in the respective CO<sub>2</sub> and steam gasification at 900 °C in TGA was also investigated for two different types of coals (Everson *et al.*, 2006:1076). It was found that both CO and H<sub>2</sub> inhibit the respective gasification reactions for CO<sub>2</sub> and steam drastically.

### 2.5.1.3 Petrographic analysis

For petrographic analysis of coal there are two distinctive methods of approach, namely, the reflected light and transmitted light techniques. The reflected light is the most widely used technique because of the relative ease in sample preparation (Ting, 1978:3). It requires that the coal samples be optically polished and free of scratches. The polished blocks are then studied with the aid of incident light microscope using oil immersion. The transmitted light technique is an earlier method in the microscopic study of coal until a new generation of coal photographers adopted reflected light techniques (Ting, 1978:3). Ting proposed a petrographic classification of coal using reflectance of vitrinite and maceral composition as the basis for coal classification (Ting, 1978:3; Meyers, 2012).

**Reflectance of vitrinite.** Vitrinite reflectance is an indication of coal rank and affects the hydrogen- and oxygen-carbon ratios, hence the gasifier performance. There are mainly two types of reflectance, namely, maximum vitrinite reflectance and random vitrinite reflectance. The average of at least 100 readings is called mean maximum reflectance of vitrinite or mean random reflectance of vitrinite (Ting, 1978:3).

## CHAPTER 2: LITERATURE OVERVIEW

---

**Maceral analysis.** The identification and classification of the microscopic, organic constituents of coal known as macerals are conducted on the basis of their morphology, source material, nature of formation and colour or level of reflectivity (Ting, 1982:7). Maceral composition is divided into three groups, namely, inertinite, vitrinite and liptinite. Various portions of macerals and minerals constitute microlithotypes (Falcon, 1987:323). The distribution of the various macerals within a particular coal, along with rank changes, controls the coal properties, and consequently affects the conversion behaviour of the coal.

**Coal char petrography.** This analysis assesses the microscopic components of the samples by virtue of their colour, reflectance, and degree of anisotropy, size, morphology and level of devolatilisation (Everson *et al.*, 2008:3082). The Combustion Working Group in Commission III of the International Committee for Coal and Organic Petrology (ICCP) assessed the char samples to compile an atlas of char images during a round robin exercise (Lester *et al.*, 2010:333). This assessment system found that more than 70% of analysers agreed on the microscopic images of the chars. The primary advantage of this morphological characterisation of coal chars is to avoid the subjectivity in the analysis and to increase the accuracy of the measurements. The impact of coal petrography on coal gasification processes was extensively investigated (Irfan *et al.*, 2011:12; Cuadrat *et al.*, 2012:91; Kapusta and Stańczyk, 2011:1927; Cao *et al.*, 2008:1720; Collot, 2006:191; Alonso *et al.*, 2001:257; Zhang *et al.*, 2013:1; Zhao *et al.*, 2011:780; Sun *et al.*, 2004:1787; Sun *et al.*, 2003:669; Chabalala *et al.*, 2011:750). Chabalala *et al.* found that the use of coal petrography and micro Raman spectroscopy on coal chars enhanced the understanding of both the evolution of coal char structure and coal conversion processes (Chabalala *et al.*, 2011:750). Alonso *et al.* found that the decrease in the intrinsic reactivity of the chars followed the order: vitrinite-rich low rank char > inertinite-rich char > vitrinite-rich high rank char (Alonso *et al.*, 2001:257). Zhao *et al.* studied the pyrolysis behaviour of vitrinite and inertinite from Chinese Pingshuo coal and found that the ultimate and XRD analyses of chars showed that the difference in elemental composition of vitrinite char and inertinite char declines with the rise of temperature (Zhao *et al.*, 2011:780). The CO<sub>2</sub> gasification kinetics of coal chars with

## CHAPTER 2: LITERATURE OVERVIEW

---

and without catalyst were investigated by Sun *et al.* (Sun *et al.*, 2004:1787). The comparison of gasification reactivity of coal chars with and without catalyst showed that vitrinite-rich chars always have higher gasification reactivity and lower activation energy than inertinite-rich chars (Sun *et al.*, 2004:1787).

**Char form analysis.** The relative magnitudes of the carbon-rich constituents/inorganic material can be established according to the method set out in the ISO Standard 7404-3, 1994 (Everson *et al.*, 2008:3082). Everson *et al.* used a system that consists of six groups with different categories comprising dense char, networks, coke, oxidised constituents, non-reacted coal, partially-reacted coal and inorganic matter, which originate from the macerals, microlithotypes and minerals present in the parent coal (Everson *et al.*, 2008:3082). The benefit of this system is that the different groups can be quantified for comprehensive comparative studies (Everson *et al.*, 2008:3082). The system also gives information on the reactive and non-reactive macerals in the parent coal as well as for the inorganic matter present and gives estimates of relative amounts of dense and porous structures (Everson *et al.*, 2008:3082).

### 2.5.1.4 Physical structural properties

The physical structural properties of coal, which include particle size, pore structure, surface area, density, is imperative for the comprehension and modelling coal conversion processes. Qian *et al.* examined the chemical structures and physical properties of coal and chars from different extent of devolatilisation and found that the different reactivity of fully devolatilized chars formed in different pyrolysis conditions mainly depends on physical properties rather than on chemical structures (Qian *et al.*, 2014:327).

**Particle size.** It was found that at low temperature the intrinsic gasification rate was similar (Irfan *et al.*, 2011:12). However, smaller char particle indicated higher

## CHAPTER 2: LITERATURE OVERVIEW

---

gasification reactivity in the high-temperature region (Irfan *et al.*, 2011:12; Gibson *et al.*, 2013:7681).

**Pore structure and surface area.** The magnitude and spatial allocations of pores and the size, distribution, and identity of the submicron size minerals are physical characteristics noted for their influence in coal conversion processes such as liquefaction and gasification. Mesopore (N<sub>2</sub>) and micropore (CO<sub>2</sub>) surface areas are derived from adsorption isotherms using the Brunauer, Emmett, and Teller (BET) and Polanyi (DP) equations, respectively (Gale *et al.*, 1996:766; Gale *et al.*, 1995:513). Coal char particles comprise dense carbonaceous components, parts of dense minerals, fine pores and cracks that can cause different reaction regimes over temperature ranges, different to low mineral porous chars (Everson *et al.*, 2011:2347). The reaction gases penetrate these particles to attack the carbon atoms, while the resultant gases diffuse through the solid structure. As pyrolysis and gasification proceeds, the pore structure of the coals changes, affecting the reaction rates (Malekshahian and Hill, 2011:5250). The overall rate of reaction on a porous char is dependent upon the degree of the internal surface and the size of the pores providing this surface. In addition to this, the pore structure of the char particles change during the gasification process. The difference in the reaction rate with carbon conversion is caused by the development of char particle structure (e.g. particle surface area) during the reaction (Liu *et al.*, 2000:617). The surface area enlarges at low conversion because of the growth of pores in the particle, and then declines slightly, as interactions and disintegration of pores and pore wall, respectively, become significant. The development of the pore structure is connected with the initial structure of the char (Liu *et al.*, 2000:617). The vitrinite-rich coal chars have higher porosity, and thus more reactivity compared with dense chars produced from inertinite-rich coals (Liu *et al.*, 2000:617).

**Helium density.** True (or skeletal) density is determined by helium pycnometry and it evaluates the physical restructuring and carbon aromatisation of chars during devolatilisation (Everson *et al.*, 2013:148; Gale *et al.*, 1995:513; Gale *et al.*, 1996:766).

## CHAPTER 2: LITERATURE OVERVIEW

---

### 2.5.2 Additional structural properties (XRD, HRTEM, NMR)

A number of more specialised characterisation techniques have emerged recently and considers coal as a heterogeneous material comprising of individual particles. These techniques are able to examine these coal particles in much greater detail. The structural transition of coal during heat treatment was studied with the help of numerous techniques, such as X-ray diffraction (XRD) high resolution transmission electron microscopy (HRTEM) and solid state Carbon-13 nuclear magnetic resonance ( $^{13}\text{C}$  NMR). Matsouka *et al.* found that XRD, HRTEM and  $^{13}\text{C}$  NMR made an immense contribution in the determination of the coal char structure and showed the limitations of elemental analysis results in structural analysis (Matsuoka *et al.*, 2008:539).

#### 2.5.2.1 The X-ray diffraction (XRD)

X-ray diffraction has been useful in the attainment of the structural information of coal and chars (Lu *et al.*, 2001:1821; Babu and Seehra, 1996:1259; Gupta, 2007:451; Zhu *et al.*, 2008:2482; Machado *et al.*, 2013:224; Bai *et al.*, 2013:202; Everson *et al.*, 2013:148; Wu *et al.*, 2007:199). The appreciation of structural ordering within carbons was first proposed in 1949 (Feng *et al.*, 2002:481). The variations in crystallite structure of coal during conversion can be observed by an analysis of XRD spectra of the char (Gupta, 2007:451). The X-ray diffraction analysis of the chars can also reveal important transitions in crystallite size for samples produced at different temperatures in a wide temperature range (900-1500 °C) (Gupta, 2007:451). It is a non-destructive and well-established technique with good reproducibility and it involves a well-defined and systematic measurement of X-ray scattering curves (Lu *et al.*, 2001:1821). The technique uses a relatively large sample proportions and collects much of the intensities scattered from the examined sample. Therefore, the produced properties are a representation of an average for the sample, rather than the local properties (Lu *et al.*, 2001:1821). In XRD spectra, coal and char produce three broad peaks, the (002), (10) and the (11) planes of the carbon crystal lattice. The position of these peaks is shown in

## CHAPTER 2: LITERATURE OVERVIEW

---

Figure 2-1 (Lu *et al.*, 2001:1821; Everson *et al.*, 2013:148). The (002) peak corresponds to the aromatic layer stacking height, while the (10) and (11) peaks represent the radial spread (interlayer spacing) of crystalline structures (Lu *et al.*, 2001:1821; Zhu *et al.*, 2008:2482). The average carbon crystallite lattice parameters known as the crystallite diameter,  $L_a$ , stacking height,  $L_c$ , and interlayer spacing,  $d_{002}$ , are calculated from XRD patterns using the Scherrer equation and Bragg's law (Equations (2.9) and (2.10) (Zhang *et al.*, 2008:3213; Van Niekerk *et al.*, 2008:290). The average number of aromatic layer per crystallite,  $N_{ave}$ , is derived from the  $d_{002}$  and the  $L_c$  (Equation (2.11)) (Trejo *et al.*, 2007:2121; Van Niekerk *et al.*, 2008:290; Everson *et al.*, 2013:148). The crystallite diameter, ( $L_a$ ), is evaluated from the (10) or the (11) peak properties (Everson *et al.*, 2013:148).

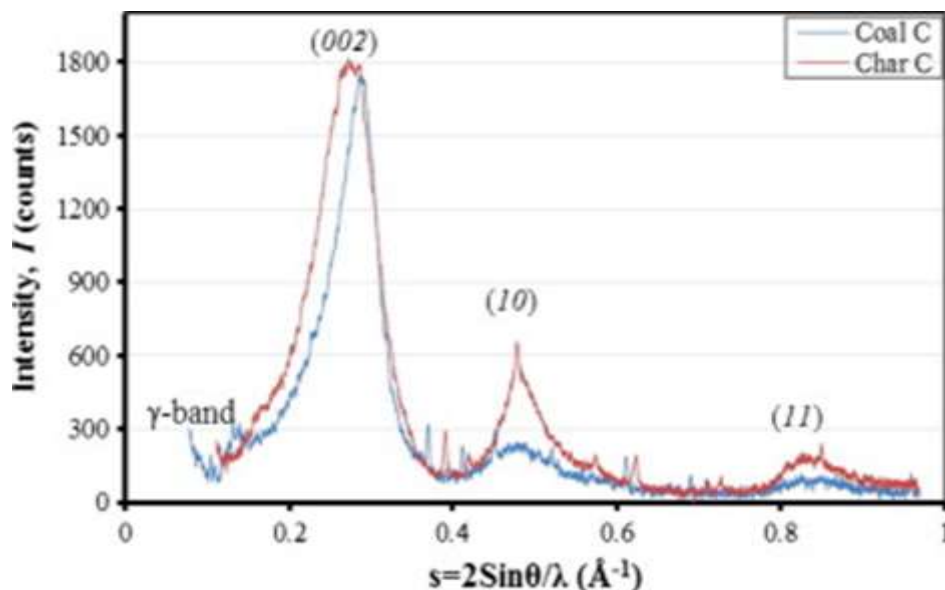


Figure 2-1. The XRD spectra showing the three characteristic peaks (Lu *et al.*, 2001:1821; Everson *et al.*, 2013:148).

$$L_c = \frac{1.84\lambda}{\beta \cos\theta} \quad (2.9)$$

## CHAPTER 2: LITERATURE OVERVIEW

---

$$d_{002} = \lambda / 2 \sin \theta_{002} \quad (2.10)$$

$$N_{ave} = \frac{L_c}{d_{002}} + 1 \quad (2.11)$$

where  $\lambda$  is the wavelength of the X-radiation,  $\beta$  represents the width of (002) peak at half-maximum intensity and  $\theta$  is the Bragg angle corresponding to the peak position in radians (Zhang *et al.*, 2008:3213).

The fraction of amorphous carbon ( $x_A$ ) does not influence peak intensity and is reflected only in the background of the intensity curve (Lu *et al.*, 2001:1821). It was found that the intensity contributed by  $x_A$  is constant over the whole scattering range and is equal to the fraction of amorphous carbon (Ergun and Tiensuu, 1959:1050; Franklin, 1950:107; Everson *et al.*, 2013:148; Lu *et al.*, 2001:1821). The amorphous fraction can be calculated according to Equation (2.12). The  $x_A$  can also be derived as a function of  $s_{max}$  from the symmetric profile of the reduced intensity curve ( $I_{max}$ ) of the (002) peak and the crystallite lattice parameters (Everson *et al.*, 2013:148). Figure 2-2 shows an example of the Guassian curve deconvolution to determine the  $x_A$  (Everson *et al.*, 2013:148).

$$\frac{I_{max} - x_A}{1 - x_A} = \frac{0.0606}{s^2} \times \frac{\sin^2(N_{ave} d_{002} \pi s_{max})}{N_{ave} \sin^2(N_{ave} d_{002} \pi s_{max})} \quad (2.12)$$

The asymmetric feature of the (002) band suggests the existence of another band ( $\gamma$ ) in its left-hand side, which represents the saturated structure of aliphatic side chains of the amorphous structures grafted on the edges of coal crystallites (Lu *et al.*, 2001:1821; Everson *et al.*, 2013:148). Aromaticity ( $f_a$ ) of the particles was determined from the area under the (002) band ( $A_{002}$ ) and the gamma ( $\gamma$ ) sideband ( $A_\gamma$ ), according Equation (2.13) (Hattingh *et al.*, 2013:3161; Van Niekerk *et al.*, 2008:290; Everson *et al.*, 2013:148; Lu *et al.*, 2001:1821).

## CHAPTER 2: LITERATURE OVERVIEW

---

$$f_a = \frac{A_{002}}{A_{002} + A_\gamma} \quad (2.13)$$

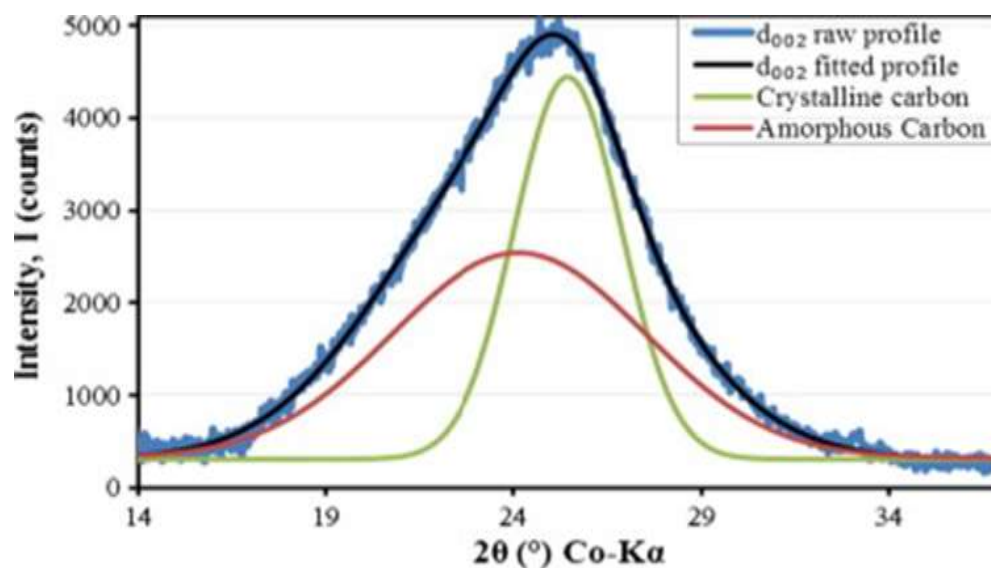


Figure 2-2. Determination of amorphous fraction of carbon ( $x_A$ ), from Gaussian curve deconvolution (Everson *et al.*, 2013:148).

Emmerich studied the variation of the dimensions  $L_a$  and  $L_c$  of the graphite-like crystallites of graphitisable and non-graphitisable carbons with heat treatment using XRD techniques (Emmerich, 1995:1709). Here, it was found that the increase of  $L_a$  and  $L_c$  with heat treatment temperature could be attributed to one or more of three processes, namely, the in-plane crystallite growth, coalescence of crystallites along the  $c$ -axis and coalescence of crystallites along the  $a$ -axis, depending on the temperature range (Emmerich, 1995:1709). In addition to this, it was found that the temperature separating the vegetative increase and the coalescent increase of  $L_a$  and  $L_c$  depended largely on the carbon used (Emmerich, 1995:1709; Feng *et al.*, 2002:481).

## CHAPTER 2: LITERATURE OVERVIEW

---

### 2.5.2.2 High resolution transmission electron microscopy

The lattice-fringe imaging mode of HRTEM is a valuable technique for the imaging of flat atomic surfaces in a carbon lattice (Davis *et al.*, 1995:31). Oberlin and co-workers used the HRTEM to perform intensive studies of carbon structure during heat treatment (Table 2-2) (Rouzaud *et al.*, 1983:75; Rouzaud, 1990:55; Rouzaud and Oberlin, 1989:517; Deurbergue *et al.*, 1987:375; Feng *et al.*, 2002:481).

Feng *et al.* studied the structural ordering of coal char during heat treatment and its impact on reactivity using the HRTEM (Feng *et al.*, 2002:481). Very well organized crystallite structure was in the vicinity of the carbon/iron interface in the coal char. Sharma *et al.* examined the structural transformations in coals, including the stacking number and layer sizes, over the heat-treatment temperatures of 427, 800 and 1200 °C using the HRTEM technique (Sharma *et al.*, 2001:1467).

The structural transition in coal is significantly dependent on whether a coal undergoes plastic stage or not and that the HRTEM technique can successfully quantify the structural transformation in coal during heating. Shim and Hurt used the HRTEM and found that materials with higher reactivity largely exhibit a higher susceptibility to annealing, leading to fractional convergence in the data at heat treatment temperatures in excess of 2000 °C (Shim, 2000:829). The contribution of Sharma *et al.* to the HRTEM analytical technique is highlighted by the development of a filtration method for HRTEM microphotographs and a computer technique to extract information such as the size of graphene layer, spacing between successive layers, the stacking number, and the distribution of image features from the post-filtered extracted HRTEM images (Figure 2-3) (Sharma *et al.*, 1999:1203).

## CHAPTER 2: LITERATURE OVERVIEW

---

Table 2-2. Four stages for the change of the micro-texture during carbonization up to 3000 °C (Feng *et al.*, 2002:481).

Stage	Temperature range	Corresponding textural changes
1	<700 °C	<ul style="list-style-type: none"><li>• The release of the aromatic CH groups.</li><li>• The aromatic layers are approximately parallel to the lamella plane.</li><li>• Basic structural units (BSUs) are less than 1 nm in diameter and isometric.</li><li>• The BSUs thickness is also about 1 nm</li><li>• The number of layers (N), varies from 1 to 3.</li><li>• The BSUs are azimuthally distributed at random in the fragments.</li></ul>
2	700 – 1500 °C	<ul style="list-style-type: none"><li>• The release of interlayer defects between two superimposed BSUs.</li><li>• The lamella shape is more pronounced and</li><li>• The lamella are thin and flexible enough to be folded.</li><li>• N jumps from stage 1 to stage 2 and reaches 8 -10.</li></ul>
3	1500 – 2000 °C	<ul style="list-style-type: none"><li>• The release of in-plane defects.</li><li>• The disappearance of the disoriented single BSU.</li><li>• A considerable increase in thickness.</li><li>• The coalescence of adjacent columns.</li><li>• The distortions of the layers progressively anneal.</li><li>• The layers inside the columns associate edge to edge.</li></ul>
4	>2000 °C	<ul style="list-style-type: none"><li>• All distortions are annealed.</li><li>• The layers are stiff and perfect.</li><li>• The heteroatoms and both the interlayer and in-plane defects have successively disappeared.</li><li>• Crystal growth may thus begin.</li></ul>

A typical HRTEM image with its lattice fringes is shown in Figure 2-4 (Sharma *et al.*, 2002:54). Mathews *et al.* extracted the HRTEM fringes of coal in conjunction with the parallelogram catenation method to assign the sizes of aromatic fraction as the starting structures of molecular representations of coal (Niekerk and Mathews, 2010:73; Mathews *et al.*, 2010:1461). Fernandez-Alos *et al.* generated the soot and char molecular representations directly from HRTEM lattice fringe images using Fringe3D (Fernandez-Alos *et al.*, 2011:1807).

## CHAPTER 2: LITERATURE OVERVIEW

---

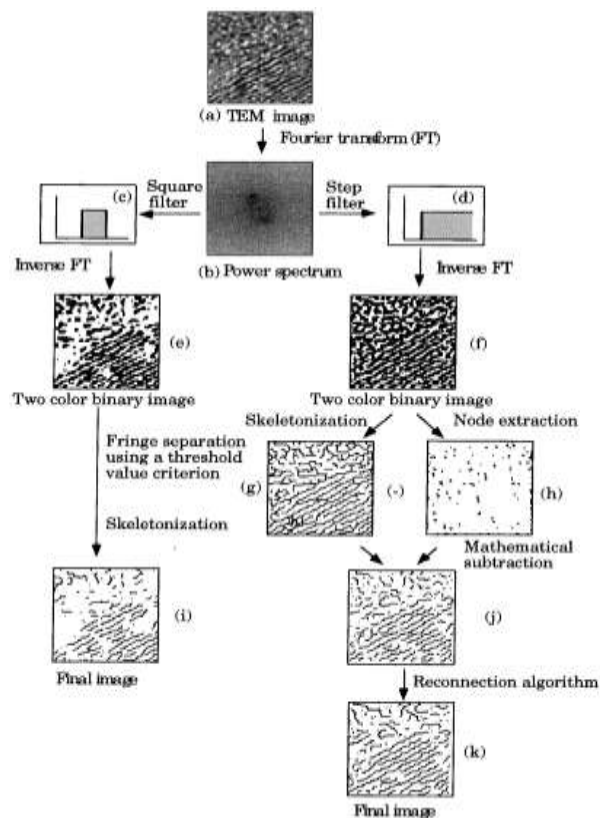


Figure 2-3. The conventional ((a)-(f) up to (i)) and the advanced filtration technique ((a)-(h) up to (j)-(k)) (Sharma *et al.*, 1999:1203).

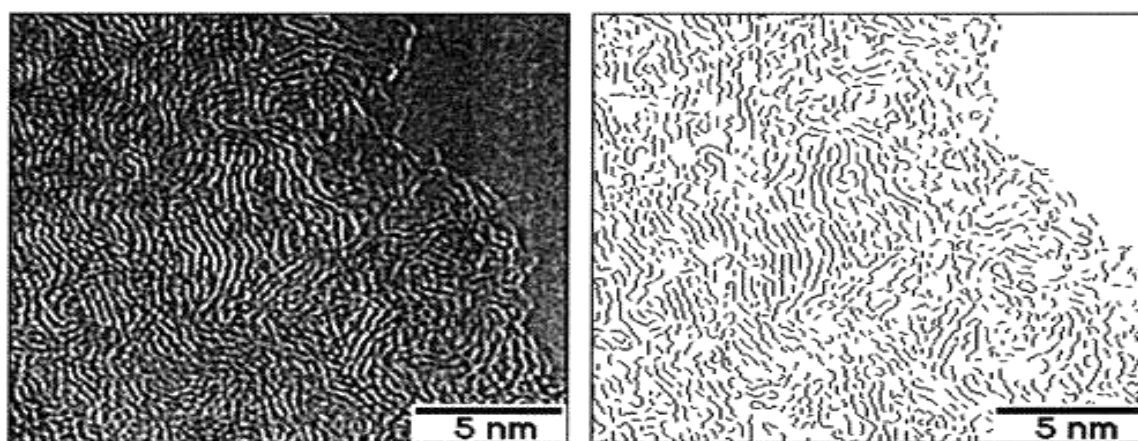


Figure 2-4. Typical HRTEM microphotograph (left-hand side) with its lattice fringes (right-hand side), after the advanced filtration technique (Sharma *et al.*, 2002:54; Sharma *et al.*, 1999:1203).

## CHAPTER 2: LITERATURE OVERVIEW

---

### 2.5.2.3 Solid state $^{13}\text{C}$ nuclear magnetic resonance spectroscopy

An improved knowledge of chemical structure of coal has remarkably risen over decades of widespread research using solid-state  $^{13}\text{C}$  nuclear magnetic resonance (NMR) spectroscopy (Perry *et al.*, 2000:2313; Fletcher *et al.*, 1991:1231; Solum *et al.*, 1989:187; Solum *et al.*, 2001:961; Van Niekerk *et al.*, 2008:290; Cao *et al.*, 2010:388). Solid-state  $^{13}\text{C}$  NMR spectroscopy is among a few methods available to study coal structure in a non-destructive manner.

The work of other researchers to study coal structure using techniques that are destructive in nature is also noted, including techniques such as pyrolysis mass spectroscopy, FTIR and pyridine extraction/chromatography (Orikasa and Tomita, 2003:1536; Yin *et al.*, 2009:895; Qi *et al.*, 2013:3130; Ledesma *et al.*, 2000:1801; Li *et al.*, 2004:1273; Van Heek, 2000:1). Solid-state  $^{13}\text{C}$  NMR spectroscopy is an appealing technique in studies related to coal structure because of its success and reliability in obtaining average chemical structural features of coal and chars. The NMR can achieve a direct measurement of the relative number of aromatic and nonaromatic carbons by the application of cross-polarization (CP), magic-angle-pinning (MAS), and dipolar-decoupling techniques (Solum *et al.*, 1989:187).

There are published results on aromaticity,  $f_a$ , for whole coals and macerals using the dipolar-dephasing (DD) techniques along with the normal CP-MAS integrations over selected chemical shift ranges to subdivide  $f_a$  values into the amount of protonated and nonprotonated carbons (Van Niekerk *et al.*, 2008:290). Researchers showed that CP/MAS NMR experiments do discriminate against aromatic carbons and that the solution for this is to perform single-pulse excitation magic-angle-spinning (SPE-MAS) NMR experiments for quantitative analysis, although with typically long analysis time (Van Niekerk *et al.*, 2008:290; Botto *et al.*, 1987:173; Franz *et al.*, 1992:598; Muntean *et al.*, 1988:108). Example of results from these solid-state  $^{13}\text{C}$  NMR techniques are presented in Table 2-3, representing the direct measurement of structural parameters for the South African vitrinite-rich Waterberg and inertinite-rich Highveld coals (Van Niekerk *et al.*, 2008:290). These are parameters obtained directly from the  $^{13}\text{C}$  NMR

## CHAPTER 2: LITERATURE OVERVIEW

analysis and describe the general carbon structure of the coal and chars. Table 2-4 show the derived lattice parameters for these coals, which give the most meaningful description of the coal molecule and are derived from the measured  $^{13}\text{C}$  NMR structural values, the elemental composition of the coal sample and a correlation (Orendt *et al.*, 1992:215). According to Solum *et al.*, a relationship between the fraction of bridgehead carbons ( $x_b$ ) and the number of aromatic carbons per cluster  $C$  was derived from an analysis of polycondensed aromatic hydrocarbons (Solum *et al.*, 1989:187). This value of  $C$  is subsequently used in the derivation of the remaining parameters. The average number of attachments to the aromatic cluster is labelled  $\sigma+1$  (Solum *et al.*, 1989:187). The fraction of intact bridges,  $P_0$ , is the proportion of these attachments that are bridges between adjacent aromatic clusters (Solum *et al.*, 1989:187).

Table 2-3. Typical structural parameters from solid-state  $^{13}\text{C}$  NMR for vitrinite-rich Waterberg and inertinite-rich Highveld coals (Van Niekerk *et al.*, 2008:290).

Sample	$f_a$	$f_a^C$	$f_a^O$	$f_a^{OO}$	$f_a^{\cdot}$	$f_a^H$	$f_a^N$	$f_a^P$	$f_a^S$	$f_a^B$	$f_{al}$	$f_{al}^H$	$f_{al}^*$	$f_{al}^O$
HV (cp)	0.85	0.03	0.01	0.02	0.82	0.28	0.54	0.07	0.18	0.29	0.15	0.11	0.04	0.03
HV (sp)	0.86	0.05	0.01	0.04	0.81	0.28	0.53	0.07	0.17	0.29	0.14	0.1	0.04	0.04
dmHV (cp)	0.85	0.05	0.02	0.03	0.8	0.3	0.5	0.07	0.17	0.26	0.15	0.11	0.04	0.03
dmHV (sp)	0.86	0.04	0.01	0.03	0.82	0.28	0.54	0.07	0.17	0.3	0.14	0.1	0.04	0.04
WB (cp)	0.74	0.04	0.01	0.03	0.7	0.23	0.47	0.08	0.18	0.21	0.26	0.17	0.09	0.04
WB (sp)	0.77	0.08	0.04	0.04	0.69	0.26	0.43	0.09	0.18	0.16	0.23	0.15	0.08	0.06
dmWB (cp)	0.73	0.03	0.01	0.02	0.7	0.26	0.44	0.08	0.18	0.18	0.27	0.18	0.09	0.05
dmWB (sp)	0.76	0.05	0.02	0.03	0.71	0.22	0.49	0.08	0.18	0.23	0.24	0.16	0.08	0.05

HV = Highveld coal, WB = Waterberg coal, dm = demineralized, sp = single-pulse experiment and cp = cross-polarization experiment. Parameters:  $f_a$  = total of  $\text{sp}^2$  carbon,  $f_a^C$  = carbonyl/carboxyl and amid carbon,  $f_a^O$  = aldehyde and ketone fraction,  $f_a^{OO}$  = acid, ester or amide fraction,  $f_a^{\cdot}$  = aromatic carbon,  $f_a^H$  = protonated aromatic carbons,  $f_a^N$  = non-protonated aromatic carbons,  $f_a^P$  = phenols or phenolic ethers  $f_a^S$  = alkylated aromatic carbons,  $f_a^B$  = aromatic bridgehead carbons,  $f_{al}$  = total  $\text{sp}^3$  carbon,  $f_{al}^H$  = CH or  $\text{CH}_2$ ,  $f_{al}^*$  = methyl and methoxy groups,  $f_{al}^O$  = total aliphatic carbon bonded to an oxygen.

The number of bridges and loops per aromatic cluster is labelled B.L. The  $^{13}\text{C}$  NMR techniques that are generally used to analyse coal structure do not have an ability to

## CHAPTER 2: LITERATURE OVERVIEW

---

distinguish between (a) bridges and (b) attachments that form a loop on the aromatic cluster. Attachments to the aromatic cluster that are not bridges or loops are known as side chains. The number of side chains per cluster is labelled S.C. The average molecular weight per aromatic cluster is labelled *M.W.* (Van Niekerk *et al.*, 2008:290).

Superior spectral-editing NMR techniques characterises the coal structure in more detail compared with routine  $^{13}\text{C}$  CP-MAS technique (Mao *et al.*, 2010:2536). These advanced  $^{13}\text{C}$  NMR techniques, with direct polarisation combined with spectral-editing techniques, selectively retain certain peaks and eliminate others to reveal different types of functional groups.

Table 2-4. Typical NMR-derived lattice parameters of vitrinite-rich Waterberg and inertinite-rich Highveld coals (Van Niekerk *et al.*, 2008:290)

Sample	$x_b$	C	$\sigma + 1$	$P_o$	B.L.	S.C.	M.W.
HV (cp)	0.354	18	5.3	0.84	4.5	0.8	308
HV (sp)	0.358	18	5.2	0.83	4.3	0.9	315
dmHV (cp)	0.325	16	4.8	0.83	4	0.8	289
dmHV (sp)	0.366	18	5.3	0.83	4.4	0.9	318
WB (cp)	0.3	15	5.4	0.65	3.5	1.9	298
WB (sp)	0.232	11	4.4	0.7	3.1	1.3	232
dmWB (cp)	0.257	12	4.6	0.65	3	1.6	251
dmWB (sp)	0.324	16	5.9	0.69	4.1	1.8	322

HV = Highveld coal, WB = Waterberg coal, dm = demineralised, sp = single-pulse experiment and cp = cross-polarisation experiment. Parameters: C = average number of aromatic carbon atoms per cluster,  $x_b$  = mole fraction of aromatic bridgehead carbons,  $\sigma + 1$  = average number of attachments (bridges, loops and side chains) per cluster,  $P_o$  = number of bridges that are intact, B.L. = number of bridges and loops per cluster, S.C. = number of side chains per cluster, M.W. = average molecular weight of the aromatic cluster. The M.W. of dmHV and dmWB were calculated using the elemental data of the original coals.

## CHAPTER 2: LITERATURE OVERVIEW

---

### 2.6 Molecular modelling

Coal is a heterogeneous material that is largely comprised of an organic macromolecular matrix with different extends of cross-linking, where smaller molecular phases are entrenched or adsorbed to the macromolecular network (Mao *et al.*, 2010:2536). There is an ongoing research to explore a more comprehensive atomic structure of the coal. Advanced analytical techniques and computational power coupled with software tools have facilitated results of models of increasing scale, structural diversity, and incorporating physical features such as: porosity, orientation, density, pore size distribution, fractal dimensionality, etc. are beginning to emerge (Mathews *et al.*, 2011:718; Mathews *et al.*, 2001:863; Mathews and Chaffee, 2012:1; Castro-Marcano *et al.*, 2012:35; Niekerk and Mathews, 2010:73). An increasing number of molecular models of coal was observed over the last 70 years, flooding the literature with more than 125 models (Mathews *et al.*, 2011:718). These models extended over the rank range, but bituminous representations dominate, with far fewer lignite, and very few subbituminous or anthracite representations (Mathews and Chaffee, 2012:1).

The ability to produce large-scale models with new technological advances, incorporating new dynamic force-fields capable to simulate reactivity behaviour in complex materials like coals, presents a new hope for the utility of coal or char molecular models to enhance the knowledge and facilitate in the scientific method rather than the current informed trial and error approach (Mathews *et al.*, 2011:718). Again, while the principal purpose of many of these models was to contribute to the knowledge of coal, several researchers have used the molecular modelling of coal to study the evolution of char structures in coal conversion processes (Jones *et al.*, 1999:1737; Chan *et al.*, 1999:1539; Domazetis *et al.*, 2008:581; Mathews *et al.*, 1998:136; Fernandez-Alos *et al.*, 2011:1807; Mathews, 1998). In the section following this one, special attention is given to the development bituminous coal models and to the participation of researchers in the atomistic modelling of coal conversion processes, particularly char formation models, more than half a century ago.

## CHAPTER 2: LITERATURE OVERVIEW

---

### 2.6.1 Molecular models for bituminous coal

Figures 2-5 and 2-6 present selected molecular models of bituminous coal (Mathews and Chaffee, 2012:1). The Fuchs model gives an impression of a structure that would be expected for an anthracite coal or char (Mathews and Chaffee, 2012:1; Fuchs and Sandhoff, 1942:567). The model enhanced the explanation of pyrolysis behaviour and conformed to “the proximate and ultimate analyses of bituminous coals, to the results of group determinations, and to the behaviours of oxidation, reduction, and thermal decomposition.” The model (84.3% C) was produced in 3D space, together with a 2D drawing (Figure 2-5a), and was used to exemplify a process (Mathews and Chaffee, 2012:1). Given's model, which was first published in the journal *Nature* (Given, 1959) prior to its reproduction in the journal *Fuel* (Given, 1960:147) (Figure 2-5b), experienced a little refinement with a tweaking of the hydroaromatic structure in 1961 (Given, 1961:427; Mathews and Chaffee, 2012:1). Subsequent to this, a secondary, lesser known variant of a “typical structure” of a bituminous coal (Given, 1961:427; Mathews and Chaffee, 2012:1). The transition was a migration from a 9,10-dihydroanthracene to a 9,10-dihydrophenanthrene conformation of fused hydroaromatic rings (Figure 2-5c) (Mathews and Chaffee, 2012:1). Meyers constructed 3D structures with the Dreiding molecular modelling kit (e.g. Figure 2-5d) (Meyers, 1981; Mathews and Chaffee, 2012:1). The 1960 model of Cartz and Hirsch (Cartz and Hirsch, 1960:557) portrayed a 2D hydroaromatic representation for a coal with 84.5% carbon based on extensive X-ray diffraction analyses determined in prior work (Figure 2-5e) (Hirsch, 1954:143; Mathews and Chaffee, 2012:1). A bigger Ladner structure, from adjustment of the Given model, appeared in a later Gibson paper (Gibson, 1978:67) as a personal communication (Figure 2-5f) (Mathews and Chaffee, 2012:1). The Solomon (Solomon, 1981:61) model (Figure 2-5g), together with the Wiser (Wiser, 1984:325) (Figure 2-5i) and Shinn (Shinn, 1984:1187) (Figure 2-5j) models, are possibly those that are the most recognised and relevant bituminous models from this period of pen and paper construction (Mathews and Chaffee, 2012:1; Mathews *et al.*, 2011:718). Solomon (Solomon, 1981:61) (Figure 2-5g) constructed his hypothetical bituminous model to contribute towards the understanding of thermal decomposition for a Pittsburgh seam

## CHAPTER 2: LITERATURE OVERVIEW

---

coal (Mathews and Chaffee, 2012:1). The Wiser (Wiser, 1984:325) model (Figure 2-5i) lacked the hydrogen bonding and there was a single molecule consisting of cross-linked entities with ether and aliphatic linkages (Mathews and Chaffee, 2012:1). The Shinn (Shinn, 1984:1187) model depicts product structures for both single and two-stage liquefaction from breaking down the cross-linked initial model (initial model is shown in Figure 2-5j) (Mathews and Chaffee, 2012:1). A model generated by Hill and Lyon was an advancement in model creativity (Hill and Lyon, 1962:36; Mathews and Chaffee, 2012:1). This high-volatile bituminous coal model was a significant increase in magnitude and structural diversity with an overall molecular weight of nearly 10000 amu; exceeding the size of previous models by a factor of five (Figure 2-5h) (Mathews and Chaffee, 2012:1).

Carlson was the first to apply computational 3D representations to coal models (Carlson, 1992:771). Subsequent to this work, 3D computational representations were generated regularly (Mathews and Chaffee, 2012:1; Carlson, 1992:771). The 3D space-filling structures for the Wiser, Given, Solomon, and Heredy models were generated (Figures 2.12a-f) (Spiro, 1981:1121; Mathews and Chaffee, 2012:1). To allow 3D space-filling structures, three of the structures required modification because of steric interferences (Mathews and Chaffee, 2012:1). The size of the high-vitrinite coking coal model of Lazarov and Marinov was a substantial molecule with two additional hydrogen-bound moieties and intra molecular hydrogen-bonding (Figure 2-7g) (Mathews and Chaffee, 2012:1; Lazarov and Marinov, 1987:411). A more complicated model of Zao Zhuang Chinese bituminous coal followed the use of an extraction process similar to one described by Takanohashi *et al.* (Takanohashi *et al.*, 1994:395), but with a more extensive fractionation to produce a model with five cuts, some with numerous fragments, that were recombined into an associated structure (“anisotropic model”) (Figure 2-7h) (Nakamura *et al.*, 1995:1003; Mathews and Chaffee, 2012:1). A model generated by Takanohashi *et al.* is presented in Figure 2-7i (Takanohashi *et al.*, 1995:788). Mathews *et al.* constructed a molecular structure for Upper Freeport and Lewiston–Stockton vitrinites (Figure 2-7j) (Mathews *et al.*, 2001:863; Mathews and Chaffee, 2012:1).

## CHAPTER 2: LITERATURE OVERVIEW

---

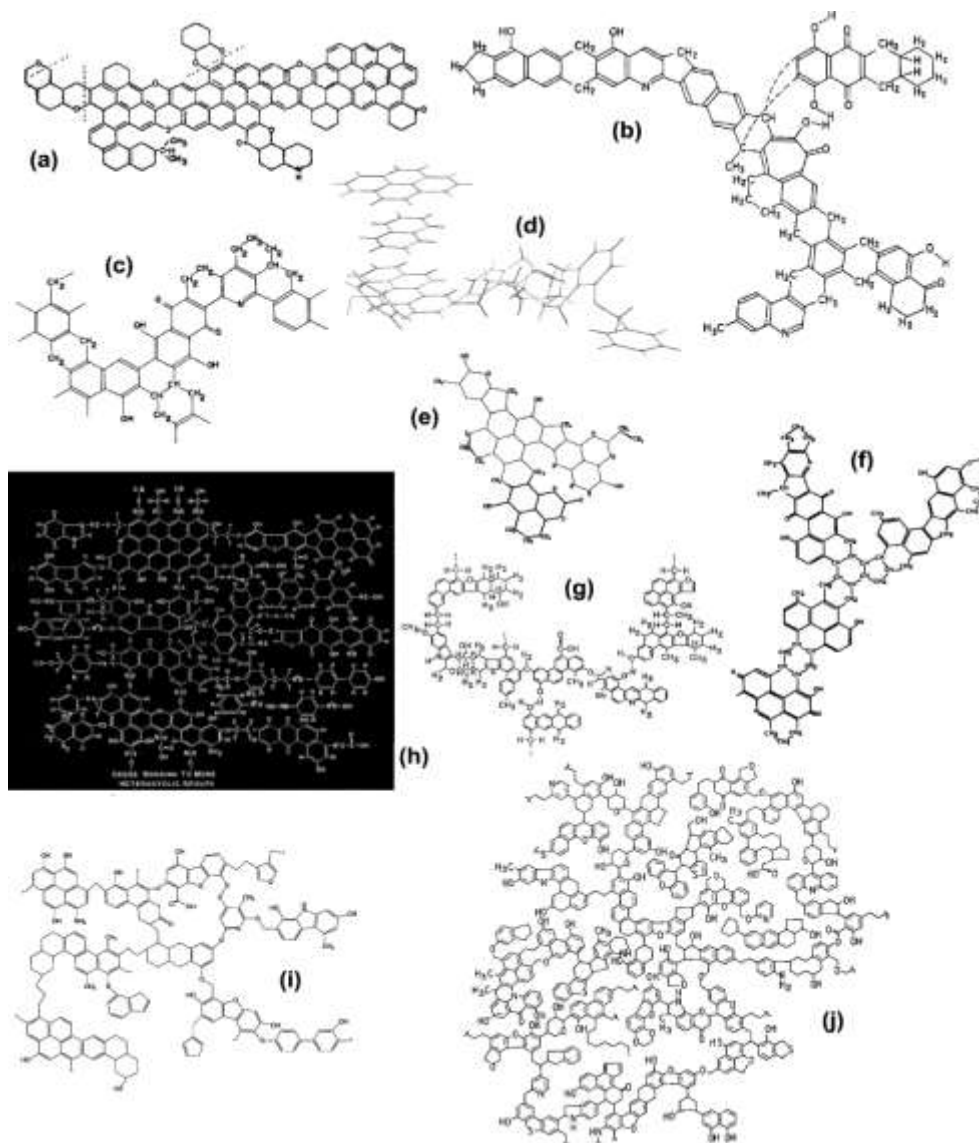


Figure 2-5. The molecular representations of bituminous coal (Mathews and Chaffee, 2012:1): (a) Fuchs and Sandoff structure (Fuchs and Sandhoff, 1942:567), (b) Given (Given, 1960:147), (c) adapted from Given (Given, 1962:39), (d) Meyers (Meyers, 1981), (e) Cartz and Hirsch (Cartz and Hirsch, 1960:557), (f) Ladner (as printed in Gibson (Mathews and Chaffee, 2012:1)) (Gibson, 1978:67), (g) Solomon (Solomon, 1981:61), (h) Hill and Lyon (Hill and Lyon, 1962:36), (i) adapted from Wisner (Wisner, 1984:325), (j) Shinn (Shinn, 1984:1187). Structures are reprinted with permission of the copyright holders (Mathews and Chaffee, 2012:1).

## CHAPTER 2: LITERATURE OVERVIEW

---

The large-scale bituminous coal model of Narkiewicz and Mathews was allowed to relax to observe volume change (178960 amu) after it was loaded with a suitable packing of water molecules, around 1% by mass (hydrogen bonded to oxygen functionality) (Narkiewicz and Mathews, 2008:3104; Mathews and Chaffee, 2012:1). The change in volume of 1% was retained and evaluated to be reasonable for the loss of bound water (Narkiewicz and Mathews, 2008:3104).

### 2.6.2 Atomistic models for the coal char formation

Models have been disintegrated in efforts to portray the pyrolysis process, char formation, and char reactivity (including the function of ion-exchangeable ions) (Mathews *et al.*, 2011:718). Similar to the pyrolysis models, direct liquefaction has been studied with a pyrolysis style approach (Mathews *et al.*, 2011:718). However, the number of coal char models is, however, much lesser than coal models. Both the Takanohashi *et al.* and Mathews *et al.* models of the Upper Freeport and Lewiston–Stockton seam coals were single molecular entities that were utilized to explore transitions to char obtained under drop-tube pyrolysis conditions (Figure 2-7(a), left-hand side) (Mathews *et al.*, 1998:136; Mathews and Chaffee, 2012:1; Takanohashi *et al.*, 1995:788; Mathews *et al.*, 2011:718). Jones *et al.* generated similar molecular structures (Figure 2-7(b), right-hand side) (Pittsburgh #8 bituminous coal) for utilization in a char formation study, the chars being generated in a wire-mesh reactor (Mathews and Chaffee, 2012:1; Jones *et al.*, 1999:1737; Mathews *et al.*, 2011:718). The molecular structures were based on an altered Shinn model to meet Pittsburgh #8 data (Figure 2-5(b), right-hand side) (Mathews *et al.*, 2011:718; Shinn, 1984:1187; Jones *et al.*, 1999:1737). Marzec constructed models of coal char as a means of probing the relationship between structure and carbonization temperature (Marzec, 1997:837; Mathews *et al.*, 2011:718). Models were based on elemental composition, XRD, TEM, Pyrolysis-Field Ionisation MS,  $^{13}\text{C}$  NMR and FTIR data (Figure 2-8(a)).

## CHAPTER 2: LITERATURE OVERVIEW

---

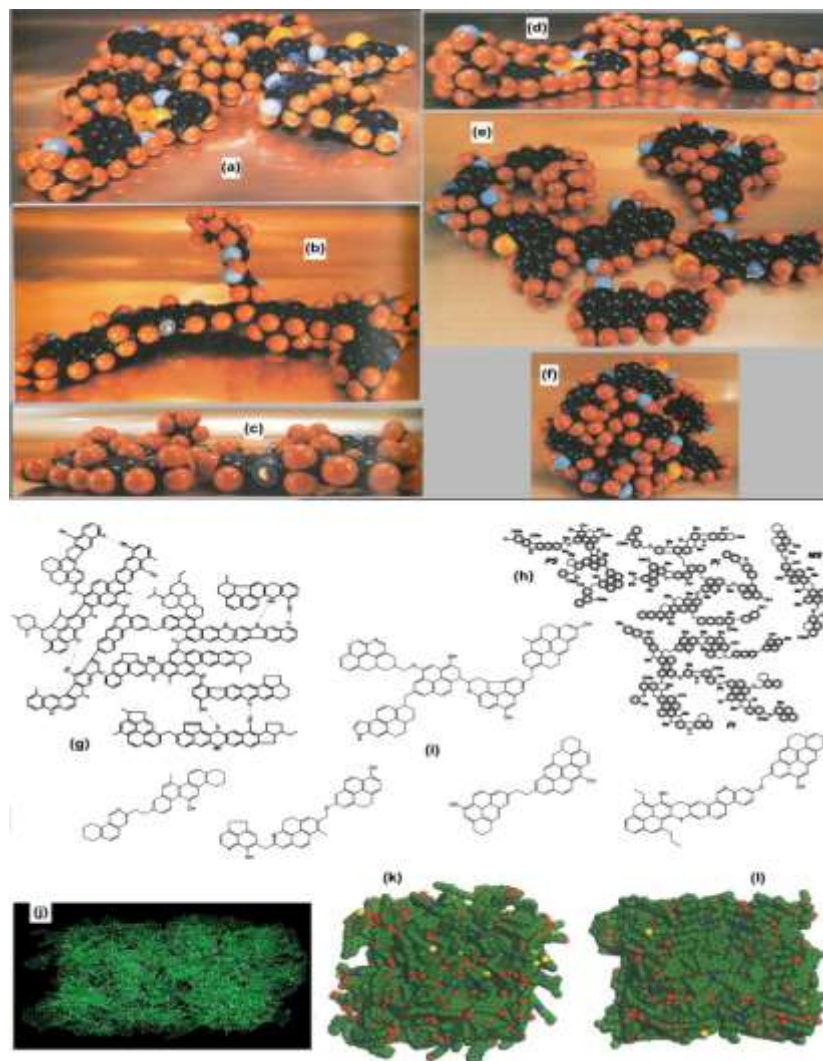


Figure 2-6. Selected molecular representations of bituminous coal (Mathews and Chaffee, 2012:1): (a-f) the space-filling representation of Spiro (Spiro, 1981:1121), (a) Wiser model, (b) Given model, (c) Solomon model, (d) Wiser model, (e) Solomon model, (f) Solomon model globular configuration, (g) Lazarov and Marinov (Lazarov and Marinov, 1987:411), (h) Zao Zhuang coal model (Nomura, Artok, Murata, Yamamoto, Hama, Gao, and Kidena) (Nomura *et al.*, 1998:512), (i) Takanohashi *et al.* Upper Freeport model (Takanohashi and Kawashima, 2002:379), (j) Narkiewicz and Mathews (Narkiewicz and Mathews, 2008:3104), (k-l) inertinite-rich and vitrinite-rich models of Van Niekerk and Mathews (Niekerk and Mathews, 2010:73). Structures were reprinted with permission of the copyright holders (Mathews and Chaffee, 2012:1).

## CHAPTER 2: LITERATURE OVERVIEW

Chars were believed to make the best representation by constructing a two-component model comprising both 'oligomeric' and 'planar' aggregates of aromatic ring structures that can both grow during charring at progressively higher temperatures (Mathews *et al.*, 2011:718; Marzec, 1997:837). Domazetis *et al.* used the semi-empirical, density functional theory and *ab initio* approach to model the brown coal chars with iron species in order to demonstrate the formation  $H_2$ , CO at an atomic level (Domazetis *et al.*, 2008:581; Domazetis *et al.*, 2007:2531; Domazetis *et al.*, 2008:3994; Domazetis *et al.*, 2008:105). The results showed that hydrogen abstraction and hydrogen formation were energetically favoured; and that the loss of CO was via decomposition of the newly formed [C-O-Fe] group (Domazetis *et al.*, 2007:2531).

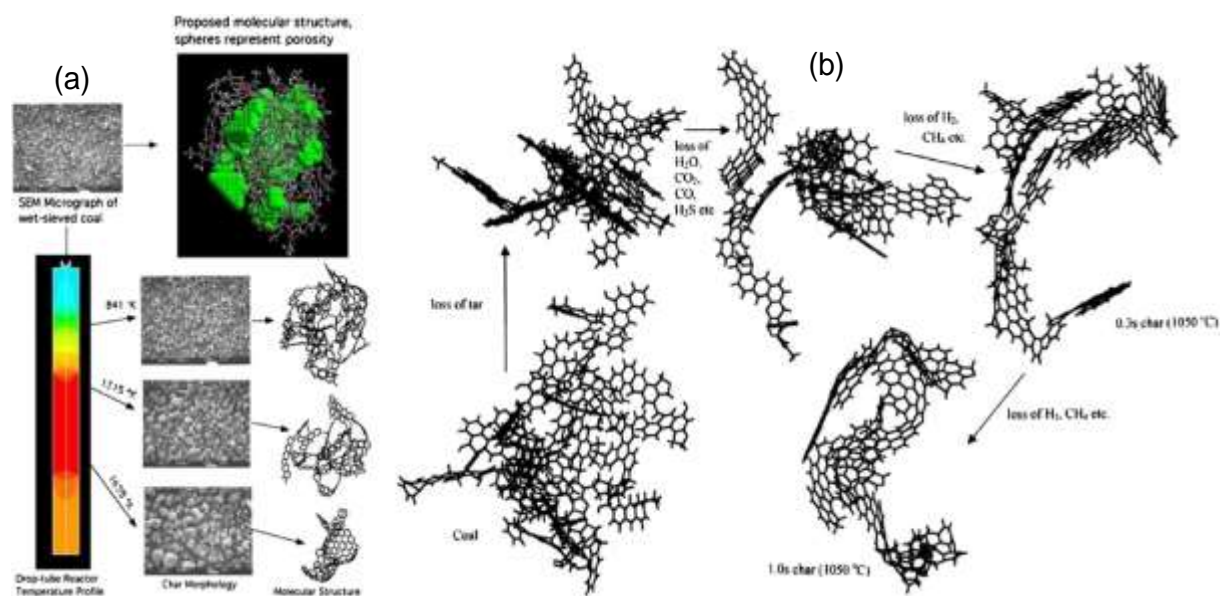


Figure 2-7. Structure of coal-to-char transitions derived via molecular modelling approaches (Mathews *et al.*, 2011:718). ((a), left-hand side) drop-tube reactor temperature profile and SEM of coal and char particles, and molecular models of coal and chars for Lewiston–Stockton vitrinite (Mathews *et al.*, 1998:136). ((b), right-hand side) Pittsburgh #8 coal to char transitions ((b), right hand side) for wire-mesh generated chars (Jones *et al.*, 1999:1737). Copyright Elsevier (1999) (Mathews *et al.*, 2011:718). Reprinted with permission (Mathews *et al.*, 2011:718).

## CHAPTER 2: LITERATURE OVERVIEW

---

Castro-Marcano *et al.* used the Fringe3D in combination with a distribution of aromatic structures from the image processing and analysis of the HRTEM micrographs, to construct Illinois No. 6 coal char structure (Figure 2-8(b)) (Castro-Marcano *et al.*, 2012:1272). The model was used to simulate combustion using molecular dynamics component (ReaxFF reactive forcefield). It was found that char oxidation process initially commenced with either thermal degradation of char structure to form small fragments, followed by their oxidation, or by hydrogen abstraction reactions by oxygen molecules and O and OH radicals (Castro-Marcano *et al.*, 2012:1272).

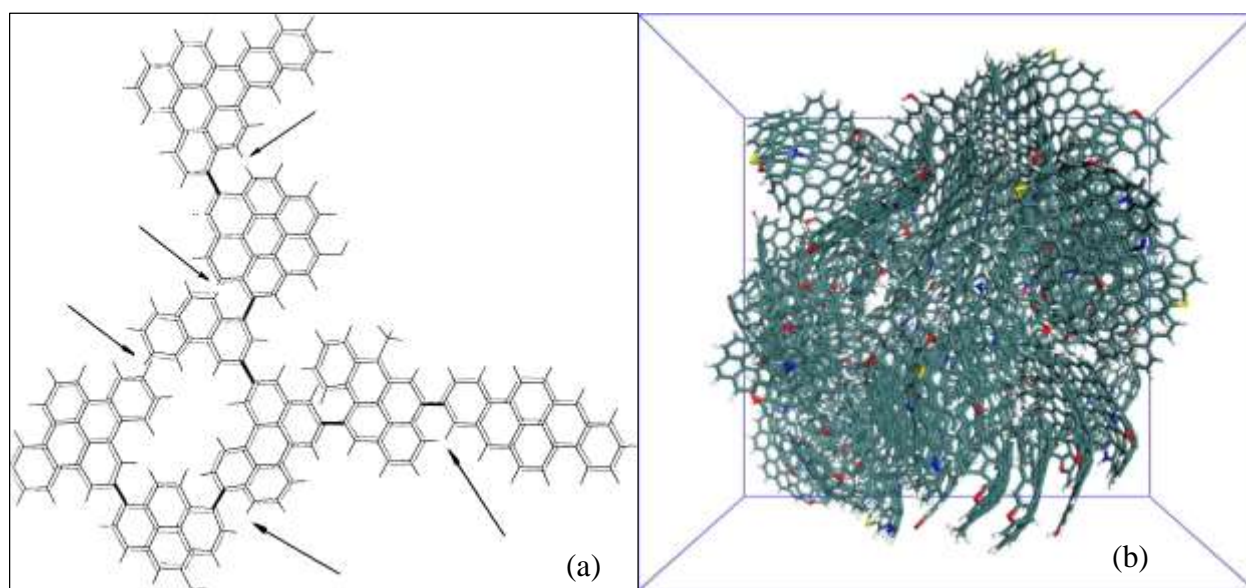


Figure 2-8. Coal char structures. ((a), left-hand side) Marzec oligomeric  $C_{173}H_{88}O_2$  model for low-temperature coal char (Marzec, 1997:837). In ((a), left-hand side), arrows indicate H atoms that are less than 0.1 nm apart; strong repulsive forces between them make the planar conformer unstable (Marzec, 1997:837). ((b), right-hand side) Castro-Marcano Illinois No. 6 coal chars; composed of 7458 atoms ( $C_{5743}H_{1511}O_{131}N_{61}S_{12}$ ) within 66 molecules (Castro-Marcano *et al.*, 2012:1272), where green = C, white = H, red = O, blue = N and yellow = S.

## CHAPTER 2: LITERATURE OVERVIEW

---

### 2.7 Reactivity of coals chars

It is vital to give more attention on what is known about gas-solid interaction in the gasification reactivities of coal. Rates of gasification of porous chars are primarily affected by three parameters: active site concentration, accessibility of the reactant gas into the internal area of the char and, hence, to active sites; as well as the presence of catalysts which are active for the dissociation of molecular species into surface complexes and carbon monoxide gases, reactive oxygen atoms or hydrogen atoms. Char gasification reactivity was believed to be proportional to the proportion of active sites in the char (Xu *et al.*, 2012:118; Irfan *et al.*, 2011:12). A higher pyrolysis temperature and slower heating rate improved the growth of the char crystalline structure and, consequently, a decrease of char surface active sites (Xu *et al.*, 2012:118). There are views that, in the primary stages of the gasification, disorganised carbons from tars are removed, rendering the inaccessible porosity open and then expanding of all sizes of pores, which enhance reactivity until up to a certain conversion (Irfan *et al.*, 2011:12). Present catalytic gasification uses salts that are in molten state at reaction temperatures. These include  $\text{FeCl}_2$ ,  $\text{SnCl}_2$ ,  $\text{KHCO}_3$  and  $\text{K}_2\text{CO}_3$ . Coetzee *et al.* investigated the gasification behaviour of large coal particles impregnated with  $\text{K}_2\text{CO}_3$  and found that these coals demonstrated high reactivity and low activation energy (Coetzee *et al.*, 2013:75).

#### 2.7.1 Reaction rate regimes

The gasification behaviour of char particles is generally expressed as the reaction rate control (Yamashita *et al.*, 2006:85). Walker *et al.* made an immense contribution to the identification of reaction rate regimes (Walker Jr *et al.*, 1959:133). These are classified into chemical-reaction rate control (zone I regime), pore-diffusion rate control (zone II regime), and bulk-diffusion rate control (zone III regime). The rate control regime differs with the temperature range. This is because the reaction rate is correlated with the intrinsic reactivity of the char and the diffusion of gaseous reactants to the particle

## CHAPTER 2: LITERATURE OVERVIEW

---

surface (Yamashita *et al.*, 2006:85). Therefore, these factors should be taken into account when modelling the gasification reaction (Yamashita *et al.*, 2006:85). The results of Hurt and Calo also found that, for the oxidation of char at oxygen gas partial pressures in the vicinity of atmospheric, a high intrinsic order in the low temperature, zone I regime (<900 K), results supported low intrinsic order in the high temperature, only slightly, zone II regime (>1200 K), and some proposal of a change toward a second higher-order regime at higher temperature, zone III regime (>about 1600 K) (Hurt and Calo, 2001:1138).

### 2.7.1.1 Chemical-reaction rate control

The chemical reaction regime is characterised by the absence of mass transfer limitation to the overall rate, which is common in char gasification (Liu *et al.*, 2000:1767). Chemically controlled reactions occur at lower temperatures (600–1000 °C) and are characteristic to the intrinsic reactivity of char-gas reactions (Ahn *et al.*, 2001:1651; Irfan *et al.*, 2011:12; Sima-Ella *et al.*, 2005:1920). Liu *et al.* characterised the pore structure for six bituminous coal chars using image analysis in order to examine the relationship between the reaction rate and the char structure under chemically controlled conditions. It was found that, as the reaction under chemically controlled conditions proceeded, the fine pores (micropores) significantly affect the reactivity of a char particle (Liu *et al.*, 2000:617). Everson *et al.* carried out TGA experiments at 87.5 kPa and 287.5 kPa between 850 °C and 900 °C with 1mm diameter particles and calculated the intrinsic reaction parameters based on the power rate law from carbon conversion versus real time results using a stepwise regression procedure (Everson *et al.*, 2008:3082). The results showed that the random pore model predictions for the carbon conversion with time using the determined parameters correlated very well with experimental results, therefore emphasising the chemical-reaction controlled reaction rate (Everson *et al.*, 2008:3082).

## CHAPTER 2: LITERATURE OVERVIEW

---

### 2.7.1.2 Diffusion-reaction rate control

The gasification reaction rate in the high-intermediate-temperature zone is controlled by diffusion (regime II) (Kajitani *et al.*, 2006:163). Pore diffusivity is an imperative element when predicting overall reaction rates for reactions limited by pore diffusion (Liu *et al.*, 2000:617). The pore diffusion regime is between the boundary layer diffusion and chemical reaction regimes (Liu *et al.*, 2000:1767). The wall thickness of the char particle, determined by the size, porosity, and shape of the particle, is one of the most significant elements in the diffusion rate in the particle (Yamashita *et al.*, 2006:85). Therefore, the wall thickness make a remarkable contribution to the temperature change between the chemical-reaction rate control regime and the pore-diffusion rate control regime (Yamashita *et al.*, 2006:85).

### 2.7.1.3 Gas film bulk-diffusion rate control

The gasification reaction rates at relatively high temperatures occur predominantly by the gas film bulk diffusion limited step at the outer surface of char particles (Dutta *et al.*, 1977:20). The carbon bulk diffusion mechanism was first proposed in 1971 to explain the observed kinetics of catalytic carbon formation on several transition metals (Lobo *et al.*, 2011:110; Lobo, 2013:210). This mechanism was applied in 1975 to the gasification of carbon deposited on metal catalysts catalysed by H<sub>2</sub>, H<sub>2</sub>O, and CO<sub>2</sub> (Figueiredo and Trimm, 1975:154; Lobo, 2013:210). The carbon bulk diffusion mechanism was also invoked to explain the observed kinetics of carbon gasification by O<sub>2</sub> and by H<sub>2</sub> catalysed by Ni, Co, Mo, their oxides and some mixtures (Silva *et al.*, 1990:239; Lobo, 2013:210).

## CHAPTER 2: LITERATURE OVERVIEW

---

### 2.7.2 Reaction rate models

#### 2.7.2.1 Background

The activation of char with oxidising gas is a gas-solid reaction influenced by pore structure and surface area of the solid particle (Irfan *et al.*, 2011:12). These structural differences and other factors such as film mass transfer, pore diffusion, and chemical reaction have to be taken into account in the modelling of the reaction concomitantly (Irfan *et al.*, 2011:12). A large number of different models has been proposed and used to illustrate coal char gasification reaction. They are principally: the homogeneous model (or volume reaction model) (Molina and Mondragon, 1998:1831), the shrinking core model (Everson *et al.*, 2006:1076), non-reacted core model (Molina and Mondragon, 1998:1831), capillary/random pore model (Bhatia and Perlmutter, 1980:379), the random capillary pore model (Gavals, 1980:577), spherical vesicle pore model (Smith, 1994; Simons, 1983:275). Here, specific attention is given to the random pore model.

#### 2.7.2.2 Random pore model

Random pore model is a rather simple but successful gasification reactivity model of Bhatia and Perlmutter and Gavals (Bhatia and Perlmutter, 1980:379; Moulijn and Kapteijn, 1995:1155; Everson *et al.*, 2008:3082; Gavals, 1980:577). The random pore model for gasification and combustion can be used to characterise the intrinsic reaction rate, which considers the competing mechanisms of pore growth and overlap in a char particle undergoing conversion (Ochoa *et al.*, 2001:161; Bhatia, 1998:2478; Everson *et al.*, 2013:148; Everson *et al.*, 2008:3082).

The important features of random pore model with application to gasification of chars can be described as follows (Bhatia and Perlmutter, 1980:379; Gavals, 1980:577): (1) The heterogeneous char-gas reaction sites occur in cylindrical pores of arbitrary size distribution, which may overlap, grow, collapse or coalesce during reaction, (2)

## CHAPTER 2: LITERATURE OVERVIEW

---

Variations of the active surface area of the char as gasification reaction progresses are accounted for by the initial char physical properties incorporated in a dimensionless structural parameter, and (3) the random pore model is capable of describing conversion that show a maximum reaction rate at certain conversion levels.

The random pore model overall reaction rate in the absence of external and internal diffusion is given by Equation 2.14 (Bhatia and Perlmutter, 1980:379; Everson *et al.*, 2008:3403). This equation consists of a lumped reaction rate term  $r^L$  accounting for chemical reaction (Equations 2.15 and 2.16) and a group of terms accounting the effect of the structural changes which is characterized by a structural parameter,  $\psi$  (Equation 2.17) (Bhatia and Perlmutter, 1980:379; Everson *et al.*, 2008:3403).

$$\frac{dX}{dt} = (1-X)\sqrt{1-\psi \ln(1-X)} \quad (2.14)$$

$$r^L = \frac{r_s S_o}{(1-\varepsilon_o)} \quad (2.15)$$

$$r_s = k_{so} \exp\left(\frac{-E_a}{RT}\right) P_{CO_2}^n \quad (2.16)$$

$$\psi = \frac{4\pi L_o(1-\varepsilon_o)}{S_o^2} \quad (2.17)$$

By the integration of Equation 2.14, Equation 2.18 for time as a function of conversion is obtained.

$$t = \frac{2}{r^L \psi} \left( \sqrt{1-\psi \ln(1-X)} - 1 \right) \quad (2.18)$$

Rearranging Equation (2.18) and expressing the carbon conversion,  $X$ , as a function of time can be obtained (Equation 2.19):

## CHAPTER 2: LITERATURE OVERVIEW

---

$$X = 1 - \exp \left[ -r^L t \left( 1 + \frac{r^L t \psi}{4} \right) \right] \quad (2.19)$$

In order to evaluate the structural parameter,  $\psi$ , Everson *et al.* (Everson *et al.*, 2008:3403) proposed the use of the reduced time, ( $t/t_{0.9}$ ), which can be derived from Equation (2.18) to give Equation 2.20.

$$\frac{t}{t_{0.9}} = \frac{\sqrt{1 - \psi \ln(1 - X)} - 1}{\sqrt{1 - \psi \ln(1 - 0.9)} - 1} \quad (2.20)$$

It can be seen that the ratio  $t/t_{0.9}$  is only dependent on the dimensionless structural parameter,  $\psi$ , and the conversion  $X$ . Thus, a plot of conversion  $X$  versus  $t/t_{0.9}$  can conveniently be used to determine the structural parameter for chemical reaction controlled reactions only.

### 2.8 Molecular reactivity modelling

Molecular modelling techniques have long been used to understand the multiple reaction paths contributing to steam- and CO<sub>2</sub>-gasification of chars, including oxygen-char chemical interactions. Although the studies mainly focused on atomic structures of carbonaceous material other than coal chars (Hennig, 1965:107; Gadsby *et al.*, 1948:357; Long and Sykes, 1948:377; Frankcombe and Smith, 2004:2921), the basis for site-specific reaction mechanisms that may be applicable to coal chars were established (Chen *et al.*, 1993:2835; Chen and Yang, 1997:421; Chen and Yang, 1998:1061; Montoya *et al.*, 2002:125; Montoya *et al.*, 2003:29; Montoya *et al.*, 2002:1863; Montoya *et al.*, 2001:6757; Radovic, 2005:907; Radovic, 2009:17166). Small carbon model clusters have been used to gather knowledge on site-specific reaction mechanism with oxygen carrying gases, the most common being the zigzag, armchair and tip models (Figure 2-9) (Espinal *et al.*, 2003:1003; Montoya *et al.*, 2003:29; Radovic, 2005:907).

## CHAPTER 2: LITERATURE OVERVIEW

---

### 2.8.1 The Dmol<sup>3</sup> and density functional theory

Delley did extensive work on quantum mechanics (Delley, 2000:7756; Delley, 2006:117; Delley, 1990:508). Whereas the quantum mechanical calculations on molecules started in the late 1920s, right after the formulation of quantum mechanics, practical calculations on polyatomic molecules with approximate wave functions became feasible with the introduction of variational Gaussian basis sets (Delley, 1990:508). Much later, the density functional theory (DFT) approach, which de-emphasises the importance of wave function and leads to a technique to approximate calculations of electronic properties, was introduced (Delley, 1990:508). The DFT starts from a theorem formulated by Hohenberg and Kohn and later generalised by Levy (Hohenberg and Kohn, 1964:B864; Levy, 1979:6062). It states that all ground state properties are functionals of the density. It particularly specifies that the ground state energy of an electron system in an external potential, i.e., the potential due to a set of nuclei in a given arrangement, can be found by minimising the functional with respect to variations in the density (Delley, 1990:508). The DMol<sup>3</sup> is originally a method for the DFT calculations of molecular clusters in the gas phase (Delley, 2006:117). However, recent developments on the DMol<sup>3</sup> method showed the possibilities for accurate calculations on the insulating and metallic solids. The method can now be applied to calculations of the enthalpy of formation of a set of molecules and solids (Delley, 2000:7756). For an example, it was found that the numerically localized basis sets yielded improved enthalpies for the formation of H, N, O, F, Cl, C, Si, S atoms. Furthermore, the DMol<sup>3</sup> is normally run to give self-consistent field (SCF) densities of high accuracy.

### 2.8.2 The Fukui function

The Fukui function ( $f(r)$ ) is among the most basic and commonly used reactivity indicators (Sablon *et al.*, 2009:1245; Bultinck *et al.*, 2007:034102), and can be defined according to Equations (2.21) - (2.23).

$$f^+(r) = [\partial\rho(r)/\partial N]_{v(r)}^+ = [\rho_{N+1}(r) - \rho_N(r)] \approx \rho_{LUMO}(r), \text{ nucleophilic attack} \quad (2.21)$$

$$f^-(r) = [\partial\rho(r)/\partial N]_{v(r)}^- = [\rho_N(r) - \rho_{N-1}(r)] \approx \rho_{HOMO}(r), \text{ electrophilic attack} \quad (2.22)$$

## CHAPTER 2: LITERATURE OVERVIEW

---

$$f^0(r) = \frac{1}{2}[f^+(r) + f^-(r)] \approx \frac{1}{2}[\rho_{LUMO}(r) + \rho_{HOMO}(r)], \text{ radical attack} \quad (2.23)$$

Where,  $f(r)$  is the Fukui function for a molecule,  $\rho(r)$  is the electron density,  $v$  is the potential acting on the electron due to all nuclei present,  $N$  is the number of electrons,  $r$  is the site, and  $\rho_{HOMO}$  and  $\rho_{LUMO}$  are the densities of the highest occupied and lowest unoccupied molecular orbitals, respectively. The function  $f^+(r)$  (Equation 2.21) is a measure of reactivity toward a donor reagent (nucleophilic attack),  $f^-(r)$  values (Equation 2.22) measure reactivity toward an acceptor reagent (electrophilic attack) and an average value of both may be taken as a measure of reactivity toward a radical  $f^0(r)$  (Equation 2.23) (Fuentelba *et al.*, 2000:2544).

The Fukui function is most often given as the change in the density function  $\rho(r, N)$  of the molecule as a result of changing the number of electrons ( $N$ ) in the molecule, under the limitation of a steady external potential ( $v$ ) (Bultinck *et al.*, 2007:034102). Fukui proposed this frontier orbital theory (FOT) that permits comprehension of a chemical reaction in respect with of the highest energy occupied molecular orbital (HOMO) and lowest energy occupied molecular orbital (LUMO) (Fukui, 1970:1). Condensed Fukui functions at each atomic site in a molecule can also be expressed with respect to the associated electron densities (Fukui, 1970:1). Parr and Yang found that sites in chemical species with the highest values of Fukui function are those with premier reactivity and are preferred reaction (active) sites (Chattaraj, 2000:511; Melin *et al.*, 2004:2487; Parr and Yang, 1984:4049). It has been shown that, with regard to soft-soft interactions, the preferred active sites in a molecule have the highest value of the Fukui function ( $f^+(r)$ ), in contrast with the hard-hard interactions that are described through the minimum value of the Fukui function (Melin *et al.*, 2004:2487; Pérez *et al.*, 2000:4756; Li and Evans, 1995:7756). Melin *et al.* (Melin *et al.*, 2004:2487) and Perez *et al.* (Pérez *et al.*, 2000:4756) emphasised that this principle frequently describes the reactivity in molecules with only one active site correctly. In other words in the case of soft-soft interaction, the highest values of Fukui function governs selectivity of the active site, selectivity being correlated with the active sites in a molecule that indicate the

## CHAPTER 2: LITERATURE OVERVIEW

---

highest inclination to react in a manner coherent with the reactivity pattern commanded by the global properties (Li and Evans, 1995:7756).

### 2.8.3 Fundamental gasification reaction mechanism

A lack of detailed information on the microscopic mechanism of gasification may be regarded as the major obstacle in modelling carbon-based gasification processes from first principles (Frankcombe and Smith, 2004:2921). Extensive research has been done on the mechanisms of the gasification reactions of carbon by oxygen-containing gases such as O<sub>2</sub>, CO<sub>2</sub>, H<sub>2</sub>O, NO, N<sub>2</sub>O, and SO<sub>2</sub> (Walker Jr *et al.*, 1959:133; Ergun, 1956:480; Ergun and Mentser, 1965; Ergun, 1962; Chen *et al.*, 1993:2835; Walker Jr *et al.*, 1991:411; Yang and Thrower, 1984:163). However, this large proportion of literature does not necessarily simplify the gasification reaction mechanism. Here, special attention is given to the gasification reaction mechanism of coal char by carbon dioxide. Ergun and co-workers particularly made a substantial contribution to the fundamental reaction mechanism of carbon dioxide with carbon surfaces (Ergun, 1956:480; Ergun, 1962; Ergun and Mentser, 1965; Ergun and Tiensuu, 1959:1050; Ergun *et al.*, 1967:403). The heterogeneity of this reaction, due to the solid-gas interaction presents numerous problems in an attempt to understand its mechanism (Montoya *et al.*, 2002:125; Montoya *et al.*, 2003:29; Montoya *et al.*, 2002:1863). The stoichiometric equation (Equation 2.24) does not expose the mechanism of the reaction, which must be understood from the overall rates of reaction under changing experimental conditions.



The understanding of this equation is largely difficult and even becomes more complex when subsidiary factors such as flow conditions, heat transfer and diffusion affects the overall reaction rates substantially. Firstly, when CO<sub>2</sub> approaches a carbon surface that

---

## CHAPTER 2: LITERATURE OVERVIEW

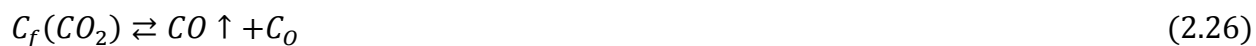
---

was primarily purified, carbon dioxide chemisorbs on the free carbon site (active site) (Montoya *et al.*, 2002:125; Montoya *et al.*, 2003:29; Montoya *et al.*, 2002:1863; Radovic, 2005:907; Zhang *et al.*, 2010:152; Liu *et al.*, 2010:1), according to Equation (2.25).



where,  $C_f$  represents a free carbon site capable of reaction (active site). Figure 2-9 illustrates the different  $CO_2$  chemisorption orientations on most common char models, which include, zigzag, armchair and tip (Montoya *et al.*, 2003:29).

Secondly,  $CO_2$  is reduced to carbon monoxide at temperatures exceeding 700 °C, by a dissociation reaction (Ergun, 1956:480; Cabrera-Sanfeliix, 2008:493; Chen *et al.*, 1993:2835; Frankcombe *et al.*, 2002:2341; Montoya *et al.*, 2003:29; Radovic, 2005:907; Liu *et al.*, 2010:1), as represented by Equation (2.26).



where an arrow facing up indicates a migration action by  $CO$  gas after  $CO_2$  dissociation; and  $C_o$  represents an occupied site, i.e., a site possessing an oxygen atom or an oxygen complex. The dissociation of  $CO_2$  is essentially an oxygen-exchange reaction and not the carbon transfer from solid to gas phase (Ergun, 1956:480). The oxygen lost by dioxide is chemically attached to the carbon surface as oxygen complex (Frankcombe *et al.*, 2002:2341; Adschiri and Furusawa, 1986:927; Montoya *et al.*, 2002:125; Suzuki *et al.*, 1994:649). Ergun found that these oxygen-exchange reactions occur relatively fast (Ergun, 1956:480).

## CHAPTER 2: LITERATURE OVERVIEW

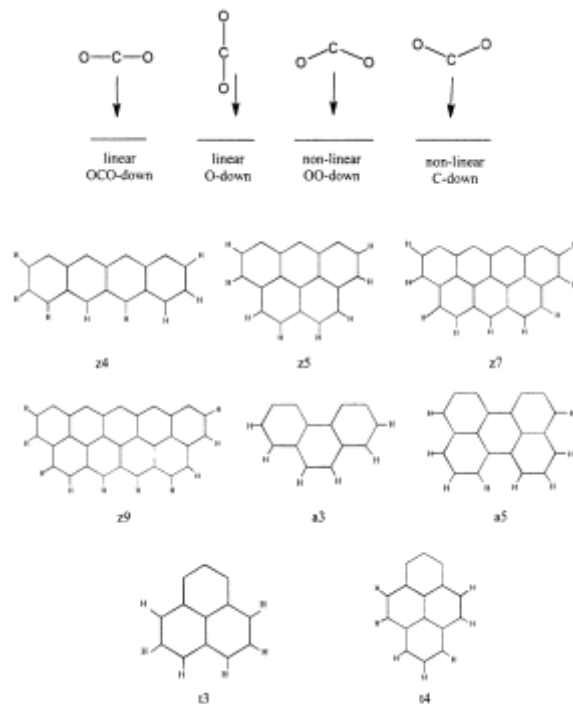


Figure 2-9. Illustration of four different CO<sub>2</sub> chemisorption orientations on different char models. Zigzag models (z4, z5, z7, z9), armchair models (a3, a5) and tip models (t3, t4). Numbers after the letters represent the number of six-membered carbon rings (Montoya *et al.*, 2003:29).

The last reaction is the transfer of carbon from solid phase (from the occupied sites in the carbon structure) to gas phase carbon atom in the form of carbon monoxide and can be expressed according to Equation (2.27) (Frankcombe *et al.*, 2002:2341; Ergun, 1956:480). This reaction essentially represents the conversion (gasification) process, where the solid carbon on the surface is converted or gasified into CO.



where,  $n$  is an integer having a value of 0, 1 or 2 when active sites are considered individually. Ergun found no evidence of reversibility of this reaction (i.e. it may be unidirectional as written in Equation (2.20)).

## CHAPTER 2: LITERATURE OVERVIEW

---

### 2.8.4 Application and behaviour of molecular models for coal and char

Mathews *et al.* have recently made an extensive review of the prevailing and evolving opportunities for coal models to support effective coal utilisation and elucidate the correlation between structure and behaviour (Mathews *et al.*, 2011:718). Application of models traverses from physical transformations (coal drying and contraction to swelling behaviours observed with solvents and gases) to chemical transformations (pyrolysis, char formation), to reactivity (including gasification and combustion) (Mathews *et al.*, 2011:718). A number of researchers have used molecular modelling techniques such as semi-empirical, density functional theory (DFT) and *ab initio*, taking one reaction mechanism at a time, to gain more insight into carbon-carbon dioxide interactions (Espinal *et al.*, 2003:1003; Montoya *et al.*, 2002:125; Montoya *et al.*, 2003:29; Montoya *et al.*, 2002:1863; Montoya *et al.*, 2001:6757; Zhu *et al.*, 2003:635; Zhu *et al.*, 2002:1359; Menéndez *et al.*, 1996:4404; Radovic, 2005:907; Bhatia, 1998:2478; Liu *et al.*, 2010:1). The atomic reactivity modelling of coal char gasification using carbon dioxide may be deduced from these studies. Chen *et al.* used semi-empirical molecular orbital calculations to study surface oxygen complexes on carbon (Chen *et al.*, 1993:2835). Chen and Yang used *ab initio* molecular orbital calculation on graphite: selection of molecular system and model chemistry (Chen and Yang, 1998:1061). Zhu *et al.* carried out a comprehensive study to compare carbon gasification using O<sub>2</sub> with carbon gasification using CO<sub>2</sub> by density functional theory calculations (Zhu *et al.*, 2002:1359). Radovic and co-workers applied a DFT computational chemistry to study the chemical nature of graphene edges, the active sites in graphene, as well as mechanism of CO<sub>2</sub> chemisorption on zigzag carbon active sites (Radovic, 2009:17166; Radovic, 2005:907; Radovic and Bockrath, 2005:5917). Montoya *et al.* performed electronic calculations at the B3LYP DFT level of theory to study the mechanism and kinetics of the desorption of CO from semiquinone carbon-oxygen complexes in carbonaceous surfaces from first principles, the CO<sub>2</sub> adsorption on carbonaceous surfaces as well as the formation of CO precursors during char gasification with O<sub>2</sub>, CO<sub>2</sub> and H<sub>2</sub>O (Menéndez *et al.*, 1996:4404; Montoya *et al.*, 2003:29; Montoya *et al.*, 2002:125).

## CHAPTER 2: LITERATURE OVERVIEW

---

Frankcombe and Smith studied the microscopic mechanism of carbon gasification using DFT molecular modelling techniques and found that the Arrhenius activation energies of both direct gasification and movement to the surface complex lie in the proximity the experimental range of 330-385 kJ mol<sup>-1</sup> (Frankcombe and Smith, 2004:2921; Hüttinger and Nill, 1990:457).

The DMol<sup>3</sup> method can be applied to calculations of the enthalpy of formation of a set of molecules and solids as discussed in (Delley, 2000:7756). The numerically localized basis sets yields improved enthalpies for the formation of H, N, O, F, Cl, C, Si, S atoms; DMol<sup>3</sup> is normally run to give accurate self-consistent field (SCF) densities (Delley, 2000:7756). The exchange-correlation potential of generalized gradient approximation (GGA) functional of Perdew and Wang (PW91) is used (Perdew and Wang, 1992:13244; Furche and Perdew, 2006:044103). This package provides electronic wave functions that are expanded in a double numerical coupled with polarization basis set (DNP). The DNP is comparable to Gaussian 6-31G\*\* basis set used for molecular and solids calculations, but the DNP is more accurate than the 6-31G\*\* set of the same size, as reported in other investigations (Roy *et al.*, 1999:8236; Kusama *et al.*, 2008:84). The default settings of a program such as the Material Studio can be used for most modelling calculations. The transition state (TS) theory is DMol<sup>3</sup> is used for potential energy surface (PES) scans, minimum energy paths. This calculations can be used to predict the activation energy ( $E_a$ ) and enthalpy ( $\Delta H$ ) of reactions at an atomistic level..

### 2.9 Experimental verification

The physical and chemical characteristics of a model can be assessed, using a range of programs now available, and compared with experimental data to give understanding into the composition of coal char. The process of constructing a coal char model to conform to certain physical properties constrains model construction and provides understanding into its composition (Mathews *et al.*, 2011:718). Experimental reactivity experiments are also vital to verify modelling data.

## CHAPTER 2: LITERATURE OVERVIEW

### Nomenclature

Symbol	Definition	Units
$(\sigma+1)$	Average number of attachments to the aromatic cluster	-
$A_{002}$	Area under the (002) peak of the XRD diffractometer	$\text{\AA}^2$
$A_\gamma$	Area under the $\gamma$ side band of the (002) peak	$\text{\AA}^2$
B.L	Number of bridges and loops per aromatic cluster	-
$C$	Number of aromatic carbons per cluster	-
$cp$	Cross polarisation	-
CP-MAS	Cross polarisation-magic angle spinning	-
$d_{002}$	Inter-layer spacing for a group of $N_{\text{ave}}$ parallel layers	$\text{\AA}$
DD	Dipolar dephasing	-
$dm$	Demineralised	-
DMol <sup>3</sup>	A modelling program that uses DFT	-
DNP	Double numerical polarization basis set	-
$E$	Activation energy	$\text{kJ mol}^{-1}$
$E_a$	Activation energy	$\text{kJ mol}^{-1}$
$f(r)$	Fukui function	-
$f(r)$	Electrophilic Fukui function	-
$f^+(r)$	Nucleophilic Fukui function	-
$f^0(r)$	Radical Fukui function	-
$f_a$	Fraction of $sp^2$ carbons	-
$f_a^*$	Fraction of $\text{CH}_3$ groups	-
$f_a'$	Fraction of $sp^2$ -hybridized carbons present in aromatic rings	-
$f_a^B$	Fraction of bridgehead carbons	-
$f_a^C$	Fraction of carboxyl and carboxyl carbons	-
$f_a^H$	Fraction of protonated aromatic carbons	-
$f_{\text{al}}$	Fraction of aliphatic carbons	-
$f_{\text{al}}^H$	Fraction of CH and $\text{CH}_2$ groups	-
$f_{\text{al}}^O$	Aliphatic carbons that are bonded to oxygen	-
$f_a^N$	Fraction of non-protonated aromatic carbons	-
$f_a^O$	Fraction of aldehyde and ketones	-
$f_a^{OO}$	Acid, ester or amide fraction	-
$f_a^P$	Fraction of phenolic carbons	-
$f_a^S$	Fraction of alkylated carbons	-

## CHAPTER 2: LITERATURE OVERVIEW

Symbol	Definition	Units
$I$	X-ray reduced intensity	Atomic counts
$I_{002}$	Reduced intensity due to (002) reflection	Atomic units
$I_{max}$	Maximum reduced intensity of (002) peak	Atomic units
$L_a$	Crystallite diameter	Å
$L_c$	Crystallite height	Å
$M_5$	Average molecular weight of a side chain or half of a bridge mass	$\text{g mol}^{-1}$
$N_{ave}$	Average number of aromatic layers per carbon crystallite	-
$P_o$	Fraction of attachments that are bridges between neighbouring aromatic clusters or fraction of intact bridges	-
$Rr$	Mean random vitrinite reflectance	%
$Rsc$	Total maceral reflectance scan	%
S.C	Number of side chains per cluster	-
$S_o$	Initial surface area	$\text{m}^2 \text{m}^{-3}$
$sp$	Single pulse experiment	-
$x_A$	Fraction of amorphous carbon	-
$x_b$	Mole fraction of aromatic bridgehead carbons	-

### Greek symbols

Symbol	Definition	Units
$\rho$	Skeletal/true density (of coals/chars)	$\text{g cm}^{-3}$
$\theta$	Peak position / XRD angle of scan	radians
$\theta_{002}$	Peak position of (002) peak	degrees (°)
$\beta$	Full width at half maximum of the corresponding	degrees (°)
$\gamma$	Gamma band/peak	-
$\lambda$	wavelength of the X-radiation	Å

### Abbreviations

Acronym	Definition
AFT	Ash fusion temperatures
BET	Brunauer, Emmett and Teller

## CHAPTER 2: LITERATURE OVERVIEW

---

Acronym	Definition
Bt	Billion tons
FT	Fischer Trøpsch
FTIR	Fourier transform infrared spectroscopy
HRTEM	High resolution transmission electron microscopy
HV	Highveld coal
ICCP	International committee for coal and organic petrology
IGCC	Integrated gasification combined cycle
ISO	International Organisation of Standardisation
L-H	Langmuir-Hinshelwood
<i>M.W.</i>	Average molecular weight of aromatic cluster
MEP	Minimum energy path
PES	Potential energy surface
<i>QOF</i>	quality of fit
<i>RPM</i>	Random pore model
SABS	South African Bureau of Standards
SAS	Sasol advanced synthol
<i>SPE</i>	Single pulse excitation
ss <sup>13</sup> C NMR	Solid state nuclear magnetic resonance spectroscopy
<i>STP</i>	Standard temperature and pressure
<i>TGA</i>	Thermogravimetric analyser
WB	Waterberg coal
XRD	X-ray diffraction

---

## CHAPTER 2: LITERATURE OVERVIEW

---

### 2.10 References

- ADSCHIRI, T. and FURUSAWA, T. 1986. Relation between CO<sub>2</sub>-reactivity of coal char and BET surface area. *Fuel*, 65, 927.
- AHN, D.; GIBBS, B.; KO, K. and KIM, J. 2001. Gasification kinetics of an Indonesian sub-bituminous coal-char with CO<sub>2</sub> at elevated pressure. *Fuel*, 80, 1651.
- ALONSO, M. J. G.; BORREGO, A. G.; ÁLVAREZ, D. and MENÉNDEZ, R. 2001. A reactivity study of chars obtained at different temperatures in relation to their petrographic characteristics. *Fuel Processing Technology*, 69, 257.
- ALVAREZ, D.; BORREGO, A. G.; MENÉNDEZ, R. and BAILEY, J. G. 1998. An unexpected trend in the combustion behavior of hvBb coals as shown by the study of their chars. *Energy & Fuels*, 12, 849.
- BABU, V. S. and SEEHRA, M. 1996. Modeling of disorder and X-ray diffraction in coal-based graphitic carbons. *Carbon*, 34, 1259.
- BAI, J.; LI, W.; LI, C.-Z.; BAI, Z.-Q. and LI, B.-Q. 2009. Influences of mineral matter on high temperature gasification of coal char. *Journal of Fuel Chemistry and Technology*, 37, 134.
- BAI, Y.; WANG, P.; YAN, L.; LIU, C.; LI, F. and XIE, K. 2013. Effects of CO<sub>2</sub> on gas evolution and char structure formation during lump coal pyrolysis at elevated pressures. *Journal of Analytical and Applied Pyrolysis*, 104, 202.
- BELL, D. A.; TOWLER, B. F. and FAN, M. 2010. *Coal gasification and its applications*, William Andrew.
- BHATIA, S. and PERLMUTTER, D. 1980. A random pore model for fluid-solid reactions: I. Isothermal, kinetic control. *AIChE Journal*, 26, 379.
- BHATIA, S. K. 1998. Reactivity of chars and carbons: New insights through molecular modeling. *AIChE Journal*, 44, 2478.
- BOTTO, R. E.; WILSON, R. and WINANS, R. E. 1987. Evaluation of the reliability of solid <sup>13</sup>C-NMR spectroscopy for the quantitative analysis of coals: study of whole coals and maceral concentrates. *Energy & Fuels*, 1, 173.
- BULTINCK, P.; FIAS, S.; VAN ALSENOY, C.; AYERS, P. and CARBÓ-DORCA, R. 2007. Critical thoughts on computing atom condensed Fukui functions. *The Journal of Chemical Physics*, 127, 034102.
- CABRERA-SANFELIX, P. 2008. Adsorption and reactivity of CO<sub>2</sub> on defective graphene sheets. *The Journal of Physical Chemistry A*, 113, 493.
- CAI, H. Y. and KANDIYOTI, R. 1995. Effect of changing inertinite concentration on pyrolysis yields and char reactivities of two South African coals. *Energy & Fuels*, 9, 956.
- CAIRNCROSS, B. 2001a. An overview of the Permian (Karoo) coal deposits of southern Africa. *African Renaissance and Geosciences*, 33, 529.
- CAIRNCROSS, B. 2001b. An overview of the Permian (Karoo) coal deposits of southern Africa. *Journal of African Earth Sciences*, 33, 529.
- CAIRNCROSS, B. and CADLE, A. B. 1988. Palaeoenvironmental control on coal formation, distribution and quality in the Permian Vryheid Formation, East Witbank Coalfield, South Africa. *International Journal of Coal Geology*, 9, 343.
- CAIRNCROSS, B.; HART, R. and WILLIS, J. 1990. Geochemistry and sedimentology of coal seams from the Permian Witbank Coalfield, South Africa; a means of identification. *International Journal of Coal Geology*, 16, 309.
- CAO, X.; RO, K. S.; CHAPPELL, M.; LI, Y. and MAO, J. 2010. Chemical structures of swine-manure chars produced under different carbonization conditions investigated by advanced solid-state <sup>13</sup>C Nuclear Magnetic Resonance (NMR) spectroscopy. *Energy & Fuels*, 25, 388.

## CHAPTER 2: LITERATURE OVERVIEW

---

- CAO, Y.; GAO, Z.; JIN, J.; ZHOU, H.; COHRON, M.; ZHAO, H.; LIU, H. and PAN, W. 2008. Synthesis gas production with an adjustable H<sub>2</sub>/CO ratio through the coal gasification process: Effects of coal ranks and methane addition. *Energy & Fuels*, 22, 1720.
- CARLSON, G. A. 1992. Computer simulation of the molecular structure of bituminous coal. *Energy & Fuels*, 6, 771.
- CARTZ, L. and HIRSCH, P. B. 1960. A contribution to the structure of coals from X-ray diffraction studies. *Philosophical Transactions of the Royal Society of London. Series A, Mathematical and Physical Sciences*, 252, 557.
- CASTRO-MARCANO, F.; KAMAT, A. M.; RUSSO JR, M. F.; VAN DUIN, A. C. T. and MATHEWS, J. P. 2012. Combustion of an Illinois No. 6 coal char simulated using an atomistic char representation and the ReaxFF reactive forcefield. *Combustion and Flame*, 159, 1272.
- CASTRO-MARCANO, F.; LOBODIN, V. V.; RODGERS, R. P.; MCKENNA, A. M.; MARSHALL, A. G. and MATHEWS, J. P. 2012. A molecular model for Illinois No. 6 Argonne Premium coal: Moving toward capturing the continuum structure. *Fuel*, 95, 35.
- CHABALALA, V. P.; WAGNER, N. and POTGIETER-VERMAAK, S. 2011. Investigation into the evolution of char structure using Raman spectroscopy in conjunction with coal petrography; Part 1. *Fuel Processing Technology*, 92, 750.
- CHAN, M. L.; JONES, J. M.; POURKASHANIAN, M. and WILLIAMS, A. 1999. The oxidative reactivity of coal chars in relation to their structure. *Fuel*, 78, 1539.
- CHATTARAJ, P. K. 2000. Chemical reactivity and selectivity: Local HSAB principle versus frontier orbital theory. *The Journal of Physical Chemistry A*, 105, 511.
- CHEN, N. and YANG, R. T. 1998. Ab initio molecular orbital calculation on graphite: Selection of molecular system and model chemistry. *Carbon*, 36, 1061.
- CHEN, S. G. and YANG, R. T. 1997. Unified mechanism of alkali and alkaline-earth catalyzed gasification reactions of carbon by CO<sub>2</sub> and H<sub>2</sub>O. *Energy & Fuels*, 11, 421.
- CHEN, S. G.; YANG, R. T.; KAPTEIJN, F. and MOULIJN, J. A. 1993. A new surface oxygen complex on carbon: toward a unified mechanism for carbon gasification reactions. *Industrial & Engineering Chemistry Research*, 32, 2835.
- COETZEE, S.; NEOMAGUS, H. W.; BUNT, J. R. and EVERSON, R. C. 2013. Improved reactivity of large coal particles by K<sub>2</sub>CO<sub>3</sub> addition during steam gasification. *Fuel Processing Technology*, 114, 75.
- COLLOT, A.-G. 2006. Matching gasification technologies to coal properties. *International Journal of Coal Geology*, 65, 191.
- COUSINS, A.; PATERSON, N.; DUGWELL, D. R. and KANDIYOTI, R. 2006. An investigation of the reactivity of chars formed in fluidized bed gasifiers: The effect of reaction conditions and particle size on coal char reactivity. *Energy & Fuels*, 20, 2489.
- CUADRAT, A.; ABAD, A.; GARCÍA-LABIANO, F.; GAYÁN, P.; DE DIEGO, L. and ADÁNEZ, J. 2012. Relevance of the coal rank on the performance of the in situ gasification chemical-looping combustion. *Chemical Engineering Journal*, 195, 91.
- DAVIS, K. A.; HURT, R. H.; YANG, N. Y. C. and HEADLEY, T. J. 1995. Evolution of char chemistry, crystallinity, and ultrafine structure during pulverized-coal combustion. *Combustion and Flame*, 100, 31.
- DELLEY, B. 1990. An all-electron numerical method for solving the local density functional for polyatomic molecules. *Journal of Chemical Physics*, 92, 508.
- DELLEY, B. 2000. From molecules to solids with the DMol3 approach. *The Journal of Chemical Physics*, 113, 7756.
- DELLEY, B. 2006. The conductor-like screening model for polymers and surfaces. *Molecular Simulation*, 32, 117.

## CHAPTER 2: LITERATURE OVERVIEW

---

- DEURBERGUE, A.; OBERLIN, A.; OH, J. and ROUZAUD, J. 1987. Graphitization of Korean anthracites as studied by transmission electron microscopy and X-ray diffraction. *International journal of coal geology*, 8, 375.
- DOMAZETIS, G.; JAMES, B. and LIESEGANG, J. 2008. Computer molecular models of low-rank coal and char containing inorganic complexes. *Journal of Molecular Modeling*, 14, 581.
- DOMAZETIS, G.; JAMES, B. D. and LIESEGANG, J. 2008. High-level computer molecular modeling for low-rank coal containing metal complexes and iron-catalyzed steam gasification. *Energy & Fuels*, 22, 3994.
- DOMAZETIS, G.; RAOARUN, M. and JAMES, B. D. 2007. Semiempirical and density functional theory molecular modeling of brown coal chars with iron species and H<sub>2</sub>, CO Formation. *Energy & Fuels*, 21, 2531.
- DOMAZETIS, G.; RAOARUN, M.; JAMES, B. D. and LIESEGANG, J. 2008. Molecular modelling and experimental studies on steam gasification of low-rank coals catalysed by iron species. *Applied Catalysis A: General*, 340, 105.
- DRY, M. E. 1996. Practical and theoretical aspects of the catalytic Fischer-Tropsch process. *Applied Catalysis A: General*, 138, 319.
- DRY, M. E. 2002. The Fischer-Tropsch process: 1950–2000. *Catalysis today*, 71, 227.
- DUTTA, S.; WEN, C. Y. and BELT, R. J. 1977. Reactivity of coal and char in carbon dioxide atmosphere. *Industrial & Engineering Chemistry Process Design and Development*, 16, 20.
- EMMERICH, F. G. 1995. Evolution with heat treatment of crystallinity in carbons. *Carbon*, 33, 1709.
- ERGUN, S. 1956. Kinetics of the reaction of carbon with carbon dioxide. *The Journal of Physical Chemistry*, 60, 480.
- ERGUN, S. 1962. *Kinetics of the reactions of carbon dioxide and steam with coke*, US Government Printing Office.
- ERGUN, S. and MENTSER, M. 1965. *Reactions of carbon with carbon dioxide and steam*, Marcel Dekker, Inc.: New York.
- ERGUN, S. and TIENSUU, V. 1959. Tetrahedral structures in amorphous carbons. *Acta Crystallographica*, 12, 1050.
- ERGUN, S.; YASINSKY, J. B. and TOWNSEND, J. R. 1967. Transverse and longitudinal optical properties of graphite. *Carbon*, 5, 403.
- ESPINAL, J. F.; MONTOYA, A.; MONDRAGÓN, F. and TRUONG, T. N. 2003. A DFT study of interaction of carbon monoxide with carbonaceous materials. *The Journal of Physical Chemistry B*, 108, 1003.
- EVERSON, R. C.; NEOMAGUS, H. W. and KAITANO, R. 2011. The random pore model with intraparticle diffusion for the description of combustion of char particles derived from mineral-and inertinite-rich coal. *Fuel*, 90, 2347.
- EVERSON, R. C.; NEOMAGUS, H. W.; KAITANO, R.; FALCON, R. and DU CANN, V. M. 2008. Properties of high ash coal-char particles derived from inertinite-rich coal: II. Gasification kinetics with carbon dioxide. *Fuel*, 87, 3403.
- EVERSON, R. C.; NEOMAGUS, H. W. J. P.; KAITANO, R.; FALCON, R.; ALPHEN, C. V. and DU CANN, V. M. 2008. Properties of high ash char particles derived from inertinite-rich coal: 1. Chemical, structural and petrographic characteristics. *Fuel*, 87, 3082.
- EVERSON, R. C.; NEOMAGUS, H. W. J. P.; KASAINI, H. and NJAPHA, D. 2006. Reaction kinetics of pulverized coal chars derived from inertinite-rich coal discards: Gasification with carbon dioxide and steam. *Fuel*, 85, 1076.
- EVERSON, R. C.; OKOLO, G. N.; NEOMAGUS, H. W. J. P. and DOS SANTOS, J.-M. 2013. X-ray diffraction parameters and reaction rate modeling for gasification and combustion of chars derived from inertinite-rich coals. *Fuel*, 109, 148.

## CHAPTER 2: LITERATURE OVERVIEW

---

- FABIANSKA, M. J. and KRUSZEWSKA, K. K. J. 2003. Relationship between petrographic and geochemical characterisation of selected South African coals. *Papers from the TSOP/ICCP session, 53rd ICCP meeting 2001, Copenhagen, Denmark, and from the 18th TSOP meeting 2002, Houston, TX, USA*, 54, 95.
- FALCON, L. M. A. F. R. M. S. 1987. The petrographic composition of southern African coals in relation to friability, hardness, and abrasive indices. *Southern African Institute of Mining and Metallurgy*, 87, 323.
- FALCON, R. 1989. Macro-and micro-factors affecting coal-seam quality and distribution in southern Africa with particular reference to the No. 2 seam, Witbank coalfield, South Africa. *International Journal of Coal Geology*, 12, 681.
- FALCON, R. M. S., SNYMAN, C. P. 1986. *An introduction to coal petrography: Atlas of petrographic constituents in the bituminous coals of southern Africa*, Johannesburg [South Africa], The Geological Society of South Africa.
- FAURE, K.; WILLIS, J. P. and CLARIS DREYER, J. 1996. The Grootegeluk Formation in the Waterberg Coalfield, South Africa: facies, palaeoenvironment and thermal history—evidence from organic and clastic matter. *International Journal of Coal Geology*, 29, 147.
- FENG, B.; BHATIA, S. K. and BARRY, J. C. 2002. Structural ordering of coal char during heat treatment and its impact on reactivity. *Carbon*, 40, 481.
- FERNANDEZ-ALOS, V.; WATSON, J. K.; WAL, R. V. and MATHEWS, J. P. 2011. Soot and char molecular representations generated directly from HRTEM lattice fringe images using Fringe3D. *Combustion and Flame*, 158, 1807.
- FIGUEIREDO, J. and TRIMM, D. 1975. Gasification of carbon deposits on nickel catalysts. *Journal of Catalysis*, 40, 154.
- FLETCHER, T. H.; SOLUM, M. S.; GRANT, D. M.; CRITCHFIELD, S. and PUGMIRE, R. J. 1991. Solid state <sup>13</sup>C and <sup>1</sup>H NMR studies of the evolution of the chemical structure of coal char and tar during devolatilization. *Twenty-Third Symposium (International) on Combustion*, 23, 1231.
- FOURIE, C.; DU PLESSIS, S. and HENRY, G. 2008. New airborne geophysical data from the Waterberg coalfield. South Africa's major future energy source.
- FRANKCOMBE, T. J.; BHATIA, S. K. and SMITH, S. C. 2002. Ab initio modelling of basal plane oxidation of graphenes and implications for modelling char combustion. *Carbon*, 40, 2341.
- FRANKCOMBE, T. J. and SMITH, S. C. 2004. On the microscopic mechanism of carbon gasification: A theoretical study. *Carbon*, 42, 2921.
- FRANKLIN, R. E. 1950. The interpretation of diffuse X-ray diagrams of carbon. *Acta Crystallographica*, 3, 107.
- FRANZ, J. A.; GARCIA, R.; LINEHAN, J. C.; LOVE, G. D. and SNAPE, C. E. 1992. Single-pulse excitation carbon-13 NMR measurements on the Argonne premium coal samples. *Energy & Fuels*, 6, 598.
- FUCHS, W. and SANDHOFF, A. 1942. Theory of coal pyrolysis. *Industrial & Engineering Chemistry*, 34, 567.
- FUENTEALBA, P.; PÉREZ, P. and CONTRERAS, R. 2000. On the condensed Fukui function. *The Journal of Chemical Physics*, 113, 2544.
- FUKUI, K. 1970. Theory of orientation and stereoselection. *Orientation and Stereoselection*. Springer Berlin Heidelberg.
- FURCHE, F. and PERDEW, J. P. 2006. The performance of semilocal and hybrid density functionals in 3d transition-metal chemistry. *The Journal of Chemical Physics*, 124, 044103.
- GADSBY, J.; LONG, F.; SLEIGHTHOLM, P. and SYKES, K. 1948. The mechanism of the carbon dioxide-carbon reaction. *Proceedings of the Royal Society of London. Series A. Mathematical and Physical Sciences*, 193, 357.

## CHAPTER 2: LITERATURE OVERVIEW

---

- GALE, T. K.; BARTHOLOMEW, C. H. and FLETCHER, T. H. 1996. Effects of pyrolysis heating rate on intrinsic reactivities of coal chars. *Energy & Fuels*, 10, 766.
- GALE, T. K.; FLETCHER, T. H. and BARTHOLOMEW, C. H. 1995. Effects of pyrolysis conditions on internal surface areas and densities of coal chars prepared at high heating rates in reactive and nonreactive atmospheres. *Energy & fuels*, 9, 513.
- GAVALS, G. R. 1980. A random capillary model with application to char gasification at chemically controlled rates. *AIChE Journal*, 26, 577.
- GIBBINS, J. R.; BEELEY, T. J.; CRELLING, J. C.; SCOTT, A. C.; SKORUPSKA, N. M. and WILLIAMSON, J. 1999. Observations of heterogeneity in large pulverized coal particles. *Energy & Fuels*, 13, 592.
- GIBSON, J. 1978. 1977 Robens coal science lecture: Constitution of coal and its relevance to coal conversion processes. *Journal of the Institute of Fuel*, 51, 67.
- GIBSON, L.; SOUNDARRAJAN, N.; SPENIK, J.; MA, J.; SHADLE, L. and PISUPATI, S. V. 2013. Application of particle population model to determine the contribution to slag, flyash, and syngas in entrained flow gasification from particle size distribution. *Energy & Fuels*, 27, 7681.
- GIVEN, P. 1959. Structure of bituminous coals: evidence from distribution of hydrogen.
- GIVEN, P. 1960. The distribution of hydrogen in coals and its relation to coal structure. *Fuel*, 39, 147.
- GIVEN, P. 1961. Dehydrogenation of coals and its relation to coal structure. *Fuel*, 40, 427.
- GIVEN, P. H. 1964. The chemical study of coal macerals. Editors; Hobson, G.D., Colombo, U. *Advances in organic geochemistry: Proceedings of the international meeting. 1962 Milan*. New York: Macmillan, New York. p. 39-48, 39.
- GUO, Z.; ZHANG, L.; WANG, P.; LIU, H.; JIA, J.; FU, X.; LI, S.; WANG, X.; LI, Z. and SHU, X. 2013. Study on kinetics of coal pyrolysis at different heating rates to produce hydrogen. *Fuel Processing Technology*, 107, 23.
- GUPTA, R. 2007. Advanced coal characterization: A review. *Energy & Fuels*, 21, 451.
- HARTGERS, W. A.; SINNINGHE DAMSTE, J. S.; DE LEEUW, J. W.; LING, Y. and DYRKACZ, G. R. 1994. Molecular characterization of flash pyrolyzates of two Carboniferous coals and their constituting maceral fractions. *Energy & Fuels*, 8, 1055.
- HATTINGH, B. B.; EVERSON, R. C.; NEOMAGUS, H. W. and BUNT, J. R. 2011. Assessing the catalytic effect of coal ash constituents on the CO<sub>2</sub> gasification rate of high ash, South African coal. *Fuel Processing Technology*, 92, 2048.
- HATTINGH, B. B.; EVERSON, R. C.; NEOMAGUS, H. W. J. P.; BUNT, J. R.; VAN NIEKERK, D.; JORDAAN, J. H. L. and MATHEWS, J. P. 2013. Elucidation of the Structural and Molecular Properties of Typical South African Coals. *Energy & Fuels*, 27, 3161.
- HENNIG, G. R. 1965. Anisotropic reactivities of graphite—I. Reactions of ozone and graphite. *Carbon*, 3, 107.
- HIGMAN, C. and TAM, S. 2013. Advances in coal gasification, hydrogenation, and gas treating for the production of chemicals and fuels. *Chemical Reviews*, 114, 1673.
- HIGMAN, C. and VAN DER BURGT, M. 2011. *Gasification*, Gulf Professional Publishing.
- HILL, G. B. and LYON, L. B. 1962. A new chemical structure for coal. *Industrial & Engineering Chemistry*, 54, 36.
- HIRSCH, P. 1954. X-ray scattering from coals. *Proceedings of the Royal Society of London. Series A. Mathematical and Physical Sciences*, 226, 143.
- HOHENBERG, P. and KOHN, W. 1964. Inhomogeneous electron gas. *Physical Review*, 136, B864.
- HOLLAND, M.; CADLE, A.; PINHEIRO, R. and FALCON, R. 1989a. Depositional environments and coal petrography of the Permian Karoo sequence: Witbank Coalfield, South Africa. *International Journal of Coal Geology*, 11, 143.

## CHAPTER 2: LITERATURE OVERVIEW

---

- HOLLAND, M. J.; CADLE, A. B.; PINHEIRO, R. and FALCON, R. M. S. 1989b. Depositional environments and coal petrography of the Permian Karoo Sequence: Witbank Coalfield, South Africa. *International Journal of Coal Geology*, 11, 143.
- HUNT, J.; FERRARI, A.; LITA, A.; CROSSWHITE, M.; ASHLEY, B. and STIEGMAN, A. E. 2013. Microwave-specific enhancement of the carbon-carbon dioxide (Boudouard) reaction. *The Journal of Physical Chemistry C*, 117, 26871.
- HURT, R. H. and CALO, J. M. 2001. Semi-global intrinsic kinetics for char combustion modeling. *Combustion and flame*, 125, 1138.
- HÜTTINGER, K. J. and NILL, J. S. 1990. A method for the determination of active sites and true activation energies in carbon gasification:(II) Experimental results. *Carbon*, 28, 457.
- IRFAN, M. F.; USMAN, M. R. and KUSAKABE, K. 2011. Coal gasification in CO<sub>2</sub> atmosphere and its kinetics since 1948: A brief review. *Energy*, 36, 12.
- ISO 2010. ISO 12902 "Solid mineral fuel – Determination of total carbon, hydrogen and nitrogen – Instrumental methods".
- JEFFREY, L. 2005. Challenges associated with further development of the Waterberg Coalfield. *Journal of the South African Institute of Mining and Metallurgy*, 105, 453.
- JEFFREY, L. 2005. Characterization of the coal resources of South Africa. *Journal of the South African Institute of Mining and Metallurgy*, 105, 95.
- JONES, J. M.; POURKASHANIAN, M.; RENA, C. D. and WILLIAMS, A. 1999. Modelling the relationship of coal structure to char porosity. *Fuel*, 78, 1737.
- KAJITANI, S.; SUZUKI, N.; ASHIZAWA, M. and HARA, S. 2006. CO<sub>2</sub> gasification rate analysis of coal char in entrained flow coal gasifier. *Fuel*, 85, 163.
- KAPUSTA, K. and STAŃCZYK, K. 2011. Pollution of water during underground coal gasification of hard coal and lignite. *Fuel*, 90, 1927.
- KRUSZEWSKA, K. J. 1998. The reactivity of pseudovitrinite in some coals. *Fuel*, 77, 1655.
- KRUSZEWSKA, K. J. 2003. Fluorescing macerals in South African coals. *Papers from the TSOP/ICCP session, 53rd ICCP Meeting 2001, Copenhagen, Denmark, and from the 18th TSOP Meeting 2002, Houston, TX, USA*, 54, 79.
- KUSAMA, H.; ORITA, H. and SUGIHARA, H. 2008. DFT investigation of the TiO<sub>2</sub> band shift by nitrogen-containing heterocycle adsorption and implications on dye-sensitized solar cell performance. *Solar Energy Materials and Solar Cells*, 92, 84.
- LAZAROV, L. and MARINOV, S. 1987. Modelling the structure of a coking coal. *Fuel processing technology*, 15, 411.
- LEDESMA, E.; KALISH, M.; NELSON, P.; WORNAT, M. and MACKIE, J. 2000. Formation and fate of PAH during the pyrolysis and fuel-rich combustion of coal primary tar. *Fuel*, 79, 1801.
- LESTER, E.; ALVAREZ, D.; BORREGO, A.; VALENTIM, B.; FLORES, D.; CLIFT, D.; ROSENBERG, P.; KWIECINSKA, B.; BARRANCO, R. and PETERSEN, H. 2010. The procedure used to develop a coal char classification—Commission III Combustion Working Group of the International Committee for Coal and Organic Petrology. *International Journal of Coal Geology*, 81, 333.
- LEVY, M. 1979. Universal variational functionals of electron densities, first-order density matrices, and natural spin-orbitals and solution of the v-representability problem. *Proceedings of the National Academy of Sciences*, 76, 6062.
- LI, X.; WU, H.; HAYASHI, J.-I. and LI, C.-Z. 2004. Volatilisation and catalytic effects of alkali and alkaline earth metallic species during the pyrolysis and gasification of Victorian brown coal. Part VI. Further investigation into the effects of volatile-char interactions. *Fuel*, 83, 1273.
- LI, Y. and EVANS, J. N. S. 1995. The Fukui function: A key concept linking frontier molecular orbital theory and the hard-soft-acid-base principle. *Journal of the American Chemical Society*, 117, 7756.
-

## CHAPTER 2: LITERATURE OVERVIEW

---

- LIANG, P.; WANG, Z. and BI, J. 2008. Simulation of coal pyrolysis by solid heat carrier in a moving-bed pyrolyzer. *Fuel*, 87, 435.
- LIU, B.; HE, Q.; JIANG, Z.; XU, R. and HU, B. 2013. Relationship between coal ash composition and ash fusion temperatures. *Fuel*, 105, 293.
- LIU, G.-S. and NIKSA, S. 2004. Coal conversion submodels for design applications at elevated pressures. Part II. Char gasification. *Progress in Energy and Combustion Science*, 30, 679.
- LIU, G.-S.; REZAEI, H.; LUCAS, J.; HARRIS, D. and WALL, T. 2000. Modelling of a pressurised entrained flow coal gasifier: the effect of reaction kinetics and char structure. *Fuel*, 79, 1767.
- LIU, G.; BENYON, P.; BENFELL, K.; BRYANT, G.; TATE, A.; BOYD, R.; HARRIS, D. and WALL, T. 2000. The porous structure of bituminous coal chars and its influence on combustion and gasification under chemically controlled conditions. *Fuel*, 79, 617.
- LIU, Z.-S.; WANG, Q.; ZOU, Z.-S. and TAN, G.-L. 2010. Reaction mechanism of carbon gasification in CO<sub>2</sub> under non-isothermal conditions. *Journal of Thermal Analysis and Calorimetry*, 1.
- LOBO, L. 2013. Catalytic carbon gasification: Review of observed kinetics and proposed mechanisms or models highlighting carbon bulk diffusion. *Catalysis Reviews*, 55, 210.
- LOBO, L.; FIGUEIREDO, J. and BERNARDO, C. 2011. Carbon formation and gasification on metals. Bulk diffusion mechanism: A reassessment. *Catalysis Today*, 178, 110.
- LONG, F. and SYKES, K. 1948. The mechanism of the steam-carbon reaction. *Proceedings of the Royal Society of London. Series A. Mathematical and Physical Sciences*, 193, 377.
- LU, L.; SAHAJWALLA, V.; KONG, C. and HARRIS, D. 2001. Quantitative X-ray diffraction analysis and its application to various coals. *Carbon*, 39, 1821.
- MACHADO, A. D. S.; MEXIAS, A. S.; VILELA, A. C. and OSORIO, E. 2013. Study of coal, char and coke fines structures and their proportions in the off-gas blast furnace samples by X-ray diffraction. *Fuel*, 114, 224.
- MALEKSHAHIAN, M. and HILL, J. M. 2011. Effect of pyrolysis and CO<sub>2</sub> gasification pressure on the surface area and pore size distribution of petroleum coke. *Energy & Fuels*, 25, 5250.
- MANGENA, S.; DE KORTE, G.; MCCRINDLE, R. and MORGAN, D. 2004. The amenability of some Witbank bituminous ultra fine coals to binderless briquetting. *Fuel Processing Technology*, 85, 1647.
- MAO, J.-D.; SCHIMMELMANN, A.; MASTALERZ, M.; HATCHER, P. and LI, Y. 2010. Structural features of a bituminous coal and their changes during low-temperature oxidation and loss of volatiles investigated by advanced solid-state NMR spectroscopy. *Energy & Fuels*, 24, 2536.
- MARZEC, A. 1997. New structural concept for carbonized coals. *Energy & fuels*, 11, 837.
- MATHEWS, J. P. 1998. *Following changes in the constitution of rapidly heated bituminous vitrinites*.
- MATHEWS, J. P. and CHAFFEE, A. L. 2012. The molecular representations of coal - A review. *Fuel*, 96, 1.
- MATHEWS, J. P.; FERNANDEZ-ALSO, V.; DANIEL JONES, A. and SCHOBERT, H. H. 2010. Determining the molecular weight distribution of Pocahontas No. 3 low-volatile bituminous coal utilizing HRTEM and laser desorption ionization mass spectra data. *Fuel*, 89, 1461.
- MATHEWS, J. P.; HATCHER, P. G. and SCARONI, A. W. 1998. Devolatilization, a molecular modeling approach. *Preprint preparation. American Chemical Society. Division of fuel chemistry, Dallas, Tx*
- MATHEWS, J. P.; HATCHER, P. G. and SCARONI, A. W. 2001. Proposed model structures for Upper Freeport and Lewiston-Stockton vitrinites. *Energy & Fuels*, 15, 863.
- MATHEWS, J. P.; VAN DUIN, A. C. T. and CHAFFEE, A. L. 2011. The utility of coal molecular models. *Fuel Processing Technology*, 92, 718.
- MATJIE, R. H.; FRENCH, D.; WARD, C. R.; PISTORIUS, P. C. and LI, Z. 2011. Behaviour of coal mineral matter in sintering and slagging of ash during the gasification process. *Fuel Processing Technology*, 92, 1426.

## CHAPTER 2: LITERATURE OVERVIEW

---

- MATSUOKA, K.; AKAHANE, T.; ASO, H.; SHARMA, A. and TOMITA, A. 2008. The size of polyaromatic layer of coal char estimated from elemental analysis data. *Fuel*, 87, 539.
- MELIN, J.; APARICIO, F.; SUBRAMANIAN, V.; GALVÁN, M. and CHATTARAJ, P. K. 2004. Is the Fukui function a right descriptor of hard-hard interactions? *The Journal of Physical Chemistry A*, 108, 2487.
- MENÉNDEZ, J. A.; PHILLIPS, J.; XIA, B. and RADOVIC, L. R. 1996. On the modification and characterization of chemical surface properties of activated carbon: In the search of carbons with stable basic properties. *Langmuir*, 12, 4404.
- MEYERS, R. 2012. *Coal structure*, Elsevier.
- MEYERS, R. A. 1981. *Coal handbook*.
- MINCHENER, A. J. 2005. Coal gasification for advanced power generation. *Fuel*, 84, 2222.
- MOLINA, A. and MONDRAGON, F. 1998. Reactivity of coal gasification with steam and CO<sub>2</sub>. *Fuel*, 77, 1831.
- MONTOYA, A.; MONDRAGÓN, F. and TRUONG, T. N. 2002. Adsorption on carbonaceous surfaces: cost-effective computational strategies for quantum chemistry studies of aromatic systems. *Carbon*, 40, 1863.
- MONTOYA, A.; MONDRAGÓN, F. and TRUONG, T. N. 2002. Formation of CO precursors during char gasification with O<sub>2</sub>, CO<sub>2</sub> and H<sub>2</sub>O. *Fuel Processing Technology*, 77-78, 125.
- MONTOYA, A.; MONDRAGÓN, F. and TRUONG, T. N. 2003. CO<sub>2</sub> adsorption on carbonaceous surfaces: a combined experimental and theoretical study. *Carbon*, 41, 29.
- MONTOYA, A.; TRUONG, T.-T. T.; MONDRAGÓN, F. and TRUONG, T. N. 2001. CO desorption from oxygen species on carbonaceous surface: 1. Effects of the local structure of the active site and the surface coverage. *The Journal of Physical Chemistry A*, 105, 6757.
- MOULIJN, J. A. and KAPTEIJN, F. 1995. Towards a unified theory of reactions of carbon with oxygen-containing molecules. *Carbon*, 33, 1155.
- MUNTEAN, J. V.; STOCK, L. M. and BOTTO, R. E. 1988. Improving the reliability of quantitative solid-state <sup>13</sup>C NMR analysis of coal. *Energy & Fuels*, 2, 108.
- NAKAMURA, K.; TAKANOHASHI, T.; IINO, M.; KUMAGAI, H.; SATO, M.; YOKOYAMA, S. and SANADA, Y. 1995. A model structure of Zao Zhuang bituminous coal. *Energy & Fuels*, 9, 1003.
- NARKIEWICZ, M. R. and MATHEWS, J. P. 2008. Improved low-volatile bituminous coal representation: Incorporating the molecular-weight distribution. *Energy & Fuels*, 22, 3104.
- NIEKERK, D. V. and MATHEWS, J. P. 2010. Molecular representations of Permian-aged vitrinite-rich and inertinite-rich South African coals. *Fuel*, 89, 73.
- NOMURA, M.; ARTOK, L.; MURATA, S.; YAMAMOTO, A.; HAMA, H.; GAO, H. and KIDENA, K. 1998. Structural evaluation of Zao Zhuang coal. *Energy & fuels*, 12, 512.
- OBOIRIEN, B. O.; ENGELBRECHT, A. D.; NORTH, B. C.; DU CANN, V. M.; VERRYIN, S. and FALCON, R. 2011. Study on the structure and gasification characteristics of selected South African bituminous coals in fluidised bed gasification. *Fuel Processing Technology*, 92, 735.
- OCHOA, J.; CASSANELLO, M.; BONELLI, P. and CUKIERMAN, A. 2001. CO<sub>2</sub> gasification of Argentinean coal chars: a kinetic characterization. *Fuel Processing Technology*, 74, 161.
- ORENDT, A. M.; SOLUM, M. S.; SETHI, N. K.; PUGMIRE, R. J. and GRANT, D. M. 1992. <sup>13</sup>C NMR techniques for structural studies of coals and coal chars. *Advances in Coal Spectroscopy*. Springer.
- ORIKASA, H. and TOMITA, A. 2003. A study of the HCN formation mechanism during the coal char gasification by O<sub>2</sub>. *Energy & fuels*, 17, 1536.
- PARR, R. G. and YANG, W. 1984. Density functional approach to the frontier-electron theory of chemical reactivity. *Journal of the American Chemical Society*, 106, 4049.

## CHAPTER 2: LITERATURE OVERVIEW

---

- PERDEW, J. P. and WANG, Y. 1992. Accurate and simple analytic representation of the electron-gas correlation energy. *Physical Review B*, 45, 13244.
- PÉREZ, P.; SIMÓN-MANSO, Y.; AIZMAN, A.; FUENTEALBA, P. and CONTRERAS, R. 2000. Empirical energy–density relationships for the analysis of substituent effects in chemical reactivity. *Journal of the American Chemical Society*, 122, 4756.
- PERRY, S.; HAMBLY, E.; FLETCHER, T.; SOLUM, M. and PUGMIRE, R. 2000. Solid-state carbon-13 NMR characterization of matched tars and chars from rapid coal devolatilization. *Proceedings of the Combustion Institute*, 28, 2313.
- PINETOWN, K. L.; WARD, C. R. and VAN DER WESTHUIZEN, W. 2007. Quantitative evaluation of minerals in coal deposits in the Witbank and Highveld Coalfields, and the potential impact on acid mine drainage. *International Journal of Coal Geology*, 70, 166.
- PONE, J. D. N.; HEIN, K. A.; STRACHER, G. B.; ANNEGARN, H. J.; FINKLEMAN, R. B.; BLAKE, D. R.; MCCORMACK, J. K. and SCHROEDER, P. 2007. The spontaneous combustion of coal and its by-products in the Witbank and Sasolburg coalfields of South Africa. *International Journal of Coal Geology*, 72, 124.
- QI, X.; WANG, D.; XIN, H. and QI, G. 2013. In situ FTIR study of real-time changes of active groups during oxygen-free reaction of coal. *Energy & Fuels*, 27, 3130.
- QIAN, L.; ZHAO, Y.; SUN, S.; CHE, H.; CHEN, H. and WANG, D. 2014. Chemical/physical properties of char during devolatilization in inert and reducing conditions. *Fuel Processing Technology*, 118, 327.
- RADOVIC, L. R. 2005. The mechanism of CO<sub>2</sub> chemisorption on zigzag carbon active sites: A computational chemistry study. *Carbon*, 43, 907.
- RADOVIC, L. R. 2009. Active sites in graphene and the mechanism of CO<sub>2</sub> formation in carbon oxidation. *Journal of the American Chemical Society*, 131, 17166.
- RADOVIC, L. R. and BOCKRATH, B. 2005. On the chemical nature of graphene edges: Origin of stability and potential for magnetism in carbon materials. *Journal of the American Chemical Society*, 127, 5917.
- RATNASAMY, C. and WAGNER, J. P. 2009. Water gas shift catalysis. *Catalysis Reviews*, 51, 325.
- ROUZAUD, J.-N. 1990. Contribution of transmission electron microscopy to the study of the coal carbonization processes. *Fuel Processing Technology*, 24, 55.
- ROUZAUD, J. and OBERLIN, A. 1989. Structure, microtexture, and optical properties of anthracene and saccharose-based carbons. *Carbon*, 27, 517.
- ROUZAUD, J.; OBERLIN, A. and BENY-BASSEZ, C. 1983. Carbon films: structure and microtexture (optical and electron microscopy, Raman spectroscopy). *Thin Solid Films*, 105, 75.
- ROY, R. K.; PAL, S. and HIRAO, K. 1999. On non-negativity of Fukui function indices. *The Journal of chemical physics*, 110, 8236.
- SABLON, N.; PROFT, F. D. and GEERLINGS, P. 2009. Molecular orbital-averaged Fukui function for the reactivity description of alkaline earth metal oxide clusters. *Journal of Chemical Theory and Computation*, 5, 1245.
- SEGGIANI, M. 1999. Empirical correlations of the ash fusion temperatures and temperature of critical viscosity for coal and biomass ashes. *Fuel*, 78, 1121.
- SHARMA, A.; KADOOKA, H.; KYOTANI, T. and TOMITA, A. 2002. Effect of microstructural changes on gasification reactivity of coal chars during low temperature gasification. *Energy & fuels*, 16, 54.
- SHARMA, A.; KYOTANI, T. and TOMITA, A. 1999. A new quantitative approach for microstructural analysis of coal char using HRTEM images. *Fuel*, 78, 1203.
- SHARMA, A.; KYOTANI, T. and TOMITA, A. 2001. Quantitative evaluation of structural transformations in raw coals on heat-treatment using HRTEM technique. *Fuel*, 80, 1467.

## CHAPTER 2: LITERATURE OVERVIEW

---

- SHINN, J. H. 1984. From coal to single-stage and two-stage products: A reactive model of coal structure. *Fuel*, 63, 1187.
- SILVA, I.; ENCINAR, J. and LOBO, L. 1990. Kinetics of carbon gasification by oxygen catalysed by Mo, Co, and Ni. *Catalysis Today*, 7, 239.
- SIMA-ELLA, E.; YUAN, G. and MAYS, T. 2005. A simple kinetic analysis to determine the intrinsic reactivity of coal chars. *Fuel*, 84, 1920.
- SIMONS, G. A. 1983. Enhanced char reactivity via a tailored pore structure. *Combustion and Flame*, 50, 275.
- SINGH, N.; RAGHAVAN, V. and SUNDARARAJAN, T. 2013. Effect of coal properties on gasification of high-ash Indian coals.
- SMITH, K. L. 1994. *The structure and reaction processes of coal*, Springer.
- SNYMAN, C. and BOTHA, W. 1993a. Coal in South Africa. *Journal of African Earth Sciences (and the Middle East)*, 16, 171.
- SNYMAN, C. P. 1989. The role of coal petrography in understanding the properties of South African coal. *International Journal of Coal Geology*, 14, 83.
- SNYMAN, C. P. and BARCLAY, J. 1989. The coalification of South African coal. *International Journal of Coal Geology*, 13, 375.
- SNYMAN, C. P. and BOTHA, W. J. 1993b. Coal in South Africa. *Geology and Development in Southern Africa*, 16, 171.
- SOLOMON, P.; FLETCHER, T. and PUGMIRE, R. 1993. Progress in coal pyrolysis. *Fuel*, 72, 587.
- SOLOMON, P., R. 1981. Coal structure and thermal decomposition. *New Approaches in Coal Chemistry*. AMERICAN CHEMICAL SOCIETY.
- SOLUM, M. S.; PUGMIRE, R. J. and GRANT, D. M. 1989. Carbon-13 solid-state NMR of Argonne-premium coals. *Energy & Fuels*, 3, 187.
- SOLUM, M. S.; SAROFIM, A. F.; PUGMIRE, R. J.; FLETCHER, T. H. and ZHANG, H. 2001. <sup>13</sup>C NMR analysis of soot produced from model compounds and a coal. *Energy & Fuels*, 15, 961.
- SPEIGHT, J. G. 2005. *Handbook of coal analysis*, John Wiley & Sons.
- SPIRO, C. L. 1981. Space-filling models for coal: a molecular description of coal plasticity. *Fuel*, 60, 1121.
- STANGER, R.; XIE, W.; WALL, T.; LUCAS, J. and MAHONEY, M. 2013. Dynamic Elemental Thermal Analysis: A technique for continuous measurement of carbon, hydrogen, oxygen chemistry of tar species evolved during coal pyrolysis. *Fuel*, 103, 764.
- SUAREZ-RUIZ, I., CRELLING, J. C. 2008. *Applied coal petrology*, Academic Press.
- SUN, Q.; LI, W.; CHEN, H. and LI, B. 2003. The variation of structural characteristics of macerals during pyrolysis. *Fuel*, 82, 669.
- SUN, Q.; LI, W.; CHEN, H. and LI, B. 2004. The CO<sub>2</sub> gasification and kinetics of Shenmu maceral chars with and without catalyst. *Fuel*, 83, 1787.
- SUZUKI, T.; OHME, H. and WATANABE, Y. 1994. Mechanisms of alkaline-earth metals catalyzed CO<sub>2</sub> gasification of carbon. *Energy & Fuels*, 8, 649.
- TAKANOHASHI, T.; IINO, M. and NAKAMURA, K. 1994. Evaluation of association of solvent-soluble molecules of bituminous coal by computer simulation. *Energy & fuels*, 8, 395.
- TAKANOHASHI, T.; IINO, M. and NISHIOKA, M. 1995. Investigation of associated structure of Upper Freeport coal by solvent swelling. *Energy & Fuels*, 9, 788.
- TAKANOHASHI, T. and KAWASHIMA, H. 2002. Construction of a model structure for Upper Freeport coal using <sup>13</sup>C NMR chemical shift calculations. *Energy & fuels*, 16, 379.
- TING, F. T. 1978. Petrographic techniques in coal analysis. *Analytical methods for coal and coal products*, 1, 3.
- TING, F. T. 1982. Coal macerals. *Coal structure*, 7.

## CHAPTER 2: LITERATURE OVERVIEW

---

- TREJO, F.; ANCHEYTA, J.; MORGAN, T. J.; HEROD, A. A. and KANDIYOTI, R. 2007. Characterization of asphaltenes from hydrotreated products by SEC, LDMS, MALDI, NMR, and XRD. *Energy & Fuels*, 21, 2121.
- VAMVUKA, D. 1999. Gasification of coal. *Energy exploration & exploitation*, 17, 515.
- VAN DYK, J.; KEYSER, M. and COERTZEN, M. 2006. Syngas production from South African coal sources using Sasol–Lurgi gasifiers. *International Journal of Coal Geology*, 65, 243.
- VAN DYK, J.; KEYSER, M. and VAN ZYL, J. 2001. Suitability of feedstocks for the Sasol-Lurgi fixed bed dry bottom gasification process. *Gasification technologies*.
- VAN HEEK, K. 2000. Progress of coal science in the 20th century. *Fuel*, 79, 1.
- VAN KREVELEN, D. W. 1993. *Coal, Typology, Physics, Chemistry, Constitution* Amsterdam, Elsevier.
- VAN NIEKERK, D. and MATHEWS, J. P. Molecular dynamic simulation of coal-solvent interactions in Permian-aged South African coals. *Fuel Processing Technology*, In Press, Corrected Proof.
- VAN NIEKERK, D. and MATHEWS, J. P. 2010. Simulation of solvent extraction of South African vitrinite- and inertinite-rich coals. *Energy & Fuels*, 24, 6393.
- VAN NIEKERK, D.; MITCHELL, G. D. and MATHEWS, J. P. 2010. Petrographic and reflectance analysis of solvent-swelled and solvent-extracted South African vitrinite-rich and inertinite-rich coals. *International Journal of Coal Geology*, 81, 45.
- VAN NIEKERK, D.; PUGMIRE, R. J.; SOLUM, M. S.; PAINTER, P. C. and MATHEWS, J. P. 2008. Structural characterization of vitrinite-rich and inertinite-rich Permian-aged South African bituminous coals. *International Journal of Coal Geology*, 76, 290.
- VÉLEZ, J. F.; CHEJNE, F.; VALDÉS, C. F.; EMERY, E. J. and LONDOÑO, C. A. 2009. Co-gasification of Colombian coal and biomass in fluidized bed: An experimental study. *Fuel*, 88, 424.
- WAGNER, N. and TLOTLENG, M. 2012. Distribution of selected trace elements in density fractionated Waterberg coals from South Africa. *International Journal of Coal Geology*, 94, 225.
- WAGNER, N. J. A petrographic reassessment of the Waterberg coalfield, South Africa. 62nd meeting of the International Committee for Coal and Organic Petrology (ICCP), 2010.
- WALKER JR, P.; RUSINKO JR, F.; AUSTIN, L.; ELEY, D.; SELWOOD, P. and WEISZ, P. 1959. Advances in Catalysis, vol. *Vol. II*, 133.
- WALKER JR, P.; TAYLOR, R. and RANISH, J. 1991. An update on the carbon-oxygen reaction. *Carbon*, 29, 411.
- WATANABE, H. and OTAKA, M. 2006. Numerical simulation of coal gasification in entrained flow coal gasifier. *Fuel*, 85, 1935.
- WISER, W. H. 1984. Conversion of bituminous coal to liquids and gases: Chemistry and representative processes. *Magnetic Resonance*. Springer.
- WU, S.; GU, J.; ZHANG, X.; WU, Y. and GAO, J. 2007. Variation of carbon crystalline structures and CO<sub>2</sub> gasification reactivity of Shenfu coal chars at elevated temperatures. *Energy & Fuels*, 22, 199.
- XU, K.; HU, S.; SU, S.; XU, C.; SUN, L.; SHUAI, C.; JIANG, L. and XIANG, J. 2012. Study on char surface active sites and their relationship to gasification reactivity. *Energy & Fuels*, 27, 118.
- YAMASHITA, T.; FUJII, Y.; MOROZUMI, Y.; AOKI, H. and MIURA, T. 2006. Modeling of gasification and fragmentation behavior of char particles having complicated structures. *Combustion and Flame*, 146, 85.
- YANG, H.; CHEN, H.; JU, F.; YAN, R. and ZHANG, S. 2007. Influence of pressure on coal pyrolysis and char gasification. *Energy & Fuels*, 21, 3165.
- YANG, R. and THROWER, P. A. 1984. Chemistry and Physics of Carbon. *Vol. 19* Marcel Dekker, New York, 163.
- YIN, Y.; ZHANG, J. and SHENG, C. 2009. Effect of pyrolysis temperature on the char micro-structure and reactivity of NO reduction. *Korean Journal of Chemical Engineering*, 26, 895.

## CHAPTER 2: LITERATURE OVERVIEW

---

- YIP, K.; WU, H. and ZHANG, D.-K. 2007. Effect of inherent moisture in Collie coal during pyrolysis due to in-situ steam gasification. *Energy & Fuels*, 21, 2883.
- ZHANG, L.-X.; KUDO, S.; TSUBOUCHI, N.; HAYASHI, J.-I.; OHTSUKA, Y. and NORINAGA, K. 2013. Catalytic effects of Na and Ca from inexpensive materials on in-situ steam gasification of char from rapid pyrolysis of low rank coal in a drop-tube reactor. *Fuel Processing Technology*, 113, 1.
- ZHANG, S.-Y.; LU, J.-F.; ZHANG, J.-S. and YUE, G.-X. 2008. Effect of pyrolysis intensity on the reactivity of coal char. *Energy & Fuels*, 22, 3213.
- ZHANG, Y.; HARA, S.; KAJITANI, S. and ASHIZAWA, M. 2010. Modeling of catalytic gasification kinetics of coal char and carbon. *Fuel*, 89, 152.
- ZHAO, Y.; HU, H.; JIN, L.; HE, X. and WU, B. 2011. Pyrolysis behavior of vitrinite and inertinite from Chinese Pingshuo coal by TG-MS and in a fixed bed reactor. *Fuel Processing Technology*, 92, 780.
- ZHU, W.; SONG, W. and LIN, W. 2008. Effect of the coal particle size on pyrolysis and char reactivity for two types of coal and demineralised coal. *Energy & Fuels*, 22, 2482.
- ZHU, Z.; LU, G. Q.; FINNERTY, J. and YANG, R. T. 2003. Electronic structure methods applied to gas-carbon reactions. *Carbon*, 41, 635.
- ZHU, Z. H.; FINNERTY, J.; LU, G. Q. and YANG, R. T. 2002. A comparative study of carbon gasification with O<sub>2</sub> and CO<sub>2</sub> by density functional theory calculations. *Energy & Fuels*, 16, 1359.

## CHAPTER 3: COAL AND CHAR CHARACTERISATION

---

### Chapter 3: Coal and char characterisation

**Publication #1.** Mokone J. Roberts, Raymond C Everson, *The characterisation of slow-heated inertinite- and vitrinite-rich pyrolysis chars from selected South African coalfields*. FUEL, 2015. 158: p. 591-601.

#### 3.1 Abstract

The development of coal char structures with pyrolysis has been extensively investigated but has traditionally been focused on the carboniferous coals in the northern Hemisphere. In this investigation, the properties of pyrolysis chars generated from inertinite- and vitrinite-rich coals (81 and 91% mmb by volume, respectively) collected from selected South African coalfields were determined. Chars were generated at 450, 700 and 1000 °C. The properties of coals and chars were examined using the chemical, physical, petrographic, solid-state <sup>13</sup>C NMR and X-ray diffraction analytical techniques. The objective was to generate results for further studies including molecular modelling and atomistic reaction kinetics.

A good correlation was found between the total maceral scan (rank) and aromaticity as the pyrolysis temperature increased, as well as between the the aromaticity measurements with XRD and NMR techniques. The chemical structure of the intertinte-rich and vitrinite-rich chars at 700-1000 °C was remarkably similar in terms of the proximate, ultimate, total maceral scan and aromaticity values. Greater transition occurred in the vitrinite-rich coal, implying a thermally more activated coal. Differences in the physical structure of the chars at these temperatures were observed in terms of the surface area using the D-R, the BET and Langmuir methods as well the microporosity from the CO<sub>2</sub> adsorption method. The macerals were not distinguishable at 700-1000 °C. However, the differences in maceral composition of the coals resulted in substantially different char forms during thermal conversion. The inertinite-rich coal formed more denser chars and higher proportions of thicker-walled networks (60-65% by volume). The vitrinite-rich coal showed higher proportions of isotropic “coke” (91-95% by volume), which contributes to a high distribution of surface area and micropores.

## CHAPTER 3: COAL AND CHAR CHARACTERISATION

---

Therefore, on a chemical level, the high temperature chars were similar. Differences existed in the physical structure at high temperatures. The physical structures, char forms and crystallite diameter ( $L_a$ ) significantly distinguished the chars at high temperatures, where  $L_a$  for inertinite-rich chars was 37.6Å compared with 30.7Å for the vitrinite-rich chars. The  $L_a$  property, in particular, makes investigations into atomistic structure and behaviour of inertinite- and vitrinite-rich chars attractive.

## CHAPTER 3: COAL AND CHAR CHARACTERISATION

---

### 3.2 Introduction and background

Vast deposits of coal in the southern Hemisphere (southern Africa, India, eastern Australia, Madagascar, South America, and Antarctica) are believed to have common origins with deposits occurring millions of years ago in the continent of Gondwana during the Permian age (Cai and Kandiyoti, 1995:956). Studies of the southern Hemisphere coals have found that the coals are rich in inertinites and more reactive than the northern Hemisphere inertinites (Cai and Kandiyoti, 1995:956). The application of more specialised analytical techniques, such as solid-state  $^{13}\text{C}$  NMR spectroscopy, X-ray diffraction analysis, FTIR spectroscopy and analytical pyrolysis in combination with gas chromatography and mass spectrometry, provided acquisition of more detailed knowledge of the structure of coal chars, and maceral influences (Yu *et al.*, 2003:1160; Jones *et al.*, 1999:1737; Fletcher *et al.*, 1991:1231; Malumbazo *et al.*, 2011:743). The X-ray diffraction technique has been used to characterise coal chars to study the structural evolution during heating (Everson *et al.*, 2013:148; Lu *et al.*, 2002:1215). Coal pyrolysis, which is described as the devolatilisation of coal in an inert gas, has been used extensively to study the properties of chars under different heating conditions (Yu *et al.*, 2003:1160; Sadhukhan *et al.*, 2009:692). The time-temperature history of the char, which is a complex carbonaceous material acting as an important intermediary during coal conversion processes, is determined by the pyrolysis temperature, the rate at which the particle temperature increases and residence time. The reactivity of carbonaceous surfaces generally relates to gas-solid interactions and continues to be the focus of many experimental investigations such as adsorption, gasification and combustion (Radovic *et al.*, 1985:311; Yamashita *et al.*, 1993:85; Montoya *et al.*, 2000:8409; Zou *et al.*, 2007:630; Chen and Yang, 1998:6348; Chen and Yang, 1997:421; Chen *et al.*, 1993:2835; Malumbazo *et al.*, 2011:743; Fu and Wang, 2001:63; Liu *et al.*, 2010:1; Wang *et al.*, 2012:1565; Wang *et al.*, 2011:3634; Zhang *et al.*, 2006:1201). This investigation concerns the characterisation of inertinite- and vitrinite-rich South African Permian-aged coals and slow-heated chars at 20 °C min<sup>-1</sup> to 450, 700, and 1000 °C, using the petrographic, chemical, physical, NMR, and XRD techniques.

## CHAPTER 3: COAL AND CHAR CHARACTERISATION

---

### 3.3 Experimental methods

Coal samples were collected from two coalfields in South Africa. Witbank coalfield supplied a run-of-mine sample of 67% inertinite content from #4 seam (Falcon, 1986; Snyman and Botha, 1993:171) and the Waterberg coalfield supplied a plant sample commercially beneficiated to 86% vitrinite content from the Upper Ecca seam (Fabińska and Kruszewska, 2003:95; Kruszewska, 1998:1655). Crushing and sieving was carried out in the laboratory to produce aliquots of particle size distribution of 300-1000  $\mu\text{m}$ . Subsequently, maceral purification products from density separation technique produced the parent coals used in this investigation.

#### 3.3.1 Sample preparation

**Maceral purification.** The coal samples were subjected to laboratory density separation using an analytical grade cesium chloride salt (Joseph *et al.*, 1991:724) in distilled water. Density separation was conducted to concentrate the inertinite in the Witbank #4 coal sample and the vitrinite in the Waterberg coal sample. The sink-float experiments on the Witbank #4 seam coal sample at a particle size of 300-1000  $\mu\text{m}$  commenced with a density of 1.5  $\text{g cm}^{-3}$ . The float fraction was again subjected to density separation with a solution density of 1.35  $\text{g cm}^{-3}$ . This two-step approach was conducted because of the relative difficulty of separating the macerals in the in Witbank #4 seam coal sample. The Waterberg sample was separated relatively easily at a density of 1.35  $\text{g cm}^{-3}$  to concentrate vitrinite-rich particles. The concentrated inertinite- and vitrinite-rich coal samples (parent coals) were then washed with excess distilled water and air-dried.

**Char generation.** Char generation was carried out in a PBR handling up to 60 g of sample per batch. Schematic representation of PBR is shown in Figure 3-1 and includes some critical measurements. Nitrogen gas is fitted to a gas flow controller and supplied through the bottom of the reactor. The control of furnace temperature is achieved by a programmable heat controller attached to the furnace unit. Two thermocouples, one in

## CHAPTER 3: COAL AND CHAR CHARACTERISATION

contact with the coal particles inside the reactor and the other positioned in the heating zone of the furnace, were used to probe the temperature during the experiments. The furnace provides a heating zone of about 300 mm vertically centred and can be programmed to work both isothermally and non-isothermally (ramp).

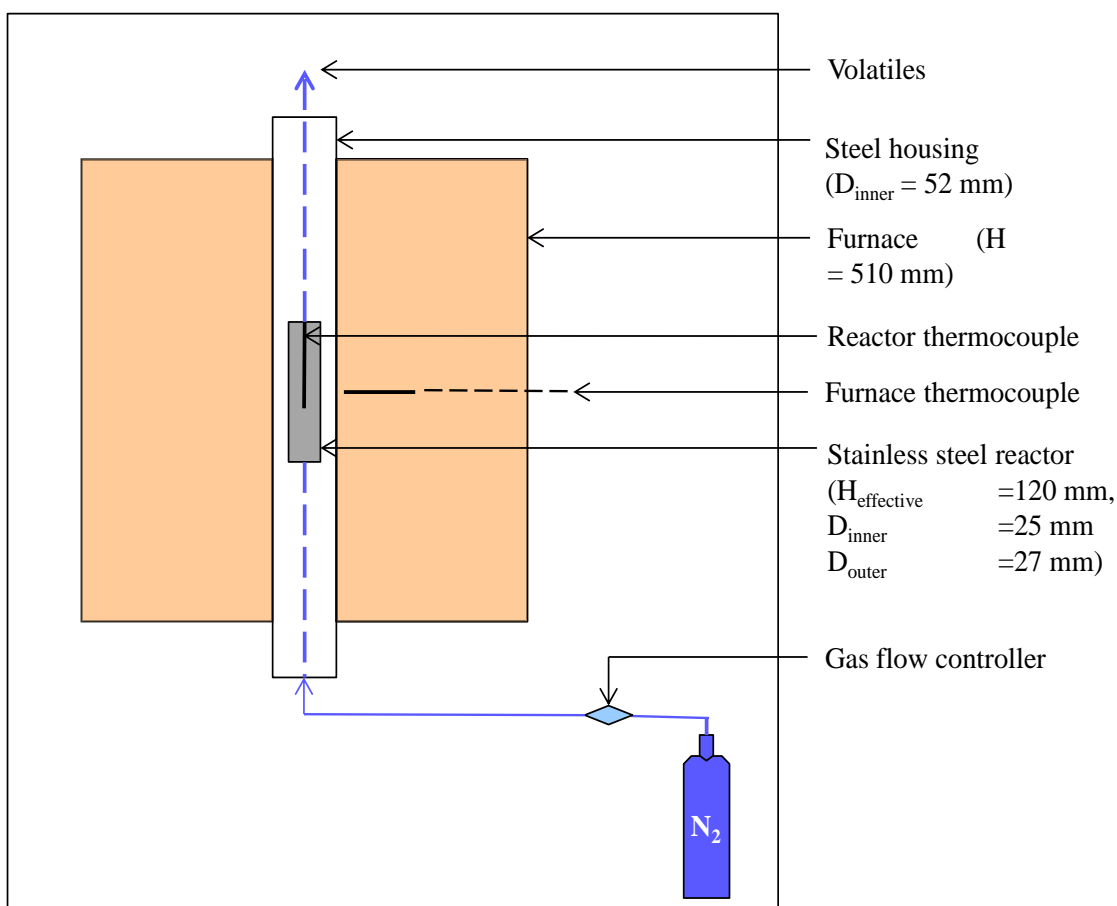


Figure 3-1. Schematic representation of char generation equipment.

Batches of 60 g coal samples were charred in the PBR at a time. Inert atmosphere was provided by a nitrogen gas flowing upwards through the bottom of the reactor at a flow rate of  $1.5 \text{ dm}^3 \text{ min}^{-1}$ . This inert gas flow rate ensured that volatile matter could escape very rapidly from the heating zone, thereby minimising secondary reactions (Xu and Tomita, 1987:627; Ahuja *et al.*, 1996:272). The inertinite- and vitrinite-rich coal samples were separately heated non-isothermally at a rate of  $20 \text{ }^\circ\text{C min}^{-1}$  and temperatures of 450, 700, and  $1000 \text{ }^\circ\text{C}$ . Slow heating rates of  $10\text{-}20 \text{ }^\circ\text{C min}^{-1}$  are typical in South Africa's

## CHAPTER 3: COAL AND CHAR CHARACTERISATION

---

pyrolysis-oriented processes. The particles were held for 60 min at these temperatures and allowed to cool down to 25 °C. All the samples, excluding those for petrographic analysis, were separately ground to <75 µm using a ceramic pestle and mortar equipment.

**Demineralisation/de-ashing.** The HCl-HF treatment was necessary to demineralise the coals and to de-ash the chars. The coals were treated for the purpose of characterisation since the chars were generated from untreated coals. The HCl-HF treatment, in particular, improved the observations made from XRD and NMR techniques (Dyrkacz and Bloomquist, 1992:357; Tekely *et al.*, 1987:225; Snape *et al.*, 1997:285). This treatment technique does not significantly alter the organic structure of parent coal and chars (Larsen *et al.*, 1989:557), although different treatments may be less vigorous (Joseph *et al.*, 1991:724; Petela and Petela, 1996:1259). The chars were separately ground to <75 µm using a ceramic pestle and mortar and stirred into a 5% HCl in a ratio of 1:5 for 24 hours using a polyethylene beaker and polyethylene-coated stirrer. The acid was separated by filtration. Hydrochloric acid was used to remove carbonates and acid-removable calcium (Önal and Ceylan, 1995:972). The retained residue was subjected to agitation for 24 hours in a 48% HF at a ratio of 1:5. The purpose of HF was to remove the predominant quartz and alumino-silicates (Wijaya and Zhang, 2011:1). The filtered sample residue was again agitated in a 5% HCl for 24 hours in a ratio of 1:5 to dissolve the fluorites that might have formed and precipitated on the char during HF treatment. All acid treatments took place at ambient temperatures and all residues were finally washed with copious amounts of distilled water before being air-dried.

**Reduction of free radicals concentration.** The demineralised char samples intended for the solid-state <sup>13</sup>C NMR experiments were treated by a method to chemically reduce the free radicals concentrations for the purpose of enhancing the fraction of observable carbon (Muntean *et al.*, 1988:108; Hattingh *et al.*, 2013:3161). Nitrogen gas was used to provide inert atmosphere at all times in a customized, potable glove box (Gilman *et al.*, 1998:61). The de-ashed char particles were stirred in a glass beaker at a ratio of 1:5

## CHAPTER 3: COAL AND CHAR CHARACTERISATION

---

with 0.1%  $\text{SmI}_2$  in THF for 24 hours, using a polyethylene-covered stirrer. The reaction mixture of char and  $\text{SmI}_2$  in THF was then quenched with distilled water and the THF was allowed to evaporate. The lanthanide ions that might have remained on the char samples were removed with a 5% HCl. Excess distilled water was applied on the chars samples (Van Niekerk *et al.*, 2008:290) followed by air drying.

### 3.3.2 Characterisation of coals and chars

**Chemical analyses.** Proximate and elemental analyses were carried out on density separated coals after demineralisation as well as on the subsequent de-ashed chars at a commercial laboratory in Pretoria, South Africa (Van Rensburg *et al.*, 2009:233). Sample preparation was done according to SABS 0135: Part 1 & 2 (1997). Proximate analysis method followed SABS ISO 1171 (1997) and SABS ISO 566 (1998) for ash yield/content and volatile matter measurements, respectively, while fixed carbon content was calculated by difference. The analysis for carbon, hydrogen and nitrogen was performed according to ISO standard 12902 (ISO, 2010). Oxygen was determined by difference.

**Physical analyses.** The helium density, which is a measure of true density (skeletal) density of coals and chars (Gale *et al.*, 1996:766), was carried out with a Micromeritics AccuPyc II 1340 gas pycnometer by measuring the pressure change of a probe gas in a calibrated volume. The mineral matter/ash value was low enough to negate the correction of data (0.5-1.7%). The microporosity of the samples was determined from carbon dioxide adsorption data for pore diameters  $\leq 5\text{\AA}$  (Webb, 2001:01). Micropore surface area of the coals and corresponding chars was measured by A-D using the D-R method on a Micromeritics ASAP 2020 System (Everson *et al.*, 2013:148). The samples (about 0.20 g each) were degassed under vacuum (10  $\mu\text{m Hg}$ ) at 90 °C for 2880 min on the degassing port of the equipment prior to adsorption analysis. Degassing was done to eliminate moisture and condensed volatiles from the pore surfaces of the samples, which could hinder adsorbate accessibility and weaken final results. After the removal of

---

## CHAPTER 3: COAL AND CHAR CHARACTERISATION

---

volatiles, the samples were analysed at 0 °C in an ice bath for CO<sub>2</sub> analysis. Automatic acquisition of adsorption data was accomplished by the ASAP 2020 v3.01 software linked to the equipment in the relative pressure range:  $0 < P/P_0 \leq 0.032$  for CO<sub>2</sub> analysis. The micropore surface areas of the samples were determined from CO<sub>2</sub> adsorption data using the D-R, the BET and Langmuir methods (Rouquerol *et al.*, 2013). The maximum micropore volume, the average micropore diameter, and the PSD of the samples were determined from the CO<sub>2</sub> adsorption results following the H-K method (Rouquerol *et al.*, 2013). The calculations were based on the entire raw non-linear sorption curves (isotherms) within the reduced pressure ranges. The reliability of the H-K method experimentally and numerically for microporous carbons have been reported (Jaroniec *et al.*, 2003:263; Kowalczyk *et al.*, 2002:125). The porosity of the coal samples was determined from the CO<sub>2</sub> adsorption data (Wang *et al.*, 2010:41).

**Petrographic analyses.** The analyses of the density-separated coals and the subsequent chars were conducted at a commercial petrography centre in Pretoria, South Africa (25°44'S, 28°11'E) (Van Rensburg *et al.*, 2009:233). Petrography involved routine preparation of coal blocks using ISO standard 7404-2 (Malumbazo *et al.*, 2011:743; Chabalala *et al.*, 2011:750). Coal blocks for point counting and analysis were prepared with liquid hardener and epoxy resin followed by drying. A Leco VP-50 machine (Model 891-702-800) was used to treat the blocks under the weights of 5.4 and 6.8 kg for grinding and polishing stages, respectively. The spinning was 140 rpm throughout. Vitrinite reflectance is a very reliable rank parameter, being independent of the vitrinite content and the grade of the coal. Vitrinite random reflectance measurements involved 100 readings on vitrinites in accordance with the ISO Standard 7404-5 (1994). The Rsc was also conducted on coals and chars, involving 250 random reflectance readings taken on all macerals over the polished surface of each petrographic block. Chemical determinations of rank may prove anomalous, particularly in the case of the inertinite-rich coals common in South Africa. The group macerals were quantified by a 500 point-count technique in accordance with the ISO standard 7404-3 (1994). This technique was also used to quantify the carbon forms and inorganic

## CHAPTER 3: COAL AND CHAR CHARACTERISATION

---

constituents. The reactive inertinite macerals were identified according to Smith *et al.* (Smith *et al.*, 1983:111), while the coal microlithotype, carbominerite and minerite analyses were carried out in accordance with the ISO 7404-4 (1988) (Everson *et al.*, 2008:3082). The microscopic components of the chars were identified by virtue of their colour, reflectance, degree of anisotropy, size, morphology, extent of devolatilisation and general response to heating (Everson *et al.*, 2008:3082). Petrography included assessment for the general “freshness” of the samples.

### 3.3.3 The NMR and XRD techniques

**Solid-state  $^{13}\text{C}$  nuclear magnetic resonance spectroscopy.** The NMR analyses were carried out using the CP-MAS on parent coals and char samples, at Stellenbosch University, Stellenbosch, South Africa (Timm *et al.*, 2010:421). The spectra were acquired on a Varian VNMRS 500 MHz two-channel spectrometer using 4 mm zirconia rotors and a 4 mm Chemagnetics<sup>TM</sup> T3 HXY MAS probe. The CP spectra were recorded at ambient temperature with proton decoupling using a recycle delay of 3s. The power parameters were optimized for the Hartmann-Hahn match; the radio frequency fields were  $\gamma\text{C}B_{1\text{C}} = \gamma\text{H}B_{1\text{H}} \approx 56$  kHz, where  $\gamma\text{C}$  and  $\gamma\text{H}$  are the magnetogyric ratios of carbon and proton, and  $B_{1\text{C}}$  and  $B_{1\text{H}}$  are their respective radio field strengths. The contact time for cross-polarization was 2.0 ms. The MAS was performed at 12 kHz and HMB was used as an external chemical shift standard where the methyl peak was referenced to 17.5 ppm. The DD experiments (Hatcher, 1988:48) were carried out under similar conditions with the interrupted decoupling time constant T1Xidref set at 40 ms. Each spectrum was phased and baseline corrected before integration. The integration reset points were set according to Solum *et al.* (Solum *et al.*, 1989:187). All spectra were processed in the same manner and at the same time to minimize operator bias.

The coal structural parameters were calculated from the integral values according to Solum *et al.* (Solum *et al.*, 1989:187). The CP efficiency is influenced by two factors, the CP rate ( $T_{\text{CH}}$ ) and the proton relaxation time in the rotating frame ( $T_{1\rho}^{\text{H}}$ ). Supaluknari *et*

## CHAPTER 3: COAL AND CHAR CHARACTERISATION

---

*al.* (Supaluknari *et al.*, 1990:509) found that the  $T_{1\rho}^H$ 's of the main carbon types present in coals are of similar ranges, while the CP rates decrease in the order of: aliphatic > aromatic > carbonyl. Consequently, the aromatic and carbonyl carbons will be discriminated against the aliphatic carbons, leading to systematic errors of the calculated structural parameters (Supaluknari *et al.*, 1990:509). In contrast to the CP-MAS, the DP, one pulse-MAS experiment is a quantitative method and therefore provides the best approximation of the actual aromatic to aliphatic ratio. These investigations showed that CP-MAS technique underestimates the aromaticity by 10 to 15% compared with DP-MAS. However the low natural abundance and long relaxation times of  $^{13}\text{C}$  result in long measurement times (typically >48 hours on one coal sample) in DP-MAS experiments while CP-MAS spectra of coals can be typically accumulated within 2 to 6 hrs. Therefore the CP-MAS in combination with dipolar dephasing are widely used for coal characterizations. The DD-MAS experiment is used to distinguish strongly proton-coupled carbons from weakly coupled or non-protonated carbons.

**X-ray diffraction.** The XRD analysis of the demineralised coals and de-ashed chars was conducted at a commercial facility in Pretoria, South Africa (Van Rensburg *et al.*, 2009:233), to get values of the aromaticity and crystallite properties for demineralised coals and de-ashed chars, at a particle size distribution of <75  $\mu\text{m}$  (Niekerk and Mathews, 2010:73; Cousins *et al.*, 2006:2489). The equipment used was a PANalytical X'Pert Pro powder diffractometer with X'Celerator detector and variable divergence and receiving slits with Fe filtered  $\text{Co-K}\alpha$  radiation. The X-ray intensities were measured in a continuous type of scan in a range of  $4.0^\circ \leq 2\theta \leq 120^\circ$ . A substantial decrease in the intensity of many peaks was usually experienced when seen in combination with the amount of mineral matter removed for the coal (Van Niekerk *et al.*, 2008:290; Sharma and Wadhwa, 1997:29; Lu *et al.*, 2001:1821), hence the demineralised coals and de-ashed chars. The X-ray intensities were scanned, recorded and baseline corrected according to Everson *et al.* (Everson *et al.*, 2013:148). Aromaticity was calculated by curve fitting using the Origin 8 data analysis and graphics software. Empirical expressions derived from Scherrer were used to calculate the average structural parameters from  $\beta$  and  $\theta$  (Lu *et al.*, 2001:1821; Lu *et al.*, 2002:1215). The  $d_{002}$  was

## CHAPTER 3: COAL AND CHAR CHARACTERISATION

---

determined from the maximum of the (002) band using the Bragg equation (Van Niekerk *et al.*, 2008:290; Trejo *et al.*, 2007:2121). The other average carbon crystallite lattice parameters such as the  $L_c$  and  $L_a$ , for both the coals and char were determined using the Bragg and Scherrer equations (Van Niekerk, 2008; Trejo *et al.*, 2007:2121; Everson *et al.*, 2013:148; Hattingh *et al.*, 2013:3161).

### 3.4 Results

#### 3.4.1 Chemical properties

**Proximate analysis.** The results for the demineralised parent coals and de-ashed chars are shown in Table 3-1. The amount of volatile matter of both the inertinite- and vitrinite-rich coal decreased with increasing pyrolysis temperature. Substantial decreases occurred at 700 °C similar to observations made by Bunt and Waanders (Bunt *et al.*, 2008:2849; Bunt and Waanders, 2009:585). Fixed carbon content increased with increasing pyrolysis temperature. The changes in these parameters were caused by the release of hydrogen-rich pyrolytes during devolatilisation (Gale *et al.*, 1996:766). A relatively high thermal effect was found with the vitrinite-rich particles, highlighting a higher thermal stability of inertinite-rich particles.

**Ultimate analysis.** The results in Table 3-1 also show that the pyrolysis of parent coals at 450, 700 and 1000 °C was accompanied by an increase in carbon content, a decrease in the hydrogen and oxygen contents and atomic H/C and O/C ratios. This was caused by the release of hydrogen-rich fragments due to thermal degradation of the coal structure. Most of the aliphatic rich and hydrogen rich species are removed during pyrolysis.

The difference between parent coals was clearly shown by the results, but the inertinite and vitrinite-rich particles became similar at 700-1000 °C.

## CHAPTER 3: COAL AND CHAR CHARACTERISATION

### 3.4.2 Physical properties

**Skeletal density.** The results in Table 3-2 indicate that true density of chars increased substantially with increasing pyrolysis temperatures of 700-1000 °C. Gale *et al.* made similar observations while studying coals of different rank (Gale *et al.*, 1996:766). An increase in true density during devolatilisation is as the result of depletion of aliphatic components, in particular when the aliphatic hydrogen is released (Gale *et al.*, 1996:766). This was corroborated by increasing volatile matter release in Table 3-1.

Table 3-1. Proximate and ultimate analysis of parent coals and chars.

	Ash %	VM %	FC %	C	H	O (by diff.)	N	S	H/C	O/C
	Proximate analyses (db)			Elemental analysis (daf)					Atomic ratio	
<u>Coal</u>										
Inertinite-rich	0.5	24.7	74.8	83.4	4.4	7.5	2.1	2.6	0.63	0.07
Vitrinite-rich	0.5	36.7	62.8	80.0	5.4	8.2	1.7	4.8	0.80	0.08
<u>Char at 450 °C</u>										
Inertinite-rich char	0.7	17.5	81.8	90.5	2.3	4.9	2.0	0.3	0.31	0.04
Vitrinite-rich char	0.8	32.6	66.6	85.3	3.5	7.2	1.9	2.0	0.49	0.06
<u>Char at 700 °C</u>										
Inertinite-rich char	0.8	7.7	91.5	92.4	0.9	4.7	1.0	1.1	0.12	0.04
Vitrinite-rich char	1.1	11.5	87.4	89.9	1.0	6.3	1.7	1.1	0.14	0.05
<u>Char at 1000 °C</u>										
Inertinite-rich char	1.7	1.4	96.9	95.9	0.8	0.9	2.0	0.4	0.10	0.01
Vitrinite-rich char	1.7	3.0	95.3	94.1	1.0	2.6	1.6	0.7	0.12	0.02

**Surface area and porosity.** The surface area and microporosity results in Table 3-2 show that the values for both the inertinite- and vitrinite-rich particles more than doubled at 700 °C and fell sharply at 1000 °C to levels lower than the parent coals for the inertinite-rich chars and to levels a little higher than parent coals for the vitrinite-rich chars (Figure 3-2). The mechanism for this behaviour is that maximum amounts hydrogen-rich species are lost as volatile matter at 700 °C, leaving behind large surface area. At higher temperatures (1000 °C), the coal structure (aromatic moiety) becomes more ordered and aligned crystallites of bituminous coals become ordered (Walker Jr *et al.*, 1959:133; Fletcher *et al.*, 1992:643; Gale *et al.*, 1996:766). This leads to a

## CHAPTER 3: COAL AND CHAR CHARACTERISATION

substantial decrease in the surface area and microporosity. These structural transformations are more thermally activated for the vitrinite-rich particles when compared with the intertinite-rich particles.

Table 3-2. Major physical and structural parameters of demineralised coals and de-ashed chars.

Property / Sample ID	Coal		Chars @450 °C		Chars @700 °C		Chars @1000 °C	
	IR	VR	IR	VR	IR	VR	IR	VR
Skeletal (Apparent) density ( $\text{g cm}^{-3}$ )	1.379	1.289	1.512	1.410	1.728	1.685	1.871	1.830
D-R surface area ( $\text{m}^2 \text{g}^{-1}$ )	138.5	151.4	275.7	287.7	306.5	329.5	89.5	180.8
BET surface area ( $\text{m}^2 \text{g}^{-1}$ )	90.0	97.3	174.8	180.5	195.2	210.4	58.4	117.2
Langmuir surface area ( $\text{m}^2 \text{g}^{-1}$ )	95.8	103.9	183.8	189.8	204.3	220.5	62.3	124.5
Mono-layer capacity ( $\text{cm}^3 \text{g}^{-1}$ )	30.3	33.1	60.4	63.0	67.1	72.1	19.6	39.6
Average micropore diameter ( $\text{Å}$ )	3.86	3.93	3.59	3.61	3.50	3.43	3.98	3.77
Micropore volume ( $\text{cm}^3 \text{g}^{-1}$ )	0.032	0.034	0.066	0.068	0.075	0.081	0.020	0.044
Characteristic Energy, $\text{kJ mol}^{-1}$	22.43	21.58	23.96	23.64	25.19	24.96	21.27	23.17
Microporosity (%) ( $d_p \leq 5\text{Å}$ )	5.47	5.46	12.81	13.00	15.85	16.67	3.13	7.83

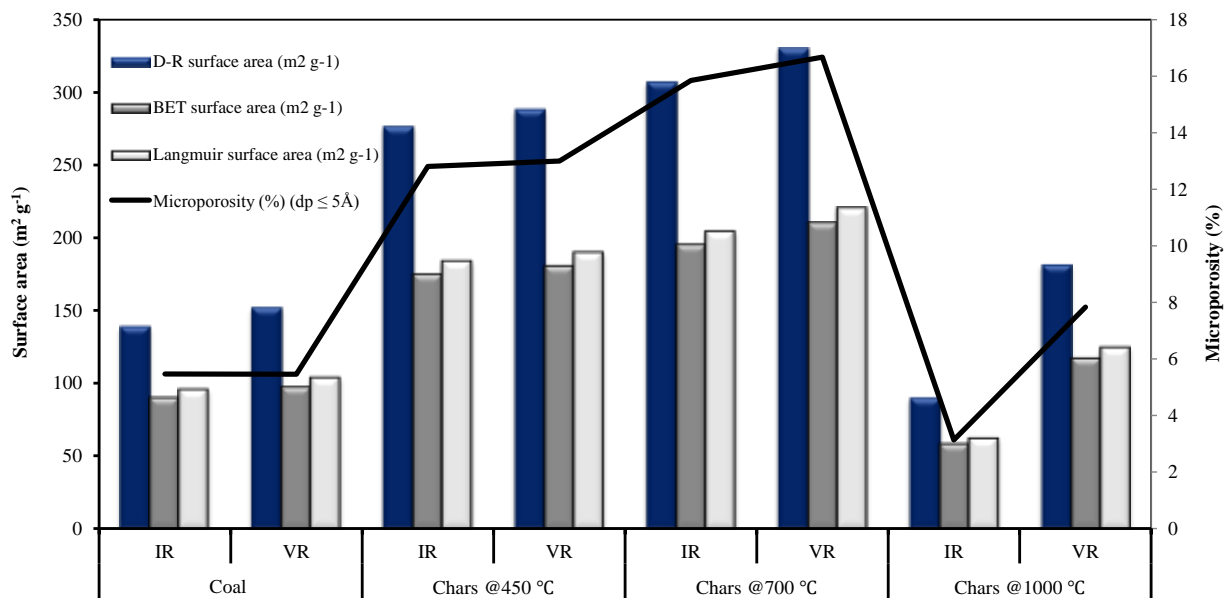


Figure 3-2. Surface area and porosity transitions of the IR and VR particles with temperature.

## CHAPTER 3: COAL AND CHAR CHARACTERISATION

---

### 3.4.3 Petrographic properties

#### 3.4.3.1 Coals

**Vitrinite random reflectance.** Random reflectance measurements (in oil immersion) for the determination of the rank of the density separated coals were conventionally taken on the vitrinite maceral telovitrinite. Table 3-3 shows the vitrinite random reflectance values 0.79 and 0.69% for the respective density separated Witbank #4 and Waterberg Upper Ecca seam coals, which were respectively classified as bituminous, medium rank C in accordance with ISO standard 11760 (2005) (ISO, 2005:9; Oboirien *et al.*, 2011:735). The vitrinite-class distributions showed standard deviations ( $\sigma$ ) of  $< 0.1$  typical of single seam, non-blend coals according to the International codification system for medium and high rank coals by the UN-ECE (UN-ECE). Total maceral reflectance scans were 1.58 and 0.72% for the respective coals.

Table 3-3. Vitrinite random reflectance for the density separated (parent) coals.

Coal seam	Mean random vitrinite reflectance (%)	Total maceral reflectance (%)
Witbank #4	0.79	1.58
Waterberg Upper Ecca	0.69	0.72

**Maceral compositions.** The two coals displayed major variations in the percentage of maceral compositions by volume on a visible mineral matter basis, as shown in Table 3-4. The Witbank #4 seam coal accounted for a total of 81% inertinite group macerals constituted according to semifusinite > inertodetrinite > fusinite/secrinite > micrinite. The total vitrinite for this coal was 11% composed of colotellinite > colodetrinite > pseudovitrinite. The balance was liptinite of sporinite/ resinite/cutinite combinations. The organic compositions for the Waterberg Upper Ecca seam coal was dominated by the vitrinite group macerals (91%) of the types: colotellinite > pseudovitrinite > colodetrinite. This coal showed extremely small amounts of inertinite and liptinite. On a

## CHAPTER 3: COAL AND CHAR CHARACTERISATION

visible mineral matter-free basis, the Witbank #4 and the Waterberg upper Ecca seam coals significantly comprised 85 and 95% inertinite- and vitrinite-group macerals, respectively, and are thus designated as inertinite- and vitrinite-rich together with corresponding chars henceforth.

Table 3-4. Maceral compositions for the parent coals (% by volume).

Coal	Maceral analysis (% by volume on visible mineral matter basis)														Visible minerals	Total reactivity*
	Vitrinite				Liptinite				Inertinite							
	Collorellinite	Coltodetrinite	Pseudovitrinite	Total vitrinite	Sporinite/Resinite/Cutinite	Alginite	Total liptinite	Reactive semi-fusinite	Inert semi-fusinite	Fusite/Secrinite	Micrinite	Reactive Inertodetrinite	Inert Inertodetrinite	Total inertinite		
Witbank #4 (inertinite-rich)	7	3	1	11	3	0	3	13	24	10	2	8	24	81	5	35
Waterberg Upper Ecca	74	4	13	91	4	0	4	0	1	0	0	0	1	2	3	95

\* = vitrinite + liptinite + reactive semifusinite + reactive inertodetrinite

The inertinite-rich coals from the Gondwana coals in the southern Hemisphere show partly reactive constituents (Smith *et al.*, 1983:111; Everson *et al.*, 2008:3082) compared with their northern Hemisphere counterparts. Individual macerals responsible for this behaviour in this group are the reactive semifusinite and reactive inertodetrinite (Nandi *et al.*, 1977:125), which respectively accounted for 13% and 8%. It is generally accepted that vitrinites and liptinites of bituminous coals are the reactive macerals. Semifusinite is characterized by irregular and deformed cell structure and high reflectance, but the “inert” part is much brighter (Falcon, 1986). Inertodetrinite is distinguished by a variety of shapes of small masses with other inertinite submacerals (Falcon, 1986). Micrinite is identified by round, small grains of inertinite in other macerals and hosts most volatile components (Falcon, 1986). Colotellinite is usually the dominant vitrinite maceral and occurs as a large and extremely homogeneous band, sometimes with fine clay/pyrite. Chemically, colotellinite portrays a highly aliphatic macromolecular structure (Falcon, 1986; Scott, 2002:119; Winston, 1986:21). Pseudovitrinite is known for desiccation cracks mainly against the plane (Falcon, 1986), indicating post-coalification oxidation *in*

## CHAPTER 3: COAL AND CHAR CHARACTERISATION

*situ* (Fabianska and Kruszewska, 2003:95; Kruszewska, 1998:1655; Kaegi, 1985:309), whereas colodetrinite is a large band of less homogeneous vitrinite containing pieces of other macerals (Falcon, 1986).

**Microlithotypes.** Microlithotypes are the microscopic bands formed by a combination of macerals and minerals in various proportions or associations; and they are useful indicators of the original environment of coal formation and of its approximate composition (Falcon, 1987:323). The four classes of microlithotypes in the inertinite and vitrinite-rich coals were analysed, namely, monomacerals, intermediates, carbominerites and minerites, as presented in Table 3-5. The inertite and vitrite microlithotypes, which constituted the monomacerals, occurred in highest proportions for the corresponding inertinite- and vitrinite-rich coals. These were followed by the intermediates for the inertinite-rich coals, which accounted for more than twice those found in the vitrinite-rich coals. The balance of microlithotypes in both inertinite- and vitrinite-rich particles was made up of small amounts of carbominerites and even smaller amounts of minerites.

Table 3-5. Microlithotype analysis of the parent coals.

Coal	Microlithotypes analysis (% by volume on mineral matter basis)									Total	
	"Pure" Monomacerals			Intermediates Maceral/maceral associations					Carbominerite Maceral/Minerite		Minerite Maceral-rich
	Vitrinite	Liptite	Inertite	Bi-macerals			Tri-macerals	Total intermediates			
				Clarite	Durite	Vitrinerite	Trimacerite				
Inertinite-rich	5	0	54	1	6	14	9	30	8	3	100
Vitrinite-rich	80	0	2	6	0	3	3	12	4	2	100

### 3.4.3.2 Chars

**Total reflectance scan (Rsc).** Figure 3-3 shows the total (mean random) reflectance scan (Rsc). The inertinite- and vitrinite-rich 450 °C chars showed very little change from that of the parent coals, respectively. A substantial increase in the levels of Rsc was

## CHAPTER 3: COAL AND CHAR CHARACTERISATION

---

attained at 700-1000 °C when the carbon-rich particles of the inertinite- and vitrinite-rich chars reacted to the char forming thermal processes. These results show that at 700-1000 °C temperatures, the macerals had transformed to an extent where it was difficult to distinguish between inertinite- and vitrinite-rich chars on reflectance level, when compared with the parent coals and 450 °C chars.

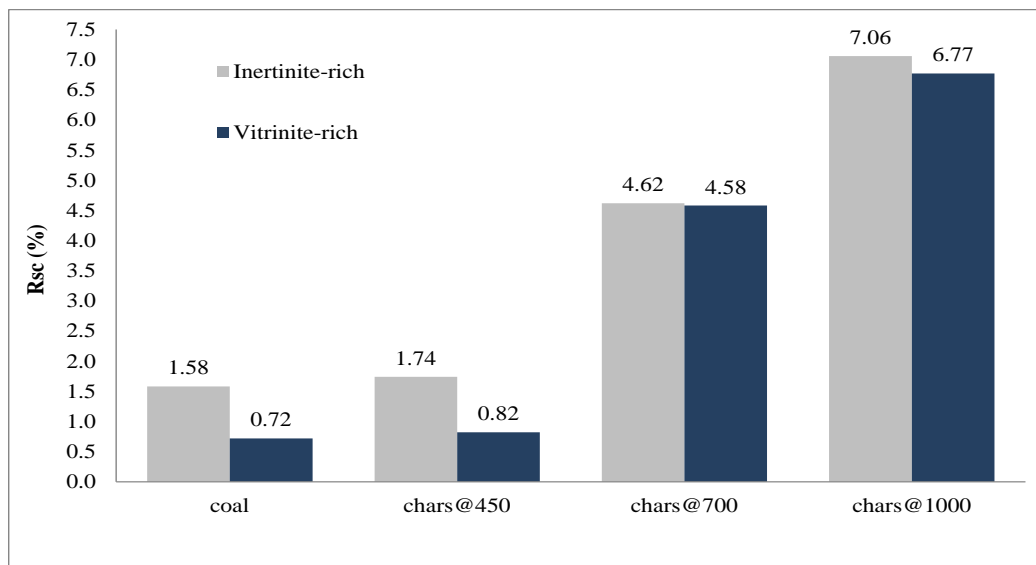


Figure 3-3. Total (Mean random) reflectance scan (Rsc%) for coals and chars.

**Maceral compositions.** Full maceral compositions in Figure 3-4 show that nearly all the macerals had reacted at 700-1000 °C, transition starting with the vitrinite-rich chars (Figure 3-4(b)). This behaviour, supported by the low amounts of inertinite macerals and traces of vitrinite macerals remaining in the inertinite-rich particles at 700 °C (Figure 3-4(a)), highlights the highest thermal stability of inertinite compared with liptinite and vitrinite. Substantial petrographic transformations start at high temperatures (700-1000 °C), while only small changes occur at low temperatures (450 °C). The classification system used for the petrographic characterisation of coal chars was outlined by Everson *et al.* (Everson *et al.*, 2008:3082).

## CHAPTER 3: COAL AND CHAR CHARACTERISATION

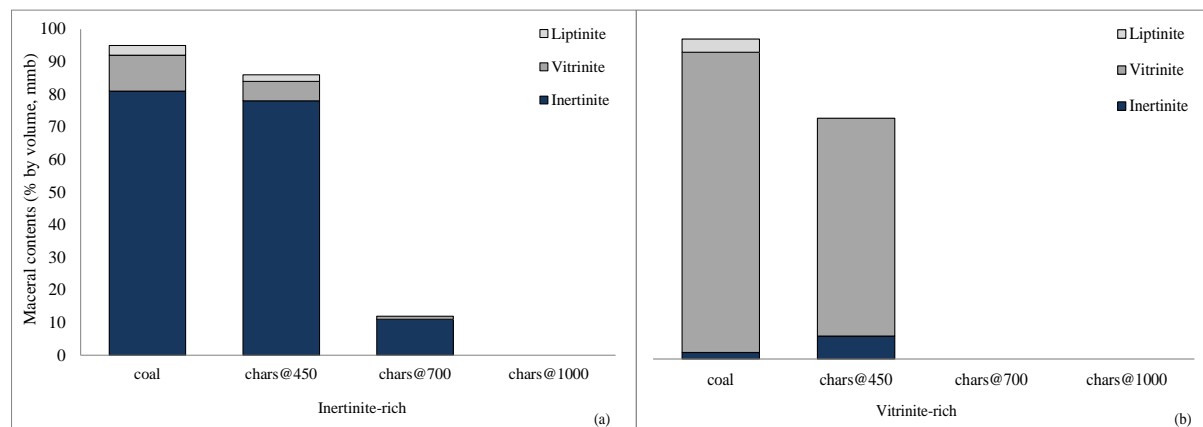


Figure 3-4. Maceral contents for (a) inertinite-rich coals and chars and (b) vitrinite-rich coals and chars, where mmb = visible mineral matter basis.

**Char form analysis.** The relatively high thermal stability of inertinite-rich particles was evident in the forms of carbon in the chars, as shown in Table 3-6. Higher proportions of denser char forms from the inertinites remained intact at 700-1000 °C (60-65%) in comparison with those from vitrinites (3%). In the contrary, the higher thermal activation of vitrinite was manifested when even a trace of denser chars from vitrinites was not observed in the vitrinite-rich coal at 700-1000 °C (0-4%), despite starting with values of the parent coals >90%. The 700-1000 °C inertinite-rich chars have higher proportions of thicker-walled networks (8-16%) derived from relatively inert components of coal particles compared with negligible amounts of the vitrinite-rich chars (1%). These networks are associated with low porosities (Everson *et al.*, 2008:3082) and may cause low reactivities with gaseous reagents due to poor ease of access to carbonaceous surfaces. In addition to this, the 700-1000 °C inertinite-rich chars have lower proportions of thick-walled isotropic coke derived from pure vitrinites (5-8%) compared with the vitrinite-rich chars (91-95%). During pyrolysis, vitrinites and other reactive macerals soften and lose volatiles, leading to the creation of pores and increases of volume and surface area as the softening walls expand (Everson *et al.*, 2008:3082). This may favour the reactivity of vitrinite-rich chars with gaseous reagents relative to the inertinite-rich chars. Additional results were included in Table 3-6 for the reader's interest. Figure 3-5 illustrates the transformation of inertinites, vitrinites and inerts from coal to char forms

## CHAPTER 3: COAL AND CHAR CHARACTERISATION

with increasing pyrolysis temperature presents, comprising the dense and more open network chars, as well as isotropic “coke”.

Table 3-6. Char form analysis and summary of major reflectance properties, following classification published in Everson *et al.* (Everson *et al.*, 2008:3082).

Group*	Cat.*	Char structure and textural analysis		IR	VR	IR	VR	IR	VR
				char@450 °C	char@700 °C	char@1000 °C	char@450 °C	char@700 °C	char@1000 °C
				(% by volume on mineral matter basis)					
A	1	Dense char – from vitrinite		0	0	3	4	3	0
		Dense char – from inertinite		0	0	60	2	65	1
	3	More open network – from inerts		0	0	8	0	16	1
Sub-total				0	0	71	6	84	2
B	7	Thick-walled “coke” – isotropic (from coal vitrinite)		1	0	5	91	8	95
D	11	Coal	Vitrinite	6	66	1	0	0	0
		unaffected	Liptinite	2	0	0	0	0	0
			Inertinite	78	7	11	0	0	0
	12	Original coal – partially reacted macerals		7	23	5	0	0	0
Sub-total				93	96	17	0	0	0
E	13	Inorganic matter - from coal		6	4	7	3	8	3
Total				100	100	100	100	100	100
Total reacted macerals (%)				0	0	81	100	100	100

Groups A and B = very highly reflecting, oxidation restricted, Group C = relatively low reflecting, exhibiting oxidation rims, Group D = low reflecting, little or no change, Isotropic = exhibiting optical properties that are the same in all directions when viewed under crossed nicols. Groups C and F; categories 2, 4-6, 8-11 and 14-15 were analysed but not detected.

## CHAPTER 3: COAL AND CHAR CHARACTERISATION

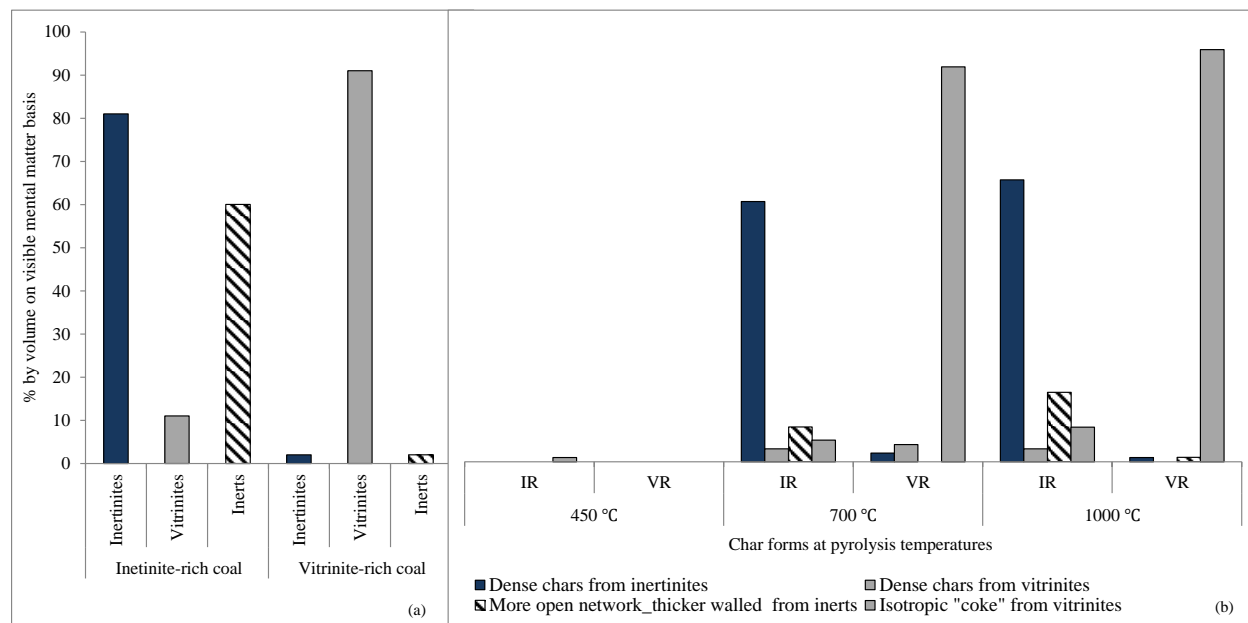


Figure 3-5. Transformation of inertinites, vitrinites and inerts from (a) coals (left-hand side) to (b) char forms (right-hand side) with increasing temperature, where IR and VR = inertinite- and vitrinite-rich, respectively.

### 3.4.4 Solid-state $^{13}\text{C}$ nuclear magnetic resonance

**Spectra.** The NMR spectra of parent coal samples and their corresponding char samples are given in Figure 3-6. The spectra exhibit two broad characteristic peaks (Van Niekerk *et al.*, 2008:290; Perry *et al.*, 2000:2313). The prominent peak is associated with carbon in the aromatic region and is represented between 90 and 240 ppm in the spectra. The second peak is represented between 0 and 90 ppm and is associated with the carbon in the aliphatic region. The aromatic peaks in the spectra of parent coals and chars generated at 1000 °C retained nearly the same shape and height, respectively. However, the spectra for chars exhibited a broadening of line in the aromatic region (Solum *et al.*, 2001:961). This line broadening phenomena has therefore prevented the calculation on structural and lattice parameters, restricting the results to  $f_a$  values only. The aliphatic peaks of the chars appear to diminish with increasing temperature, leaving an enriched aromatic fraction that is probably

## CHAPTER 3: COAL AND CHAR CHARACTERISATION

---

responsible for the increasing similarity in chars, as observed with the atomic contents and ratios.

**Structural parameters.** The results are given in Table 3-7, where a clear relationship between pyrolysis temperature and carbon structures can be seen. The results show that inertinite-rich coal was more aromatic (75%) than vitrinite-rich coal (67%). Similar results on these types of coal have been reported (Van Niekerk *et al.*, 2008:290). When heated, the two coals showed an increase in aromaticity of up to 100% at maximum pyrolysis temperature of 1000 °C, with the inertinite char maintaining higher values until 700 °C. As shown by the diminishing aliphatic band, the difference in the aromaticity values between the inertinite and vitrinite chars became smaller at higher pyrolysis temperature until they became the same at the maximum pyrolysis temperature used, emphasizing a strong similarity in the chemistry of chars generated from inertinite-rich coals and vitrinite-rich coals. The difference in the values for  $f_a^S$  was minor between the two coals but became larger with increasing pyrolysis temperature when a larger fraction of alkylated carbon structures remained in the vitrinite chars. Aliphatic structures comprising entirely the  $CH$  and  $CH_2$  group,  $f_{al}^H$ , were present in both compounds up to 700 °C, but the vitrinite-rich coals and their chars dominated those of inertinite up to 450 °C and were nearly similar at 700 °C. Inertinite-rich compounds showed higher bridgehead carbon values at lower temperatures (450 °C) and became exactly the same at higher temperatures (700 °C). Inertinite-rich particles showed more polycondensed aromatic structures at low temperatures compared with vitrinite-rich particles. Included in the table are the lattice parameters of the two coals and their corresponding chars at different pyrolysis temperatures. The cluster size of inertinite-rich coal (28), which is defined as the number of aromatic carbon per cluster (Solum *et al.*, 1989:187), was larger than that of vitrinite-rich coal (24). Similar observations were made by Van Niekerk *et al.* for the raw coals (Van Niekerk *et al.*, 2008:290). At higher temperatures (700-1000 °C), little or no change in the inertinite cluster size and between the two maceral samples.

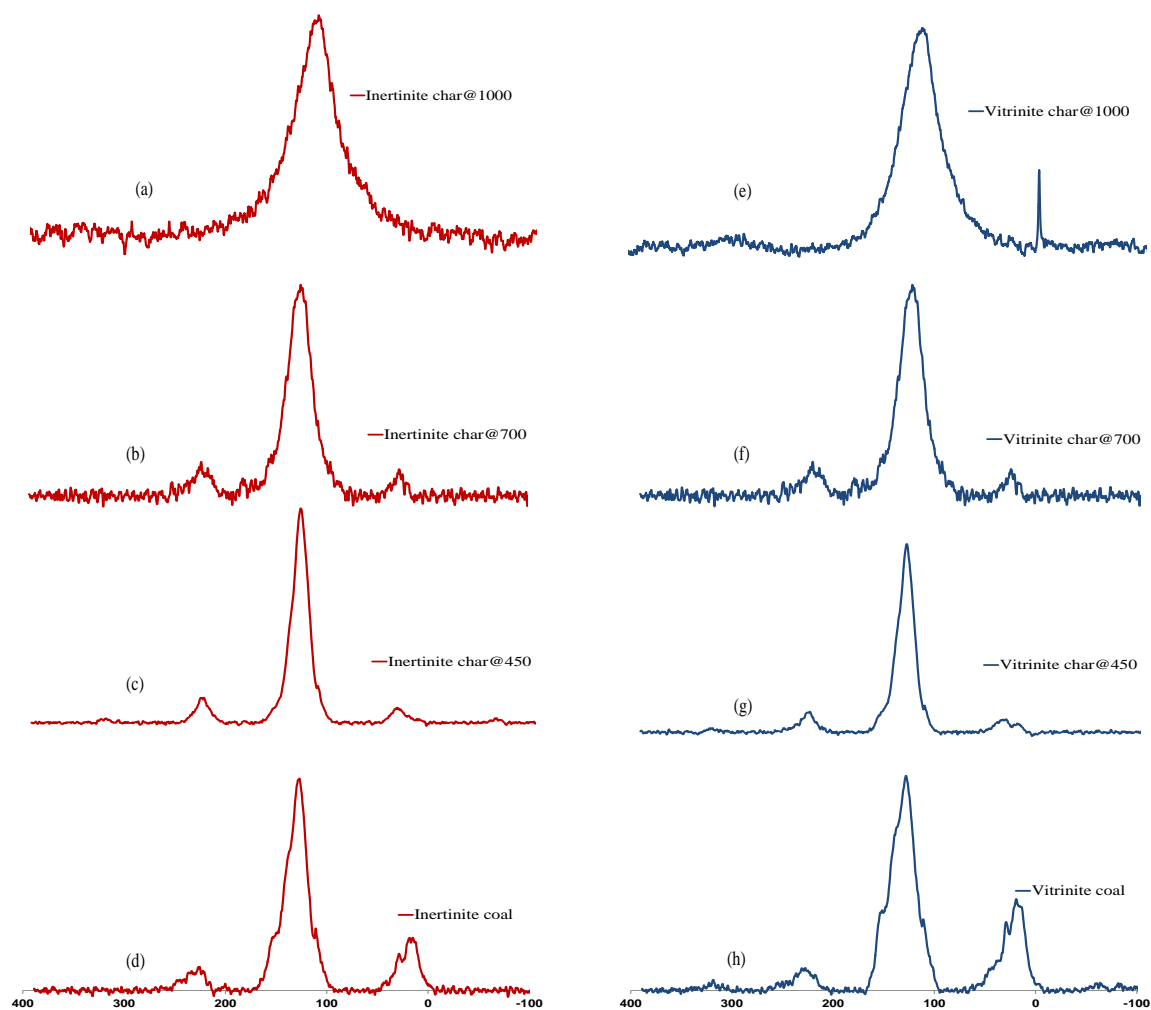


Figure 3-6. The NMR spectra, where: (a) - (d) = inertinite-rich particles (chars-coal) and (e) – (h) = vitrinite-rich particles (chars - coal); @numbers = temperatures in °C.

The values other than  $f_a$  for the chars at 1000 °C were unrealistic and thus, not reported. Firstly, the chars at these temperatures and more are hydrogen-depleted carbon-rich material of which a significant fraction may not readily cross-polarise and will not be properly represented in CP-MAS  $^{13}\text{C}$  signal (Gilman *et al.*, 1998:61). Secondly, these chars may contain significant amount of particles with unpaired electrons or free radicals leading to paramagnetic centres (Gilman *et al.*, 1998:61). These potentially cause the appearance of extensive line broadening, which prevents accurate calculation

## CHAPTER 3: COAL AND CHAR CHARACTERISATION

of structural parameters (Solum *et al.*, 2001:961; Gilman *et al.*, 1998:61). Generally, the difference in the structural and lattice values between the inertinite and vitrinite chars tended to be similar at 700-1000 °C). The  $f_a$  of 1000 °C chars was 100%.

Table 3-7. Structural and lattice parameters for inertinite and vitrinite coals and chars.

Structural parameters												
Compound	$f_a$	$f_a^*$	$f_{al}$	$f_{al}^O$	$f_a^{CO}$	$f_a^P$	$f_a^S$	$f_a^N$	$f_a^H$	$f_a^B$	$f_{al}^{N^*}$	$f_{al}^H$
<u>Inertinite-rich coal (cp)</u>	0.75	0.72	0.25	0.00	0.00	0.06	0.16	0.60	0.11	0.39	0.00	0.25
Char @450 °C	0.88	0.83	0.12	0.00	0.00	0.06	0.17	0.71	0.12	0.48	0.00	0.12
Char @700 °C	0.98	0.91	0.02	0.00	0.00	0.04	0.17	0.73	0.16	0.52	0.00	0.05
Char @1000 °C (spe)	1.00	*	*	*	*	*	*	*	*	*	*	*
<u>Vitrinite-rich coal (cp)</u>	0.67	0.64	0.33	0.00	0.01	0.06	0.14	0.52	0.12	0.31	0.00	0.33
Char @450 °C	0.77	0.72	0.23	0.00	0.02	0.08	0.19	0.65	0.07	0.37	0.00	0.23
Char @700 °C	0.95	0.90	0.05	0.00	0.01	0.06	0.22	0.81	0.10	0.52	0.00	0.02
Char @1000 °C (spe)	1.00	*	*	*	*	*	*	*	*	*	*	*
Lattice parameters												
Compound	$X_b$	$C$	$\sigma + 1$	$P_0$	B.L.	S.C.	MW	$M_\delta$	$M_G$			
<u>Inertinite-rich coal (cp)</u>	0.54	28	8.44	1.00	8.4	0.0	563	26.37	0.16			
Char @450 °C	0.58	32	9.13	1.00	9.1	0.0	518	13.84	0.14			
Char @700 °C	0.58	32	7.68	1.00	7.7	0.0	461	8.86	0.18			
Char @1000 °C (spe)	*	*	*	*	*	*	*	*	*			
<u>Vitrinite-rich coal (cp)</u>	0.49	24	7.79	1.00	7.8	0.0	573	35.52	0.19			
Char @450 °C	0.51	26	9.90	1.00	9.9	0.0	511	20.46	0.10			
Char @700 °C	0.58	32	10.08	1.00	10.1	0.0	476	8.88	0.12			
Char @1000 °C (spe)	*	*	*	*	*	*	*	*	*			

\* = values not available due to line-broadening phenomenon

### 3.4.5 X-ray diffraction

**Diffractograms.** The XRD technique was used to investigate the effect of pyrolysis temperature on the carbon structure. The diffractograms in Figure 3-7 show three peaks

## CHAPTER 3: COAL AND CHAR CHARACTERISATION

of the broad (002), (10) and (11) (Figure 3-7(a). The peak (002) in the low-angle zone relates to the stacking of the graphitic basal planes in char crystallites (Zhang *et al.*, 2008:3213). The other two peaks in the higher angle zone, designated as (10) and (11) are ascribed to the hexagonal ring structure in char crystallites (Zhang *et al.*, 2008:3213). In general, the sharper and narrower the peak (002) and the peak (10) on XRD spectra, the more ordered the carbon structure (Zhang *et al.*, 2008:3213). Inertinite coals and chars have a more ordered carbon structure as indicated by the relatively sharper and more intense (002) and (10) peaks. However, in both cases of maceral types, the (002) and (10) peaks became more prominent with increasing pyrolysis temperature and even protruded substantially on the char samples generated at 1000 °C.

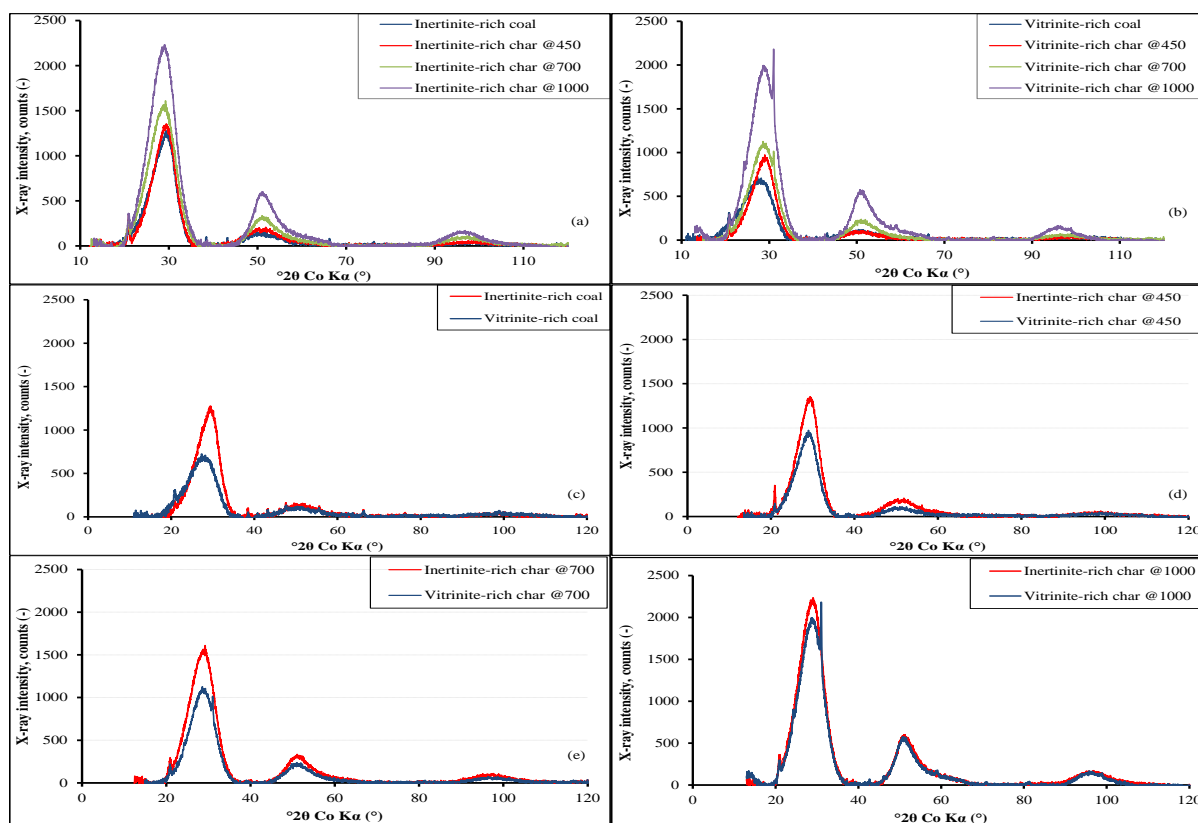


Figure 3-7. Baseline corrected and smoothed XRD diffractograms of coals and chars, where: (a) and (b) = inertinite- and vitrinite-rich particles, respectively; (c)–(f) = inertinite- vs vitrinite-rich particles. Numbers in the legends = temperatures in °C.

## CHAPTER 3: COAL AND CHAR CHARACTERISATION

---

Table 3-8 shows the structural parameters extracted from the diffractograms. It was found that the  $L_c$ ,  $d_{002}$  and  $N_{ave}$  of both chars remained nearly unchanged at the maximum pyrolysis temperature when compared to their parent coals. Emmerich (Emmerich, 1995:1709) has made similar observations in the investigation of the evolution of crystallinity in carbon with heat treatment, where the  $L_c$  did not change during similar heat treatment conditions. The reason for this is that since the growth of  $L_c$  is caused by the coalescence of crystallites along the c-axis during heating, it usually starts to occur above heat treatment temperatures of 1200 °C and applies to both graphitisable and non-graphitisable carbons (Xu *et al.*, 2012:118). Fermoso *et al.* (Fermoso *et al.*, 2010:5586) has also observed that up to 1000 °C the devolatilisation temperature did not appear to have any significant effect on char morphology. At elevated temperatures, polynuclear aromatic compounds still diffuse gradually and begin to condense with the removal of H<sub>2</sub> (Zhu and Sheng, 2010:837; Yu *et al.*, 2007:135; Xu *et al.*, 2012:118; Cousins *et al.*, 2006:2489). The conventional analyses results corroborated the declining H/C and O/C atomic ratios (Table 3-1). In the case of the  $d_{002}$ , Zhang *et al.* have observed similar trends on coal chars prepared below 1000 °C when this crystallite changed only little as the pyrolysis temperature increased and even dropped suddenly at 900 °C (Zhang *et al.*, 2008:3213). The  $d_{002}$  parameter is a good indicator for char crystallite order in that the smaller the  $d_{002}$  value, the higher the carbon crystallite order. Chars generated from inertinite-rich coal have a higher carbon crystallite order because their  $d_{002}$  values slightly lagged behind those of chars generated from vitrinite-rich coal. Both the inertinite- and vitrinite-rich chars experienced an increase in the crystallite diameter ( $L_a$ ) as the pyrolysis temperature increased. This increase in  $L_a$  is caused by the crystallites coming together along the a-axis with a side by side convergence of the graphite-like layers (Zhang *et al.*, 2008:3213), as shown in Table 3-8.

The  $L_a$  parameter increases with temperatures because of the strong cross-linking between neighbouring crystallites and randomly oriented crystallites (Emmerich, 1995:1709). Generally, XRD results showed that the chars generated from inertinite- and vitrinite-rich coals at 700-1000 °C were nearly similar. The  $L_a$  value elucidated the

## CHAPTER 3: COAL AND CHAR CHARACTERISATION

difference between these chars, where larger magnitudes were associated with the inertinite-rich chars.

Table 3-8. Summary of structural parameters extracted from the XRD diffractograms.

Property / Sample ID	Coal		Char @450		Char @700		Char @1000	
	IR	VR	IR	VR	IR	VR	IR	VR
Inter-layer spacing, $d_{002}$ (Å)	3.50	3.52	3.53	3.55	3.52	3.57	3.49	3.51
Crystallite height, $L_c$ (Å)	12.74	13.89	14.64	14.71	13.11	13.28	12.19	11.76
Ave. No. of aromatic layers, $N_{ave}$ (-)	4.64	4.95	5.15	5.15	4.73	4.73	4.49	4.35
Crystallite diameter, $L_a(10)$ (Å)	15.58	16.36	16.57	17.94	22.87	21.74	37.61	30.74
Crystallite diameter, $L_a(11)$ (Å)	16.23	18.11	18.34	19.78	27.08	24.88	39.39	32.47
Aromaticity $f_a$ (-)	0.81	0.74	0.85	0.81	0.90	0.86	0.98	0.96
Fraction of amorphous carbon $X_A$ (-)	0.52	0.61	0.40	0.52	0.19	0.40	0.10	0.12
Index of disorder, $IOD$ (-)	0.61	0.71	0.49	0.61	0.27	0.48	0.12	0.15

### 3.4 Discussion

In this paper the properties of chars generated by slow heating of South Africa's inertinite- and vitrinite-rich coals from Seam 4 of the Witbank and Upper Ecca of the Waterberg Coalfields, respectively, are reported using data from various analytical techniques. The objective of this investigation was to correlate the results with detailed subsequent studies of the molecular structures of chars that may give rise to different reactivity behaviours with CO<sub>2</sub> gas (Chapters 4 and 5) (Roberts *et al.*, 2015:9; Roberts *et al.*, 2015:295). Consequently, the chars at the highest temperature (1000 °C) drew more attention for these studies. Analytical results presented here were used to construct molecular structures of inertinite- and vitrinite-rich chars comprising

## CHAPTER 3: COAL AND CHAR CHARACTERISATION

---

polyaromatic hydrocarbons with oxygen, nitrogen and sulphur functionalities, as published in Roberts *et al.* (Roberts *et al.*, 2015:9). The elemental composition, skeletal density measurements and aromaticity results presented in Tables 3.1, 2.2 and 3.8 provided constraining data for the model constructions. The aromatic layer stacking height,  $L_c$ , interlayer spacing  $d_{002}$  and average number of aromatic layers per stack,  $N_{ave}$ , of the 1000 °C chars in Table 3.8 provided the test and validation of the respective char models in Roberts *et al.* (Roberts *et al.*, 2015:9), since these parameters were not controlled during the model construction process. In addition to this, the XRD results reported here compare fairly well with the HRTEM results reported in Roberts *et al.* (Roberts *et al.*, 2015:295). In particular, the current crystallite diameter,  $L_a$  (10), from the XRD technique, of 37.6Å for the 1000 °C inertinite-rich chars, fell within the range of minimum-maximum length of the 11x11 aromatic fringes (27-45Å) from the HRTEM; the  $L_a$  (10) of 30.7Å for the vitrinite-rich chars fell fairly close to the minimum-maximum length range of 17-28Å (Roberts *et al.*, 2015:295). The structural and lattice parameters obtained for the chars using the XRD technique compare well with published data in open literature (Emmerich, 1995:1709; Cousins *et al.*, 2006:2489; Yu *et al.*, 2007:135; Xu *et al.*, 2012:118; Malumbazo *et al.*, 2011:743; Everson *et al.*, 2013:148). The line broadening phenomena exhibited by the NMR spectra for the 1000 °C chars was also reported by Solum *et al.* (Solum *et al.*, 2001:961).

### 3.5 Conclusions

Systematic characterisation of the chemical- and physical-structural properties of inertinite- and vitrinite-rich chars was achieved using various analytic techniques. There was a good correlation between the Rsc and aromaticity measurements as determined by both the XRD and NMR techniques when these properties increased substantially at 700-1000 °C the difference between them became smaller. The chemical structure of the inertinite-rich and vitrinite-rich chars at 700-1000 °C was remarkably similar in terms of the proximate, ultimate Rsc and aromaticity. A greater

## CHAPTER 3: COAL AND CHAR CHARACTERISATION

---

transition occurred in vitrinite-rich coals to ultimately match the inertinite-rich coals at high temperatures. Differences in the physical structure of the chars at these temperatures were observed in terms of the BET, D-R and Langmiur surface areas and microporosity at 700-1000 °C. The distinction between the macerals diminished at 700-1000 °C. However, the differences in maceral composition of the parent coals resulted in the different char forms during thermal conversion. A higher proportion of isotropic “coke” derived from pure coal vitrinites occurred in the vitrinite-rich chars (91-95%) than in the inertinite-rich chars (5-8%) at 700-1000 °C. Therefore, on a chemical level the high temperature chars are similar. Differences exist in the physical structure at high temperatures. The internite-rich particles were associated with larger magnitudes of the mean crystallite diameter (37.6Å) compared with vitrinite-rich particles (30.7Å) at 1000 °C. This property makes investigations into the atomistic properties of the inertinite- and vitrinite-rich chars attractive, including their reactivity behaviour with carbon dioxide gas.

## CHAPTER 3: COAL AND CHAR CHARACTERISATION

### Nomenclature

Symbol	Definition	Units
$(\sigma+1)$	Average number of attachments to the aromatic cluster	-
A-D	CO <sub>2</sub> adsorption data	-
B.L	Number of bridges and loops per aromatic	-
C	Number of aromatic carbons per cluster	-
CP-MAS	Cross polarisation-magic angle spinning	-
$d_{002}$	Inter-layer spacing for a group of $N_{ave}$ parallel	Å
DD	Dipolar dephasing	-
$D_{inner}$	Inner diameter	mm
$D_{outer}$	Outer diameter	mm
D-R	Dubin-Radushkevich method	-
$f_a$	Fraction of sp <sup>2</sup> carbons (aromatics)	-
$f_a^*$	Corrected fraction aromatics	-
$f_a^B$	Fraction of bridgehead carbons	-
$f_a^H$	Fraction of protonated aromatic carbons	-
$f_{al}$	Fraction of aliphatic carbons	-
$f_{al}^H$	Aliphatic CH + CH <sub>2</sub>	-
$f_{al}^O$	Aliphatic carbons that are bonded to oxygen	-
$f_a^N$	Fraction of non-protonated aromatic carbons	-
$f_a^{N^*}$	Fraction non-protonated carbon + methyl groups in aliphatic region	-
$f_a^P$	Fraction of phenolic carbons	-
$f_a^S$	Fraction of alkylated carbons	-
H	Height	mm
$H_{effective}$	Effective height	mm
H-K	Horvath-Kawazoe	-
L	Langmuir method	-
$L_a$	Crystallite diameter	Å
$L_a(10)$	Crystallite diameter on peak (10) approximations	Å
$L_a(11)$	Crystallite diameter on peak (11) approximations	Å
$L_c$	Crystallite height	Å
$M_\delta$	Average molecular weight of a side chain or half of a bridge mass	g mol <sup>-1</sup>

## CHAPTER 3: COAL AND CHAR CHARACTERISATION

Symbol	Definition	Units
$N_{ave}$	Average number of aromatic layers per carbon crystallite	-
$P_A$	Partial pressure of the gasifying agent	kPa
$P_o$	Fraction of attachments that are bridges between neighbouring aromatic clusters or fraction of intact bridges	-
$Rr$	Random vitrinite reflectance	%
$Rsc$	Total maceral reflectance scan	%
S.C	Number of side chains per cluster	-
$x_A$	Fraction of amorphous carbon	-
$X_b$	Mole fraction of aromatic bridgehead carbons	-

### Greek symbols

Symbol	Definition	Units
$\theta$	Peak position / XRD angle of scan	Degrees ( $^{\circ}$ )
$\gamma$	Gamma band/peak	-
$\rho$	Skeletal/true density (of coals/chars)	$\text{g cm}^{-3}$
#	Number	-
$\beta$	Peak widths at half-maximum intensity	-

### Abbreviations

Acronym	Definition
BET	Brunauer, Emmett and Teller method
CP-MAS	Cross polarisation-magic angle and spinning
DD	Dipolar dephasing
DP	Direct polarization
FTIR	Fourier transform infrared spectroscopy
HF	Hydrofluoric acid
HCl	Hydrochloric acid
HMB	Hexamethylbenzene
HRTEM	High resolution transmission electron microscopy

## CHAPTER 3: COAL AND CHAR CHARACTERISATION

---

Acronym	Definition
<i>M.W</i>	Average molecular weight of aromatic cluster
NMR	Solid state $^{13}\text{C}$ nuclear magnetic resonance spectroscopy
PBR	Packed bed reactor
PSD	Pore size distribution
<i>rpm</i>	Revolutions per minute
SAS	Sasol advanced synthol
$\text{SmI}_2$	Samarium (II) iodide
<i>SPE</i>	Single pulse excitation
THF	Tetrahydrofuran
UN-ECE	United Nations Economic Commission for Europe
XRD	X-ray diffraction

---

## CHAPTER 3: COAL AND CHAR CHARACTERISATION

---

### 3.6 References

- AHUJA, P.; KUMAR, S. and SINGH, P. C. 1996. A model for primary and heterogeneous secondary reactions of wood pyrolysis. *Chemical engineering & technology*, 19, 272.
- BUNT, J.; JOUBERT, J. and WAANDERS, F. 2008. Coal char temperature profile estimation using optical reflectance for a commercial-scale Sasol-Lurgi FBDB gasifier. *Fuel*, 87, 2849.
- BUNT, J. and WAANDERS, F. 2009. Pipe reactor gasification studies of a south african bituminous coal blend. Part 1—Carbon and volatile matter behaviour as function of feed coal particle size reduction. *Fuel*, 88, 585.
- CAI, H. Y. and KANDIYOTI, R. 1995. Effect of changing inertinite concentration on pyrolysis yields and char reactivities of two South African coals. *Energy & Fuels*, 9, 956.
- CHABALALA, V. P.; WAGNER, N. and POTGIETER-VERMAAK, S. 2011. Investigation into the evolution of char structure using Raman spectroscopy in conjunction with coal petrography; Part 1. *Fuel Processing Technology*, 92, 750.
- CHEN, N. and YANG, R. T. 1998. Ab initio molecular orbital study of the unified mechanism and pathways for gas-carbon reactions. *The Journal of Physical Chemistry A*, 102, 6348.
- CHEN, S. and YANG, R. 1997. Unified mechanism of alkali and alkaline earth catalyzed gasification reactions of carbon by CO<sub>2</sub> and H<sub>2</sub>O. *Energy & fuels*, 11, 421.
- CHEN, S. G.; YANG, R. T.; KAPTEIJN, F. and MOULIJN, J. A. 1993. A new surface oxygen complex on carbon: toward a unified mechanism for carbon gasification reactions. *Industrial & Engineering Chemistry Research*, 32, 2835.
- COUSINS, A.; PATERSON, N.; DUGWELL, D. R. and KANDIYOTI, R. 2006. An investigation of the reactivity of chars formed in fluidized bed gasifiers: The effect of reaction conditions and particle size on coal char reactivity. *Energy & Fuels*, 20, 2489.
- DYRKACZ, G. R. and BLOOMQUIST, C. A. A. 1992. Use of continuous flow centrifugation techniques for coal maceral separation. 1. Fundamentals. *Energy & Fuels*, 6, 357.
- EMMERICH, F. G. 1995. Evolution with heat treatment of crystallinity in carbons. *Carbon*, 33, 1709.
- EVERSON, R. C.; NEOMAGUS, H. W. J. P.; KAITANO, R.; FALCON, R.; ALPHEN, C. V. and DU CANN, V. M. 2008. Properties of high ash char particles derived from inertinite-rich coal: 1. Chemical, structural and petrographic characteristics. *Fuel*, 87, 3082.
- EVERSON, R. C.; OKOLO, G. N.; NEOMAGUS, H. W. J. P. and DOS SANTOS, J.-M. 2013. X-ray diffraction parameters and reaction rate modeling for gasification and combustion of chars derived from inertinite-rich coals. *Fuel*, 109, 148.
- FABIANSKA, M. J. and KRUSZEWSKA, K. K. J. 2003. Relationship between petrographic and geochemical characterisation of selected South African coals. *Papers from the TSOP/ICCP session, 53rd ICCP meeting 2001, Copenhagen, Denmark, and from the 18th TSOP meeting 2002, Houston, TX, USA*, 54, 95.
- FALCON, L. M. A. F. R. M. S. 1987. The petrographic composition of southern African coals in relation to friability, hardness, and abrasive indices. *Southern African Institute of Mining and Metallurgy*, 87, 323.
- FALCON, R. M. S., SNYMAN, C. P. 1986. *An introduction to coal petrography: Atlas of petrographic constituents in the bituminous coals of southern Africa*, Johannesburg [South Africa], The Geological Society of South Africa.
- FERMOSO, J.; GIL, M. V.; BORREGO, A. G.; PEVIDA, C.; PIS, J. J. and RUBIERA, F. 2010. Effect of the pressure and temperature of devolatilization on the morphology and steam gasification reactivity of coal chars. *Energy & Fuels*, 24, 5586.

## CHAPTER 3: COAL AND CHAR CHARACTERISATION

---

- FLETCHER, T. H.; SOLUM, M. S.; GRANT, D. M.; CRITCHFIELD, S. and PUGMIRE, R. J. 1991. Solid state  $^{13}\text{C}$  and  $^1\text{H}$  NMR studies of the evolution of the chemical structure of coal char and tar during devolatilization. *Twenty-Third Symposium (International) on Combustion*, 23, 1231.
- FLETCHER, T. H.; SOLUM, M. S.; GRANT, D. M. and PUGMIRE, R. J. 1992. Chemical structure of char in the transition from devolatilization to combustion. *Energy & Fuels*, 6, 643.
- FU, W.-B. and WANG, Q.-H. 2001. A general relationship between the kinetic parameters for the gasification of coal chars with  $\text{CO}_2$  and coal type. *Fuel processing technology*, 72, 63.
- GALE, T. K.; BARTHOLOMEW, C. H. and FLETCHER, T. H. 1996. Effects of pyrolysis heating rate on intrinsic reactivities of coal chars. *Energy & Fuels*, 10, 766.
- GILMAN, J. W.; LOMAKIN, S.; KASHIWAGI, T.; VANDERHART, D. L. and NAGY, V. 1998. Characterization of flame-retarded polymer combustion chars by solid-state  $^{13}\text{C}$  and  $^{29}\text{Si}$  NMR and EPR. *Fire and Materials*, 22, 61.
- HATCHER, P. G. 1988. Dipolar-dephasing  $^{13}\text{C}$  NMR studies of decomposed wood and coalified xylem tissue: evidence for chemical structural changes associated with defunctionalization of lignin structural units during coalification. *Energy & Fuels*, 2, 48.
- HATTINGH, B. B.; EVERSON, R. C.; NEOMAGUS, H. W. J. P.; BUNT, J. R.; VAN NIEKERK, D.; JORDAAN, J. H. L. and MATHEWS, J. P. 2013. Elucidation of the Structural and Molecular Properties of Typical South African Coals. *Energy & Fuels*, 27, 3161.
- ISO 2005. Classification of coals. ISO 11760:2005 9.
- ISO 2010. ISO 12902 "Solid mineral fuel – Determination of total carbon, hydrogen and nitrogen – Instrumental methods".
- JARONIEC, M.; CHOMA, J. and KRUK, M. 2003. Assessment of reliability of the Horvath–Kawazoe pore size analysis method using argon adsorption isotherms on ordered mesoporous silicas. *Colloids and Surfaces A: Physicochemical and Engineering Aspects*, 214, 263.
- JONES, J. M.; POURKASHANIAN, M.; RENA, C. D. and WILLIAMS, A. 1999. Modelling the relationship of coal structure to char porosity. *Fuel*, 78, 1737.
- JOSEPH, J. T.; FISHER, R. B.; MASIN, C. A.; DYRKACZ, G. R.; BLOOMQUIST, C. A. and WINANS, R. E. 1991. Coal maceral chemistry. 1. Liquefaction behavior. *Energy & Fuels*, 5, 724.
- KAEGI, D. D. 1985. On the identification and origin of pseudovitrinite. *International journal of coal geology*, 4, 309.
- KOWALCZYK, P.; TERZYK, A. P.; GAUDEN, P. A. and SOLARZ, L. 2002. Numerical analysis of Horvath–Kawazoe equation. *Computers & chemistry*, 26, 125.
- KRUSZEWSKA, K. J. 1998. The reactivity of pseudovitrinite in some coals. *Fuel*, 77, 1655.
- LARSEN, J. W.; PAN, C. S. and SHAWVER, S. 1989. Effect of demineralization on the macromolecular structure of coals. *Energy & Fuels*, 3, 557.
- LIU, Z.-S.; WANG, Q.; ZOU, Z.-S. and TAN, G.-L. 2010. Reaction mechanism of carbon gasification in  $\text{CO}_2$  under non-isothermal conditions. *Journal of Thermal Analysis and Calorimetry*, 1.
- LU, L.; KONG, C.; SAHAJWALLA, V. and HARRIS, D. 2002. Char structural ordering during pyrolysis and combustion and its influence on char reactivity. *Fuel*, 81, 1215.
- LU, L.; SAHAJWALLA, V.; KONG, C. and HARRIS, D. 2001. Quantitative X-ray diffraction analysis and its application to various coals. *Carbon*, 39, 1821.
- MALUMBAZO, N.; WAGNER, N. J.; BUNT, J. R.; VAN NIEKERK, D. and ASSUMPTION, H. 2011. Structural analysis of chars generated from South African inertinite coals in a pipe-reactor combustion unit. *Fuel Processing Technology*, 92, 743.
- MONTOYA, A.; TRUONG, T. N. and SAROFIM, A. F. 2000. Application of density functional theory to the study of the reaction of  $\text{NO}$  with char-bound nitrogen during combustion. *The Journal of Physical Chemistry A*, 104, 8409.

## CHAPTER 3: COAL AND CHAR CHARACTERISATION

---

- MUNTEAN, J. V.; STOCK, L. M. and BOTTO, R. E. 1988. Improving the reliability of quantitative solid-state  $^{13}\text{C}$  NMR analysis of coal. *Energy & Fuels*, 2, 108.
- NANDI, B. N.; BROWN, T. D. and LEE, G. K. 1977. Inert coal macerals in combustion. *Fuel*, 56, 125.
- NIEKERK, D. V. and MATHEWS, J. P. 2010. Molecular representations of Permian-aged vitrinite-rich and inertinite-rich South African coals. *Fuel*, 89, 73.
- OBOIRIEN, B. O.; ENGELBRECHT, A. D.; NORTH, B. C.; DU CANN, V. M.; VERRYIN, S. and FALCON, R. 2011. Study on the structure and gasification characteristics of selected South African bituminous coals in fluidised bed gasification. *Fuel Processing Technology*, 92, 735.
- ÖNAL, Y. and CEYLAN, K. 1995. Effects of treatments on the mineral matter and acidic functional group contents of Turkish lignites. *Fuel*, 74, 972.
- PERRY, S. T.; HAMBLY, E. M.; FLETCHER, T. H.; SOLUM, M. S. and PUGMIRE, R. J. 2000. Solid-state  $^{13}\text{C}$  NMR characterization of matched tars and chars from rapid coal devolatilization. *Proceedings of the Combustion Institute*, 28, 2313.
- PETELA, R. and PETELA, G. 1996. Indices for coal desulfurization and de-ashing processes. *Fuel*, 75, 1259.
- RADOVIC, L. R.; STECZKO, K.; WALKER JR, P. L. and JENKINS, R. G. 1985. Combined effects of inorganic constituents and pyrolysis conditions on the gasification reactivity of coal chars. *Fuel Processing Technology*, 10, 311.
- ROBERTS, M. J.; EVERSON, R. C.; DOMAZETIS, G.; NEOMAGUS, H. W. J. P.; JONES, J. M.; VAN SITTERT, C. G. C. E.; OKOLO, G. N.; NIEKERK, D. V. and MATHEWS, J. P. 2015. Density functional theory molecular modelling and experimental particle kinetics for  $\text{CO}_2$ -char gasification. *Carbon*, 93, 295.
- ROBERTS, M. J.; EVERSON, R. C.; NEOMAGUS, H. W. J. P.; VAN NIEKERK, D.; MATHEWS, J. P. and BRANKEN, D. J. 2015. Influence of maceral composition on the structure, properties and behaviour of chars derived from South African coals. *Fuel*, 142, 9.
- ROUQUEROL, J.; ROUQUEROL, F.; LLEWELLYN, P.; MAURIN, G. and SING, K. S. 2013. *Adsorption by powders and porous solids: principles, methodology and applications*, Academic press.
- SADHUKHAN, A. K.; GUPTA, P. and SAHA, R. K. 2009. Characterization of porous structure of coal char from a single devolatilized coal particle: Coal combustion in a fluidized bed. *Fuel Processing Technology*, 90, 692.
- SCOTT, A. C. 2002. Coal petrology and the origin of coal macerals: a way ahead? *International Journal of Coal Geology*, 50, 119.
- SHARMA, D. and WADHWA, G. 1997. Demineralization of coal by stepwise bioleaching: a comparative study of three Indian coals by fourier transform infra red and X-ray diffraction techniques. *World Journal of Microbiology and Biotechnology*, 13, 29.
- SMITH, W.; ROUX, H. and STEYN, J. 1983. The classification of coal macerals and their relation to certain chemical and physical parameters of coal. *Geol Soc South Africa*, 7, 111.
- SNAPE, C. E.; MCGHEE, B. J.; MARTIN, S. C. and ANDRESEN, J. M. 1997. Structural characterisation of catalytic coke by solid-state  $^{13}\text{C}$ -NMR spectroscopy. *Catalysis Today*, 37, 285.
- SNYMAN, C. and BOTHA, W. 1993. Coal in South Africa. *Journal of African Earth Sciences (and the Middle East)*, 16, 171.
- SOLUM, M. S.; PUGMIRE, R. J. and GRANT, D. M. 1989. Carbon-13 solid-state NMR of Argonne-premium coals. *Energy & Fuels*, 3, 187.
- SOLUM, M. S.; SAROFIM, A. F.; PUGMIRE, R. J.; FLETCHER, T. H. and ZHANG, H. 2001.  $^{13}\text{C}$  NMR analysis of soot produced from model compounds and a coal. *Energy & Fuels*, 15, 961.
- SUPALUKNARI, S.; BURGAR, I. and LARKINS, F. P. 1990. High-resolution solid-state  $^{13}\text{C}$  NMR studies of Australian coals. *Organic Geochemistry*, 15, 509.

## CHAPTER 3: COAL AND CHAR CHARACTERISATION

---

- TEKELY, P.; NICOLE, D.; DELPUECH, J.-J.; TOTINO, E. and MULLER, J. 1987. Chemical structure changes in coals after low-temperature oxidation and demineralization by acid treatment as revealed by high resolution solid state  $^{13}\text{C}$  NMR. *Fuel processing technology*, 15, 225.
- TIMM, A.; GEERTSEMA, H. and WARNICH, L. 2010. Population genetic structure of economically important Tortricidae (Lepidoptera) in South Africa: a comparative analysis. *Bulletin of entomological research*, 100, 421.
- TREJO, F.; ANCHEYTA, J.; MORGAN, T. J.; HEROD, A. A. and KANDIYOTI, R. 2007. Characterization of asphaltenes from hydrotreated products by SEC, LDMS, MALDI, NMR, and XRD. *Energy & Fuels*, 21, 2121.
- UN-ECE. *International codification system for medium and high rank coals*. United Nations publication [Online]. Available: <http://www.unece.org/fileadmin/DAM/ie/se/pdfs/codee.pdf> [Accessed August 30 2014].
- VAN NIEKERK, D. 2008. *Structural elucidation, molecular representation and solvent interactions of vitrinite-rich and inertinite-rich South African coals*, ProQuest.
- VAN NIEKERK, D.; PUGMIRE, R. J.; SOLUM, M. S.; PAINTER, P. C. and MATHEWS, J. P. 2008. Structural characterization of vitrinite-rich and inertinite-rich Permian-aged South African bituminous coals. *International Journal of Coal Geology*, 76, 290.
- VAN RENSBURG, B. J.; PEACOCK, D. S. and ROBERTSON, M. P. 2009. Biotic homogenization and alien bird species along an urban gradient in South Africa. *Landscape and Urban Planning*, 92, 233.
- WALKER JR, P.; RUSINKO JR, F.; AUSTIN, L.; ELEY, D.; SELWOOD, P. and WEISZ, P. 1959. Advances in Catalysis, vol. *Vol. II*, 133.
- WANG, B.; SUN, L.; SU, S.; XIANG, J.; HU, S. and FEI, H. 2012. Char Structural Evolution during Pyrolysis and Its Influence on Combustion Reactivity in Air and Oxy-Fuel Conditions. *Energy & Fuels*, 26, 1565.
- WANG, C. A.; LIU, Y.; ZHANG, X. and CHE, D. 2011. A study on coal properties and combustion characteristics of blended coals in Northwestern China. *Energy & Fuels*, 25, 3634.
- WANG, K.; GUO, X.; ZHAO, P. and ZHENG, C. 2010. Cyclic  $\text{CO}_2$  capture of CaO-based sorbent in the presence of metakaolin and aluminum (hydr) oxides. *Applied Clay Science*, 50, 41.
- WEBB, P. A. 2001. Volume and density determinations for particle technologists. *Micromeritics Instrument Corp*, 2, 01.
- WIJAYA, N. and ZHANG, L. 2011. A Critical review of coal demineralization and its implication on understanding the speciation of organically bound metals and submicrometer mineral grains in coal. *Energy & Fuels*, 25, 1.
- WINSTON, R. B. 1986. Characteristics features and compaction of plant tissues traced from permineralized peat to coal in Pennsylvanian coals (Desmoinesian) from the Illinois basin. *International Journal of Coal Geology*, 6, 21.
- XU, K.; HU, S.; SU, S.; XU, C.; SUN, L.; SHUAI, C.; JIANG, L. and XIANG, J. 2012. Study on char surface active sites and their relationship to gasification reactivity. *Energy & Fuels*, 27, 118.
- XU, W.-C. and TOMITA, A. 1987. Effect of coal type on the flash pyrolysis of various coals. *Fuel*, 66, 627.
- YAMASHITA, H.; TOMITA, A.; YAMADA, H.; KYOTANI, T. and RADOVIC, L. R. 1993. Influence of char surface chemistry on the reduction of nitric oxide with chars. *Energy & Fuels*, 7, 85.
- YU, J.; LUCAS, J.; STREZOV, V. and WALL, T. 2003. Swelling and char structures from density fractions of pulverized coal. *Energy & Fuels*, 17, 1160.
- YU, J.; LUCAS, J. A. and WALL, T. F. 2007. Formation of the structure of chars during devolatilization of pulverized coal and its thermoproperties: A review. *Progress in Energy and Combustion Science*, 33, 135.

## CHAPTER 3: COAL AND CHAR CHARACTERISATION

---

ZHANG, L.; HUANG, J.; FANG, Y. and WANG, Y. 2006. Gasification reactivity and kinetics of typical Chinese anthracite chars with steam and CO<sub>2</sub>. *Energy & fuels*, 20, 1201.

ZHANG, S.-Y.; LU, J.-F.; ZHANG, J.-S. and YUE, G.-X. 2008. Effect of pyrolysis intensity on the reactivity of coal char. *Energy & Fuels*, 22, 3213.

ZHU, X. and SHENG, C. 2010. Influences of carbon structure on the reactivities of lignite char reacting with CO<sub>2</sub> and NO. *Fuel Processing Technology*, 91, 837.

ZOU, J. H.; ZHOU, Z. J.; WANG, F. C.; ZHANG, W.; DAI, Z. H.; LIU, H. F. and YU, Z. H. 2007. Modeling reaction kinetics of petroleum coke gasification with CO<sub>2</sub>. *Chemical Engineering and Processing: Process Intensification*, 46, 630.

## CHAPTER 4: LARGE-SCALE MOLECULAR MODELLING OF CHARS

---

### Chapter 4: Large-scale molecular modelling of chars

**Publication #2.** Mokone J. Roberts, Raymond C. Everson, Hein W.J.P. Neomagus, Daniel Van Niekerk, Jonathan P. Mathews, David J. Branken. *Influence of maceral composition on the structure, properties and behaviour of chars derived from South African coals*. FUEL, 2015. 142: p. 9-20.

#### 4.1 Abstract

The generation of coal chars is an important intermediate step in coal conversion processes such as combustion and gasification. The char structure impacts their behaviour in these processes. Detailed investigations on slow-heated coal chars utilizing molecular modelling approaches are limited in comparison to the more extensive work on coal. Also South African (SA) coal is generally not as well studied as the vitrinite-rich coals in the Northern Hemisphere. Both inertinite-rich and vitrinite-rich coals are available in SA, formed with the same inputs but in different depositional environments, thus providing an opportunity to examine maceral influences without the challenges associated with maceral separation. Experimental work was performed to characterise de-ashed chars generated by heating the inertinite- and vitrinite-rich South African Gondwana coals of the Permian-age under inert atmosphere (nitrogen gas) to 1000 °C at a rate of 20 °C min and maintained this temperature for 60 minutes before cooling. Experimental work included petrographic analysis, elemental analysis, helium density, <sup>13</sup>C NMR, XRD, and HRTEM analyses. The maceral purity was enhanced with density separation prior to pyrolysis. Analytical data was used to construct molecular structures comprising polyaromatic hydrocarbons with oxygen, nitrogen and sulphur functionalities. Aromaticity and skeletal density measurements provided additional constraining data. The inertinite-rich char model comprised 106 molecules constructed from a total of 42929 atoms with a composition (normalized to 1000 carbon atoms) of C<sub>1000</sub>H<sub>105</sub>O<sub>14</sub>N<sub>22</sub>S<sub>1</sub>, while the vitrinite-rich char model was made up of 185 molecules

## CHAPTER 4: LARGE-SCALE MOLECULAR MODELLING OF CHARS

---

consisting of a total of 44315 atoms with a normalized composition of  $C_{1000}H_{125}O_{21}N_{22}S_3$ . The two chars were thus chemically similar; however, the size of polyaromatic molecules differed, as observed from HRTEM and XRD data. The inertinite-rich chars contained larger molecules ( $L_a(10) = 37.61 \pm 2.32\text{\AA}$ ) than the vitrinite-rich chars ( $L_a(10) = 30.74 \pm 0.77\text{\AA}$ ). This will influence the fraction of active carbon sites located on the crystallite edges and defects of the basal planes that may contribute to the lower reactivity of inertinite-rich chars in comparison to vitrinite-rich chars. Atomistic representations of these chars was constructed capturing a portion of the structural diversity observed from image analysis of the HRTEM lattice fringe micrographs. While the char generation parameters used in this study produced similar chars derived from the South African inertinite- and vitrinite-rich coals, the crystallite diameter,  $L_a$ , was found to be the property that distinguished the two chars significantly. This may hold promise for exploring structural-reactivity relationships.

## CHAPTER 4: LARGE-SCALE MOLECULAR MODELLING OF CHARs

---

### 4.2 Introduction and background

Coal structure is challenging due to its inherent complexity and heterogeneity. However, the relationship of coal structure to its reactivity in gasification, combustion, pyrolysis and liquefaction is of significant interest. With more advanced analytical techniques, such as high resolution transmission electron microscope (HRTEM), Fourier-transform infrared spectroscopy (FTIR), solid-state  $^{13}\text{C}$  nuclear magnetic resonance spectroscopy (NMR), X-ray analysis and pyrolysis gas chromatography mass spectrometry (GCMS), a more detailed picture of coal structure has been obtained (Sharma *et al.*, 2000:1219; Sharma *et al.*, 1999:1203; Mathews *et al.*, 2001:863; Nip *et al.*, 1992:125; Fletcher *et al.*, 1992:643; Perry *et al.*, 2000b:2313). Larger-scale atomistic representations that incorporate elemental data and structural information from the analytical techniques are emerging and are supported by advanced computer programs that facilitate construction and evaluation (Niekerk and Mathews, 2010:73; Castro-Marcano *et al.*, 2012:35; Mathews *et al.*, 2001:863; Narkiewicz and Mathews, 2008:3104). The majority of coals that have experienced this level of research are from the carboniferous deposits of the Laurasian-age in the Northern Hemisphere. Carlson pioneered the use of computational techniques to represent various coal models (Carlson, 1992:771) and showed that molecular modelling could be a valuable tool to study the non-bonding interactions present in coal (Niekerk and Mathews, 2010:73). Hatcher *et al.* published a structural model for coalified wood of high-volatile bituminous coal using elemental, solid-state  $^{13}\text{C}$  NMR, and pyrolysis gas chromatography mass spectrometry results (Hatcher *et al.*, 1992:813). Faulon *et al.* examined various techniques to construct computational molecular models for bituminous coals and developed the SIGNATURE software for an automatic construction a molecular diverse coal structure using experimental results (Faulon *et al.*, 1993:1062; Niekerk and Mathews, 2010:73). Mathews *et al.* constructed computational models for Upper Freeport and Lewiston-Stockton vitrinites using SIGNATURE to generate covalently linked structures using various analytical results (Mathews *et al.*, 2001:863; Van Niekerk, 2008). Takanoashi and Kawashima constructed a computational model for Upper Freeport coal from  $^{13}\text{C}$  NMR chemical shift calculations (Takanoashi *et al.*, 1995:788; Niekerk and Mathews,

## CHAPTER 4: LARGE-SCALE MOLECULAR MODELLING OF CHARs

---

2010:73). Patrakov *et al.* constructed an average molecular structure for a liptinite-rich coal using results from liquefaction in tetralin (Patriakov *et al.*, 2005:189; Niekerk and Mathews, 2010:73). A review of the hand-drawn and computational representations of coal is available (Mathews *et al.*, 2011:718). The structural representations of coals of Permian-age in the Southern Hemisphere are limited to only two models of an inertinite- and vitrinite-rich coal from South Africa (Niekerk and Mathews, 2010:73). Much of the coal in the Southern Hemisphere was deposited during the Permian age on the continent of Gondwana (Cai and Kandiyoti, 1995:956; Cairncross *et al.*, 1990:309). The Southern Hemisphere coals are known to be rich in inertinite, but exhibit higher reactivity than their Northern Hemisphere counterparts (Cai and Kandiyoti, 1995:956).

The relationships between coal, char structure and reactivity in gasification, pyrolysis and combustion have been explored extensively. Coal pyrolysis, which is described as the devolatilisation of coal in an inert atmosphere, has been used extensively to study the structure of coal, including that of pyrolysis products such as char and tar (Sadhukhan *et al.*, 2009:692; Fernandez-Alos *et al.*, 2011:1807; Feng *et al.*, 2002:481; Cai and Kandiyoti, 1995:956; Jones *et al.*, 1999:1737; Zhu and Sheng, 2009:152; Zhu and Sheng, 2010:837). The structure of coal char is affected by the temperature–time history experienced by the coal particles inside the reactor, i.e. the heating rate, the maximum temperature experienced, the residence time at this temperature, and the gaseous atmosphere; and not only by the properties of the parent coal (Doctor, 1995:F11; Chan *et al.*, 1999:1539). The impact of reactivity of chars in the kinetics of gasification and combustion processes makes research in its micro-structural properties valuable. Both Mathews *et al.* and Jones *et al.* constructed the molecular structures of chars generated from the Pittsburgh #8 coal as it developed during devolatilisation (Jones *et al.*, 1999:1737; Mathews *et al.*, 1998:136). Castro-Marciano *et al.* provided an improved direct char construction methodology and also demonstrated the application of a reactive molecular dynamics approach (ReaxFF) to perform combustion simulations with a molecular representation for a rapidly-heated Illinois No. 6 coal char to examine the transformation of char structure and chemical processes related to combustion at very high temperatures (Castro-Marciano *et al.*, 2012:1272). In this paper

## CHAPTER 4: LARGE-SCALE MOLECULAR MODELLING OF CHARs

---

the properties of chars generated by slow heating of South Africa's inertinite- and vitrinite-rich coals from Seam 4 of the Witbank and Upper Ecca of the Waterberg Coalfields, respectively, are reported using data from various analytical techniques. Atomistic representations were constructed using the analytical data. A special interest was put on chars formed at lower heating rate using large coal particles (typically in fixed-bed gasification and metallurgical coking).

### 4.3 Experimental methods

Detailed experimental methods were discussed in Chapter 3, Section 3.3.

#### 4.3.1 Coal and char characterisation

The standard and advanced properties of coal and char were discussed in Chapter 3, Section 3.3. An additional characterisation technique (HRTEM) will be discussed in this chapter.

#### 4.3.2 High-resolution transmission electron microscopy (HRTEM)

The lattice-fringe imaging mode of HRTEM, which is only practical for instruments with a low spherical aberration coefficient, is a very valuable method for the imaging of atomic planes in a carbon lattice (Davis *et al.*, 1995:31). The de-ashed char was re-ground to an ultra-fine powder using a mortar and pestle. The powder was suspended in acetone and 3 $\mu$ L of sample was applied to a 300 mesh Quantifoil R2/2 holey carbon copper grid. The samples were blotted and allowed to dry. The samples were examined using a 200 kV Tecnai F20 field emission gun transmission electron microscope and photographed using a Gatan CCD camera (Model 895). The minimum dose method of observation was used as the samples were found to be beam sensitive. There are essentially three

## CHAPTER 4: LARGE-SCALE MOLECULAR MODELLING OF CHARs

---

modes: search, focus and exposure. In search mode, the grids were scanned at low magnification (x6500) to find individual sharp-edged particles, which was situated at least partially across the holes in the carbon film. The particle edge had to be a single layer, to avoid superposition of fringes (Sharma *et al.*, 2000:1219). Once a thin enough particle edge was identified, the focus mode was activated, focusing on the image from a distance 0.15 $\mu$ m. The focusing was performed at the same magnification (x700 000) at which the micrographs were created. After focusing and correcting for astigmatism, the exposure mode was chosen and the image was taken at 100 nm underfocus for 1 s (Hattingh *et al.*, 2013:3161). Several pictures were taken from different spots to get the best images and a general view (Sharma *et al.*, 2001:54). Image analysis was conducted using the image processing toolkit from the Reindeer Graphics in conjunction with Photoshop CS5 software (Hattingh *et al.*, 2013:3161). Between 5 and 7 images were analysed. Each image of the char was cropped into suitable dissections (Figure 4.1). Image processing techniques (Sharma *et al.*, 1999:1203) were applied on the cropped images to produce the lattice fringes of the chars. A threshold level given by the program, of between the default 28 and 8 was set up depending on the quality of the photomicrograph during image processing and analysis circles to convert images to binary form. A maximum of five conditional smoothing circles were used to achieve clean individual standing fringes. These individual fringes were further enhanced by removing nodes noise, branches (Y and T shapes). Overlapping fringes and those that touched the edges of the image were removed using trimming tools (Sharma *et al.*, 1999:1203; Mathews *et al.*, 2010:1461; Van Niekerk *et al.*, 2008:290). The trimming action included manual noise rejection by using the eraser tool in the software to generate clean images with individual standing lattice fringes.

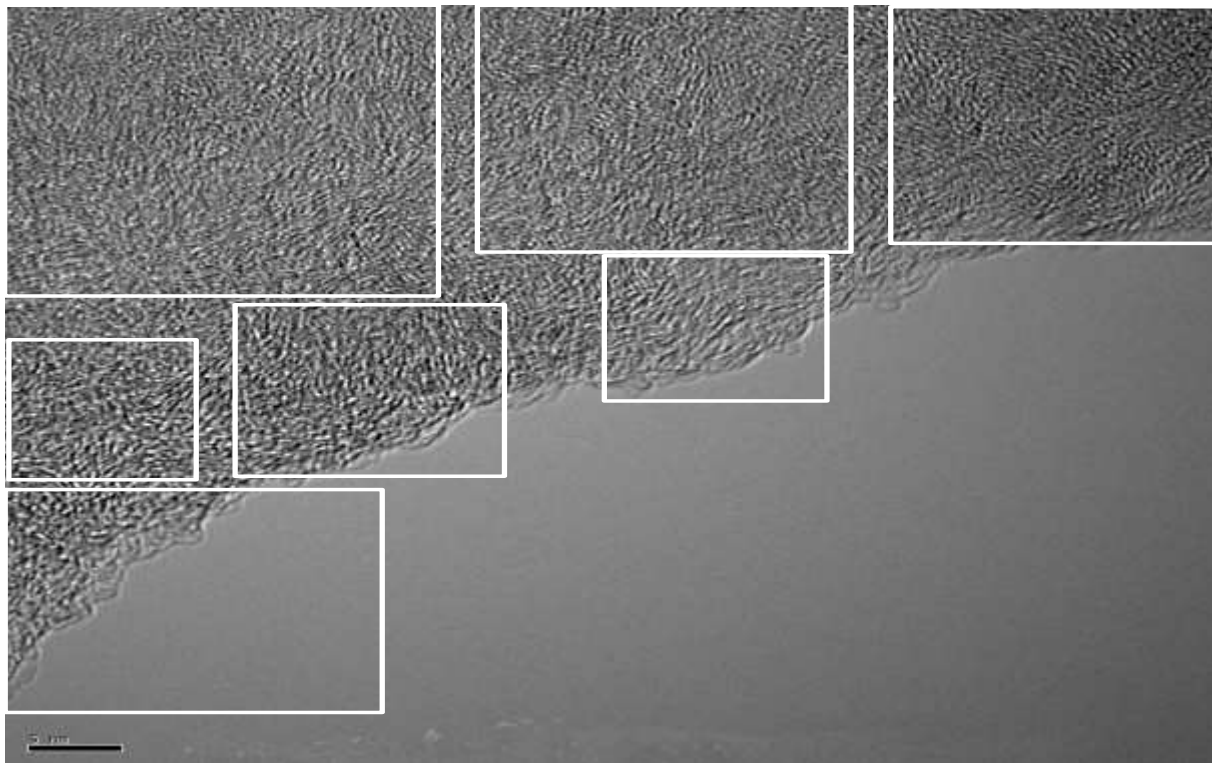


Figure 4-1. Dissections showing cropped HRTEM images.

### 4.3.3 Computational requirements and molecular modelling procedure

The construction of atomistic models was performed with classical mechanics programs in the Accelrys Material Studio<sup>®</sup> software (version 6.0) using both the North-West University's Laboratory for Advanced Molecular Modelling (LAMM) in Potchefstroom and the National Centre for High Performance Computing (CHPC) facility in Cape Town. The techniques used included the molecular mechanics and molecular dynamics for structural constructions and relaxations and the Materials Visualiser provided the tools required to construct, manipulate, view, and analyse the graphical models of coal char molecules, including the ability to develop spreadsheets. The Amorphous Cell module was used to generate layered structures of char models in a 3D periodic cell. The Forcite module is an advanced classical molecular mechanics tool in the Material Studio<sup>®</sup> that was used to determine reliable geometry optimisation of molecules (Musa *et al.*, 2012:176) and the 3D molecular systems of coal chars. Forcite also offered a

## CHAPTER 4: LARGE-SCALE MOLECULAR MODELLING OF CHARs

---

molecular dynamics task to simulate how the atoms in the 3D char structures will move under the influence of computed forces. These modules offered the SMART algorithm and DREIDING force field during the entire classical modelling process over 100 000 iterations. The perspective in DREIDING is to apply general force constants and geometric considerations centred on simple hybridisation factors rather than separate force constants and geometric considerations in respect with the particular combination of atoms affected in the bond, angle, or torsion conditions (Mayo *et al.*, 1990:8897). Consequently, all bond distances are calculated from atomic radii, while there is a single force constant each for bonds, angles, and inversions and only six different values for torsional barriers (Mayo *et al.*, 1990:8897). Parameters are described for all likely mixtures of atoms and new atoms can be added to the forcefield rather easily. The expression for DREIDING energy is represented by Equation (4.1) (Niekerk and Mathews, 2010:73).

$$E = E_B + E_A + E_T + E_I + E_{vdw} + E_Q + E_{hb} \quad (4.1)$$

where:  $E_B$  = bond stretch energy,  $E_A$  = bond-angle bend energy,  $E_T$  = dihedral angle torsion energy,  $E_I$  = inversion energy,  $E_{vdw}$  = van der Waals energy,  $E_Q$  = electrostatic energy and  $E_{hb}$  = hydrogen bond energy.

The density of constructed char models on ash free basis was adjusted to match the experimental helium density results (Castro-Marcano *et al.*, 2012:35). Molecular dynamics simulations using the Forcite module were executed on the 3D periodic molecular systems of chars over 20 annealing cycles. A thermodynamic ensemble of constant normal pressure and temperature (NPT) was selected at a time interval of 1.0 fs. The periodic cell was allowed to experience annealing cycle starting at 25 °C and reaching 1000 °C at the mid-point of each cycle at a pressure of 3.0 GPa. All calculations were performed using thermodynamic ensemble of Berendsen (Matsubayashi *et al.*, 2012:15578). A Forcite Anneal Task was used to search for a relaxed structure. Here a few frames including those with desired densities and upper and lower densities were individually assigned to Forcite Annealing calculations at the

## CHAPTER 4: LARGE-SCALE MOLECULAR MODELLING OF CHARs

---

same temperature settings used in dynamics calculations, but different pressure settings. The calculations ended on a structure with a density that matched the experimental helium density.

The aromaticity of char models was matched with the aromaticity values from the XRD experiments and NMR parameters. The identification and assignment of a characteristic forcefield for each atom were both manual and by default. The forcefield type of each atom was calculated with a revised polymer consistent forcefield (PCFF) (Peng *et al.*, 2010:1501; Sun, 1998:7338) and the process included manual assignment of forcefield to selected atoms. PCFF is associated with the consistent species of forcefields that are intimately connected second-generation forcefields. These forcefields were parameterised against a wide-ranging experimental observables for organic compounds comprising H, C, N, O, S, P, halogen atoms and ions, alkali metal cations, and numerous biochemically significant divalent metal cations.

### 4.4 Results and Discussion

The results were extracted from a full presentation in Chapter 3 of this thesis.

#### 4.4.1 Petrographic analyses

The density separation experiments upgraded the run-of-mine coal sample from Witbank coalfield to 85% inertinite by volume and on visible mineral matter basis. This sample, together with the corresponding chars, was defined as inertinite-rich in this investigation. In the same way, the coal sample from Waterberg coalfield was cleaned to 93% vitrinite and was regarded as vitrinite-rich, including chars derived from it. The vitrinite random reflectance measurements were 0.79 and 0.69% for the inertinite- and vitrinite-rich coals, respectively. Therefore, these coals were classified as bituminous,

## CHAPTER 4: LARGE-SCALE MOLECULAR MODELLING OF CHARs

---

Medium Rank C in accordance with ISO standard 11760 (2005) (ISO, 2005:9; Oboirien *et al.*, 2011:735).

### 4.4.2 Proximate and ultimate analysis

The ultimate analyses results on dry ash-free basis are presented in Table 4-1. The carbon contents of the inertinite-rich and vitrinite-rich chars generated at 1000 °C were 95.9% and 94.1% on daf, respectively. These chars had hydrogen and oxygen contents of 0.8% and 1.0%, respectively. The atomic H/C ratio of the inertinite-rich chars was 0.10 and for the vitrinite-rich chars was 0.12, while the atomic O/C ratios for the inertinite- and vitrinite-rich chars were respectively 0.01 and 0.02. The atomic H/C ratio is related to the aromaticity of the particles (Davis *et al.*, 1995:31). The lower the H/C ratio, the higher the aromaticity and the more polycondensed is the sample. These low values indicate a highly aromatic structure with very little to no aliphatic groups and highly polycondensed.

Table 4-1. Proximate and ultimate analysis of parent coal and char

Compound	Ash %	VM %	FC %	C	H	O (by diff.)	N	S	H/C	O/C
	Proximate analyses (db)									
<u>Coal</u>										
Inertinite-rich	0.5	24.7	74.8	83.4	4.4	7.5	2.1	2.6	0.63	0.07
Vitrinite-rich	0.5	36.7	62.8	80.0	5.4	8.2	1.7	4.8	0.80	0.08
<u>Char at 1000 °C</u>										
Inertinite-rich char	1.7	1.4	96.9	95.9	0.8	0.9	2.0	0.4	0.10	0.01
Vitrinite-rich char	1.7	3.0	95.3	94.1	1.0	2.6	1.6	0.7	0.12	0.02

db = dry basis, daf = dry ash-free basis, FC = fixed carbon

### 4.4.3 Skeletal density

The true density of 1000 °C inertinite- and vitrinite-rich chars was 1.87 and 1.82 g cm<sup>-3</sup>, respectively.

### 4.4.4 Solid-state <sup>13</sup>C nuclear magnetic resonance (NMR)

The <sup>13</sup>C NMR spectra of the parent coal samples and their corresponding char samples generated at 1000 °C are given in Figure 4-2. The spectra exhibit two broad characteristic peaks (Van Niekerk *et al.*, 2008:290; Perry *et al.*, 2000b:2313). The prominent peak is associated with carbon in the aromatic region and is represented between 90 ppm and 240 ppm in the spectra. The second peak is represented between 0 ppm to 90 ppm and is associated with the carbon in the aliphatic region. The aromatic peaks in the spectra of parent coals and chars retained nearly the same shape and height, respectively. However, the spectra for the chars exhibited extensive line-broadening in the aromatic region (Solum *et al.*, 2001:961) and may be attributed to the formation of aromatic free radicals (Perry *et al.*, 2000b:2313), which began to change the relaxation behaviour of aromatic carbons (Perry *et al.*, 2000b:2313). This extensive line-broadening phenomenon usually prevents the accurate calculation of structural and lattice parameters, restricting the results to aromaticity ( $f_a$ ) values only. The aliphatic peaks of the chars appear to diminish, leaving an enriched aromatic fraction that is probably responsible for the similarity between these two chars, as corroborated by the increasing similarity of the atomic contents and ratios.

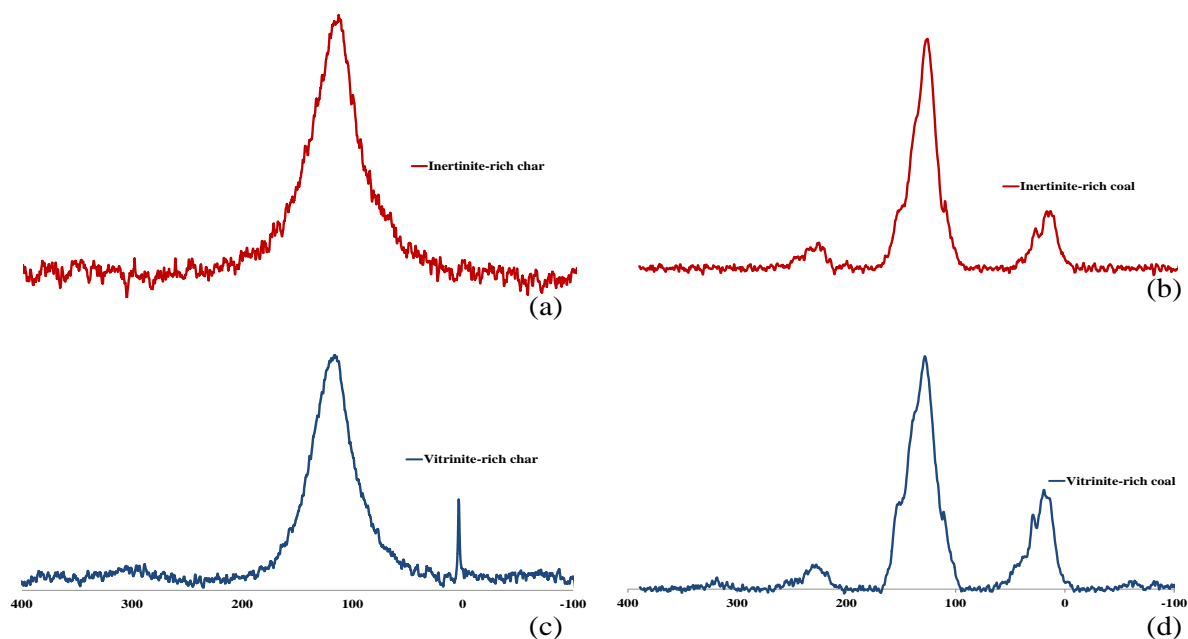


Figure 4-2. The  $^{13}\text{C}$  NMR spectra of the inertinite- and vitrinite-rich chars generated at 1000 °C ((a) and (c), left-hand side) and their corresponding parent coals ((b) and (d), right-hand side).

The lack of aliphatic functionality was confirmed by the very low atomic H/C ratios, indicating highly aromatic molecular structures. The CP-MAS showed that inertinite-rich parent coal was more aromatic (75%) than the vitrinite-rich coal (67%), as also observed by Van Niekerk *et al.* (Van Niekerk *et al.*, 2008:290) on similar South African coals. Single-pulse dipolar-dephasing experiment (SPE-DD) showed that the aromaticity values of the chars generated from the inertinite-rich coals and the vitrinite-rich coals were 100%, respectively. An attempt to calculate the mole fraction of aromatic bridgeheads ( $X_b$ ) values of the chars, from which the cluster size in terms of the number of aromatic carbons per cluster could be determined, showed that inertinite-rich chars had larger aromatic clusters than vitrinite-rich chars. However, the enormous size of the respective clusters was likely unrealistic due to the line-broadening phenomenon (Perry *et al.*, 2000a:2313; Solum *et al.*, 2001:961).

### 4.4.5 X-ray diffraction (XRD)

The diffractograms for the de-ashed chars and parent coals are shown in Figure 4-3, where three distinct peaks of the broad (002), (10) and (11) can be seen. The peak (002) in the low-angle zone relates to the stacking of the graphitic basal planes in char crystallites (Zhang *et al.*, 2008:3213). The other two peaks in the higher angle region, designated as (10) and (11) are ascribed to the graphite-like structure in char crystallites (Zhang *et al.*, 2008:3213). The sharper, narrower and more intense the peaks (002) and (10) on XRD spectra indicate more ordered char structure (Zhang *et al.*, 2008:3213). The demineralisation/de-ashing conducted on the samples reduced the amount of mineral matter/ash since a substantial decrease in the intensity of many peaks was associated with amount of mineral matter/ash in coal and chars (Van Niekerk *et al.*, 2008:290; Sharma and Wadhwa, 1997:29; Lu *et al.*, 2001:1821). It was found that both the inertinite- and vitrinite-rich chars had more ordered structures than the corresponding parent coals, but with more substantial transformations for the vitrinite-rich particles. Figure 4-3(a) shows that the difference between the peaks for inertinite- and vitrinite-rich chars was smaller compared with the parent coals (Figure 4-3(b)), due to the apparent similarity between these chars with these techniques. Table 4-2 shows the structural parameters extracted from the diffractograms. The aromatic layer stacking height ( $L_c$ ), interlayer spacing ( $d_{002}$ ) and average number of aromatic layers ( $N_{ave}$ ) showed small increases when compared with their parent coals. The difference in these values between the inertinite- and vitrinite-rich chars was small, indicating a remarkable similarity between these chars using this technique. The crystallite diameter ( $L_a$ ) of both the inertinite- and vitrinite-rich chars nearly doubled when compared with the parent coals. The difference in  $L_a$  between the inertinite- and vitrinite-rich chars was significant and the larger magnitudes were associated with the inertinite-rich chars. In summary, the XRD results showed that the chars generated from inertinite- and vitrinite-rich coals were remarkably similar in crystal structure. However, the  $L_a$  was the major property that distinguished the two chars.

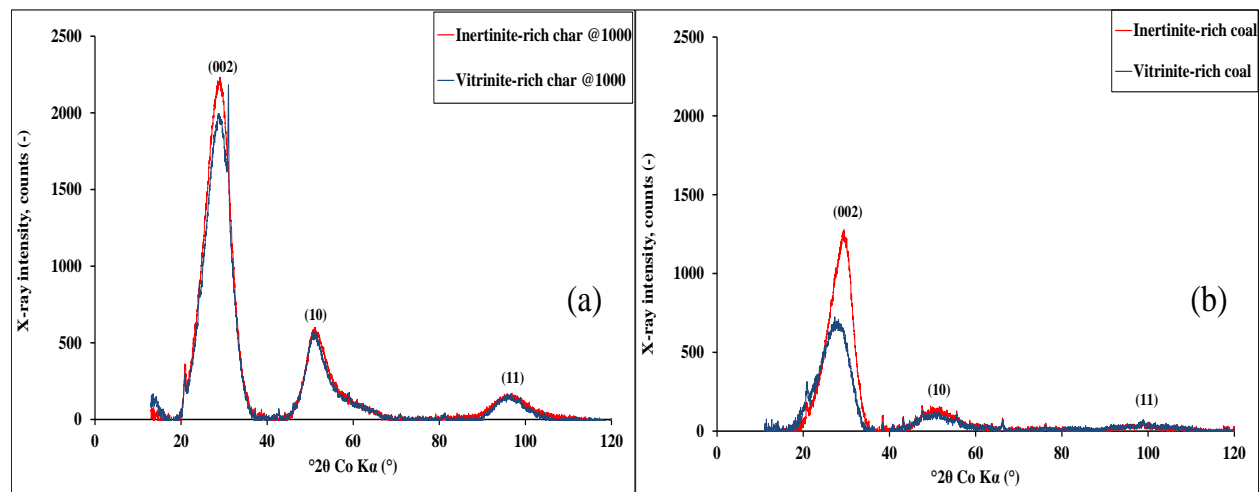


Figure 4-3. Baseline corrected and smoothed XRD diffractograms of chars generated at 1000 °C ((a), left-hand side) and parent coals ((b), right-hand side).

Table 4-2. Summary of structural parameters extracted from the XRD diffractograms

Property / Sample ID	Inertinite-rich coal	Char @1000	Vitrinite-rich coal	Char @1000
Inter-layer spacing, $d_{002}$ (Å)	$3.499 \pm 0.016$	$3.493 \pm 0.006$	$3.519 \pm 0.016$	$3.508 \pm 0.017$
Crystallite height, $L_c$ (Å)	$12.74 \pm 0.37$	$12.19 \pm 0.33$	$13.89 \pm 0.18$	$11.76 \pm 0.24$
Ave. No. of aromatic layers, $N_{ave}$ (-)	$4.642 \pm 0.90$	$4.489 \pm 0.095$	$4.948 \pm 0.068$	$4.352 \pm 0.060$
Crystallite diameter, $L_a$ (10) (Å)	$15.58 \pm 0.73$	$37.61 \pm 2.32$	$16.36 \pm 0.77$	$30.74 \pm 0.77$
Crystallite diameter, $L_a$ (11) (Å)	$16.23 \pm 0.61$	$39.39 \pm 2.31$	$18.11 \pm 1.17$	$32.47 \pm 1.15$
Aromaticity $f_a$ (-)	$0.771 \pm 0.006$	$0.960 \pm 0.016$	$0.685 \pm 0.005$	$0.946 \pm 0.002$
Fraction of amorphous carbon $X_A$ (-)	$0.522 \pm 0.014$	$0.101 \pm 0.012$	$0.613 \pm 0.008$	$0.118 \pm 0.005$
Index of disorder, $IOD$ (-)	$0.614 \pm 0.010$	$0.122 \pm 0.015$	$0.712 \pm 0.005$	$0.152 \pm 0.006$

## 4.4.6 High-resolution transmission electron microscopy

The HRTEM results will be discussed in perspective with the construction and properties of large-scale molecular models of chars in the next sections.

### 4.5 Construction of 3D molecular models of chars

The construction of individual molecules was followed by geometry optimisation. A three dimensional (3D) amorphous cell was constructed and filled with these individual molecules. The distributions, concentrations, size and shapes of molecules were based on the HRTEM lattice fringe image analysis (Castro-Marcano *et al.*, 2012:35; Mathews *et al.*, 2010:1461), as described in Section (4.3.2) and which will be further discussed in the subsections below. These discussions include additional refinement of the molecules to account for different functional groups.

#### 4.5.1 The HRTEM and the aromatic skeleton of chars

Structurally, coal char (ash free basis) consists of polyaromatic hydrocarbons (PAHs) with a macromolecular network in which the hetero atoms such as O, N and S are dispersed (Chen *et al.*, 2010:2562). Various studies discovered that HRTEM is a successful technique to quantitatively examine the distribution of the aromatic layers in coal and chars (Niekerk and Mathews, 2010:73; Sharma *et al.*, 2000:1219; Mathews *et al.*, 2010:1461). In this investigation, the properties of the aromatic fraction of chars in terms of layer size were used as the core in the initial stages of char model constructions (Niekerk and Mathews, 2010:73). Image processing techniques (Sharma *et al.*, 1999:1203) were applied on the cropped images (Figure 4.4(a)) to produce the lattice fringes of the chars (Figure 4-4(b)).

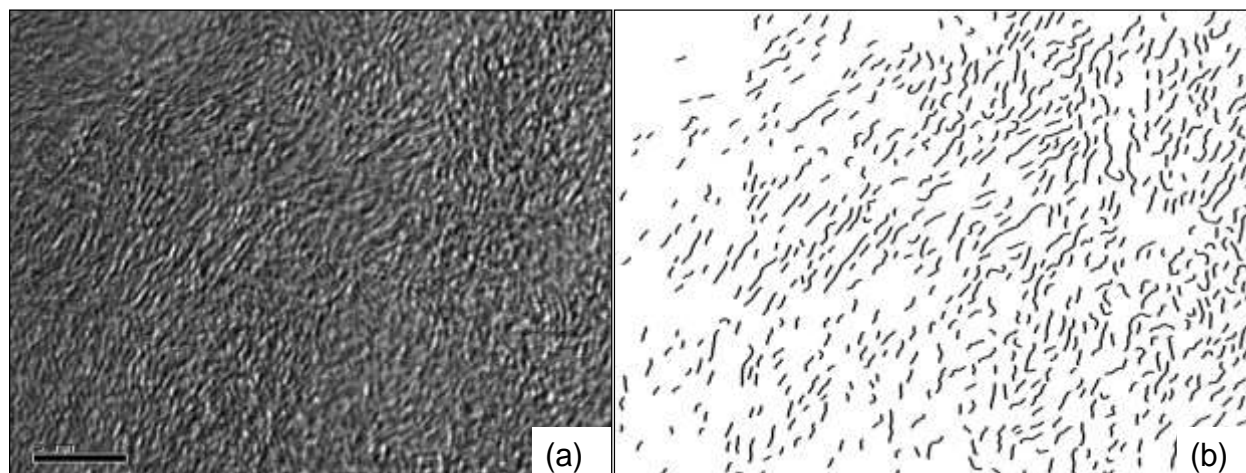


Figure 4-4. HRTEM results. HRTEM results. Cropped image ((a), left-hand side) and skeletonised image after image processing ((b), right-hand side).

Solum *et al.* took into account linear and circular catenations when determining the lattice structure for coal and soot using NMR (Solum *et al.*, 1989:187; Solum *et al.*, 2001:961; Niekerk and Mathews, 2010:73). In this study, however, an approach suggested by Mathews *et al.* was used to allocate aromatic sizes to the extracted HRTEM fringes (Niekerk and Mathews, 2010:73; Mathews *et al.*, 2010:1461). This approach assumes that the aromatic fringes adopt the shape of parallelograms (Niekerk and Mathews, 2010:73). Furthermore, this method took into account that the parallelogram-shaped aromatic sheets do not actually portray the aromatic units in coal, but merely a technique that can be used as an initial step to represent the diversity and distribution of the aromatic units present in coal and chars (Niekerk and Mathews, 2010:73). Figure 4-5 shows an example of a 21x21 aromatic fragment comprising two typical lengths. The maximum length (MaxL) and minimum length (MinL) for a sequence of parallelogram-shaped aromatic fringes (sequence ranging from 3x3 to 42x42 parallelogram fringe) were determined using molecular modelling (Niekerk and Mathews, 2010:73).

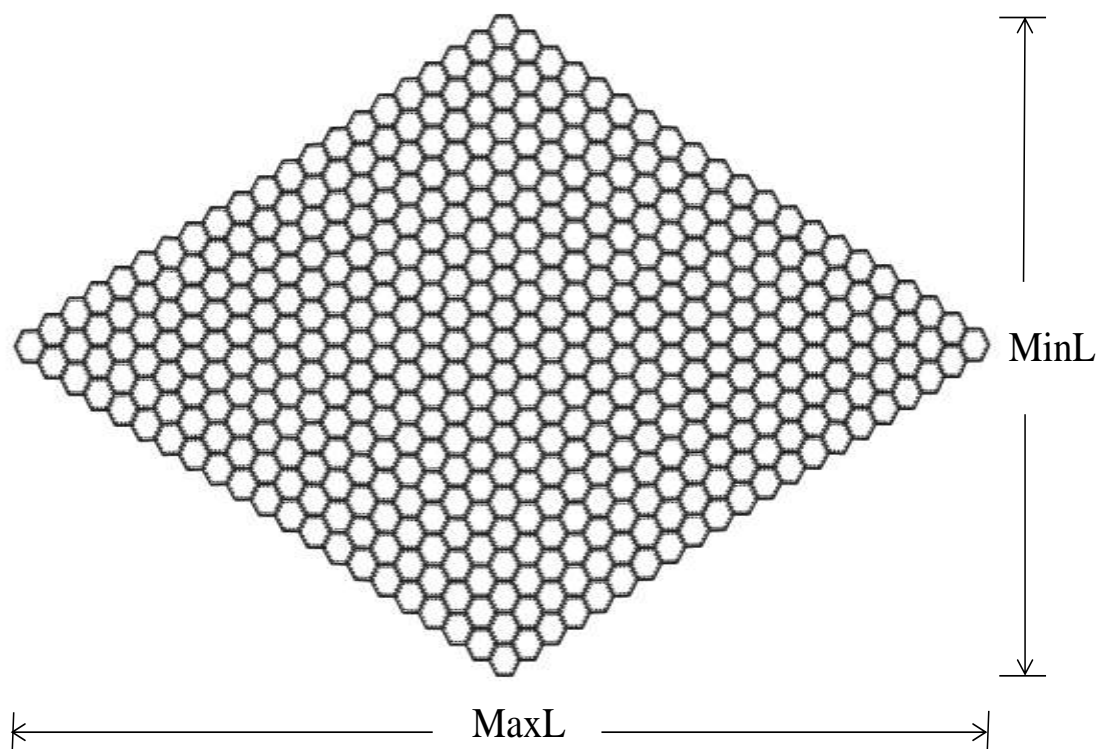


Figure 4-5. A 21x21 parallelogram-shaped aromatic fringe showing maximum (MaxL) and minimum (MinL) lengths.

A puzzle with assessing lattice fringes in HRTEM micrographs is the alignment of the fringes because it is not recognised whether a fringe is being seen from the MaxL or MinL edge view orientation (Niekerk and Mathews, 2010:73). To overcome this, the value of an average length was used to allocate an aromatic structure to each fringe (Niekerk and Mathews, 2010:73) (Table 4-3). All the lattice fringes  $<10\text{\AA}$  were assumed to be the noise and ignored. Fringes were analysed for length distribution using the parallelogram catenation method (Mathews *et al.*, 2010:1461; Fernandez-Alos *et al.*, 2011:1807), as shown in Figure 4-6.

The two chars consisted of the same aromatic molecules. This similarity between the chars was corroborated by the results of the ultimate analysis and XRD in terms of the atomic ratios and the aromatic layer stacking height ( $L_a$ ), interlayer spacing ( $d_{002}$ ) and

## CHAPTER 4: LARGE-SCALE MOLECULAR MODELLING OF CHARs

---

average number of aromatic layers ( $N_{ave}$ ), respectively. However, the two chars displayed the different distribution of aromatic fringes from the HRTEM, where the chars generated from inertinite-rich coals depicted a higher distribution of larger fringes when compared with the chars generated from the vitrinite-rich coals.

The results from the XRD and HRTEM techniques showed a reasonable agreement. The crystallite diameter,  $L_a(10)$ , of  $37.61 \pm 2.32 \text{ \AA}$  for the 1000 °C inertinite-rich chars, fell within the range of minimum-maximum length of the 11x11 aromatic fringes (27-45 Å). The  $L_a(10)$  of  $30.74 \pm 0.77 \text{ \AA}$  for the vitrinite-rich chars fell slightly above minimum-maximum length range of 17-28 Å. The  $L_a$  value for inertinite-rich chars was 3.8 nm compared with 3.1 nm of vitrinite chars based on peak (10) approximations.

## CHAPTER 4: LARGE-SCALE MOLECULAR MODELLING OF CHARs

---

Table 4-3. Allocation of parallelogram-shaped aromatic fringes from the HRTEM fringe results

Aromatic Sheet	MinL (Å)	MaxL (Å)	Average.L (Å)	Grouping (Å)
Benzene	2.5	2.9	2.7	<3
Naphthalene	2.9	5.1	4.0	<4.4
Anthracene	2.9	7.3	5.1	<5.9
2X2	4.9	7.1	6.0	5.9.0-9.9
3X3	7.4	11.3	9.3	10.0-14.9
4X4	9.8	15.5	12.7	15.0-19.9
5X5	12.3	19.8	16.0	20.0-24.9
6X6	14.7	24.0	19.4	25.0-29.9
7X7	17.2	28.3	22.7	30.0-34.9
8X8	19.6	32.5	26.1	35.0-39.9
9X9	22.1	36.8	29.4	40.0-44.9
10X10	24.5	41.0	32.8	45.0-49.9
11X11	27.0	45.2	36.1	50.0-54.9
12X12	29.4	49.5	39.5	55.0-59.9
13X13	31.9	53.7	42.8	60.0-64.9
14X14	34.3	58.0	46.2	65.0-69.9
15X15	36.8	62.2	49.5	70.0-74.9
16X16	39.2	66.5	52.8	75.0-79.9
17X17	41.7	70.7	56.2	80.0-84.9
18X18	44.1	74.9	59.5	85.0-89.9
19X19	46.6	79.1	62.8	90.0-94.9
20X20	49.0	83.3	66.2	95.0-99.9
21X21	52.5	90.3	71.4	100.0-104.9
22X22	54.6	94.2	74.4	105.0-109.9
23X23	57.1	98.5	77.8	110.0-114.9
24X24	60.0	103.5	81.7	115.0-119.9
25X25	61.9	107.0	84.5	120.0-124.9
26X26	64.8	112.0	88.4	125.0-129.9
27X27	67.1	116.0	91.5	130.0-134.9
28X28	69.8	120.7	95.3	135.0-139.9
29X29	74.6	128.4	101.5	140.0-144.9
30X30	74.5	129.1	101.8	145.0-149.9
31X31	77.1	133.6	105.3	150.0-154.9
32X32	79.5	137.7	108.6	155.0-159.9
33X33	81.9	141.9	111.9	160.0-164.9
34X34	86.5	149.4	118.0	165.0-169.9
35X35	88.8	153.4	121.1	170.0-174.9
36X36	91.0	157.3	124.1	175.0-179.9
37X37	92.0	159.3	125.6	180.0-184.9
38X38	96.1	166.1	131.1	185.0-189.9
39X39	99.4	171.6	135.5	190.0-194.9
40X40	101.0	174.6	137.8	195.9-199.9
41X41	103.5	178.8	141.2	200.0-204.9
42X42	107.8	185.1	146.5	205.0-209.9

## CHAPTER 4: LARGE-SCALE MOLECULAR MODELLING OF CHARs

Various studies found that  $L_a$  governs the reaction of carbon active sites found on the crystallite edges of carbonaceous material since the crystallite growth was generally related with the loss of active sites (Zhang *et al.*, 2008:3213; Jones *et al.*, 1999:1737). Figure 4-7 shows 21 parallelogram-shaped aromatic models of 3x3 to 23x23 fringes from the HRTEM, which were used in different and suitable combinations during the model constructions of chars.

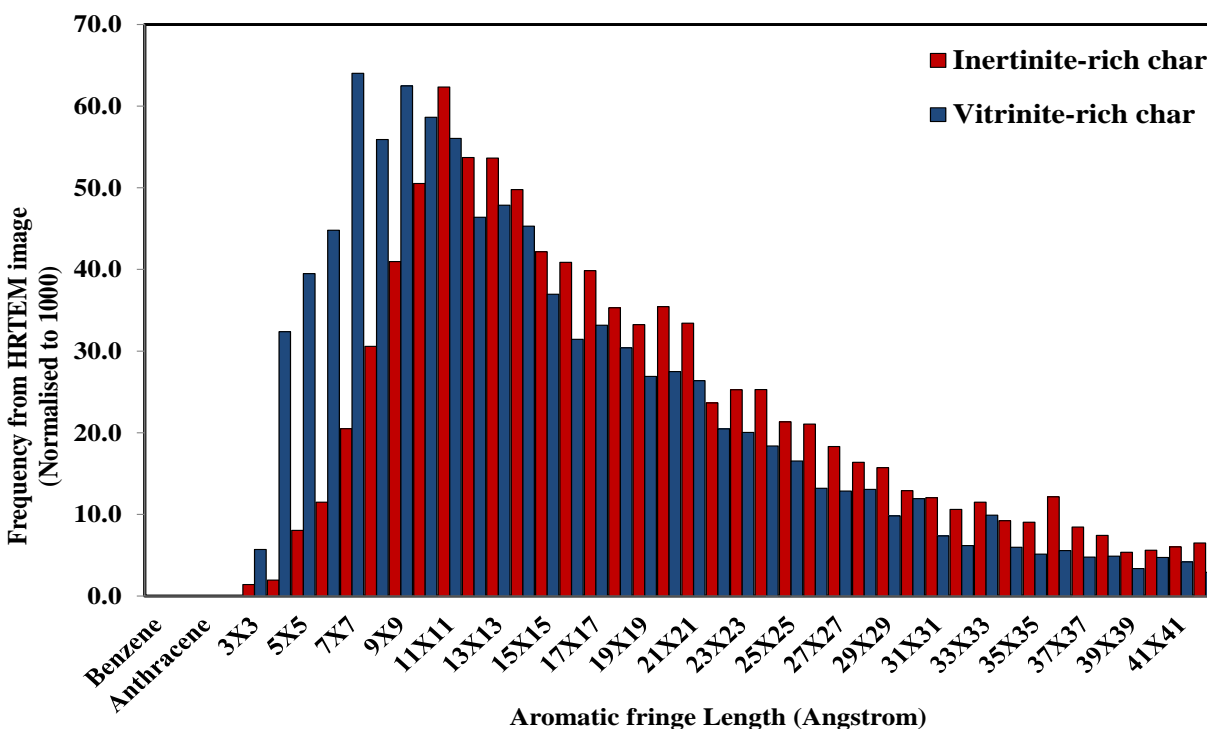


Figure 4-6. Aromatic fringe length distributions from the HRTEM.

### 4.5.2 Trimming

Different sizes of the parallelogram-shaped aromatic fringes of chars were trimmed to produce geometric representations according to the shapes of the lattice fringes of chars as obtained from the HRTEM image processing results.

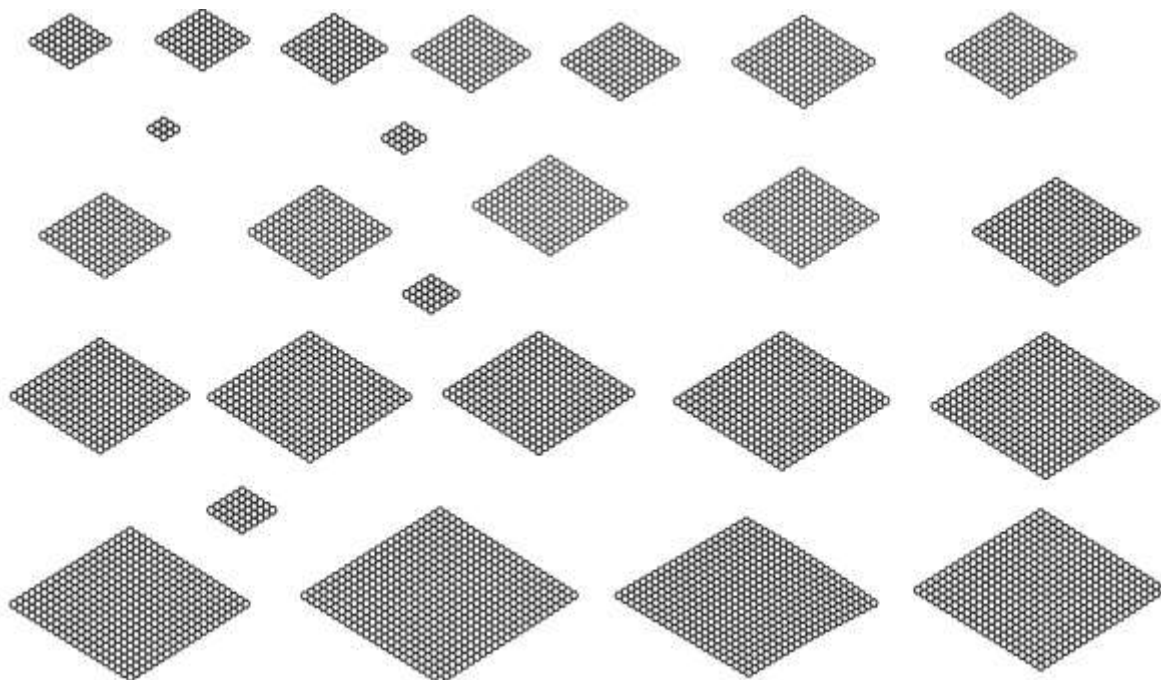


Figure 4-7. An example of 25 aromatic fringes of length distributions from the HRTEM, used during the model constructions.

The technique of correcting the organic molecules to match with the desired properties in molecular systems involves trimming of length of existing molecules, cutting and joining of molecules, degradation of molecules or generation of new set of molecules (Weimershaus *et al.*, 2013:90; Nelson *et al.*, 1997:628). Trimming often modifies the geometric representation of organic molecules by shortening the length of carbon chains (Heifetz and Eisenstein, 2003:179). Therefore, aromatic fringes were trimmed along the length and a random selection of 6-membered carbon rings was replaced with 5-membered carbons rings until the aggregate atom accounts matched with the ultimate analysis results. An example of 11x11 aromatic fringe that was trimmed into four different geometric representations is shown in Figure 4-8.

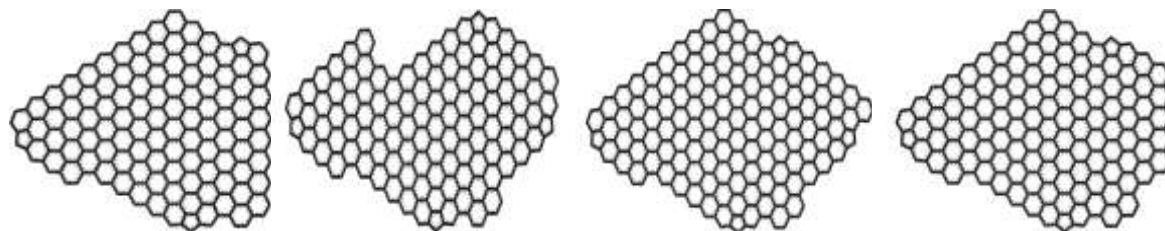


Figure 4-8. Example of geometric representations of char molecules after trimming an 11x11 aromatic fringe.

### 4.5.3 Hydrogen and oxygen functional atoms

Fletcher *et al.* studied the chemical structure of coal chars from the Sandia coal devolatilisation laboratory, where it was found that the attachments to aromatic clusters consisted of alkyl groups and oxygen functional groups including ethers (Fletcher *et al.*, 1992:643). Charland *et al.* used the thermogravimetry with Fourier transform infrared analysis (TG-FTIR) to determine the amount of organic oxygen in a collection of coals of varying rank and found that the functional groups resulting in CO are remarkably stable above 600 °C and involve ether-type oxygen (Charland *et al.*, 2003:211). Chen *et al.* used the semi-empirical molecular orbital calculations on carbon material and found that structures with carbonyl terminations gave rise to more stable oxygen complexes in gasification reactions (Chen *et al.*, 1993:2835). Zhou *et al.* characterised the oxygen surface complexes of carbon nanofibres with FTIR and X-ray photoelectron spectroscopy (XPS) and found that the carbonyl-type oxygen complexes only start to decompose after 780 °C (Zhou *et al.*, 2007:785). In this study the adjustments of hydrogen and oxygen contents were, therefore, achieved by the introduction of the ether-type oxygen in the 5-membered rings and the termination of selected 6-member carbon rings with carbonyl-type oxygen. Figure 4-9(a) shows joint molecules derived from 8x8 and 3x3 aromatic fringes, which comprise a total of three oxygen functional atoms of one carbonyl-type, one closed ether-type and one ether bridge-type. Figure 4-9(b) shows a molecule originating from 14x14 aromatic fringe, which consists of three carbonyl and two closed ether types of oxygen.

### 4.5.4 Nitrogen and sulphur functional atoms

The nitrogen functionalities in the char models were added as pyridinic nitrogen atoms in selected 6-membered rings located at the edges of the char molecules and as quaternary nitrogen atoms in the basal plane. This was in accordance with the work of Pels *et al.*, which showed that in coals that have experienced severe pyrolysis conditions, all nitrogen is eventually present in these two forms (Pels *et al.*, 1995:1641). Kelemen *et al.* also found that quaternary and pyridinic nitrogen forms were the dominant forms in severely pyrolysed chars derived from the Argonne Premium Coal Sample Program, while performing the XPS experiments (Kelemen *et al.*, 1998:159). In essence, the dominant pyrrolic nitrogen in parent coals is completely converted into quaternary and pyridinic nitrogen during pyrolysis (Zhang *et al.*, 2010:240). Accordingly, the molecule shown in Figure 4-9(a) consists of two pyridinic and one quaternary nitrogen.

A single thiophenic sulphur is represented in Figure 4-9(b). Lui *et al.* studied the sulphur transformation of two Chinese coals during pyrolysis in a fixed-bed reactor under nitrogen and hydrogen atmospheres at temperatures ranging from 400 to 700 °C, using XPS (Liu *et al.*, 2007:360).

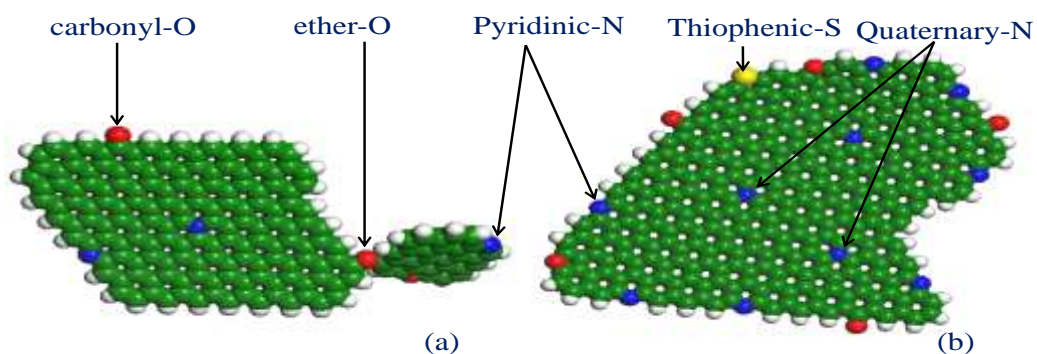


Figure 4-9. Cross-linked ((a), left-hand side) and individual ((b), right-hand) molecules with their functional atoms. Green = C and white = H.

## CHAPTER 4: LARGE-SCALE MOLECULAR MODELLING OF CHARs

---

It was found that sulphur in the thiophenic form remained present in the high-rank coal up to the maximum pyrolysis temperature under a nitrogen atmosphere, indicating that the sulphur could transfer from the bulk to the char surface during pyrolysis. Zhang and Telfer carried out a similar experiment on low-rank Australian coals and found that the thiophenic sulphur forms were too complex to decompose even at temperatures exceeding 800 °C (Zhang and Telfer, 1998:1703). Therefore, the atomic sulphur content of the chars was accounted for by replacing the carbon atoms on selected 5-member rings with thiophenic-type sulphur atoms.

### 4.6 Evaluation of large-scale molecular models of chars

During the model construction process, several Perl scripts within Material Studio were adapted and modified from previous work (Niekerk and Mathews, 2010:73; Castro-Marcano *et al.*, 2012:35) to aid in the evaluation and refinement of chemical structural parameters, e.g. elemental composition, XRD aromaticity and skeletal density. These refinements were followed by 3D structural reconstructions and intensive equilibrations as described in Section (4.3.3). However, the evaluation of the distance between successive char molecules ( $d_{002}$ ), average number of char molecules per stack and classes of heteroatoms are regarded as a test of the model since these parameters were not controlled during model construction (Castro-Marcano *et al.*, 2012:35). Using manual measurements, it was found that the  $d_{002}$  ranged between 3.41-3.62Å. These values compared well with the XRD's for both the inertinite- and vitrinite-rich chars (3.49-3.50Å). A good comparison was also found between the average number of molecules per stack measured manually on the large-scale char models (Figure 4-10) and the XRD values.

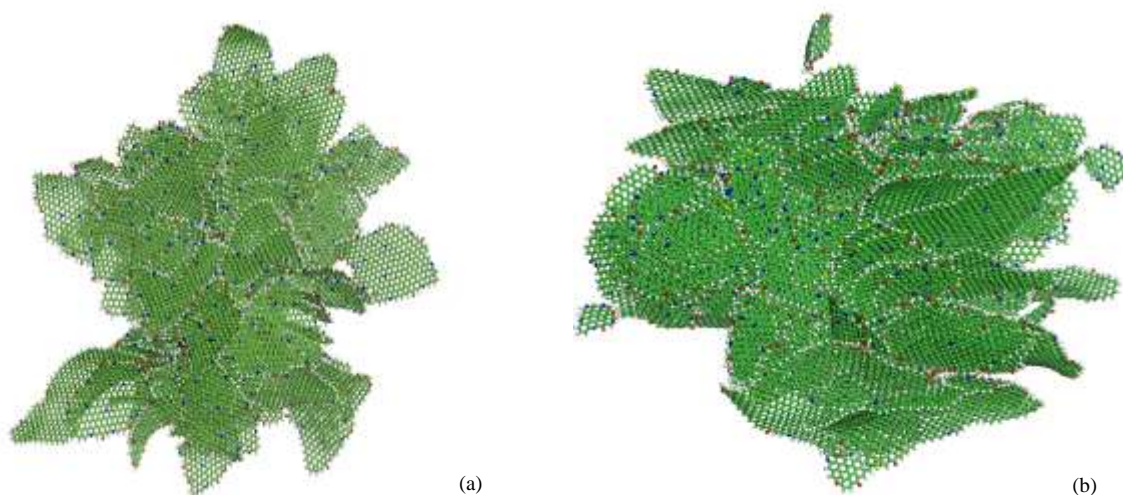


Figure 4-10. Geometry optimised and annealed 3D molecular models of inertinite-rich chars ((a), left-hand side) and vitrinite-rich chars ((b), right-hand side). Green = C, white = H, red = O, blue = N and yellow = S.

The aromaticity results for the inertinite-rich char model (98%) and the vitrinite-rich char model (96%) matched exactly that of XRD experiments. However, the NMR data indicated a 100%  $f_a$  values because NMR detects medium- to high-temperature chars (>700 °C) as ~100% aromatic. The XRD values were close to 100%. The stabilisation energy was used to evaluate the appropriateness of the molecular assembly. The stabilisation energies for the models were determined by calculating the sum of all the energies of the individual fragments used to build the 3D amorphous model and then subtracting the total energy of the final constructed char model according to Equation (4.2) (Niekerk and Mathews, 2010:73).

$$\text{Stabilisation energy} = \sum E_{\text{molecules}} - E_{\text{Final model}} \quad (4.2)$$

The calculated sum of energies of all the molecules ( $\sum E_{\text{molecules}}$ ) for the inertinite- and vitrinite-rich char models was 177902 kcal.mol<sup>-1</sup> and 181846 kcal mol<sup>-1</sup>, respectively. The corresponding constructed model energies ( $E_{\text{Final model}}$ ) were 166797 kcal mol<sup>-1</sup> for the inertinite-rich char model and 166534 kcal.mol<sup>-1</sup> for the vitrinite-rich char model.

## CHAPTER 4: LARGE-SCALE MOLECULAR MODELLING OF CHARs

---

Thus, the stabilisation energies were 11105 kcal mol<sup>-1</sup> for the inertinite-rich char model and 15312 kcal mol<sup>-1</sup> for the vitrinite-rich char model. A molecular system is regarded as stable if the stabilisation energy in Equation 4.2 yielded a positive value. Indeed a positive value of stabilisation energy for each char model was obtained, confirming that the large-scale 3D char structures were stable. The characterisation of the two char models using Perl script calculations showed that the inertinite-rich char model comprised 42929 atoms contained in 106 molecules, while the vitrinite-rich char model was made up of 44315 atoms held by 185 molecules (Table 4-4).

Table 4-4. Comparison between the inertinite- and vitrinite-rich char models

Property	Inertinite-rich char model	Vitrinite-rich char model
Total molecules	106	185
Total atoms	42929	44315
Total C	37585	37830
Total H	3939	4725
Total O	520	785
Total N	830	850
Total S	55	125
H/C atomic ratio	0.10	0.12
O/C atomic ratio	0.01	0.02
N/C atomic ratio	0.02	0.02
S/C atomic ratio	0.001	0.003
$f_a$ (%)	98	96
Helium density (g.cm <sup>-3</sup> )	1.87	1.82

These results show a remarkable similarity between the inertinite- and vitrinite-rich char models when described in terms of the number of atoms but also a significant difference in terms of the total number of molecules. Consequently, the size of the molecules present in each char model was the distinguishing property. Other Perl scripts

## CHAPTER 4: LARGE-SCALE MOLECULAR MODELLING OF CHARs

calculations revealed that the atomic ratios of the inertinite-rich char model in terms of H/C and O/C (0.10 and 0.01, respectively) were similar to those of vitrinite char model (0.12 and 0.02). Calculations for the aromaticity of the two char models showed that the aromaticity of 98% for the inertinite-rich char model was much closer to the 96% for the vitrinite-rich char model. These values matched with the XRD results and were close to the approximate value of 100%  $f_a$  estimated by the NMR technique. Furthermore, the molecular dynamics simulations on the 3D periodic cells of the respective char models resulted in the relaxed structures, where the final densities of the inertinite- and vitrinite-rich char models were 1.87 g.cm<sup>-3</sup> and 1.82 cm<sup>-3</sup>, respectively, comparing well with the experimental values (Table 4-5). The total number of carbon atoms in the char models was normalised to 1000 in order to compare the experimental and modelling results in terms of the elemental analysis (Table 4-5). This data was used to predict the chemical formulae of the inertinite-rich char (C<sub>1000</sub>H<sub>105</sub>O<sub>14</sub>N<sub>22</sub>S<sub>1</sub>) and vitrinite-rich char (C<sub>1000</sub>H<sub>125</sub>O<sub>21</sub>N<sub>22</sub>S<sub>3</sub>) models.

Table 4-5. Model and experimental results for the inertinite- and vitrinite-rich chars with C normalised to 1000

Property	Inertinite char		Vitrinite char	
	Experimental	Model	Experimental	Model
Total molecules		106		185
Total atoms	1130	1142	1162	1171
Total C	1000	1000	1000	1000
Total H	104	105	123	125
Total O	7	14	21	21
Total N	18	22	15	22
Total S	1	1	3	3
H/C atomic ratio	0.10	0.10	0.12	0.12
O/C atomic ratio	0.01	0.01	0.02	0.02
N/C atomic ratio	0.02	0.02	0.02	0.02
S/C atomic ratio	0.001	0.001	0.003	0.003
Helium density (g.cm-3)	1.87	1.87	1.82	1.82
$f_a$ (%) (from XRD)	98	98.0	96	96.0
Formula	C <sub>1000</sub> H <sub>104</sub> O <sub>7</sub> N <sub>18</sub> S <sub>1</sub>	C <sub>1000</sub> H <sub>105</sub> O <sub>14</sub> N <sub>22</sub> S <sub>1</sub>	C <sub>1000</sub> H <sub>123</sub> O <sub>21</sub> N <sub>15</sub> S <sub>3</sub>	C <sub>1000</sub> H <sub>125</sub> O <sub>21</sub> N <sub>22</sub> S <sub>3</sub>

### 4.7 Conclusions

Characterization of chars derived from South Africa's inertinite-rich and vitrinite-rich Gondwana coals formed in the Permian Age was carried out to construct detailed, large scale molecular structures. The data used for the model constructions was derived from the ultimate analysis, helium density measurements, XRD and HRTEM analyses. The inertinite-rich char model comprised 106 molecules constructed from a total of 42929 atoms, while the vitrinite-rich char model was made up of 185 molecules consisting of a total of 44315 atoms. It was found that both the inertinite-rich char model and vitrinite-rich char model were similar in terms of the number of atoms but different in terms of total number of molecules. Consequently, the size of the molecules was the major property that distinguished the two char models. The atomic ratios of the inertinite-rich char model in terms of H/C and O/C (0.10 and 0.01, respectively) were similar to those of vitrinite-rich char model (0.12 and 0.02). Moreover, the aromaticity results of 98% for the inertinite-rich chars and 96% for the vitrinite-rich chars also showed that the two char models were similar. The NMR data indicated that both char models should be approximately 100% aromatic because the NMR technique detects the medium- to high-temperature chars (>700 °C) as ~100% aromatic. However, this value compares well with the aromaticity of the constructed char models, which was close to 100%. Helium densities of inertinite and vitrinite char models were 1.87 and 1.82 g cm<sup>-3</sup>, respectively. The formula of inertinite char model was C<sub>1000</sub>H<sub>105</sub>O<sub>14</sub>N<sub>22</sub>S<sub>1</sub> and for the vitrinite char model was C<sub>1000</sub>H<sub>125</sub>O<sub>21</sub>N<sub>22</sub>S<sub>3</sub>. The physical and chemical properties of both the inertinite- and vitrinite-rich char models were in good agreement with the experimental data. These molecular char structures may have utility in exploring microstructure–reactivity relationships (Jones *et al.*, 1999:1737; Green *et al.*, 1984:589; Mathews *et al.*, 2011:718).

## CHAPTER 4: LARGE-SCALE MOLECULAR MODELLING OF CHARS

---

### Nomenclature

Symbol	Definition	Units
Å	Angstrom	Å
<i>CP-MAS</i>	Cross polarisation-magic angle spinning	-
$d_{002}$	Inter-layer spacing for a group of $N_{ave}$ parallel layers	Å
<i>DD</i>	Dipolar dephasing	-
$L_a$	Crystallite diameter	Å
$L_c$	Crystallite height	Å
$N_{ave}$	Average number of aromatic layers per carbon crystallite	-

### Greek symbols

Symbol	Definition	Units
$\theta$	Peak position / XRD angle of scan	radians
$\gamma$	Gamma band/peak	-
$\rho$	Skeletal/true density (of coals/chars)	$\text{g cm}^{-3}$

### Abbreviations

Acronym	Definition
<i>CP-MAS</i>	Cross polarisation-magic angle and spinning
HRTEM	High resolution transmission electron microscopy
<i>SPE</i>	Single pulse excitation
ss $^{13}\text{C}$ NMR	Solid state nuclear magnetic resonance spectroscopy
XRD	X-ray diffraction

## CHAPTER 4: LARGE-SCALE MOLECULAR MODELLING OF CHARs

---

### 4.8 References

- CAI, H. Y. and KANDIYOTI, R. 1995. Effect of changing inertinite concentration on pyrolysis yields and char reactivities of two South African coals. *Energy & Fuels*, 9, 956.
- CAIRNCROSS, B.; HART, R. J. and WILLIS, J. P. 1990. Geochemistry and sedimentology of coal seams from the Permian Witbank Coalfield, South Africa; a means of identification. *International Journal of Coal Geology*, 16, 309.
- CARLSON, G. A. 1992. Computer simulation of the molecular structure of bituminous coal. *Energy & Fuels*, 6, 771.
- CASTRO-MARCANO, F.; KAMAT, A. M.; RUSSO JR, M. F.; VAN DUIN, A. C. T. and MATHEWS, J. P. 2012. Combustion of an Illinois No. 6 coal char simulated using an atomistic char representation and the ReaxFF reactive forcefield. *Combustion and Flame*, 159, 1272.
- CASTRO-MARCANO, F.; LOBODIN, V. V.; RODGERS, R. P.; MCKENNA, A. M.; MARSHALL, A. G. and MATHEWS, J. P. 2012. A molecular model for Illinois No. 6 Argonne Premium coal: Moving toward capturing the continuum structure. *Fuel*, 95, 35.
- CHAN, M. L.; JONES, J. M.; POURKASHANIAN, M. and WILLIAMS, A. 1999. The oxidative reactivity of coal chars in relation to their structure. *Fuel*, 78, 1539.
- CHARLAND, J. P.; MACPHEE, J. A.; GIROUX, L.; PRICE, J. T. and KHAN, M. A. 2003. Application of TG-FTIR to the determination of oxygen content of coals. *Fuel Processing Technology*, 81, 211.
- CHEN, L.; YANG, J. and LIU, M. 2010. Kinetic modeling of coal swelling in solvent. *Industrial & Engineering Chemistry Research*, 50, 2562.
- CHEN, S. G.; YANG, R. T.; KAPTEIJN, F. and MOULIJN, J. A. 1993. A new surface oxygen complex on carbon: toward a unified mechanism for carbon gasification reactions. *Industrial & Engineering Chemistry Research*, 32, 2835.
- DAVIS, K. A.; HURT, R. H.; YANG, N. Y. C. and HEADLEY, T. J. 1995. Evolution of char chemistry, crystallinity, and ultrafine structure during pulverized-coal combustion. *Combustion and Flame*, 100, 31.
- DOCTOR, R. D. 1995. Fundamentals of coal combustion for clean and efficient use, L. Douglas Smoot, Elsevier, Amsterdam, The Netherlands (1993) 751 pages,. *Environmental Progress*, 14, F11.
- FAULON, J. L.; CARLSON, G. A. and HATCHER, P. G. 1993. Statistical models for bituminous coal: a three-dimensional evaluation of structural and physical properties based on computer-generated structures. *Energy & Fuels*, 7, 1062.
- FENG, B.; BHATIA, S. K. and BARRY, J. C. 2002. Structural ordering of coal char during heat treatment and its impact on reactivity. *Carbon*, 40, 481.
- FERNANDEZ-ALOS, V.; WATSON, J. K.; WAL, R. V. and MATHEWS, J. P. 2011. Soot and char molecular representations generated directly from HRTEM lattice fringe images using Fringe3D. *Combustion and Flame*, 158, 1807.
- FLETCHER, T. H.; SOLUM, M. S.; GRANT, D. M. and PUGMIRE, R. J. 1992. Chemical structure of char in the transition from devolatilization to combustion. *Energy & Fuels*, 6, 643.
- GREEN, A. E. S.; MEYREDDY, R. R. and PAMIDIMUKKALA, K. M. 1984. A molecular model of coal pyrolysis. *International Journal of Quantum Chemistry*, 26, 589.
- HATCHER, P. G.; FAULON, J. L.; WENZEL, K. A. and CODY, G. D. 1992. A structural model for lignin-derived vitrinite from high-volatile bituminous coal (coalified wood). *Energy & Fuels*, 6, 813.
- HATTINGH, B. B.; EVERSON, R. C.; NEOMAGUS, H. W. J. P.; BUNT, J. R.; VAN NIEKERK, D.; JORDAAN, J. H. L. and MATHEWS, J. P. 2013. Elucidation of the Structural and Molecular Properties of Typical South African Coals. *Energy & Fuels*, 27, 3161.

## CHAPTER 4: LARGE-SCALE MOLECULAR MODELLING OF CHARs

---

- HEIFETZ, A. and EISENSTEIN, M. 2003. Effect of local shape modifications of molecular surfaces on rigid-body protein docking. *Protein Engineering*, 16, 179.
- ISO 2005. Classification of coals. ISO 11760:2005 9.
- JONES, J. M.; POURKASHANIAN, M.; RENA, C. D. and WILLIAMS, A. 1999. Modelling the relationship of coal structure to char porosity. *Fuel*, 78, 1737.
- KELEMEN, S. R.; GORBATY, M. L.; KWIA TEK, P. J.; FLETCHER, T. H.; WATT, M.; SOLUM, M. S. and PUGMIRE, R. J. 1998. Nitrogen transformations in coal during pyrolysis. *Energy & Fuels*, 12, 159.
- LIU, F.; LI, W.; CHEN, H. and LI, B. 2007. Uneven distribution of sulfurs and their transformation during coal pyrolysis. *Fuel*, 86, 360.
- LU, L.; SAHAJWALLA, V.; KONG, C. and HARRIS, D. 2001. Quantitative X-ray diffraction analysis and its application to various coals. *Carbon*, 39, 1821.
- MATHEWS, J. P.; FERNANDEZ-ALSO, V.; DANIEL JONES, A. and SCHOBERT, H. H. 2010. Determining the molecular weight distribution of Pocahontas No. 3 low-volatile bituminous coal utilizing HRTEM and laser desorption ionization mass spectra data. *Fuel*, 89, 1461.
- MATHEWS, J. P.; HATCHER, P. G. and SCARONI, A. W. 1998. Devolatilization, a molecular modeling approach. *Preprint preparation. American Chemical Society. Division of fuel chemistry, Dallas, TX*
- MATHEWS, J. P.; HATCHER, P. G. and SCARONI, A. W. 2001. Proposed model structures for Upper Freeport and Lewiston-Stockton vitrinites. *Energy & Fuels*, 15, 863.
- MATHEWS, J. P.; VAN DUIN, A. C. T. and CHAFFEE, A. L. 2011. The utility of coal molecular models. *Fuel Processing Technology*, 92, 718.
- MATSUBAYASHI, A.; FUKUNAGA, K. and TANAKA, K. 2012. Metal ions/ion clusters transport in glassy polymer films: construction of multi-layered polymer and metal composite films. *Journal of Materials Chemistry*, 22, 15578.
- MAYO, S. L.; OLAFSON, B. D. and GODDARD, W. A. 1990. DREIDING: a generic force field for molecular simulations. *The Journal of Physical Chemistry*, 94, 8897.
- MUSA, A. Y.; JALGHAM, R. T. and MOHAMAD, A. B. 2012. Molecular dynamic and quantum chemical calculations for phthalazine derivatives as corrosion inhibitors of mild steel in 1M HCl. *Corrosion Science*, 56, 176.
- NARKIEWICZ, M. R. and MATHEWS, J. P. 2008. Improved low-volatile bituminous coal representation: Incorporating the molecular-weight distribution. *Energy & Fuels*, 22, 3104.
- NELSON, C. A.; VIDA VSKY, I.; VINER, N. J.; GROSS, M. L. and UNANUE, E. R. 1997. Amino-terminal trimming of peptides for presentation on major histocompatibility complex class II molecules. *Proceedings of the National Academy of Sciences*, 94, 628.
- NIEKERK, D. V. and MATHEWS, J. P. 2010. Molecular representations of Permian-aged vitrinite-rich and inertinite-rich South African coals. *Fuel*, 89, 73.
- NIP, M.; DE LEEUW, J. W. and CRELLING, J. C. 1992. Chemical structure of bituminous coal and its constituting maceral fractions as revealed by flash pyrolysis. *Energy & Fuels*, 6, 125.
- OBOIRIEN, B. O.; ENGELBRECHT, A. D.; NORTH, B. C.; DU CANN, V. M.; VERRY N, S. and FALCON, R. 2011. Study on the structure and gasification characteristics of selected South African bituminous coals in fluidised bed gasification. *Fuel Processing Technology*, 92, 735.
- PATRAKOV, Y. F.; KAMYANOV, V. F. and FEDYAEVA, O. N. 2005. A structural model of the organic matter of Barzas liptobiolith coal. *Fuel*, 84, 189.
- PELS, J. R.; KAPTEIJN, F.; MOULIJN, J. A.; ZHU, Q. and THOMAS, K. M. 1995. Evolution of nitrogen functionalities in carbonaceous materials during pyrolysis. *Carbon*, 33, 1641.
- PENG, Z.; YOU, H. and YANG, H. 2010. Composition-dependent formation of platinum silver nanowires. *ACS Nano*, 4, 1501.

## CHAPTER 4: LARGE-SCALE MOLECULAR MODELLING OF CHARs

---

- PERRY, S.; HAMBLY, E.; FLETCHER, T.; SOLUM, M. and PUGMIRE, R. 2000a. Solid-state carbon-13 NMR characterization of matched tars and chars from rapid coal devolatilization. *Proceedings of the Combustion Institute*, 28, 2313.
- PERRY, S. T.; HAMBLY, E. M.; FLETCHER, T. H.; SOLUM, M. S. and PUGMIRE, R. J. 2000b. Solid-state <sup>13</sup>C NMR characterization of matched tars and chars from rapid coal devolatilization. *Proceedings of the Combustion Institute*, 28, 2313.
- SADHUKHAN, A. K.; GUPTA, P. and SAHA, R. K. 2009. Characterization of porous structure of coal char from a single devolatilized coal particle: Coal combustion in a fluidized bed. *Fuel Processing Technology*, 90, 692.
- SHARMA, A.; KADOOKA, H.; KYOTANI, T. and TOMITA, A. 2001. Effect of microstructural changes on gasification reactivity of coal chars during low temperature gasification. *Energy & Fuels*, 16, 54.
- SHARMA, A.; KYOTANI, T. and TOMITA, A. 1999. A new quantitative approach for microstructural analysis of coal char using HRTEM images. *Fuel*, 78, 1203.
- SHARMA, A.; KYOTANI, T. and TOMITA, A. 2000. Direct observation of raw coals in lattice fringe mode using high-resolution transmission electron microscopy. *Energy & Fuels*, 14, 1219.
- SHARMA, D. and WADHWA, G. 1997. Demineralization of coal by stepwise bioleaching: a comparative study of three Indian coals by fourier transform infra red and X-ray diffraction techniques. *World Journal of Microbiology and Biotechnology*, 13, 29.
- SOLUM, M. S.; PUGMIRE, R. J. and GRANT, D. M. 1989. Carbon-13 solid-state NMR of Argonne-premium coals. *Energy & Fuels*, 3, 187.
- SOLUM, M. S.; SAROFIM, A. F.; PUGMIRE, R. J.; FLETCHER, T. H. and ZHANG, H. 2001. <sup>13</sup>C NMR analysis of soot produced from model compounds and a coal. *Energy & Fuels*, 15, 961.
- SUN, H. 1998. COMPASS: An ab initio forcefield optimized for condensed-phase applications. Overview with details on alkane and benzene compounds. *The Journal of Physical Chemistry B*, 102, 7338.
- TAKANOHASHI, T.; IINO, M. and NISHIOKA, M. 1995. Investigation of associated structure of Upper Freeport coal by solvent swelling. *Energy & Fuels*, 9, 788.
- VAN NIEKERK, D. 2008. *Structural elucidation, molecular representation and solvent interactions of vitrinite-rich and inertinite-rich South African coals*, ProQuest.
- VAN NIEKERK, D.; PUGMIRE, R. J.; SOLUM, M. S.; PAINTER, P. C. and MATHEWS, J. P. 2008. Structural characterization of vitrinite-rich and inertinite-rich Permian-aged South African bituminous coals. *International Journal of Coal Geology*, 76, 290.
- WEIMERSHAUS, M.; EVNOUCHIDOU, I.; SAVEANU, L. and VAN ENDERT, P. 2013. Peptidases trimming MHC class I ligands. *Current Opinion in Immunology*, 25, 90.
- ZHANG, D.-K. and TELFER, M. 1998. Sulfur transformation in a south Australian low-rank coal during pyrolysis. *Symposium (International) on Combustion*, 27, 1703.
- ZHANG, S.-Y.; LU, J.-F.; ZHANG, J.-S. and YUE, G.-X. 2008. Effect of pyrolysis intensity on the reactivity of coal char. *Energy & Fuels*, 22, 3213.
- ZHANG, Y.; ZHANG, J.; SHENG, C.; CHEN, J.; LIU, Y.; ZHAO, L. and XIE, F. 2010. X-ray photoelectron spectroscopy (XPS) investigation of nitrogen functionalities during coal char combustion in O<sub>2</sub>/CO<sub>2</sub> and O<sub>2</sub>/Ar atmospheres. *Energy & Fuels*, 25, 240.
- ZHOU, J.-H.; SUI, Z.-J.; ZHU, J.; LI, P.; CHEN, D.; DAI, Y.-C. and YUAN, W.-K. 2007. Characterization of surface oxygen complexes on carbon nanofibers by TPD, XPS and FT-IR. *Carbon*, 45, 785.
- ZHU, X. and SHENG, C. 2009. Evolution of the Char Structure of Lignite under Heat Treatment and Its Influences on Combustion Reactivity†. *Energy & Fuels*, 24, 152.
- ZHU, X. and SHENG, C. 2010. Influences of carbon structure on the reactivities of lignite char reacting with CO<sub>2</sub> and NO. *Fuel Processing Technology*, 91, 837.

## CHAPTER 5: DENSITY FUNCTIONAL THEORY MOLECULAR MODELLING AND EXPERIMENTAL PARTICLE KINETICS

---

Chapter 5: Density functional theory molecular modelling and experimental particle kinetics for CO<sub>2</sub>-char gasification.

**Publication 3.** Mokone J. Roberts, Raymond C. Everson, George Domazetis, Hein W.J.P. Neomagus, Cornelia G.C.E. Van Sittert, Gregory N. Okolo, J.M. Jones, Daniel Van Niekerk, Jonathan P. Mathews. *Density functional theory molecular modelling and experimental particle kinetics for the CO<sub>2</sub>-char gasification*. CARBON, 2015. 93: p. 295-314.

### 5.1 Abstract

Experimental measurements and DFT atomistic modelling were conducted to elucidate the mechanisms for gasification chemistry of char with CO<sub>2</sub> gas. The molecular models used were based on experimental representations of coal chars derived from the vitrinite- and inertinite-rich South African coals at 1000 °C. The HRTEM and XRD techniques were used to construct parallelogram-shaped PAH stacks of highest frequency in the vitrinite-rich (7x7) and inertinite-rich (11x11) char structures. Computations were executed to get the nucleophilic Fukui functions, at DFT-DNP level, to elucidate the nature and proportions of carbon active sites and quantify their reactivity. The DFT-DNP-computed reaction pathways and transition states, to obtain the energy of reaction and activation energies for the gasification reactions of CO<sub>2</sub> with active carbon sites were examined. These results were compared with TGA experimental results at 900-980°C. The mean nucleophilic Fukui function of the H-terminated char models and active sites located at similar edge positions decreased with increasing size of char molecules and followed the sequence: zigzag > armchair > tip active sites. The mean DFT-DNP values for the activation energy of 233 kJ mol<sup>-1</sup> at the reactive carbon edge was in agreement with the experimental 191±25 kJ mol<sup>-1</sup> and 210±8 kJ mol<sup>-1</sup> for the respective chars.

## CHAPTER 5: DENSITY FUNCTIONAL THEORY MOLECULAR MODELLING AND EXPERIMENTAL PARTICLE KINETICS

---

### 5.2 Introduction

Economic and environmental constraints necessitate research into higher efficiency coal utilisation, to develop advanced technologies with reduced greenhouse gas emissions. A study of coal gasification is part of this effort. Coal gasification is a complex process that involves reactions with  $O_2$ ,  $H_2O$ ,  $H_2$  and  $CO_2$ , either as a single component reactant or a mixture of two or more of the gaseous reagents. Gasification reactions have been studied using a variety of experimental and theoretical techniques (Everson *et al.*, 2008:3082; Everson *et al.*, 2006:1076; Chen and Yang, 1998:1061; Collot, 2006:191; Cousins *et al.*, 2006:2489; Everson *et al.*, 2013:148; Hattingh *et al.*, 2011:2048; Golovina and Klimov, 1999:393; Irfan *et al.*, 2011:12; Kajitani *et al.*, 2002:539; Kajitani *et al.*, 2006:163; Kajitani *et al.*, 2013:7; Umemoto *et al.*, 2013:14; Zhang *et al.*, 2010:152) over a lengthy period (Bhatia, 1998:2478) because of their importance to a variety of applications.

Various aspects of coal gasification by  $CO_2$  and its application to oxy-combustion has been reviewed by Irfan *et al.* (Irfan *et al.*, 2011:12), where the dependence on coal rank, pressure, temperature, gas composition, catalyst and the minerals present inside the coal, heating rate, particle size, and diverse reactor types was established. A large volume of literature has been devoted to mechanisms for the gasification reactions of carbon by oxygen-containing gases through experimental methods that included thermogravimetric techniques, evolved gas analysis, TPD, transient kinetics, as well as other characterisation techniques such as SEM, HRTEM and XRD (Gale *et al.*, 1996:766; Johnson *et al.*, 1986:1284; Matsui *et al.*, 1987:95; Wu *et al.*, 2007:199; Everson *et al.*, 2013:148). This work highlighted the effect of structural properties of chars in gasification reaction mechanism and continues to elucidate the intricacies of coal gasification. Quantum mechanics modelling studies have contributed to the evaluation of medium- to high-temperature interactions between carbonaceous material and oxygen carrying gases (Chen *et al.*, 1993:2835; Frankcombe and Smith, 2004:2921; Chen and Yang, 1989:481; Chen and Yang, 1997a:421; Espinal *et al.*,

## CHAPTER 5: DENSITY FUNCTIONAL THEORY MOLECULAR MODELLING AND EXPERIMENTAL PARTICLE KINETICS

---

2003:1003; García *et al.*, 2004:1507; Espinal *et al.*, 2009:3010; Frankcombe *et al.*, 2002:2341; Radovic, 2005:907). High-level molecular modelling techniques used to carry out comprehensive study of coal gasification reactions are often confronted with the complex nature of the large coal and char structures, which present challenging computational requirements. A better understanding of associated atomistic reaction mechanism may facilitate improvements in the evaluation of the coal char gasification kinetics, including rates and efficiencies. Rates of gasification of porous carbons are affected by parameters such as active site concentration, accessibility of the reactant gas into the internal area of the char, and presence of active catalysts that mediate in reactions with gasification agents (Espinal *et al.*, 2003:1003; Radovic *et al.*, 1985:311; Radović *et al.*, 1983:849; Walker Jr *et al.*, 1959:133; Walker Jr *et al.*, 1991:411; Domazetis *et al.*, 2008:581; Domazetis *et al.*, 2007:2531; Domazetis *et al.*, 2008:105; Samaras *et al.*, 1996:1108; Petersen *et al.*, 2004:2457).

While molecular modelling studies have been conducted into the reactivity of oxygen, steam and CO<sub>2</sub> with carbonaceous material (Montoya *et al.*, 2002:4236; Montoya *et al.*, 2003:29; Sendt and Haynes, 2005:2141; Sendt and Haynes, 2011:1851; Sendt and Haynes, 2005:629; Radovic, 2005:907; Radovic, 2009:17166), the models used were not directly derived models from high rank coal. Other work has focused on the chemisorption of oxygen-carrying gases on carbonaceous surfaces (Montoya *et al.*, 2003:29; Sendt and Haynes, 2005:2141; Sendt and Haynes, 2005:629; Radovic, 2005:907), while Montoya *et al.* used *ab initio* techniques to model the kinetics of elementary reaction in carbonaceous material (Montoya *et al.*, 2002:4236). Radovic *et al.* compared different chars in the C-CO<sub>2</sub> reaction using DFT and found that char gasification may be a structure-sensitive reaction (Radovic *et al.*, 1991:68). DFT was used to model the active carbon sites responsible for reaction with the oxygen-carrying gases and to highlight a dissociative-chemisorption reaction of CO<sub>2</sub> on active carbon sites (Radovic, 2009:17166; Radović *et al.*, 1983:849; Radovic, 2005:907).

## CHAPTER 5: DENSITY FUNCTIONAL THEORY MOLECULAR MODELLING AND EXPERIMENTAL PARTICLE KINETICS

---

The present investigation deals specifically with the gasification reaction mechanism between the CO<sub>2</sub> and coal chars, using DFT molecular modelling, and experimental techniques, to evaluate the chemistry at active sites in char, and to evaluate the structure-reactivity relationship of slow-heated, or hard-cooked, and de-ashed chars derived from the South African inertinite- and vitrinite-rich coals.

### 5.3 Chars and Methodology

#### 5.3.1 Char molecular models

Experimental work relevant to molecular models is based on: (i) the characterisation of two de-ashed chars, and (ii) constructing a molecular model based on HRTEM data from these chars (Roberts *et al.*, 2015:9).

The chars were prepared by heating inertinite- and vitrinite-rich South African Gondwana coals of the Permian Age to 1000 °C in a packed bed reactor, at 20 °C min<sup>-1</sup>, in Nitrogen, maintaining this temperature for 60 min, and then cooling (Roberts *et al.*, 2015:9). The Nitrogen flow rate was 1.5 dm<sup>3</sup> min<sup>-1</sup> to ensure a rapid escape of volatile matter in an inert atmosphere, and averting secondary reactions (Ahuja *et al.*, 1996:272; Xu and Tomita, 1987:627; Roberts *et al.*, 2015:9). The chars were de-ashed by HCl-HF treatments (Dyrkacz and Bloomquist, 1992:374; Bolat *et al.*, 1998:93; Joseph *et al.*, 1991:724; Van Niekerk *et al.*, 2008:290; Wijaya and Zhang, 2011:1) and characterized using petrographic, HRTEM, NMR and XRD techniques, similar to Roberts *et al.* (Roberts *et al.*, 2015:9).

The char models used for modelling studies were based on the HRTEM results shown in Figure 5-1; the method of parallelogram catenations by Mathews *et al.* was used to calculate size distribution of aromatic carbon sheets (Mathews *et al.*, 2010:1461; Niekerk and Mathews, 2010:73). This technique involves intensive image processing of the photo-micrographs (Figure 5-1(a)) to extract skeletonised lattice fringes (Figure 5-

## CHAPTER 5: DENSITY FUNCTIONAL THEORY MOLECULAR MODELLING AND EXPERIMENTAL PARTICLE KINETICS

---

1(b)) following an approach of Sharma *et al.* (Sharma *et al.*, 1999:1203). A relationship between these lattice fringes and aromatic carbon sheets of coals (Figure 5-1(c)) was used to calculate the distribution of the parallelogram-shaped aromatic molecules of the chars (Figure 5-1(d)) (Mathews *et al.*, 2010:1461). The detailed table of results is presented in Roberts *et al.* (Roberts *et al.*, 2015:9). The modal values, calculated from Equation (5.1), of the grouped aromatic fringe length distributions for the inertinite- and vitrinite-rich chars were 36.8 and 21.0Å, respectively. Both distributions were positively skewed at 2.4 and 3.1, respectively, according to Pearson's second coefficient of skewness (Panik, 2005), Equation (5.2), where the vitrinite-rich char was more skewed to smaller values. The modal values correspond with the 11 by 11 and 7 by 7 carbon rings of the respective chars, based on the assumption that the fringes are as deep as they are wide, of parallel catenation, and that the number of carbon atoms, and thus number of rings, can be determined as the mean from the longest and shortest possible orientations (Fernandez-Alos *et al.*, 2011:1807; Mathews *et al.*, 2010:1461). It also assumes no curvature or defects (Fernandez-Alos *et al.*, 2011:1807; Castro-Marcano *et al.*, 2012:1272). The results from XRD and HRTEM techniques showed a reasonable agreement. The HRTEM modal value for the 1000 °C inertinite-rich chars compares well with the crystallite diameter measured by the XRD technique,  $L_a$  (10), of 37.6Å. However, the  $L_a$  (10) of 30.7Å for the vitrinite-rich chars was higher than the corresponding modal value.

$$Mode = L + \left( \frac{\Delta_1}{\Delta_1 + \Delta_2} \right) c \quad (5.1)$$

$$SK = \frac{3(\bar{X} - M)}{s} \quad (5.2)$$

## CHAPTER 5: DENSITY FUNCTIONAL THEORY MOLECULAR MODELLING AND EXPERIMENTAL PARTICLE KINETICS

---

### 5.3.2 The DFT computational methods

The DFT computational requirements restrict the model size for tractable calculations. The SCF convergence for the 11x11 and 7x7 char models was difficult even if the convergence were accelerated by the smearing tool from the default value of  $13.1 \text{ kJ mol}^{-1}$ , with small increases up to  $525.1 \text{ kJ mol}^{-1}$ . Thermal smearing is a setting applied to the orbital occupation to improve the SCF convergence within the specified number of iterations. Consequently, it was necessary to reduce the aromatic carbon sheets of 7x7 from the vitrinite-rich char and 11x11 from the inertinite-rich char, to smaller sizes of 3x3 and 5x5, respectively, by applying a factor of approximately two. However, the authors acknowledge that if the number of electrons in two structures are different, then one cannot compare the electronic energy directly. In addition to this, the 4x4-carbon ring structure was included to create additional data point, since it was also present in both the vitrinite- and inertinite-rich chars (Roberts *et al.*, 2015:9). While this approach was taken, it was noted that the electronic states of the graphene models are greatly dependent on the model size so that the energetic values such as adsorption energies and activation energies are affected, as pointed out by Pham and Truong (Pham and Truong, 2012:75). Therefore, this investigation recognises the sensitivity of the results to experiments conducted. The edge carbons of the aromatic carbon sheets from the HRTEM were terminated with hydrogen to give polyaromatic hydrocarbon (PAHs) char models, following Radovic and Bockrath assertions that structures with entirely free edge carbons were unlikely, but likely with hydrogen termination. However, hydrogen termination may be appropriate for lower temperature chars, but less so for chars at high temperatures (Radovic and Bockrath, 2005:5917). Under gasification conditions at high temperatures, thermal decomposition and abstraction of edge hydrogen would be anticipated (Sendt and Haynes, 2011:1851).

It is understood that gasification includes other reactants ( $\text{H}_2$ ,  $\text{H}_2\text{O}$ ,  $\text{CO}_2$  and  $\text{O}_2$ ), but the current modelling deals solely with reactions involving  $\text{CO}_2$  (Sendt and Haynes, 2011:1851; Marinov *et al.*, 1996:211; Kuniyoshi *et al.*, 2002:292). It is necessary to

## CHAPTER 5: DENSITY FUNCTIONAL THEORY MOLECULAR MODELLING AND EXPERIMENTAL PARTICLE KINETICS

---

restrict the present modeling to reactions involving CO<sub>2</sub>, as modeling gasification involving a number of gases is outside our current capabilities. Our focus is relatively on simple systems to provide insights on likely mechanisms in complicated, practical systems. The modelling study commences with the loss of H to form a reactive carbon edge or free active sites, followed by chemisorption of CO<sub>2</sub> and subsequent formation of CO. The modelling results are compared with the experimental to assert the viability of the proposed mechanisms for CO<sub>2</sub> gasification of char derived from bituminous coal medium C rank.

Molecular models were proposed to simulate structures with various types of active sites, e.g. the basal plane, armchair, zigzag and tip (Radovic and Bockrath, 2005:5917; Radovic, 2005:907; Espinal *et al.*, 2003:1003; Montoya *et al.*, 2001:6757; Montoya *et al.*, 2003:29; Montoya *et al.*, 2002:1863; Sendt and Haynes, 2005:2141; Sendt and Haynes, 2011:1851; Sendt and Haynes, 2005:629). Solid-state <sup>13</sup>C nuclear magnetic resonance (NMR) techniques (Solum *et al.*, 2001:961; Solum *et al.*, 1989:187), have shown that coal chars commonly consist of structures of aromatic stack/clusters of 12-25 aromatic carbon atoms (3-7 benzene rings) (Montoya *et al.*, 2002:4236; Perry *et al.*, 2000a:2313). NMR analysis of 1000 °C chars however, encounters line broadening which prevents calculation of structural parameters, and thus it cannot predict the aromatic carbon cluster size under these conditions (Solum *et al.*, 2001:961). Line broadening is attributed to aromatic free radicals that begin to change the relaxation behaviour of the aromatic carbons (Perry *et al.*, 2000b:2313). Most characterization results have indicated that the 1000 °C inertinite- and vitrinite-rich coal chars behaved in a similar way, except for the aromatic fringes and  $L_a$  (10) values from the HRTEM and XRD techniques, respectively. These considerations indicated that the reduced modal PAH structures of 7x7 and 11x11 PAHs were reasonable models of the respective inertinite- and vitrinite-rich chars, for DFT computations.

## CHAPTER 5: DENSITY FUNCTIONAL THEORY MOLECULAR MODELLING AND EXPERIMENTAL PARTICLE KINETICS

---

### 5.3.2.1 The DFT reactivity modelling with the Fukui function

The DFT geometry optimization of our char models were performed using with the DMol<sup>3</sup> method in the Accelrys Material Studio<sup>®</sup> software (version 6.0) using the Laboratory of Applied Molecular Modelling (LAMM) high performance computing (HPC) resources of the North-West University in Potchefstroom and the National Centre for HPC in Cape Town, South Africa. The DMol<sup>3</sup> calculations give accurate self-consistent field (SCF) densities as discussed in (Delley, 2000:7756) and numerically localized basis sets yields improved enthalpies for the formation of H, N, O, F, Cl, C, Si, S atoms. The exchange-correlation potential of generalized gradient approximation (GGA) functional of Perdew and Wang (PW91) was used (Perdew and Wang, 1992:13244; Furche and Perdew, 2006:044103). Delley found that the DFT performance in predicting molecular enthalpies of formation of metallic solids was significantly improved for the Perdew–Burke–Ernzerhof (PBE) functional in comparison with PW91 (Delley, 2000:7756). However, several publications on investigations similar to the current (search for transition state) used PW91 functional (Henkelman *et al.*, 2002:269; Henkelman *et al.*, 2000:9901; Sheppard *et al.*, 2008; Jónsson *et al.*, 1998:385). This package provides electronic wave functions which are expanded in a double numerical coupled with polarization basis set (DNP) truncated at a real space cut-off of 4.4Å. The DNP is comparable to Gaussian 6-31G\*\* basis set used for molecular and solids calculations, but the DNP is reported to be more accurate than the 6-31G\*\* set of the same size (Roy *et al.*, 1999:8236; Kusama *et al.*, 2008:84). All the calculations were spin-unrestricted. The default convergence tolerances used for the energy, force, and displacement were of 0.1 kJ mol<sup>-1</sup> ( $2 \times 10^{-5}$  Ha), 10.5 kJ mol<sup>-1</sup>Å<sup>-1</sup> (0.004 Ha Å<sup>-1</sup>) and  $5 \times 10^{-4}$  nm (0.005Å), respectively. The SCF was left on fermi, which required up to eight times the maximum number of iterations (1000) for convergence. This was coupled with the direct inversion of the iterative subspace (DIIS) technique developed by Pulay (Pulay, 1982:556).

## CHAPTER 5: DENSITY FUNCTIONAL THEORY MOLECULAR MODELLING AND EXPERIMENTAL PARTICLE KINETICS

---

The 1-scf energy calculations were performed with the Accelrys Material Studio<sup>®</sup> software package on geometry optimised structures to determine the reactivity indicator using the Fukui function. The Fukui function,  $f(r)$ , is among the most commonly used reactivity indicators, as discussed in (Sablon *et al.*, 2009:1245; Bultinck *et al.*, 2007:034102). The Fukui function is usually given as the change in the density function of the molecule as a consequence of changing the number of electrons in the molecule (Bultinck *et al.*, 2007:034102) and allows a chemical reaction to be understood in terms of the highest occupied molecular orbitals and lowest unoccupied molecular orbitals (Fukui, 1970:1). The function  $f^+(r)$  is a measure of reactivity toward a donor reagent (nucleophilic attack),  $f^-(r)$  values measure reactivity toward an acceptor reagent (electrophilic attack) and an average value of both may be taken as a measure of reactivity toward a radical  $f^{\cdot}(r)$  (Fuentelba *et al.*, 2000:2544). Parr and Yang showed that sites in chemical species with the largest  $f(r)$  value are those with highest reactivity and are the preferred reaction site(s) (Chattaraj, 2000:511; Melin *et al.*, 2004:2487; Parr and Yang, 1984:4049). Research has emphasised that hardness-softness  $f(r)$  derived from the DFT are powerful tools to predict active sites of a molecule (Melin *et al.*, 2004:2487; Pérez *et al.*, 2000:4756; Li and Evans, 1995:7756). The  $f(r)$  defines the reactivity of an atom in a molecule and, together with local softness, are suitable to describe reactivity of different substrates (Fusaro *et al.*, 2013:303), including symmetrical char structures. Here, the objective is to predict reactivity of all H-terminated and selected, free edge carbon atoms from simplified coal char structures/molecules with oxygen atoms from CO<sub>2</sub> gas molecules, which is anticipated as the first chemical interaction step associated with the CO<sub>2</sub>-char gasification reaction mechanism. The O from the CO<sub>2</sub> atom participates as electron donor to chemisorb to the free edge carbon atom, thus making the nucleophilic Fukui function,  $f^+(r)$ , the preferred index to predict reactivity. The  $f^+(r)$ -based reactivity analyses were first conducted on H-terminated edge carbon sites to gather the rationale for the free active sites (reactive edge) to be used in the CO<sub>2</sub>-char gasification reaction mechanism. The energetics of the loss of H were examined using the TS theory approaches

## CHAPTER 5: DENSITY FUNCTIONAL THEORY MOLECULAR MODELLING AND EXPERIMENTAL PARTICLE KINETICS

---

available in the Accelrys Material Studio<sup>®</sup> software package. The relative accuracy of these computations were inevitably restricted by the very large computational resources required for these calculations.

### 5.3.2.2 The DFT modelling of char-CO<sub>2</sub> gasification reaction mechanism

A general mechanism of the reaction of CO<sub>2</sub> gas with solid carbon surfaces is given by Equations (5.3)-(5.6) (Ergun *et al.*, 1967:403). Initially, the CO<sub>2</sub> gas molecule is chemisorbed on the active site  $C_f$  on the char surface (Montoya *et al.*, 2002:125; Moulijn and Kapteijn, 1995:1155; Montoya *et al.*, 2002:1863; Radovic, 2005:907; Radović *et al.*, 1983:849).



This is followed by dissociation of the adsorbed CO<sub>2</sub> to form CO according to Equation (5.4), and an oxygen surface complex (quinone) on the char surface,  $C_f(O)$ , which is (Moulijn and Kapteijn, 1995:1155; Chen and Yang, 1997b:421; Radovic, 2005:907).



The subsequent formation of an additional CO molecule results from the O-complex forming CO, (gasifying) with the solid carbon on the edge of the char surface, and escaping as a CO gas molecule as in Equation (5.5) (Chen and Yang, 1997b:421; Chen *et al.*, 1993:2835; Irfan *et al.*, 2011:12). Montoya *et al.* has shown that the six-member ring containing the O-complex ( $C_f(O)$ ) undergoes bond weakening and breaking to form the CO gas molecule. This ring may collapse to form a five-member ring with loss of CO, or the loss of CO may accompany the formation of a defect which would act as another active carbon site, to continue the process of CO<sub>2</sub> gasification (Montoya *et al.*, 2002:4236).

## CHAPTER 5: DENSITY FUNCTIONAL THEORY MOLECULAR MODELLING AND EXPERIMENTAL PARTICLE KINETICS

---



Equations (5.3)-(5.5) summarise the Boudouard reaction shown in Equation (5.6) (Walker Jr *et al.*, 1959:133; Hunt *et al.*, 2013:26871); the mechanisms however include intermediate reactions associated with the bond weakening, breaking, and re-arrangements.



The Boudouard reaction (Walker Jr *et al.*, 1959:133; Hunt *et al.*, 2013:26871) mechanism was examined by application of TS theory, based on a generalized synchronous transit scheme, which  $E_{\text{reac}}$  and  $\Delta E_b$  (Govind *et al.*, 2003:250; Andzelm *et al.*, 2006:58; Andersen *et al.*, 2008:1025) from DFT modelling of the char- $CO_2$  gasification reaction using the 3x3 model. Transition state theory enables consideration of transition rates in diffusion reactions and also energy profiles between reactants and products, as discussed in (Henkelman *et al.*, 2000:9901; Wigner, 1938:29; McLafferty and Pechukas, 1974:511; Pechukas and Miller, 1976:269); the TS for a reaction is the geometry corresponding to the highest energy along the (MEP), which gives the activation energy. In the context of reaction rates, the reactant(s) and product(s) have an initial and a final state, both of which are local minima on the PES scan accurately locating the transition state.

The TS were searched by LST/QST methods (Andersen *et al.*, 2008:1025; Andzelm *et al.*, 2006:58; Govind *et al.*, 2003:250; Wang *et al.*, 2006:9976). Usually after the second QST optimization the CG refinement successfully finds the transition state. However, in systems such as those used here, accomplishment and refinement of TS geometries can require unrealistically lengthy computations, especially when the system has two or more imaginary frequencies. The computations were therefore restrained to the location of likely TS within the context of the proposed mechanisms. However, often the frequency calculations on the TS showed that there was only one imaginary frequency, which allowed a TS confirmation. The major thrust is based on DFT results of reaction

## CHAPTER 5: DENSITY FUNCTIONAL THEORY MOLECULAR MODELLING AND EXPERIMENTAL PARTICLE KINETICS

---

energies for each reaction site and energy barriers. These results can be compared with experimental data, and therefore enable a direct comparison between modelling and measured data. The energetics were determined for the char-CO<sub>2</sub> interactions for the C-H bond breakdown, CO<sub>2</sub> chemisorption, CO formation through CO<sub>2</sub> dissociation and C-C decomposition reactions.

### 5.3.3 Experimentation: Char-CO<sub>2</sub> reactivity (Particle kinetics)

The objective of the experimentation undertaken was to validate the results (activation energy) obtained from the reaction rate modelling based on the molecular structure (atomic reaction rate) with results obtained using particle reaction kinetics. For this purpose, experimentation was carried out using a thermogravimetric analyser with the random pore model reaction modelling (Everson *et al.*, 2013:148; Everson *et al.*, 2008:3403; Bhatia and Perlmutter, 1980:379).

#### 5.3.3.1 Thermogravimetric analyser

Isothermal char-CO<sub>2</sub> gasification experiment was carried out on a TA instruments' SDT Q600 TGA supplied by ALS, South Africa, using de-ashed chars derived from inertinite-rich and vitrinite-rich South African coals. The SDT Q600 TGA can work within the temperature control range of ambient +5 to 1500 °C, with a platinum-rhodium Type R thermocouple; with a temperature accuracy, precision and DTA sensitivity of ± 1 °C, ± 0.5 °C and 0.001 °C respectively. The TGA uses an alumina horizontal beam null balance with a weight sensitivity of 0.1 µg, weight accuracy of ±0.1% and a repeatability of 99.9%. The controlled temperature zone of the furnace is 50 mm. Gas flow through the TGA furnace is uni-directional over the horizontal balance, thus, a purge gas counter-flow is not needed during experiments. The TGA also come with two in-built mass flow controllers, which control the gas flow rates.

## CHAPTER 5: DENSITY FUNCTIONAL THEORY MOLECULAR MODELLING AND EXPERIMENTAL PARTICLE KINETICS

---

### 5.3.3.2 Experimental procedure

The isothermal gasification experiments were carried out with CO<sub>2</sub> gas at atmospheric pressure and isothermal temperatures of 900, 920, 940, 960 and 980 °C. Sample mass of 10 ± 1 mg of -75 μm particle size was used for each of the experiments on the TGA. The sample was loaded into a 90 μL porous alumina sample holder carefully placed on the balance pan before closing the furnace. The set-up (furnace and sample) was flushed with nitrogen gas at 100 cm<sup>3</sup> min<sup>-1</sup> for 25 min to evacuate any oxidizing species in the furnace, as well as to stabilize the balance. The sample was heated at 30 °C min<sup>-1</sup> under the N<sub>2</sub> gas flow to the required temperatures. The N<sub>2</sub> gas was automatically turned off and the CO<sub>2</sub> gas entered at a flow rate of 45 cm<sup>3</sup> min<sup>-1</sup> for the isothermal gasification experiments. Reaction times for the experiments varied from 36 to >48 hours, similar to Everson *et al.* (Everson *et al.*, 2008:3082; Everson *et al.*, 2013:148).

### 5.3.3.3 Calculation of activation energies

The intrinsic reaction rate equation based on the random pore model was evaluated according to the method proposed by Everson *et al.* (Everson *et al.*, 2008:3403) involving essentially: (1) the determination of the lumped reaction rate consisting of the intrinsic reaction rate and the initial physical properties of the chars, and (2) the determination of the activation energies and pre-exponential factors using the Arrhenius equation using the lumped reaction rate determined from the experimental results.

The relevant random pore model is given in Equations (5.7)-(5.13) with a brief description of the calculation procedure. The equation for the conversion of carbon, on ash free basis, involves the reaction rate and structural behaviour, as well as characterised by the lumped reaction rate and structural parameter.

$$X = 1 - \exp \left[ -r^L t \left( 1 + \frac{r^L t \psi}{4} \right) \right] \quad (5.7)$$

## CHAPTER 5: DENSITY FUNCTIONAL THEORY MOLECULAR MODELLING AND EXPERIMENTAL PARTICLE KINETICS

---

$$r^L = \frac{r_s S_o}{(1 - \varepsilon_o)} \quad (5.8)$$

$$r_s = k_{so} \exp\left(\frac{-E_a}{RT}\right) \cdot P_{CO_2}^n \quad (5.9)$$

$$\psi = \frac{4\pi L_o(1 - \varepsilon_o)}{S_o^2} \quad (5.10)$$

For the evaluation of the lumped reaction rate, the structural parameter needs to be evaluated, which can be accomplished with Equation (5.11) involving regression with the unknown structural parameter. This equation can be derived from Equation (5.7) and can be seen to be independent of temperature (reaction rate) and is a convenient method to determine the structural parameter.

$$\frac{t}{t_{0.9}} = \frac{\sqrt{1 - \psi \ln(1 - X)} - 1}{\sqrt{1 - \psi \ln(1 - 0.9)} - 1} \quad (5.11)$$

With a known structural parameter, the lumped reaction parameters can be calculated also by regression with the Equation (5.7) and the experimental results. From a knowledge of the lumped reaction rate as a function of temperature, the Arrhenius equation parameters can be calculated using the logarithmic form of a combination of Equations (5.8) and (5.9), to yield Equations (5.12) and (5.13) (Everson *et al.*, 2008:3403; Everson *et al.*, 2013:148).

$$\ln(r^L) = -\frac{E_a}{RT} + n \ln(P_{CO_2}) + \ln(k'_{so}) \quad (5.12)$$

$$\ln(r^L) = F_1(T) + F_2(P_{CO_2}, n, k'_{so}) \quad (5.13)$$

## CHAPTER 5: DENSITY FUNCTIONAL THEORY MOLECULAR MODELLING AND EXPERIMENTAL PARTICLE KINETICS

---

### 5.4 Results and Discussion

The present work involves the size of the graphene structure consistent with the low energy differences reported by Pham and Truong (Pham and Truong, 2012:75). This work also uses the Fukui function as an indicator of reactivity (Sablon *et al.*, 2009:1245; Bultinck *et al.*, 2007:034102) for edges on the graphene structure. The standard Fukui function concept of conceptual DFT includes contribution from the HOMO and the LUMO (Fukui, 1970:1), but also from other chemically relevant orbitals. While the treatment by Radovic may provide particular insights related to electronic states and spin crossover effects, some of the DFT results (e.g. suggesting exothermic chemistry involved in the interactions between small graphene ribbons and CO<sub>2</sub>) appear counter intuitive (Radovic, 2005:907). Of greater concern is the large difference between the molecular structure of a single graphene sheet, and that of freshly formed coal-char, which is three-dimensional and disordered to varying degrees, and may form a variety of active sites during pyrolysis of coal. These considerations have caused the present investigation to emphasise the endothermic aspects of char gasification by CO<sub>2</sub>, and to seek results on the energy of reaction from the model for comparison with experimental results. Detailed studies of electronic states would need additional work with a larger char model, requiring considerably greater computational resources than are currently available and such work may require a separate treatment from the current investigation. However, the reader can find a table of spin states in Appendix D.

Fukui function as a reactivity indicator, allowed for the modelling sequence that commences with loss of hydrogen to form active C\* sites, followed by chemisorption of CO<sub>2</sub> gas molecule and the energies obtained for thermal dissociation of CO<sub>2</sub> to form the first CO gas molecule, ultimately the thermal breakdown to yield the second CO gas molecule. Clearly, this sequence is a simplification of the actual gasification process observed in practice. Some aspects of the mechanism(s) however, can be elucidated using both computed values of  $\Delta E_b$  and  $E_{\text{reac}}$  and their comparison with experimental data.

## CHAPTER 5: DENSITY FUNCTIONAL THEORY MOLECULAR MODELLING AND EXPERIMENTAL PARTICLE KINETICS

### 5.4.2 DFT reactivity modelling and the Fukui function

Substantial research have found that the chemical interactions between carbon molecules and reactant gases take place at the edge active carbon atoms for coal based char models and also for non-coal char models (Chen and Yang, 1998:1061; Radovic, 2005:907; Radovic, 2009:17166; Radovic and Bockrath, 2005:5917; Raj *et al.*, 2011:1516; Sander *et al.*, 2009:866; Montoya *et al.*, 2002:1863; Montoya *et al.*, 2003:29; Montoya *et al.*, 2000:8409), and Zhang *et al.* found that the carbons in the basal plane of large, fused-ring aromatic domains of chars, were inert (Zhang *et al.*, 2008:3213). Figure 5-1 shows results from the HRTEM technique, which were used to derive the char models used here (Roberts *et al.*, 2015:9).

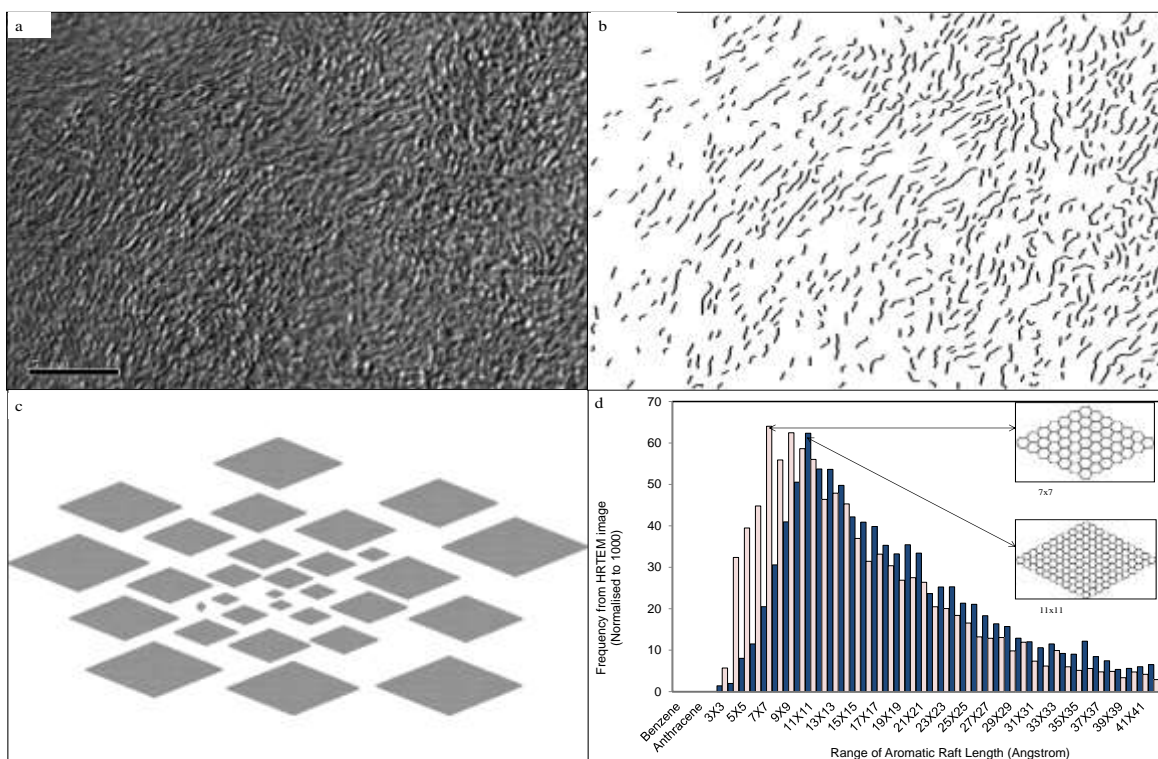


Figure 5-1. HRTEM results. Microphotograph for the inertinite-rich chars ((a), top left) with scale bar = 5 nm. Lattice after image processing ((b), top right). Parallelogram catenations ((c), bottom left). Distributions of aromatic raft lengths ((d), bottom right), where, dark and light bars = inertinite- and vitrinite-rich chars, respectively.

## CHAPTER 5: DENSITY FUNCTIONAL THEORY MOLECULAR MODELLING AND EXPERIMENTAL PARTICLE KINETICS

The reaction schemes to depict the char-CO<sub>2</sub> reaction mechanism commenced with reactivity analysis of the H-terminated edge carbon atoms using the  $f^+(r)$ , the data of which was used to rationalise the selection of free active edge carbon atoms, which involved a qualitative account for the loss of H using the transition state theory. The definition, position and numbering of H-terminated C active sites are presented in Table 5-1 accompanied by Figure 5-2. The  $f^+(r)$  results are presented in Table 5-2(a)-(c) at an accuracy of  $\pm 0.001$ . The  $f^+(r)$  is a dimensionless reactivity index.

Table 5-1. Definition of H-terminated edge carbons, including position and quantity.

Edge C name	Symbol	3x3	4x4	5x5
Tip	Ct	C1, C29	C1, 47	C1, C69
Zigzag, proximate to tip	Cz	C2, C6, C28, C30	C2, C6, C46, C48	C2, C6, C68, C70
Zigzag, remote from tip and armchair	Czi	C7, C13, C23, C27	C7, C14, C21, C22, C31, C40, C43, C45	C7, C14, C15, C25, C26, C33, C49, C54, C55, C62, C65, C66
Armchair	Cr1, Cr2	C14, C15, C20, C21	C15, C16, C28, C29	C21, C22, C34, C35

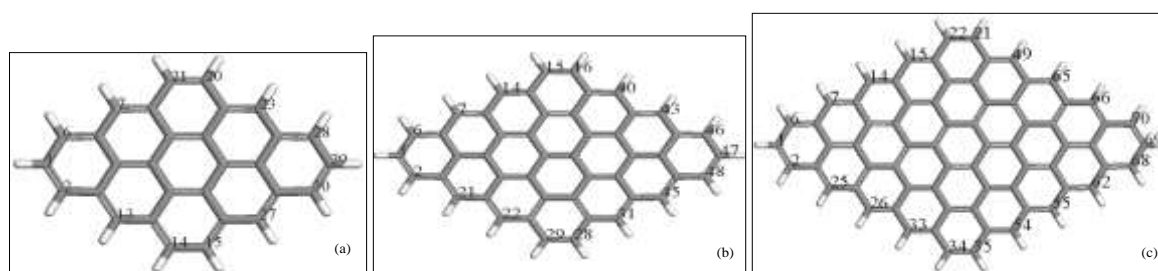


Figure 5-2. The PAH char models used to determine the nucleophilic Fukui values of the edge carbon sites, where (a), (b) and (c) = 3x3, 4x4 and 5x5 structures, respectively.

## CHAPTER 5: DENSITY FUNCTIONAL THEORY MOLECULAR MODELLING AND EXPERIMENTAL PARTICLE KINETICS

---

The results indicate that reactivity of H-terminated char models and active sites located at similar edge positions decreases with increasing size. In addition to this, the reactivity analysis of the respective char models show that the  $f^+(r)$  of all zigzag ( $C_z$ ) carbon sites adjacent to the tip was similar, but decreased with remoteness of intermediate zigzag sites ( $C_{zi}$ ) from the tip. The reactivity is distributed according to the sequence: zigzag > armchair > tip.

The Fukui function values on the H-terminated edge carbons are taken as indicative of the sites that would form  $C^*$  active sites (reactive edge) after loss of H. This reactivity indicator also shows that the reactivity of sites located at similar edge positions of the respective 3x3, 4x4 and 5x5 PAH char models was similar. This outcome was observed even if the “use symmetry” option of the program were not utilised during computations.

## CHAPTER 5: DENSITY FUNCTIONAL THEORY MOLECULAR MODELLING AND EXPERIMENTAL PARTICLE KINETICS

Table 5-2. Reactivity of 3x3 ((a), left-hand side), 4x4 ((b), middle) and 5x5 ((b), right-hand side) coal char models from  $f^+(r)$ .

(a) 3x3 PAH				(b) 4x4 PAH				(c) 5x5 PAH			
Edge site	$f^+(r)$ Mulliken	Reactivity level	Edge type	Edge site	$f^+(r)$ Mulliken	Reactivity level	Edge type	Edge site	$f^+(r)$ Mulliken	Reactivity level	Edge type
C1	0.004	4	C <sub>t</sub>	C1	0.003	5	C <sub>t</sub>	C1	0.003	6	C <sub>t</sub>
C2	0.039	1	C <sub>z</sub>	C2	0.033	1	C <sub>z</sub>	C2	0.026	1	C <sub>z</sub>
C6	0.039	1	C <sub>z</sub>	C6	0.033	1	C <sub>z</sub>	C6	0.026	1	C <sub>z</sub>
C7	0.033	2	C <sub>zi</sub>	C7	0.028	2	C <sub>zi</sub>	C7	0.024	2	C <sub>zi</sub>
C13	0.033	2	C <sub>zi</sub>	C14	0.016	3	C <sub>zi</sub>	C14	0.017	3	C <sub>zi</sub>
C14	0.014	3	C <sub>r</sub>	C15	0.008	4	C <sub>r</sub>	C15	0.011	4	C <sub>zi</sub>
C15	0.014	3	C <sub>r</sub>	C16	0.007	4	C <sub>r</sub>	C21	0.005	5	C <sub>r</sub>
C20	0.014	3	C <sub>r</sub>	C21	0.028	2	C <sub>zi</sub>	C22	0.006	5	C <sub>r</sub>
C21	0.014	3	C <sub>r</sub>	C22	0.016	3	C <sub>zi</sub>	C25	0.023	2	C <sub>zi</sub>
C23	0.033	2	C <sub>zi</sub>	C28	0.007	4	C <sub>r</sub>	C26	0.017	3	C <sub>zi</sub>
C27	0.033	2	C <sub>zi</sub>	C29	0.008	4	C <sub>r</sub>	C33	0.010	4	C <sub>zi</sub>
C28	0.039	1	C <sub>z</sub>	C31	0.016	3	C <sub>zi</sub>	C34	0.005	5	C <sub>r</sub>
C29	0.004	4	C <sub>t</sub>	C40	0.016	3	C <sub>zi</sub>	C35	0.006	5	C <sub>r</sub>
C30	0.039	1	C <sub>z</sub>	C43	0.028	2	C <sub>zi</sub>	C49	0.010	4	C <sub>zi</sub>
Mean	0.025			C45	0.028	2	C <sub>zi</sub>	C54	0.010	4	C <sub>zi</sub>
				C46	0.032	1	C <sub>z</sub>	C55	0.017	3	C <sub>zi</sub>
				C47	0.003	5	C <sub>t</sub>	C62	0.023	2	C <sub>zi</sub>
				C48	0.032	1	C <sub>z</sub>	C65	0.017	3	C <sub>zi</sub>
				Mean	0.019			C66	0.023	2	C <sub>zi</sub>
								C68	0.025	1	C <sub>z</sub>
								C69	0.003	6	C <sub>t</sub>
								C70	0.025	1	C <sub>z</sub>
								Mean	0.015		

The results indicate that reactivity of H-terminated char models and active sites located at similar edge positions decreases with increasing size. In addition to this, the reactivity analysis of the respective char models show that the  $f^+(r)$  of all zigzag (C<sub>z</sub>) carbon sites adjacent to the tip was similar, but decreased with remoteness of intermediate zigzag sites (C<sub>zi</sub>) from the tip. The reactivity is distributed according to the sequence: zigzag > armchair > tip.

## CHAPTER 5: DENSITY FUNCTIONAL THEORY MOLECULAR MODELLING AND EXPERIMENTAL PARTICLE KINETICS

---

The Fukui function values on the H-terminated edge carbons are taken as indicative of the sites that would form C\* active sites (reactive edge) after loss of H. This reactivity indicator also shows that the reactivity of sites located at similar edge positions of the respective 3x3, 4x4 and 5x5 PAH char models was similar. This outcome was observed even if the “use symmetry” option of the program were not utilised during computations.

In this investigation, it was postulated that during CO<sub>2</sub> gasification, the higher reactive sites such as C<sub>z</sub> and C<sub>zi</sub>, from the 3x3, will preferentially lose H. Annealing during pyrolysis however, may give rise to active sites of lower reactivity as the 3x3 grows to 5x5 sizes, because at high temperatures, and chemically-controlled gasification process, char undergoes thermal annealing in competition with gasification (Zhang *et al.*, 2008:3213; Senneca *et al.*, 1997:141; Jones and Jones, 2007:677). This causes the growth of crystallite diameter,  $L_a$ , by the coalescence of crystallites along the *a*-axis (e.g. from 3x3 to 5x5 aromatic fringes) (Xu *et al.*, 2012:118) for both graphitisable and non-graphitisable carbons (Xu *et al.*, 2012:118). Zhang *et al.* studied the effects of pyrolysis intensity on the reactivity of coal char in chemically-controlled CO<sub>2</sub> gasification experiments and found the largest difference in coal char reactivity was observed in the initial stage of gasification, but, as the process continues, the active sites of high activity were preferentially removed by CO<sub>2</sub> or annealed into less active site and the active sites with lower reactivity were left in residual coal char (Zhang *et al.*, 2008:3213). Suuberg also found that the inherent reactivity of the chars was attributed to the changes in the active site concentrations, which were often thermally induced (Suuberg, 1991:269). Hence, under high temperature regimes and chemically-controlled gasification process, the char actually undergoes a process of thermal annealing (pyrolysis) in competition with gasification (Zhang *et al.*, 2008:3213; Senneca *et al.*, 1997:141; Jones and Jones, 2007:677). With the increase of carbon conversion or when the higher reactive sites in the 3x3 model are removed/annealed, the reactivity, and the number of reactive carbon sites reach similar levels and the difference in char reactivities becomes smaller (Zhang *et al.*, 2008:3213; Suuberg, 1991:269).

## CHAPTER 5: DENSITY FUNCTIONAL THEORY MOLECULAR MODELLING AND EXPERIMENTAL PARTICLE KINETICS

---

Consequently, the carbon edge (reactive edge) composed of reactive sites  $C_t$ ,  $C_z$ ,  $C_{zi}$ ,  $C_{r1}$  and  $C_{r2}$  shown in Figure 5-5(b) was used to model  $CO_2$ -char gasification reactivity and to examine relative reactivities at each site.

### 5.4.3 DFT modelling for char- $CO_2$ gasification reaction mechanism

#### 5.4.3.1 The loss of H to form an active site

Char models have generally used selected active sites for DFT studies on the interactions of carbonaceous surfaces and gaseous reactants, with the remaining edge carbons capped with hydrogen atoms (Chen *et al.*, 1993:2835; Montoya *et al.*, 2003:29; Espinal *et al.*, 2003:1003; Radovic, 2005:907; Frankcombe *et al.*, 2002:2341; Kyotani and Tomita, 1999:3434). Radovic detailed the challenges associated with the loss of hydrogen from the C-H edge carbons to form the active sites (Radovic, 2005:907), while Domazetis *et al.*, used semi-empirical modelling techniques to describe H abstraction (Domazetis *et al.*, 2008:581). In the current work, we modelled the loss of H at the following sites:  $C_t$ ,  $C_z$ ,  $C_{zi}$ ,  $C_{r1}$  and  $C_{r2}$ . From Table 5-2, the initial reactions are likely to be at the  $C_z$  and  $C_{zi}$  sites.

Initially, the C-H bond breakdown for the well known molecule benzene molecule, as shown in Figures 5-3(a)-(d), was evaluated to obtain the activation energy (energy barrier),  $\Delta E_b$  and reaction energies (bond dissociation energies),  $E_{reac}$  for this simple system, defined by Equation (5.14) and (5.15) respectively.

$$\Delta E_b = \text{Energy of the transition state} - \text{Energy of the reactant} \quad (5.14)$$

$$E_{reac} = \text{Energy of products} - \text{Energy of reactants} \quad (5.15)$$

## CHAPTER 5: DENSITY FUNCTIONAL THEORY MOLECULAR MODELLING AND EXPERIMENTAL PARTICLE KINETICS

---

Figure 5-3 shows the structures examined for H-loss from *para*-, *meta*-, and *ortho*-carbons, and the results in Table 5-3 show  $\Delta E_b$  values of 484, 452 and 485 kJ mol<sup>-1</sup>, respectively.

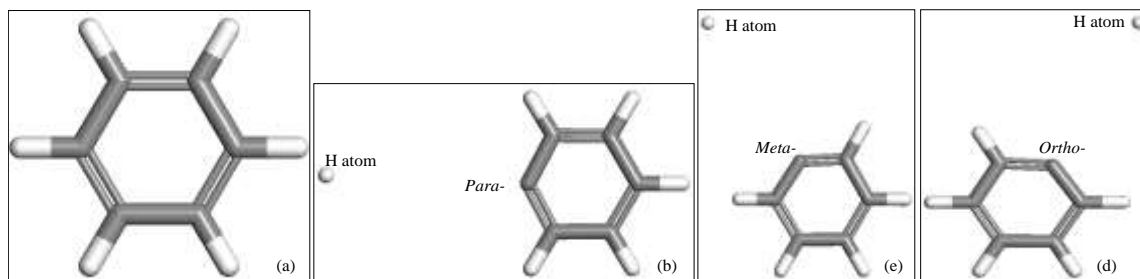


Figure 5-3. Geometry optimized structures for H-loss from (a) benzene molecule at (b) *para*-, (c) *meta*- and (d) *ortho*-carbon sites.

The mean  $\Delta E_b$  value of approximately 474 kJ mol<sup>-1</sup> (113 kcal mol<sup>-1</sup>) for a free C-edge in benzene and  $E_{\text{reac}}$  (comparable to  $\Delta H$ ) for the reaction:  $C_6H_6 \rightleftharpoons C_6H_5 + H$  (Denisov and Denisova, 1999) of 440.7, 440.4 and 443.1 kJ mol<sup>-1</sup> respectively, was obtained. The values compare well with the published value of  $464.0 \pm 8.4$  kJ mol<sup>-1</sup> ( $110.9 \pm 2.0$  kcal mol<sup>-1</sup>) (Michaelides *et al.*, 2003:3704; Chandra and Uchamaru, 2000:9244). These DFT-DNP procedures, used to examine loss of H in the 3x3 PAH char model shown in Figure 5-4(a)-(f) at C<sub>t</sub>-, C<sub>z</sub>-, C<sub>zi</sub>- C<sub>r1</sub>, and C<sub>r2</sub>-carbons, to form free active carbon edge (shown in Figure 5-5b), gave  $\Delta E_b$  values of 489.3, 494.2, 465.9, 455.7 and 459.1 kJ mol<sup>-1</sup> (Table 5-3).

## CHAPTER 5: DENSITY FUNCTIONAL THEORY MOLECULAR MODELLING AND EXPERIMENTAL PARTICLE KINETICS

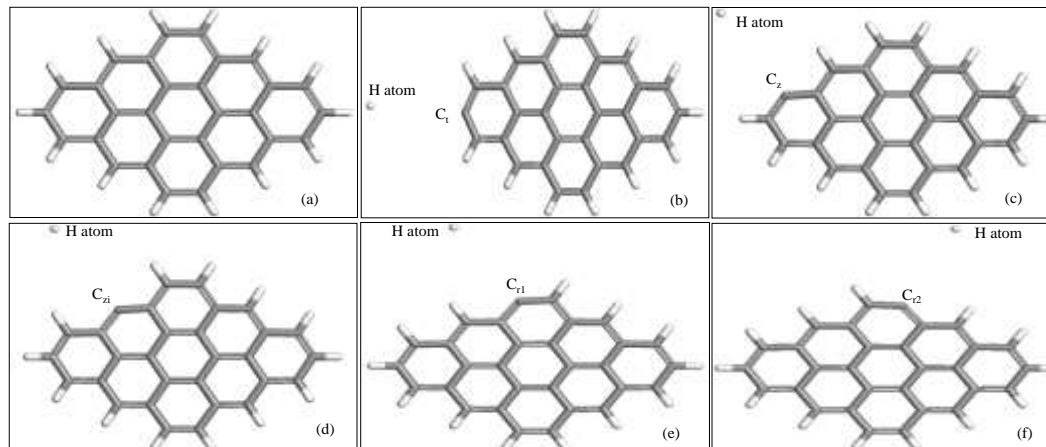


Figure 5-4. Geometry optimised structures for H-loss from (a) 3x3 char structure at (b)-(f) =  $C_{1^-}$ ,  $C_{2^-}$ ,  $C_{zi^-}$ ,  $C_{r1}$  and  $C_{r2^-}$ -carbons, respectively.

The average energy barrier  $\Delta E_b$  was  $472 \text{ kJ mol}^{-1}$  and an average  $E_{\text{reac}}$  (similar to  $\Delta H$ ) value was  $446 \text{ kJ mol}^{-1}$ , for the char structure shown in Figure 5-5(b). The average value for the loss of H to form an active carbon site (reactive edge) is similar to that obtained for benzene, and similar to values for smaller and larger PAHs discussed by others (Michaelides *et al.*, 2003:3704; Chandra and Uchamaru, 2000:9244). It can be argued that the behaviour of the respective edge carbon sites may appear symmetrical while the site is still H-terminated, but becomes unique and does not necessarily obey the symmetry of the molecule in respect with the activation energy  $\Delta E_b$  for loss of H. This argument is supported by the fact that the average  $\Delta E_b$  is in good agreement with reported values.

# CHAPTER 5: DENSITY FUNCTIONAL THEORY MOLECULAR MODELLING AND EXPERIMENTAL PARTICLE KINETICS

Table 5-3. Calculated  $\Delta E_b$  and  $E_{\text{reac}}$  values for the loss of H from the benzene and 3x3 char structures.

<u>Benzene molecule</u>		
Edge C positions for H-loss	$\Delta E_b$ (kJ mol <sup>-1</sup> )	$E_{\text{reac}}$ (kJ mol <sup>-1</sup> )
Para-	484.8	440.6
meta-	452.2	440.4
ortho-	484.4	443.1
Average	473.8	441.4
<u>3x3 PAH char model</u>		
C <sub>t</sub>	489.3	440.6
C <sub>z</sub>	494.2	445.6
C <sub>zi</sub>	464.9	448.6
C <sub>r1</sub>	454.7	452.6
C <sub>r2</sub>	459.1	443.0
Average	472.5	446.1

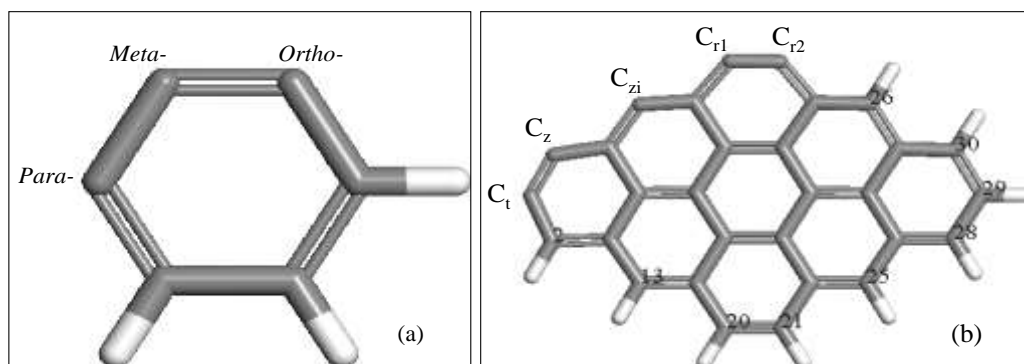


Figure 5-5. Structures with free edge carbon sites, where (a) = Benzene (left-hand side) and (b) = 3x3 char (right-hand side).

## CHAPTER 5: DENSITY FUNCTIONAL THEORY MOLECULAR MODELLING AND EXPERIMENTAL PARTICLE KINETICS

---

### 5.4.3.2 CO<sub>2</sub> chemisorption on reactive edge



The reactive edge was treated as a 3x3 structure with five H-free edge carbon sites, following the loss of H. A distinction between the modelling approaches for the freeing of the reactive edge and the reactivity characteristics of the reactive edge is noted. The freeing of the reactive edge was in terms of the energetics and the treatment of the reactive edge was in terms of the Fukui function (reactivity index). Correlation between these two approaches is not clear from the results obtained. Chemisorption of CO<sub>2</sub> on the active sites in char has been an important area of research and has been extensively discussed (Radovic, 2005:907; Wu and Radovic, 2004:9180; Radovic, 2009:17166; Radović *et al.*, 1983:849; Radovic and Bockrath, 2002:428; Radovic and Bockrath, 2001; Montoya *et al.*, 2003:29; Montoya *et al.*, 2002:1863; Kyotani *et al.*, 1996:2303; Zhu *et al.*, 2002:1359). The  $f^+(r)$  values were computed for the respective reactive sites to evaluate the likely locations for chemisorption and also to obtain the energy of reaction  $E_{\text{reac}}$  and the energy barrier  $\Delta E_b$  for the gasification mechanism at each of these sites. The DFT computations for the 5x5 char model require excessive computer resources, thus effort was restricted to the 3x3 char model. Montoya *et al.* have indicated that the heats of CO<sub>2</sub> chemisorption remained nearly constant as the model size increased, emphasising the chemisorption energies depend significantly on nature of the active site (Montoya *et al.*, 2003:29). Table 5-4 shows the  $f^+(r)$  values for active sites in the 3x3 char model, and the values follow the sequence:  $C_{zi} > C_{r1} > C_t > C_{r2} > C_z$ . The  $f^+(r)$  values indicate the preferred active site is  $C_{zi}$  for CO<sub>2</sub> chemisorption.

## CHAPTER 5: DENSITY FUNCTIONAL THEORY MOLECULAR MODELLING AND EXPERIMENTAL PARTICLE KINETICS

Table 5-4. Distribution of Fukui indices on the 3x3 char model with a reactive edge.

Edge C	C <sub>t</sub>	C <sub>z</sub>	C <sub>zi</sub>	C <sub>r1</sub>	C <sub>r2</sub>	C <sub>2</sub>	C13	C20	C21	C25	C26	C28	C29	C30
Mulliken $f^*(r)$	0.075	0.027	0.266	0.087	0.029	0.017	0.005	0.005	0.011	0.021	0.032	0.026	0.008	0.022

The reaction pathways for gasification of coal chars with CO<sub>2</sub> gas are based on the gasification reaction mechanism shown in Equations (5.3)-(5.5). Figure 5-6(c) is the 3x3-coal char structure and CO<sub>2</sub> at 0.5 nm distance from C<sub>zi</sub> and Figure 5-6(d) shows the DFT-DNP optimised and chemisorbed CO<sub>2</sub> at site C<sub>zi</sub>. Structural configurations shown in Figures 5-6(e)-(h) depict the CO<sub>2</sub> chemisorbed to sites C<sub>r1</sub>, C<sub>t</sub>, C<sub>z</sub>, and C<sub>r2</sub>.

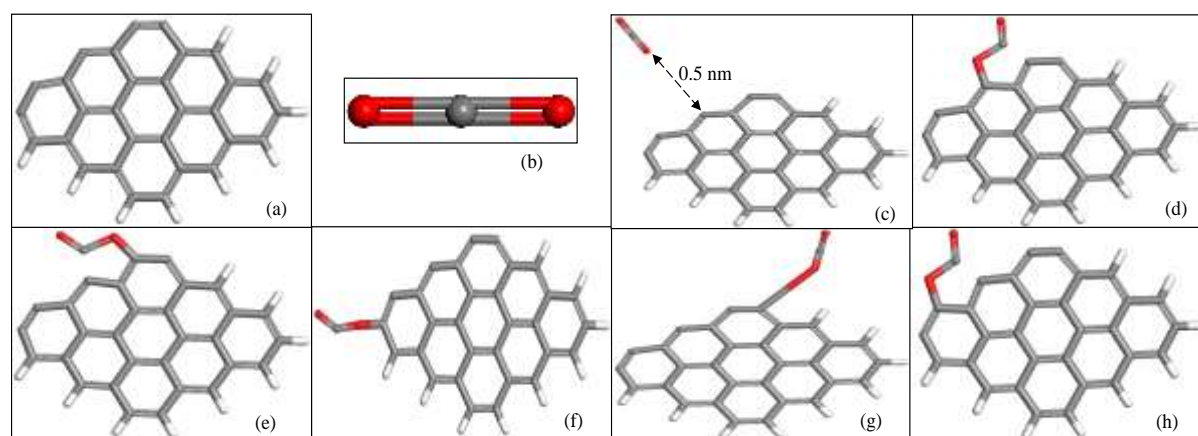


Figure 5-6. Various optimised structures for the CO<sub>2</sub> chemisorption on single active sites in the reactive C\* edge. Top left is 3x3 char model (a), Top right is CO<sub>2</sub> model (b), (c) is the 3x3 char model with free active sites and (d) to (h) the chemisorption structures. Red = oxygen atoms.

The values for  $\Delta E_b$  and  $E_{\text{reac}}$  were computed relative to the initial ground state structures of the CO<sub>2</sub> at distance (e.g. Figure 5-6c) and CO<sub>2</sub> adsorbed on the respective active site (e.g. Figure 5-6d-h). The results in Table 5-5 indicate that these are energetically

## CHAPTER 5: DENSITY FUNCTIONAL THEORY MOLECULAR MODELLING AND EXPERIMENTAL PARTICLE KINETICS

---

favoured, with  $E_{\text{reac}}$  value consistent with CO<sub>2</sub> chemisorbed on the active sites and low  $\Delta E_{\text{b}}$  energy barriers, with a mean  $\Delta E_{\text{b}}$  value of 3.4 kJ mol<sup>-1</sup> and mean  $E_{\text{reac}}$  value of -11.9 kJ mol<sup>-1</sup>. Chemisorption of CO<sub>2</sub> on various carbonaceous models was an exothermic process associated with low adsorption energies (Cao *et al.*, 2009:2991; Radovic, 2009:17166; Radovic, 2005:907; Myers, 2002:145; Liu *et al.*, 2010:1). These values are in contrast to high values reported for perfect and defective basal carbon planes reported by Cabrera-Sanfeliix (Cabrera-Sanfeliix, 2008:493). The optimized configurations for CO<sub>2</sub> at sites -C<sub>zi</sub>, -C<sub>r1</sub>, -C<sub>t</sub>, and -C<sub>z</sub> show approximately similar bond bending behaviour of the chemisorbed CO<sub>2</sub>, highlighting that the mechanism of CO<sub>2</sub> chemisorption obtained from the zigzag models is not significantly different from that obtained from armchair models (Zhu *et al.*, 2002:1359; Kyotani and Tomita, 1999:3434).

These  $E_{\text{reac}}$  values for the CO<sub>2</sub> chemisorption are larger than the theoretical adsorption energies from -355.6 to -25.1 kJ mol<sup>-1</sup> at B3LYP/6-31G(d) DFT level of theory for the different char models found by Montoya *et al.* (Montoya *et al.*, 2003:29). The difference in these computed adsorption energies is more likely due to the physical models and the differences in the electronic states used (Montoya *et al.*, 2001:6757).

## CHAPTER 5: DENSITY FUNCTIONAL THEORY MOLECULAR MODELLING AND EXPERIMENTAL PARTICLE KINETICS

Table 5-5. Simulation energetics for CO<sub>2</sub>-char chemisorption at the reactive edge.

Reactive edge (active C* sites)	$\Delta E_b$ (kJ mol <sup>-1</sup> )	$E_{\text{reac}}$ (kJ mol <sup>-1</sup> )
C <sub>zi</sub>	1.3	-8.4
C <sub>r1</sub> ‡	-	-
C <sub>t</sub>	4.1	-19.2
C <sub>r2</sub> ‡	-	-
C <sub>z</sub>	4.7	-8.2
Average reactive C edge	3.4	-11.9

‡ = Unable to find potential energy maximum for transition state.

The results indicate CO<sub>2</sub> chemisorption is favoured on the C<sub>zi</sub> site. Examination of bond distances on the structures of CO<sub>2</sub> adsorbed on C<sub>zi</sub> as shown in Figure 5-7a, shows that, upon chemisorption, the CO<sub>2</sub> gas molecule assumed a zigzag shape towards C<sub>r1</sub> and the O-C-O bond lengths of the CO<sub>2</sub> gas molecule were elongated from less than 1.2Å to 1.5Å between the chemisorbed O atom and C and more than 1.2Å between the C and the other O atom, while the CO<sub>2</sub>-char bond length was 1.4Å. The chemisorbed CO<sub>2</sub> molecule also bent towards C<sub>r1</sub> is at a distance of 1.5Å. Analyses of these distances with respect to formation and breakage of bonds show that C<sub>zi</sub> is an ideal site for the formation of a quinone char(O)-complex and CO gas molecule from CO<sub>2</sub> dissociation. Similar inferences could be made with CO<sub>2</sub> chemisorption at C<sub>r1</sub> and C<sub>z</sub> in Figure 5-7(b) and (d), respectively. The ground state interactions of C<sub>t</sub>- and C<sub>r2</sub>-CO<sub>2</sub> respectively show weak representations for CO<sub>2</sub> chemisorption, but may be suitable for physisorption processes.

## CHAPTER 5: DENSITY FUNCTIONAL THEORY MOLECULAR MODELLING AND EXPERIMENTAL PARTICLE KINETICS

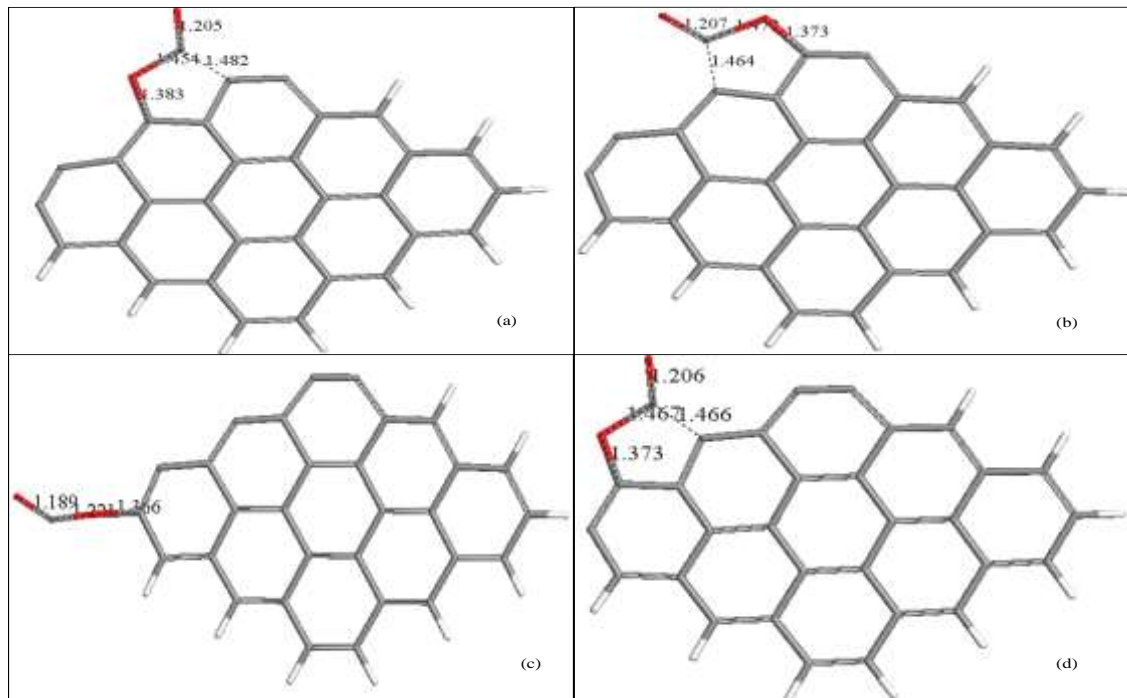


Figure 5-7. Bond bending and elongations of geometry optimised CO<sub>2</sub>-C\* chemisorption structures, where: red = oxygen atoms.

The  $E_{\text{reac}}$  and  $\Delta E_b$  values were not obtained for the CO<sub>2</sub>-C<sub>r1</sub> and CO<sub>2</sub>-C<sub>r2</sub> chemisorption, because of the occurrences of multiple imaginary frequencies (soft modes) in the geometry optimised reactants and products structures, indicative of an absence of TS. Similar observations were reported by Radovic (Radovic, 2009:17166).

### 5.4.3.3 The loss of first CO gas molecule through dissociation of adsorbed CO<sub>2</sub> gas molecule



In this investigation, adsorption of CO<sub>2</sub> on an active site is followed by the loss of CO through the dissociation of the adsorbed CO<sub>2</sub>. This mechanism is the breakage of the char(O---CO) bond. The MEP computation provided the energy barrier corresponding

## CHAPTER 5: DENSITY FUNCTIONAL THEORY MOLECULAR MODELLING AND EXPERIMENTAL PARTICLE KINETICS

---

to a TS (Accelrys, 2011). The  $E_{\text{reac}}$  value for loss of the first CO was obtained as the difference in between the char(CO<sub>2</sub>) structure, and the final products of char(O) plus free CO, as shown in Figure 5-8(a)-(b). The reaction energies for the loss of CO from the respective active sites were endothermic as presented in Table 5-6 (Liu *et al.*, 2010:1), and thus consistent with bond breaking chemical events. The values of 576-588 kJ mol<sup>-1</sup> for C<sub>r1</sub>, C<sub>t</sub> and C<sub>r2</sub> compare fairly well with CO<sub>2</sub> dissociation energy of 526 kJ mol<sup>-1</sup> in literature (Stans). The energy of reaction,  $E_{\text{reac}}$ , and activation energy,  $\Delta E_b$ , of 200.6 and 199.2 kJ mol<sup>-1</sup> for CO<sub>2</sub> chemisorbed on the active site C<sub>zi</sub> are nearly the same, signifying the most favourable pathway for CO<sub>2</sub> dissociation reaction at this site. It can be argued that these values are consistent with an endothermic thermal breakdown of the C—(CO) bond in the chemisorbed CO<sub>2</sub> molecule, but the range of values for all of the active sites is site-dependent and may be as a result of modelling using a number of actives sites. In addition to this, the differences between CO<sub>2</sub> dissociation energetics ( $\Delta E_b$  and  $E_{\text{reac}}$ ) on C<sub>zi</sub> and C<sub>z</sub> are small, therefore, making a zigzag carbon edge the more preferred site (structure) for dissociative chemisorption of CO<sub>2</sub> than the tip and armchair carbon edges. The mean value of energy barrier of 193 kJ mol<sup>-1</sup> on the zigzag carbon edge, comprising C<sub>zi</sub> and C<sub>z</sub> is in good agreement with CO desorption activation energy of 130-205 kJ mol<sup>-1</sup> reported by Montoya *et al.* (Montoya *et al.*, 2001:6757).

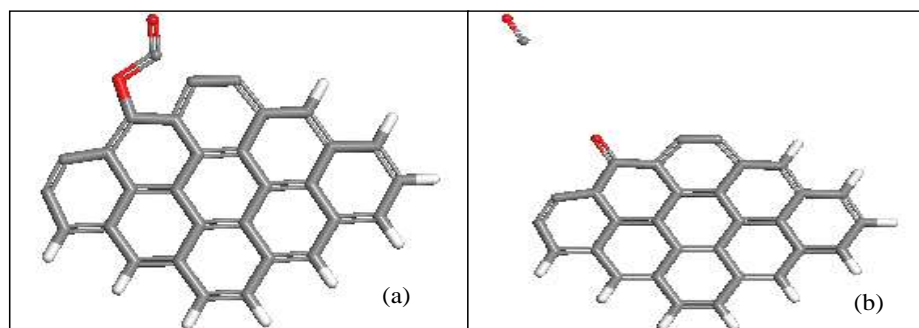


Figure 5-8. Ground state reactants (a), (left-hand side) and products (b), (right-hand side) structures used for the computation of CO<sub>2</sub> dissociation on C<sub>zi</sub>.

## CHAPTER 5: DENSITY FUNCTIONAL THEORY MOLECULAR MODELLING AND EXPERIMENTAL PARTICLE KINETICS

---

Furthermore, from the bond distance analysis of the ground state structure of  $C_z$  in Figure 5-7(d), it is found that the CO from the dissociation reaction stands equal chances of being lost or (re)adsorbed on the adjacent  $C_{zi}$  active site as it is formed. The (re)adsorption option essentially corroborates the highest reactivity margin of  $C_{zi}$ , with the maximum nucleophilic Fukui value,  $f^+(r)$ , of 0.266, as discussed in Section 5.4.1.

Table 5-6. Computed  $E_{\text{reac}}$  and  $\Delta E_b$  for loss of the first CO gas molecule.

Reactive edge (active C* sites)	$\Delta E_b$ (kJ mol <sup>-1</sup> )	$E_{\text{reac}}$ (kJ mol <sup>-1</sup> )
$C_{zi}$	199.2	200.6
$C_{r1}$	587.9	142.1
$C_t$	575.7	155.3
$C_{r2}$	575.8	132.5
$C_z$	185.8	168.3
Average reactive C edge	424.9	159.8

When the transition state is sufficiently refined, the computational procedure will provide  $v_{\text{TS}}$  consistent with a TS complex. The refinement of the TS, however, can require extremely large amount of computer time for large and predicted structures such as the current ones. In view of the modelling limitations involving the large char molecular systems, extremely large computer resources were required, but proved impractical. Consequently, the available computational capabilities were used to obtain values for  $E_{\text{reac}}$  and  $\Delta E_b$  only. For the current purpose, the  $E_{\text{reac}}$  value is similar to  $\Delta H$  values obtained by considering the reactants and products of each step in the mechanisms considered. The most likely transition state for  $\text{CO}_2$  dissociation involves the  $C_{zi}$  site as

## CHAPTER 5: DENSITY FUNCTIONAL THEORY MOLECULAR MODELLING AND EXPERIMENTAL PARTICLE KINETICS

---

shown in Figure 5-9(a), from the TS computations. The CO molecule is situated at a distance of 2.510Å from the quinone oxygen complex, and 2.606Å from the C\* atom on the adjacent aromatic ring. This places the CO almost equidistant from the closest atoms on the char edge, indicating that the CO just formed may result in its (re)adsorption or loss, depending on the reactivity,  $f^*(r)$ , of C\*. Therefore, CO<sub>2</sub> chemisorption was not always accompanied by simple dissociation/loss of CO, as found by Zhu *et al.* (Zhu *et al.*, 2002:1359).

### 5.4.3.4 Formation of the second CO gas molecule



The chemistry considered in this investigation is that of thermal decomposition of the six membered carbon ring to five-membered at elevated temperatures. However, Espinal *et al.* found that the six-membered carbon ring containing the armchair and tip active sites can also form four- and three-membered carbon rings (Espinal *et al.*, 2003:1003). The loss of the second CO would occur by thermal decomposition of a six-member quinone-type (CO) group, and the result is the loss of gaseous CO and formation of either a five member ring in the char substrate, or loss of CO and formation of additional active C\* sites for further chemisorption of additional CO<sub>2</sub> molecules. The bond lengths of the 6-member carbon ring from the geometry optimised 3x3-coal char structure, shown in Figure 5-9(b) (for the C<sub>zi</sub> active site), predict the loss of second CO through the decomposition reaction. These results are in good agreement with those of Montoya *et al.*, where investigations involved the loss of CO from semiquinone carbon-oxygen species in carbonaceous surfaces using *ab initio*/DFT (B3LYP/6-31G(d)) levels of theory (Montoya *et al.*, 2002:4236).

## CHAPTER 5: DENSITY FUNCTIONAL THEORY MOLECULAR MODELLING AND EXPERIMENTAL PARTICLE KINETICS

---

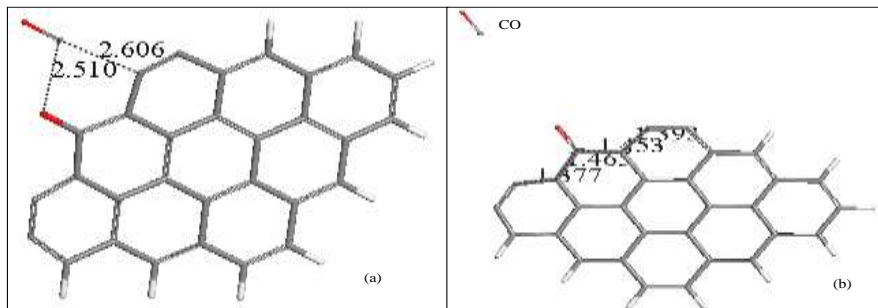


Figure 5-9. Transition state structure at  $C_{zi}$  (a) (left-hand side). Ground state char(C=O) quinone structure (b) (reactants) for the loss of second CO on  $C_{zi}$ . Numbers = bond lengths in Å.

Figure 5-10 shows the transition state structures for the decomposition reactions. The decomposition of the 6-member carbon ring yields a CO ( $C_{zi}O$ ) gas molecule. However, the formation of a five-member carbon ring is considered unlikely at  $C_{zi}$  site, instead the formation of more active  $C^*$  sites (Montoya *et al.*, 2003:29). Ring formation is unlikely because of the long C---C distance in the resulting structure, as shown in Figure 5-10(a). It was found that, from the decomposition reaction energetics presented in Table 5-7, both the high-energy barrier,  $\Delta E_b$ , of  $587.4 \text{ kJ mol}^{-1}$  to the formation of the second CO from  $C_{zi}$  site and endothermic reaction energy,  $E_{\text{reac}}$ , of  $187.9 \text{ kJ mol}^{-1}$  are indicative of the stability of this site. Therefore, loss of the second CO at  $C_{zi}$  site would require relatively higher temperatures. High-energy barrier observed for the loss of second CO group was also reported by others (Chen and Yang, 1998:6348; Sendt and Haynes, 2005:629). Activation energy of approximately  $360 \text{ kJ mol}^{-1}$  was reported by of Chen and Yang (Chen and Yang, 1998:6348) and  $\sim 340 \text{ kJ mol}^{-1}$  was found by Sendt and Haynes (Sendt and Haynes, 2005:629). The high activation energy suggests that this type of semiquinone complex has an important effect on the rate-limiting step in the char gasification mechanism and, in essence, defines gasification (Zhu *et al.*, 2002:1359; Chen and Yang, 1998:6348). The energy barriers,  $\Delta E_b$ , obtained for the  $C_t$ ,  $C_z$ ,  $C_{r1}$  and  $C_{r2}$  sites of 68.4, 136.0, 189.5 and  $183.5 \text{ kJ mol}^{-1}$ , respectively, are

## CHAPTER 5: DENSITY FUNCTIONAL THEORY MOLECULAR MODELLING AND EXPERIMENTAL PARTICLE KINETICS

substantially lower than  $\Delta E_b$  for the  $C_{zi}$  site; these values may be compared with reported values for similar models (83-369 kJ mol<sup>-1</sup> cf 142-334 kJ mol<sup>-1</sup> (Zhu *et al.*, 2002:1359; Espinal *et al.*, 2003:1003)). The mean value for  $\Delta E_b$  of 233 kJ mol<sup>-1</sup> is in good agreement with the experimental value of  $191 \pm 25$  kJ mol<sup>-1</sup> and  $210 \pm 8$  kJ mol<sup>-1</sup> for the de-ashed vitrinite- and inertinite-rich chars, respectively (Section 4). This decomposition reaction is defined as gasification in essence because of its distinction as rate limiting (Zhu *et al.*, 2002:1359; Chen and Yang, 1998:6348).

Table 5-7. Computed  $\Delta E_b$  and  $E_{\text{reac}}$  for loss of second CO gas molecule.

Reactive edge (active C* sites)	$\Delta E_b$ (kJ mol <sup>-1</sup> )	$E_{\text{reac}}$ (kJ mol <sup>-1</sup> )
$C_{zi}$	587.4	187.9
$C_{r1}$	189.5	169.5
$C_t$	68.4	64.5
$C_{r2}$	183.5	173.5
$C_z$	136.0	139.9
Average reactive C edge	233.0	147.0

The structures shown in Figure 5-10(b)-(e) indicate that the  $C_t$ ,  $C_z$ ,  $C_{r1}$  and  $C_{r2}$  sites, respectively, caused decomposition of six-membered rings to five-membered rings with conventional C-C bond lengths. The distances between the newly formed CO and the char = 4.3Å for (b), 2.5Å for (b), 2.8Å for (d) and 3.8Å for (e). Similar distances for (a) are 2.1 and 2.4Å. These results are consistent with the  $\Delta E_b$  values, which show that loss of CO is likely to be easier from structures (b) to (e), but more difficult from structure (a). An average value was used to compare with the experimental results. However, the  $\Delta E_b$

## CHAPTER 5: DENSITY FUNCTIONAL THEORY MOLECULAR MODELLING AND EXPERIMENTAL PARTICLE KINETICS

---

and  $E_{\text{reac}}$  are the lowest at  $C_t$ , indicative of the likelihood for gasification reaction (i.e. yield of second CO gas molecule) to commence at  $C_t$ , given a chemical-reaction rate control.

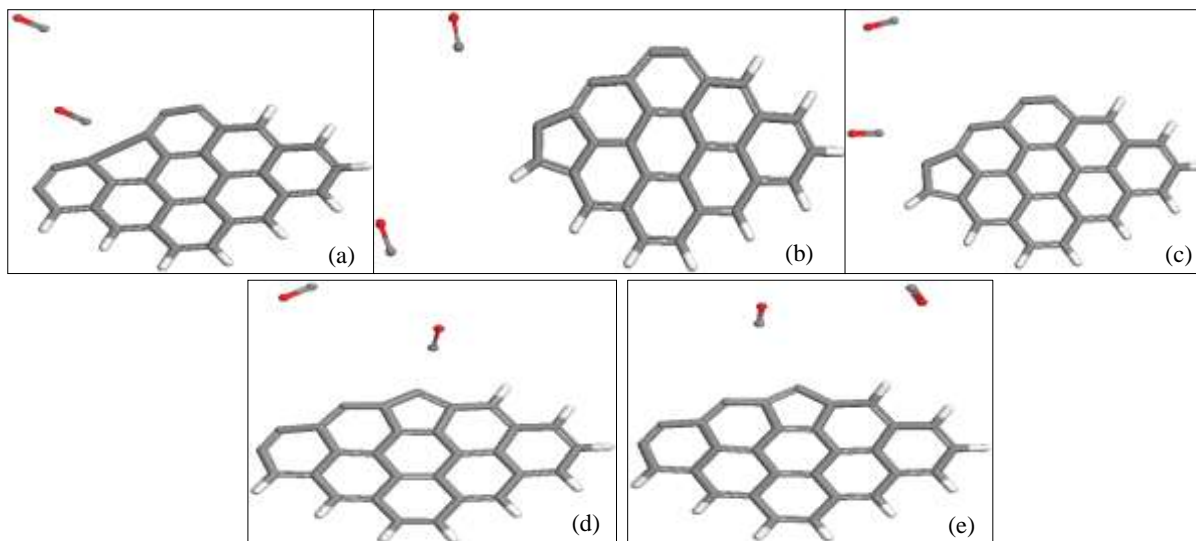


Figure 5-10. Transition state structures for the decomposition reactions at respective active sites (i.e. reactive edge), where, (a)-(e) = results at  $C_{zi}$ ,  $C_t$ ,  $C_z$ ,  $C_{r1}$  and  $C_{r2}$ , respectively. Red = oxygen atoms.

The major focus of the current investigation has been to compare computer molecular modelling results obtained using a simple molecular model with experimental results from char gasification. The surface transformations for the formation of both the first CO gas molecule from the  $\text{CO}_2$  dissociation reactions and the second CO from the decomposition reactions were accompanied by large endothermic energies. These results are consistent with the bond-breaking occurrences for the yield of CO gas molecules.

## CHAPTER 5: DENSITY FUNCTIONAL THEORY MOLECULAR MODELLING AND EXPERIMENTAL PARTICLE KINETICS

---

The exothermic energies obtained for CO<sub>2</sub> chemisorption are taken as relative indicators of the preferred sites for adsorption on a reactive edge. An observation is made of the mean activation energy  $\Delta E_b$  for the CO<sub>2</sub> dissociation reactions that is significantly larger. An inference from this is that the CO<sub>2</sub> chemisorption on a graphene molecule was not always accompanied by dissociation at certain active sites in graphene, as discussed by Zhu et al. [119]. Therefore, in the event that the dissociation of CO<sub>2</sub> did not take place, the gas on active site would desorb. The experimental results obtained for coal-char, however, clearly shows that CO<sub>2</sub> gasification and the activation energy obtained from experimental  $E_a$  results is consistent with the mean values obtained from the modelling results.

### 5.5 Experimental reactivity and parameters (Particle kinetics)

The conversion versus-time results for the char-CO<sub>2</sub> gasification reactions are shown in Figure 5-11, together with the predictions from the random pore model, Equation (5.7). The results are consistent with increasing conversion with increasing temperature and there is good agreement between the experimental results and the RPM prediction with the regressed parameters (structural parameter and lumped reaction parameters), in Equation (5.7). The structural parameters were found to be 2.08 and 1.08 for the inertenite- and vitrinite-rich chars, respectively, which depend on the initial properties of the chars, Equation (5.8). Since the limiting value for pore growth according to the random pore model is greater than a value of 2 (Everson *et al.*, 2008:3403; Everson *et al.*, 2013:148; Bhatia and Perlmutter, 1980:379; Miura *et al.*, 1990:580; Zhang *et al.*, 2008:3213) both chars can be considered to have experienced mainly pore growth and pore coalescence during the initial stage of the char-CO<sub>2</sub> gasification reaction.

## CHAPTER 5: DENSITY FUNCTIONAL THEORY MOLECULAR MODELLING AND EXPERIMENTAL PARTICLE KINETICS

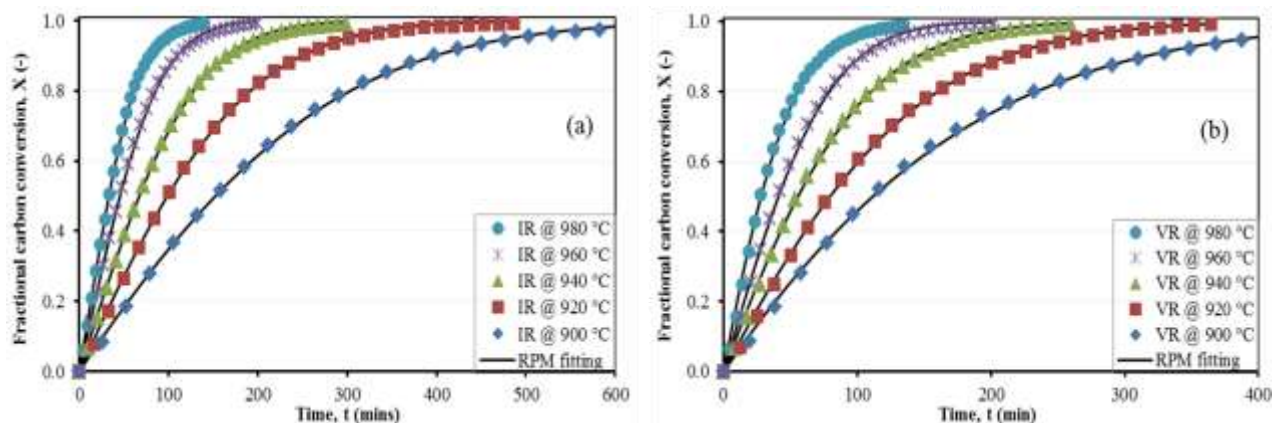


Figure 5-11. Conversion-time plot for inertinite- and vitrinite-rich chars, where, (a), left-hand side = inertinite-rich char and (b), right-hand side = vitrinite-rich chars.

The determined values for the lumped reaction rates as a function of temperature, Figure 5-12, show that the vitrinite-rich char is more reactive than the inertinite-rich char. This difference is attributed to the effect of the char physical properties, Equation (5.8), in addition to the intrinsic reaction rate, which needs to be examined.

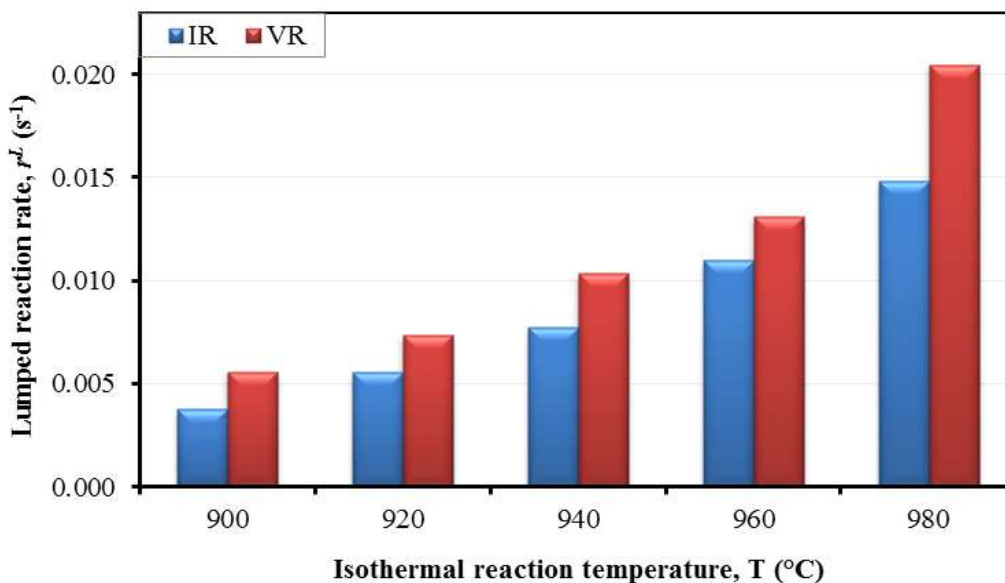


Figure 5-12. Influence of isothermal reaction temperatures on the lumped reaction rates of the chars.

## CHAPTER 5: DENSITY FUNCTIONAL THEORY MOLECULAR MODELLING AND EXPERIMENTAL PARTICLE KINETICS

---

### 5.5.1 Validation of activation energy

The experimental results consisting of the lumped reaction rates derived with the application of the random pore model, given in Figure 5-12, was used to validate the activation energy obtained by the DFT-DNP molecular modelling technique. The result for the two chars are shown in Figure 5-13. The calculation consisted of plotting the results on a graph with semi logarithmic coordinates ( $\ln r^L$  versus  $1/T$ ) and comparing the results obtained from Equation (5.10), using the activation energy of  $233 \text{ kJ mol}^{-1}$  reported in Section 5.4.3.4 together with suitable values for  $r^L$  in Equation (5.12), to ensure the best fit according to linear regression procedure. The agreement was found to be very good within the limits of experimental uncertainty at 95% confidence interval, as shown with the estimated activation energies in Figure 5-15.

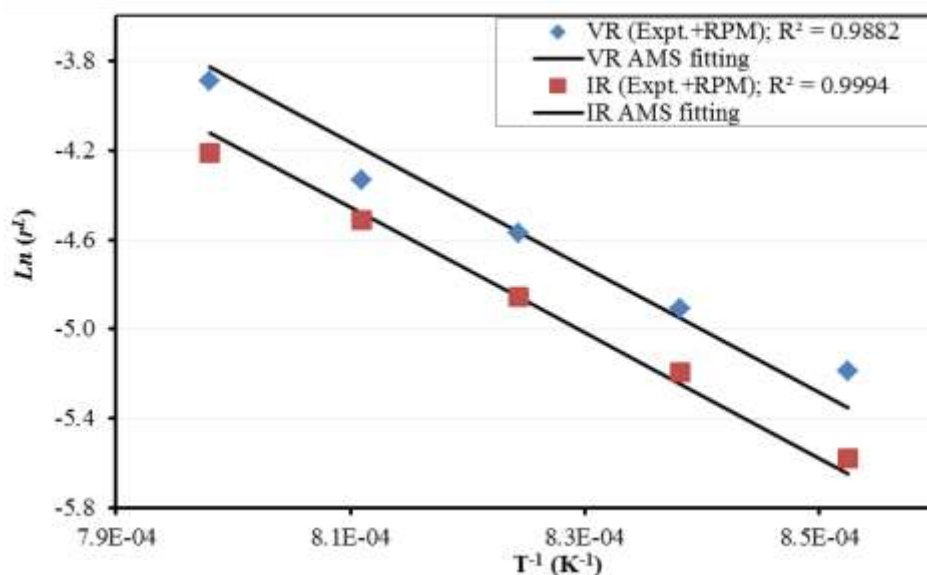


Figure 5-13. Validation of activation energy calculated according to atomistic reaction kinetics with experimental results obtained from thermogravimetric experimentation.

## CHAPTER 5: DENSITY FUNCTIONAL THEORY MOLECULAR MODELLING AND EXPERIMENTAL PARTICLE KINETICS

The results obtained from Equation (5.12) with respect to the lumped reaction rate (experimentally calculated and RPM evaluated) and the activation energy are also in good agreement with the results obtained from the atomistic modelling as shown in Figure 5-14. The pre-exponential factor was calculated from Equation (5.12) for CO<sub>2</sub> gas pressure of 875 kPa and using an order of reaction,  $n$  of 0.6 (Everson *et al.*, 2008:3403; Everson *et al.*, 2013:148). The reaction kinetic parameters for the calculations are shown in Table 5-8. A comparison between the activation energy obtained from the respective procedures is presented in Figure 5-15.

Table 5-8. Estimated reaction parameters.

	Regressed Results		Atomistic modelling results (Activation energy validation)	
	IR	VR	IR	VR
$E_a$ (kJ/mol)	210 ± 8	191 ± 25	233	233
$k'_{S_0}$	1.3E+05	9.7E+04	8.4E+07	1.1E+08

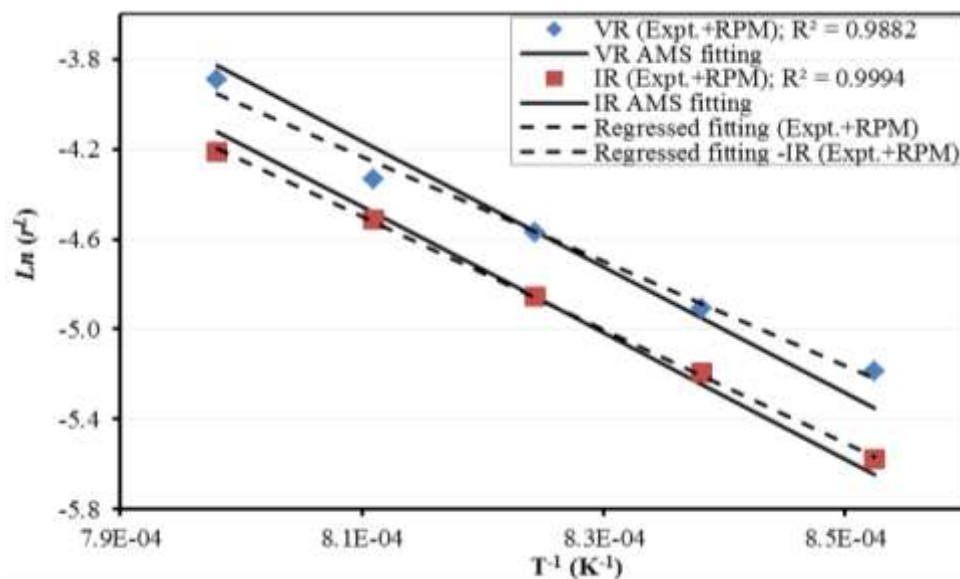


Figure 5-14. Comparison of experimental and model predictions.

## CHAPTER 5: DENSITY FUNCTIONAL THEORY MOLECULAR MODELLING AND EXPERIMENTAL PARTICLE KINETICS

---

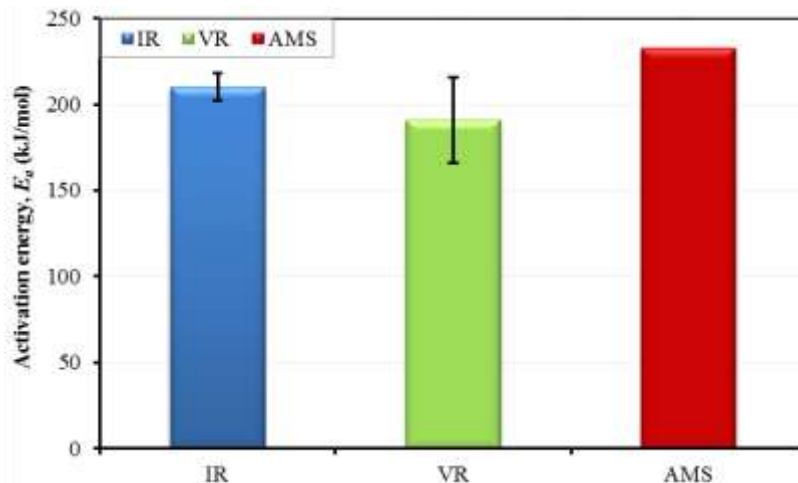


Figure 5-15. Comparison of activation energies.

### 5.5.2 Mechanisms of char gasification by $\text{CO}_2$

The  $\text{CO}_2$  gasification occurs in regime I, which is chemically controlled. The salient features are the formation and accessibility of active sites, which in turn depends mostly on the surface area formed during pyrolysis and formation of each char. The  $\Delta E_b$  value for loss of H from C-H edges to form  $\text{C}^*$  active sites was calculated at a mean value of  $472.5 \text{ kJ mol}^{-1}$ . This value is higher than the computed mean barrier  $\Delta E_b$  for dissociation of  $\text{CO}_2$  to yield the first CO molecule,  $424.9 \text{ kJ mol}^{-1}$ , for all active sites comprising the reactive edge. It is also higher than the mean value for loss of the second CO,  $\Delta E_b$  of  $233 \text{ kJ mol}^{-1}$ , which is defined as gasification in essence because of its distinction as rate-limiting (Zhu *et al.*, 2002:1359; Chen and Yang, 1998:6348). The major step in the mechanism of  $\text{CO}_2$  gasification is thus to liberate the active sites in char. Reaction will occur preferentially at the most reactive sites  $\text{C}_z$  and  $\text{C}_{zi}$ , which are relatively abundant in chars.

The experimental values  $E_a$ , was  $191 \pm 25 \text{ kJ mol}^{-1}$  and  $210 \pm 8 \text{ kJ mol}^{-1}$  for the deashed vitrinite- and inertinite-rich chars, respectively. The results are in agreement with

## CHAPTER 5: DENSITY FUNCTIONAL THEORY MOLECULAR MODELLING AND EXPERIMENTAL PARTICLE KINETICS

---

the computed values and support mechanism that commences with the presence of active sites on the char, formed during pyrolysis and char formation.

The CO<sub>2</sub> gasification begins when active sites are liberated. Therefore, the following descriptive mechanism is proposed and presented in Figure 5-16:

- I. Chemisorption of CO<sub>2</sub> to active sites in char: The various C\* sites located at a reactive edge may be classified as weak and strong. (This should not be confused with the strong and weak adsorption sites for CO<sub>2</sub> reported by Xu *et al* (Xu *et al.*, 2012:118), related to the presence of inorganics in char). Strong adsorption is related to the formation of five member rings between two adjacent C\* sites and adsorbed CO<sub>2</sub>, whereas weakly adsorbed CO<sub>2</sub> occurs at a single C\* site.
  
- I. Yield of the first CO molecule: Two structures may form; one is a stable chemisorbed CO<sub>2</sub> molecule which encounters a lower energy barrier to dissociation, and the other a linear CO<sub>2</sub> molecule adsorbed on a single C\* sites, which encounters a higher energy barrier to dissociation. The latter is expected to result in the desorption of the CO<sub>2</sub> gas molecule and the energetics imply that this is a relatively less favourable reaction.
  
- II. Yield of the second CO: A number of quinone-type char(CO) structures form after loss of the first CO. Those structures may decompose to form CO and relatively stable five member carbon rings in char; however where the stable five-member rings are not energetically favoured, these do not undergo ring formation but instead form additional C\* active sites for further gasification with CO<sub>2</sub>. This decomposition reaction is defined as gasification because of its distinction as rate limiting (Zhu *et al.*, 2002:1359; Chen and Yang, 1998:6348).

## CHAPTER 5: DENSITY FUNCTIONAL THEORY MOLECULAR MODELLING AND EXPERIMENTAL PARTICLE KINETICS

---

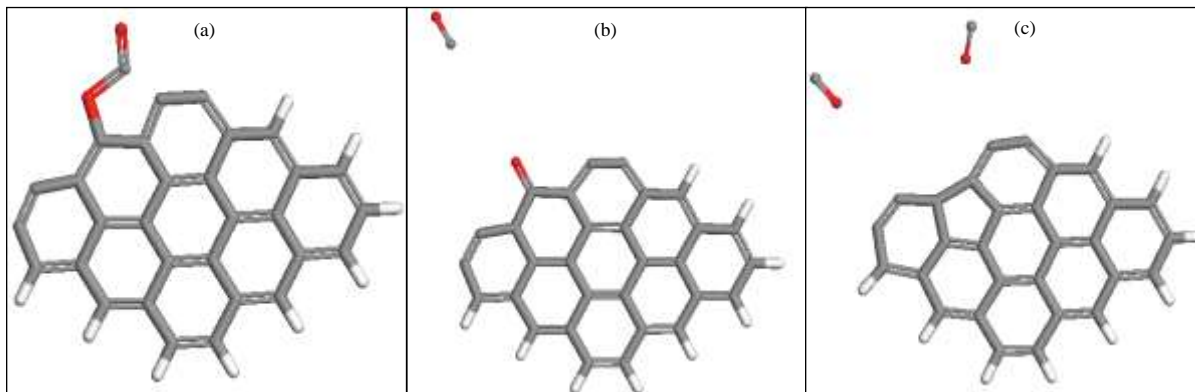


Figure 5-16. Mechanisms of char gasification by CO<sub>2</sub>, where (a) = chemisorption of CO<sub>2</sub> to active sites in char, (b) = yield of first CO and (c) = yield of second CO.

### 5.6 Conclusions

The DFT modelling of CO<sub>2</sub> char gasification for the de-ashed vitrinite- and inertinite-rich chars provides details of the nature of reactive sites in chars structures. A combination of computer modelling and experimental techniques elucidated the diverse nature of active sites in these structures, the various mechanisms for chemisorption of CO<sub>2</sub> on active sites, dissociation of CO<sub>2</sub> into CO and O-complex; the loss of O-complex as CO and resulting char structures. The Fukui function  $f^+(r)$  was a useful indicator of the preferred site for chemisorption of CO<sub>2</sub>. The mean reactivity of H-saturated edge carbons decreased with increasing char molecules and was distributed according to the sequence: zigzag > armchair > tip active sites. In particular, the reactivity of the zigzag active sites decreased with increasing distances from the tip carbons. The average computed energy barrier of 233 kJ mol<sup>-1</sup> compares well with the experimentally measured activation energy of 191 ± 25 kJ mol<sup>-1</sup> and 210 ± 8 kJ mol<sup>-1</sup> for the de-ashed vitrinite- and inertinite-rich chars, respectively. Consequently, the results show a reasonable agreement between DFT modelling outcomes and experimental results.

## CHAPTER 5: DENSITY FUNCTIONAL THEORY MOLECULAR MODELLING AND EXPERIMENTAL PARTICLE KINETICS

---

## CHAPTER 5: DENSITY FUNCTIONAL THEORY MOLECULAR MODELLING AND EXPERIMENTAL PARTICLE KINETICS

### Nomenclature

Symbol	Definition	Units
$\bar{X}$	Arithmetic mean	-
$\Delta_1$	Frequency of modal class minus that of previous class	-
AMS	Atomistic modelling setup	
$\Delta_2$	Frequency of modal class minus that of following class	-
$\Delta E_b$	Atomistic activation energy by generalized synchronous transit method ( $\sim E_a$ )	$\text{kJ mol}^{-1}$
$\Delta H$	Enthalpy	$\text{kJ mol}^{-1}$
1-scf	Single point energy calculations (Simulations)	-
$C$	Number of aromatic carbons per cluster	-
$c$	Size of interval	-
$C^*$	(Re)active carbon site	-
$C_f$	(Re)active carbon site	-
CP-MAS	Cross polarisation-magic angle spinning	-
$d_{002}$	Inter-layer spacing for a group of $N_{\text{ave}}$ parallel layers	$\text{\AA}$
DMol <sup>3</sup>	A modelling program that uses DFT	-
$E_a$	Activation energy	$\text{kJ mol}^{-1}$
$E_{\text{reac}}$	Reaction energy by generalized synchronous transit method ( $\sim \Delta H$ )	$\text{kJ mol}^{-1}$
$f(r)$	Fukui function	-
$f(r)$	Electrophillic Fukui function	-
$f^+(r)$	Nucleophillic Fukui function	-
$f^0(r)$	Radical Fukui function	-
$F_1$	A regression with the activation energy term	-
$F_2$	Constant term	-
$F_a$	Carbon aromaticity	-
$k'_{\text{so}}$	Lumped pre-exponential factor	$\text{min}^{-1} \text{bar}^{-m}$
$L$	Lower boundary of median interval	$\text{\AA}$
$L_0$	Total pore length per unit volume	$\text{m m}^{-3}$
$L_a$	Crystallite diameter	$\text{\AA}$
$M$	Median	$\text{\AA}$

## CHAPTER 5: DENSITY FUNCTIONAL THEORY MOLECULAR MODELLING AND EXPERIMENTAL PARTICLE KINETICS

Symbol	Definition	Units
$N$	Number of data points used	-
$n$	Reaction order	-
$P_{\text{CO}_2}$	Partial pressure of CO <sub>2</sub> gas	Pa
$R_i$	Initial reactivity of chars	min <sup>-1</sup>
$\bar{r}$	Lumped reaction rate	m s <sup>-1</sup>
$r_s$	Reaction rate	m min <sup>-1</sup>
$S$	Standard deviation	-
$S_0$	Initial surface area	m <sup>2</sup> m <sup>-3</sup>
$t$	time	s
$T$	Absolute temperature	K
$t_{0.9}$	Time for fractional carbon conversion of 90%	s
$\nu_{\text{TS}}$	Single negative frequency from generalized synchronous transit method	cm <sup>-1</sup>
$X$	Fractional conversion of carbon	-

### Greek symbols

Symbol	Definition	Units
$\epsilon_0$	Initial porosity of char samples	%
$\theta$	Peak position / XRD angle of scan	radians
$\gamma$	Gamma band/peak	-
$\psi$	Dimensionless structural parameter for char pores	-

### Abbreviations

Acronym	Definition
ALS	Advanced Laboratory Solutions
C-C	Carbon to carbon
CHPC	(National) Centre for high performance computing (Cape Town)
DFT	Density functional theory
DIIS	Direct inversion of the iterative subspace (for SCF convergence)

## CHAPTER 5: DENSITY FUNCTIONAL THEORY MOLECULAR MODELLING AND EXPERIMENTAL PARTICLE KINETICS

---

---

Acronym	Definition
<i>DNP</i>	Double numerical polarization basis set
<i>DTA</i>	Differential thermal analyser
<i>f(r)</i>	Fukui function
<i>GGA</i>	Generalized gradient approximation
<i>HPC</i>	High performance computing (NWU)
<i>HRTEM</i>	High resolution transmission electron microscopy
<i>LAMM</i>	Laboratory of applied molecular modelling (NWU)
<i>LST</i>	Linear synchronous transit (method to search for TS)
<i>MEP</i>	Minimum energy pathway
<i>NMR</i>	Solid state nuclear magnetic resonance spectroscopy
<i>NWU</i>	North-West University
<i>PAH</i>	Polyaromatic hydrocarbons
<i>PES</i>	Potential energy surface
<i>QOF</i>	Quality of fit
<i>QST</i>	Quadratic synchronous transit (method to search for TS)
<i>RMS</i>	Root-mean-square for convergence
<i>RPM</i>	Random pore model
<i>SCF</i>	Self-consistent forcefield
<i>SEM</i>	Scanning electron microscopy
<i>TGA</i>	Thermogravimetric analyser
<i>TPD</i>	Temperature-programmed desorption
<i>TS</i>	Transition state
<i>XRD</i>	X-ray diffraction

---

# CHAPTER 5: DENSITY FUNCTIONAL THEORY MOLECULAR MODELLING AND EXPERIMENTAL PARTICLE KINETICS

---

## 5.7 References

- ACCELRYS, E. C. W. 2011. *RE: Material Studio DMol<sup>3</sup> V6.0. Density Functional Theory Electronic Structure Program. Support Division.*
- AHUJA, P.; KUMAR, S. and SINGH, P. C. 1996. A model for primary and heterogeneous secondary reactions of wood pyrolysis. *Chemical engineering & technology*, 19, 272.
- ANDERSEN, A.; GOVIND, N. and SUBRAMANIAN, L. 2008. Theoretical study of the mechanism behind the para-selective nitration of toluene in zeolite H-Beta. *Molecular Simulation*, 34, 1025.
- ANDZELM, J.; GOVIND, N. and MAITI, A. 2006. Nanotube-based gas sensors—Role of structural defects. *Chemical Physics Letters*, 421, 58.
- BHATIA, S. and PERLMUTTER, D. 1980. A random pore model for fluid-solid reactions: I. Isothermal, kinetic control. *AIChE Journal*, 26, 379.
- BHATIA, S. K. 1998. Reactivity of chars and carbons: New insights through molecular modeling. *AIChE Journal*, 44, 2478.
- BOLAT, E.; SAGLAM, S. and PISKIN, S. 1998. Chemical demineralization of a Turkish high ash bituminous coal. *Fuel Processing Technology*, 57, 93.
- BULTINCK, P.; FIAS, S.; VAN ALSENOY, C.; AYERS, P. and CARBÓ-DORCA, R. 2007. Critical thoughts on computing atom condensed Fukui functions. *The Journal of Chemical Physics*, 127, 034102.
- CABRERA-SANFELIX, P. 2008. Adsorption and reactivity of CO<sub>2</sub> on defective graphene sheets. *The Journal of Physical Chemistry A*, 113, 493.
- CAO, D.-B.; LI, Y.-W.; WANG, J. and JIAO, H. 2009. CO<sub>2</sub> dissociation on Ni(111). *Surface Science*, 603, 2991.
- CASTRO-MARCANO, F.; KAMAT, A. M.; RUSSO JR, M. F.; VAN DUIN, A. C. T. and MATHEWS, J. P. 2012. Combustion of an Illinois No. 6 coal char simulated using an atomistic char representation and the ReaxFF reactive forcefield. *Combustion and Flame*, 159, 1272.
- CHANDRA, A. K. and UCHIMARU, T. 2000. A DFT study on the CH bond dissociation enthalpies of haloalkanes: Correlation between the bond dissociation enthalpies and activation energies for hydrogen abstraction. *The Journal of Physical Chemistry A*, 104, 9244.
- CHATTARAJ, P. K. 2000. Chemical reactivity and selectivity: Local HSAB principle versus frontier orbital theory. *The Journal of Physical Chemistry A*, 105, 511.
- CHEN, J. P. and YANG, R. T. 1989. Chemisorption of hydrogen on different planes of graphite — A semi-empirical molecular orbital calculation. *Surface Science*, 216, 481.
- CHEN, N. and YANG, R. T. 1998. Ab initio molecular orbital calculation on graphite: Selection of molecular system and model chemistry. *Carbon*, 36, 1061.
- CHEN, N. and YANG, R. T. 1998. Ab initio molecular orbital study of the unified mechanism and pathways for gas-carbon reactions. *The Journal of Physical Chemistry A*, 102, 6348.
- CHEN, S. and YANG, R. 1997a. Unified mechanism of alkali and alkaline earth catalyzed gasification reactions of carbon by CO<sub>2</sub> and H<sub>2</sub>O. *Energy & fuels*, 11, 421.
- CHEN, S. G. and YANG, R. T. 1997b. Unified mechanism of alkali and alkaline earth catalyzed gasification reactions of carbon by CO<sub>2</sub> and H<sub>2</sub>O. *Energy & Fuels*, 11, 421.
- CHEN, S. G.; YANG, R. T.; KAPTEIJN, F. and MOULIJN, J. A. 1993. A new surface oxygen complex on carbon: toward a unified mechanism for carbon gasification reactions. *Industrial & Engineering Chemistry Research*, 32, 2835.

## CHAPTER 5: DENSITY FUNCTIONAL THEORY MOLECULAR MODELLING AND EXPERIMENTAL PARTICLE KINETICS

---

- COLLOT, A.-G. 2006. Matching gasification technologies to coal properties. *International Journal of Coal Geology*, 65, 191.
- COUSINS, A.; PATERSON, N.; DUGWELL, D. R. and KANDIYOTI, R. 2006. An investigation of the reactivity of chars formed in fluidized bed gasifiers: The effect of reaction conditions and particle size on coal char reactivity. *Energy & Fuels*, 20, 2489.
- DELLEY, B. 2000. From molecules to solids with the DMol3 approach. *The Journal of Chemical Physics*, 113, 7756.
- DENISOV, E. T. and DENISOVA, T. 1999. *Handbook of antioxidants: bond dissociation energies, rate constants, activation energies, and enthalpies of reactions*, CRC press.
- DOMAZETIS, G.; JAMES, B. and LIESEGANG, J. 2008. Computer molecular models of low-rank coal and char containing inorganic complexes. *Journal of Molecular Modeling*, 14, 581.
- DOMAZETIS, G.; RAOARUN, M. and JAMES, B. D. 2007. Semiempirical and density functional theory molecular modeling of brown coal chars with iron species and H<sub>2</sub>, CO Formation. *Energy & Fuels*, 21, 2531.
- DOMAZETIS, G.; RAOARUN, M.; JAMES, B. D. and LIESEGANG, J. 2008. Molecular modelling and experimental studies on steam gasification of low-rank coals catalysed by iron species. *Applied Catalysis A: General*, 340, 105.
- DYRKACZ, G. R. and BLOOMQUIST, C. A. A. 1992. Use of continuous flow centrifugation techniques for coal maceral separation. 2. Multiple density fractionations of coals. *Energy & Fuels*, 6, 374.
- ERGUN, S.; YASINSKY, J. B. and TOWNSEND, J. R. 1967. Transverse and longitudinal optical properties of graphite. *Carbon*, 5, 403.
- ESPINAL, J. F.; MONDRAGÓN, F. and TRUONG, T. N. 2009. Thermodynamic evaluation of steam gasification mechanisms of carbonaceous materials. *Carbon*, 47, 3010.
- ESPINAL, J. F.; MONTOYA, A.; MONDRAGÓN, F. and TRUONG, T. N. 2003. A DFT study of interaction of carbon monoxide with carbonaceous materials. *The Journal of Physical Chemistry B*, 108, 1003.
- EVERSON, R. C.; NEOMAGUS, H. W.; KAITANO, R.; FALCON, R. and DU CANN, V. M. 2008. Properties of high ash coal-char particles derived from inertinite-rich coal: II. Gasification kinetics with carbon dioxide. *Fuel*, 87, 3403.
- EVERSON, R. C.; NEOMAGUS, H. W. J. P.; KAITANO, R.; FALCON, R.; ALPHEN, C. V. and DU CANN, V. M. 2008. Properties of high ash char particles derived from inertinite-rich coal: 1. Chemical, structural and petrographic characteristics. *Fuel*, 87, 3082.
- EVERSON, R. C.; NEOMAGUS, H. W. J. P.; KASAINI, H. and NJAPHA, D. 2006. Reaction kinetics of pulverized coal chars derived from inertinite-rich coal discards: Gasification with carbon dioxide and steam. *Fuel*, 85, 1076.
- EVERSON, R. C.; OKOLO, G. N.; NEOMAGUS, H. W. J. P. and DOS SANTOS, J.-M. 2013. X-ray diffraction parameters and reaction rate modeling for gasification and combustion of chars derived from inertinite-rich coals. *Fuel*, 109, 148.
- FERNANDEZ-ALOS, V.; WATSON, J. K.; WAL, R. V. and MATHEWS, J. P. 2011. Soot and char molecular representations generated directly from HRTEM lattice fringe images using Fringe3D. *Combustion and Flame*, 158, 1807.
- FRANKCOMBE, T. J.; BHATIA, S. K. and SMITH, S. C. 2002. Ab initio modelling of basal plane oxidation of graphenes and implications for modelling char combustion. *Carbon*, 40, 2341.
- FRANKCOMBE, T. J. and SMITH, S. C. 2004. On the microscopic mechanism of carbon gasification: A theoretical study. *Carbon*, 42, 2921.

## CHAPTER 5: DENSITY FUNCTIONAL THEORY MOLECULAR MODELLING AND EXPERIMENTAL PARTICLE KINETICS

---

- FUENTEALBA, P.; PÉREZ, P. and CONTRERAS, R. 2000. On the condensed Fukui function. *The Journal of Chemical Physics*, 113, 2544.
- FUKUI, K. 1970. Theory of orientation and stereoselection. *Orientation and Stereoselection*. Springer Berlin Heidelberg.
- FURCHE, F. and PERDEW, J. P. 2006. The performance of semilocal and hybrid density functionals in 3d transition-metal chemistry. *The Journal of Chemical Physics*, 124, 044103.
- FUSARO, M.; BARONE, V.; CAUSA, M.; D'AMORE, M. and GARZILLO, C. 2013. Theoretical analysis of the reactivity of carbon nanotubes: local versus topological effects. *Topological Modelling of Nanostructures and Extended Systems*. Springer.
- GALE, T. K.; BARTHOLOMEW, C. H. and FLETCHER, T. H. 1996. Effects of pyrolysis heating rate on intrinsic reactivities of coal chars. *Energy & Fuels*, 10, 766.
- GARCÍA, P.; ESPINAL, J. F.; SALINAS MARTÍNEZ DE LECEA, C. and MONDRAGÓN, F. 2004. Experimental characterization and molecular simulation of nitrogen complexes formed upon NO-char reaction at 270 °C in the presence of H<sub>2</sub>O and O<sub>2</sub>. *Carbon*, 42, 1507.
- GOLOVINA, E. and KLIMOV, A. 1999. On the true kinetic constant of the heterogeneous C+CO<sub>2</sub> gasification reaction. *Combustion, Explosion, and Shock Waves*, 35, 393.
- GOVIND, N.; PETERSEN, M.; FITZGERALD, G.; KING-SMITH, D. and ANDZELM, J. 2003. A generalized synchronous transit method for transition state location. *Computational materials science*, 28, 250.
- HATTINGH, B. B.; EVERSON, R. C.; NEOMAGUS, H. W. and BUNT, J. R. 2011. Assessing the catalytic effect of coal ash constituents on the CO<sub>2</sub> gasification rate of high ash, South African coal. *Fuel Processing Technology*, 92, 2048.
- HENKELMAN, G.; JÓHANNESSON, G. and JÓNSSON, H. 2002. Methods for finding saddle points and minimum energy paths. In: SCHWARTZ, S. (ed.) *Theoretical Methods in Condensed Phase Chemistry*. Springer Netherlands.
- HENKELMAN, G.; UBERUAGA, B. P. and JÓNSSON, H. 2000. A climbing image nudged elastic band method for finding saddle points and minimum energy paths. *The Journal of Chemical Physics*, 113, 9901.
- HUNT, J.; FERRARI, A.; LITA, A.; CROSSWHITE, M.; ASHLEY, B. and STIEGMAN, A. E. 2013. Microwave-specific enhancement of the carbon-carbon dioxide (Boudouard) reaction. *The Journal of Physical Chemistry C*, 117, 26871.
- IRFAN, M. F.; USMAN, M. R. and KUSAKABE, K. 2011. Coal gasification in CO<sub>2</sub> atmosphere and its kinetics since 1948: A brief review. *Energy*, 36, 12.
- JOHNSON, C. A.; PATRICK, J. W. and MARK THOMAS, K. 1986. Characterization of coal chars by Raman spectroscopy, X-ray diffraction and reflectance measurements. *Fuel*, 65, 1284.
- JONES, J. M. and JONES, D. H. 2007. Modelling the competition between annealing and oxidation in the carbon-oxygen reaction. *Carbon*, 45, 677.
- JÓNSSON, H.; MILLS, G. and JACOBSEN, K. W. 1998. Nudged elastic band method for finding minimum energy paths of transition. *Classical and quantum dynamics in condensed phase simulations*. World Scientific.
- JOSEPH, J. T.; FISHER, R. B.; MASIN, C. A.; DYRKACZ, G. R.; BLOOMQUIST, C. A. and WINANS, R. E. 1991. Coal maceral chemistry. 1. Liquefaction behavior. *Energy & Fuels*, 5, 724.
- KAJITANI, S.; HARA, S. and MATSUDA, H. 2002. Gasification rate analysis of coal char with a pressurized drop tube furnace. *Fuel*, 81, 539.

## CHAPTER 5: DENSITY FUNCTIONAL THEORY MOLECULAR MODELLING AND EXPERIMENTAL PARTICLE KINETICS

---

- KAJITANI, S.; SUZUKI, N.; ASHIZAWA, M. and HARA, S. 2006. CO<sub>2</sub> gasification rate analysis of coal char in entrained flow coal gasifier. *Fuel*, 85, 163.
- KAJITANI, S.; TAY, H.-L.; ZHANG, S. and LI, C.-Z. 2013. Mechanisms and kinetic modelling of steam gasification of brown coal in the presence of volatile–char interactions. *Fuel*, 103, 7.
- KUNIOSHI, N. L.; TOUDA, M. and FUKUTANI, S. 2002. Computational study on the formation of five-membered rings in pah through reaction with O<sub>2</sub>. *Combustion and flame*, 128, 292.
- KUSAMA, H.; ORITA, H. and SUGIHARA, H. 2008. DFT investigation of the TiO<sub>2</sub> band shift by nitrogen-containing heterocycle adsorption and implications on dye-sensitized solar cell performance. *Solar Energy Materials and Solar Cells*, 92, 84.
- KYOTANI, T.; ITO, K. I.; TOMITA, A. and RADOVIC, L. R. 1996. Monte Carlo simulation of carbon gasification using molecular orbital theory. *AIChE journal*, 42, 2303.
- KYOTANI, T. and TOMITA, A. 1999. Analysis of the reaction of carbon with NO/N<sub>2</sub>O using ab initio molecular orbital theory. *The Journal of Physical Chemistry B*, 103, 3434.
- LI, Y. and EVANS, J. N. S. 1995. The Fukui function: A key concept linking frontier molecular orbital theory and the hard-soft-acid-base principle. *Journal of the American Chemical Society*, 117, 7756.
- LIU, Z.-S.; WANG, Q.; ZOU, Z.-S. and TAN, G.-L. 2010. Reaction mechanism of carbon gasification in CO<sub>2</sub> under non-isothermal conditions. *Journal of Thermal Analysis and Calorimetry*, 1.
- MARINOV, N.; PITZ, W.; WESTBROOK, C.; CASTALDI, M. and SENKAN, S. 1996. Modeling of aromatic and polycyclic aromatic hydrocarbon formation in premixed methane and ethane flames. *Combustion Science and Technology*, 116, 211.
- MATHEWS, J. P.; FERNANDEZ-ALSO, V.; DANIEL JONES, A. and SCHOBERT, H. H. 2010. Determining the molecular weight distribution of Pocahontas No. 3 low-volatile bituminous coal utilizing HRTEM and laser desorption ionization mass spectra data. *Fuel*, 89, 1461.
- MATSUI, I.; KOJIMA, T.; KUNII, D. and FURUSAWA, T. 1987. Study of char gasification by carbon dioxide. 2. Continuous gasification in fluidized bed. *Industrial & Engineering Chemistry Research*, 26, 95.
- MCLAFFERTY, F. J. and PECHUKAS, P. 1974. Quantum transition state theory. *Chemical Physics Letters*, 27, 511.
- MELIN, J.; APARICIO, F.; SUBRAMANIAN, V.; GALVÁN, M. and CHATTARAJ, P. K. 2004. Is the Fukui function a right descriptor of hard–hard interactions? *The Journal of Physical Chemistry A*, 108, 2487.
- MICHAELIDES, A.; LIU, Z.-P.; ZHANG, C.; ALAVI, A.; KING, D. A. and HU, P. 2003. Identification of general linear relationships between activation energies and enthalpy changes for dissociation reactions at surfaces. *Journal of the American Chemical Society*, 125, 3704.
- MIURA, K.; MAKINO, M. and SILVESTON, P. L. 1990. Correlation of gasification reactivities with char properties and pyrolysis conditions using low rank Canadian coals. *Fuel*, 69, 580.
- MONTOYA, A.; MONDRAGÓN, F. and TRUONG, T. N. 2002. Adsorption on carbonaceous surfaces: cost-effective computational strategies for quantum chemistry studies of aromatic systems. *Carbon*, 40, 1863.
- MONTOYA, A.; MONDRAGÓN, F. and TRUONG, T. N. 2002. First-principles kinetics of CO desorption from oxygen species on carbonaceous surface. *The Journal of Physical Chemistry A*, 106, 4236.
- MONTOYA, A.; MONDRAGÓN, F. and TRUONG, T. N. 2002. Formation of CO precursors during char gasification with O<sub>2</sub>, CO<sub>2</sub> and H<sub>2</sub>O. *Fuel Processing Technology*, 77-78, 125.
- MONTOYA, A.; MONDRAGÓN, F. and TRUONG, T. N. 2003. CO<sub>2</sub> adsorption on carbonaceous surfaces: a combined experimental and theoretical study. *Carbon*, 41, 29.

## CHAPTER 5: DENSITY FUNCTIONAL THEORY MOLECULAR MODELLING AND EXPERIMENTAL PARTICLE KINETICS

---

- MONTOYA, A.; TRUONG, T.-T. T.; MONDRAGÓN, F. and TRUONG, T. N. 2001. CO desorption from oxygen species on carbonaceous surface: 1. Effects of the local structure of the active site and the surface coverage. *The Journal of Physical Chemistry A*, 105, 6757.
- MONTOYA, A.; TRUONG, T. N. and SAROFIM, A. F. 2000. Application of density functional theory to the study of the reaction of NO with char-bound nitrogen during combustion. *The Journal of Physical Chemistry A*, 104, 8409.
- MOULIJN, J. A. and KAPTEIJN, F. 1995. Towards a unified theory of reactions of carbon with oxygen-containing molecules. *Carbon*, 33, 1155.
- MYERS, A. L. 2002. Thermodynamics of adsorption in porous materials. *AIChE Journal*, 48, 145.
- NIEKERK, D. V. and MATHEWS, J. P. 2010. Molecular representations of Permian-aged vitrinite-rich and inertinite-rich South African coals. *Fuel*, 89, 73.
- PANIK, M. J. 2005. *Advanced statistics from an elementary point of view*, Academic Press.
- PARR, R. G. and YANG, W. 1984. Density functional approach to the frontier-electron theory of chemical reactivity. *Journal of the American Chemical Society*, 106, 4049.
- PECHUKAS, P. and MILLER, W. 1976. Dynamics of molecular collisions. *Part, 2*, 269.
- PERDEW, J. P. and WANG, Y. 1992. Accurate and simple analytic representation of the electron-gas correlation energy. *Physical Review B*, 45, 13244.
- PÉREZ, P.; SIMÓN-MANSO, Y.; AIZMAN, A.; FUENTEALBA, P. and CONTRERAS, R. 2000. Empirical energy-density relationships for the analysis of substituent effects in chemical reactivity. *Journal of the American Chemical Society*, 122, 4756.
- PERRY, S.; HAMBLY, E.; FLETCHER, T.; SOLUM, M. and PUGMIRE, R. 2000a. Solid-state carbon-13 NMR characterization of matched tars and chars from rapid coal devolatilization. *Proceedings of the Combustion Institute*, 28, 2313.
- PERRY, S. T.; HAMBLY, E. M.; FLETCHER, T. H.; SOLUM, M. S. and PUGMIRE, R. J. 2000b. Solid-state <sup>13</sup>C NMR characterization of matched tars and chars from rapid coal devolatilization. *Proceedings of the Combustion Institute*, 28, 2313.
- PETERSEN, T.; YAROVSKY, I.; SNOOK, I.; MCCULLOCH, D. G. and OPLETAL, G. 2004. Microstructure of an industrial char by diffraction techniques and Reverse Monte Carlo modelling. *Carbon*, 42, 2457.
- PHAM, B. Q. and TRUONG, T. N. 2012. Electronic spin transitions in finite-size graphene. *Chemical Physics Letters*, 535, 75.
- PULAY, P. 1982. Improved SCF convergence acceleration. *Journal of Computational Chemistry*, 3, 556.
- RADOVIC, L. R. 2005. The mechanism of CO<sub>2</sub> chemisorption on zigzag carbon active sites: A computational chemistry study. *Carbon*, 43, 907.
- RADOVIC, L. R. 2009. Active sites in graphene and the mechanism of CO<sub>2</sub> formation in carbon oxidation. *Journal of the American Chemical Society*, 131, 17166.
- RADOVIC, L. R. and BOCKRATH, B. On some key questions in the application of computational chemistry to carbon reactivity. *Proc. Conf. Carbon*, 2001.
- RADOVIC, L. R. and BOCKRATH, B. 2002. What exactly is on the edges of graphene layers in carbon: the unfolding story. *Preprints Paper-American Chemical Society, Division of Fuel Chemistry*, 47, 428.
- RADOVIC, L. R. and BOCKRATH, B. 2005. On the chemical nature of graphene edges: Origin of stability and potential for magnetism in carbon materials. *Journal of the American Chemical Society*, 127, 5917.
- RADOVIC, L. R.; JIANG, H. and LIZZIO, A. A. 1991. A transient kinetics study of char gasification in carbon dioxide and oxygen. *Energy & fuels*, 5, 68.

## CHAPTER 5: DENSITY FUNCTIONAL THEORY MOLECULAR MODELLING AND EXPERIMENTAL PARTICLE KINETICS

---

- RADOVIC, L. R.; STECZKO, K.; WALKER JR, P. L. and JENKINS, R. G. 1985. Combined effects of inorganic constituents and pyrolysis conditions on the gasification reactivity of coal chars. *Fuel Processing Technology*, 10, 311.
- RADOVIĆ, L. R.; WALKER JR, P. L. and JENKINS, R. G. 1983. Importance of carbon active sites in the gasification of coal chars. *Fuel*, 62, 849.
- RAJ, A.; ZAINUDDIN, Z.; SANDER, M. and KRAFT, M. 2011. A mechanistic study on the simultaneous elimination of soot and nitric oxide from engine exhaust. *Carbon*, 49, 1516.
- ROBERTS, M. J.; EVERSON, R. C.; NEOMAGUS, H. W. J. P.; VAN NIEKERK, D.; MATHEWS, J. P. and BRANKEN, D. J. 2015. Influence of maceral composition on the structure, properties and behaviour of chars derived from South African coals. *Fuel*, 142, 9.
- ROY, R. K.; PAL, S. and HIRAO, K. 1999. On non-negativity of Fukui function indices. *The Journal of chemical physics*, 110, 8236.
- SABLON, N.; PROFT, F. D. and GEERLINGS, P. 2009. Molecular orbital-averaged Fukui function for the reactivity description of alkaline earth metal oxide clusters. *Journal of Chemical Theory and Computation*, 5, 1245.
- SAMARAS, P.; DIAMADOPOULOS, E. and SAKELLAROPOULOS, G. P. 1996. The effect of mineral matter and pyrolysis conditions on the gasification of Greek lignite by carbon dioxide. *Fuel*, 75, 1108.
- SANDER, M.; RAJ, A.; INDERWILDI, O.; KRAFT, M.; KURETI, S. and BOCKHORN, H. 2009. The simultaneous reduction of nitric oxide and soot in emissions from diesel engines. *Carbon*, 47, 866.
- SENDT, K. and HAYNES, B. S. 2005. Density functional study of the chemisorption of O<sub>2</sub> on the armchair surface of graphite. *Proceedings of the Combustion Institute*, 30, 2141.
- SENDT, K. and HAYNES, B. S. 2005. Density functional study of the chemisorption of O<sub>2</sub> on the zig-zag surface of graphite. *Combustion and Flame*, 143, 629.
- SENDT, K. and HAYNES, B. S. 2011. Density functional study of the reaction of O<sub>2</sub> with a single site on the zigzag edge of graphene. *Proceedings of the Combustion Institute*, 33, 1851.
- SENNECA, O.; RUSSO, P.; SALATINO, P. and MASI, S. 1997. The relevance of thermal annealing to the evolution of coal char gasification reactivity. *Carbon*, 35, 141.
- SHARMA, A.; KYOTANI, T. and TOMITA, A. 1999. A new quantitative approach for microstructural analysis of coal char using HRTEM images. *Fuel*, 78, 1203.
- SHEPPARD, D.; TERRELL, R. and HENKELMAN, G. 2008. Optimization methods for finding minimum energy paths. *The Journal of Chemical Physics*, 128.
- SOLUM, M. S.; PUGMIRE, R. J. and GRANT, D. M. 1989. Carbon-13 solid-state NMR of Argonne-premium coals. *Energy & Fuels*, 3, 187.
- SOLUM, M. S.; SAROFIM, A. F.; PUGMIRE, R. J.; FLETCHER, T. H. and ZHANG, H. 2001. <sup>13</sup>C NMR analysis of soot produced from model compounds and a coal. *Energy & Fuels*, 15, 961.
- STANS, M. H. Bond Dissociation Energies in Simple Molecules.
- SUUBERG, E. M. 1991. Thermally induced changes in reactivity of carbons. In: LAHAYE, J. & EHRBURGER, P. (eds.) *Fundamental issues in control of carbon gasification reactivity*. Springer Netherlands.
- UMEMOTO, S.; KAJITANI, S. and HARA, S. 2013. Modeling of coal char gasification in coexistence of CO<sub>2</sub> and H<sub>2</sub>O considering sharing of active sites. *Fuel*, 103, 14.
- VAN NIEKERK, D.; PUGMIRE, R. J.; SOLUM, M. S.; PAINTER, P. C. and MATHEWS, J. P. 2008. Structural characterization of vitrinite-rich and inertinite-rich Permian-aged South African bituminous coals. *International Journal of Coal Geology*, 76, 290.
- WALKER JR, P.; RUSINKO JR, F.; AUSTIN, L.; ELEY, D.; SELWOOD, P. and WEISZ, P. 1959. Advances in Catalysis, vol. Vol. II, 133.
-

## CHAPTER 5: DENSITY FUNCTIONAL THEORY MOLECULAR MODELLING AND EXPERIMENTAL PARTICLE KINETICS

---

- WALKER JR, P.; TAYLOR, R. and RANISH, J. 1991. An update on the carbon-oxygen reaction. *Carbon*, 29, 411.
- WANG, S.-G.; CAO, D.-B.; LI, Y.-W.; WANG, J. and JIAO, H. 2006. CO<sub>2</sub> reforming of CH<sub>4</sub> on Ni(111): A density functional theory calculation. *The Journal of Physical Chemistry B*, 110, 9976.
- WIGNER, E. 1938. The transition state method. *Trans. Faraday Soc.*, 34, 29.
- WIJAYA, N. and ZHANG, L. 2011. A Critical review of coal demineralization and its implication on understanding the speciation of organically bound metals and submicrometer mineral grains in coal. *Energy & Fuels*, 25, 1.
- WU, S.; GU, J.; ZHANG, X.; WU, Y. and GAO, J. 2007. Variation of carbon crystalline structures and CO<sub>2</sub> gasification reactivity of Shenfu coal chars at elevated temperatures. *Energy & Fuels*, 22, 199.
- WU, X. and RADOVIC, L. R. 2004. Ab initio molecular orbital study on the electronic structures and reactivity of Boron-substituted carbon. *The Journal of Physical Chemistry A*, 108, 9180.
- XU, K.; HU, S.; SU, S.; XU, C.; SUN, L.; SHUAI, C.; JIANG, L. and XIANG, J. 2012. Study on char surface active sites and their relationship to gasification reactivity. *Energy & Fuels*, 27, 118.
- XU, W.-C. and TOMITA, A. 1987. Effect of coal type on the flash pyrolysis of various coals. *Fuel*, 66, 627.
- ZHANG, S.-Y.; LU, J.-F.; ZHANG, J.-S. and YUE, G.-X. 2008. Effect of pyrolysis intensity on the reactivity of coal char. *Energy & Fuels*, 22, 3213.
- ZHANG, Y.; HARA, S.; KAJITANI, S. and ASHIZAWA, M. 2010. Modeling of catalytic gasification kinetics of coal char and carbon. *Fuel*, 89, 152.
- ZHU, Z. H.; FINNERTY, J.; LU, G. Q. and YANG, R. T. 2002. A comparative study of carbon gasification with O<sub>2</sub> and CO<sub>2</sub> by density functional theory calculations. *Energy & Fuels*, 16, 1359.

## CHAPTER 6: GASIFICATION EXPERIMENTS OF CHARs WITH CO<sub>2</sub>

---

### Chapter 6: Gasification experiments of 1000 °C chars with CO<sub>2</sub> gas

#### 6.1 Introduction

The description of the experimentation and determination of the reaction rate model and the associated parameters for the gasification of the chars prepared at 1000 °C is presented in this chapter. The results were required for the validation of the atomistic reactive studies reported in Chapter 5, involving essentially the relative activation energies. The gasification involved reaction with pure carbon dioxide in a thermogravimetric analyser (TGA) operating under chemical reaction rate controlling conditions. A full description of the TGA and the associated equipment and the procedure followed is presented in detail. An account of the random pore model used for the model evaluation with the required equations is given followed by detailed presentation and analyses of results consisting of experimentation and modelling. A comparison between the reactive properties of the chars is established involving the activation energies which were considered suitable for the validation of results obtained from the atomistic studies in Chapter 5.

#### 6.2 Reaction rate modelling

##### 6.2.1 Reaction rate models

Many models incorporating structural effects in addition to the intrinsic kinetics have been examined for predicting overall reaction rates, of which the shrinking core model and the random pore model with variations and modifications have been used successfully for many chars (Kajitani *et al.*, 2006:163; Everson *et al.*, 2008:3403; Everson *et al.*, 2013:148; Gavals, 1980:577; Bhatia and Perlmutter, 1980:379; Radovic *et al.*, 1985:311; Ochoa *et al.*, 2001:161; Miura *et al.*, 1990:580). The random pore model (Everson *et al.*, 2008:3403; Everson *et al.*, 2013:148; Bhatia and Perlmutter, 1980:379) accounts for inner pore surface area variations during reaction. The random

## CHAPTER 6: GASIFICATION EXPERIMENTS OF CHARs WITH CO<sub>2</sub>

---

pore model has also been improved to account for non-uniform pore size distributions and for high ash discards (Lu and Do, 1992:21).

### 6.2.2 The random pore model

The important features of random pore model with application to gasification of chars can be described as follows (Bhatia and Perlmutter, 1980:379; Gavals, 1980:577): (1) The heterogeneous char-gas reaction sites occur in cylindrical pores of arbitrary size distribution, which may overlap, grow, collapse or coalesce during reaction, (2) Variations of the active surface area of the char as gasification reaction progresses are accounted for by the initial char physical properties incorporated in a dimensionless structural parameter, and (3) the random pore model is capable of describing conversion that show a maximum reaction rate at certain conversion levels.

The random pore model overall reaction rate in the absence of external and internal diffusion is given by Equation 6.1 (Bhatia and Perlmutter, 1980:379; Everson *et al.*, 2008:3403). This equation consists of a lumped reaction rate term  $r^L$  accounting for chemical reaction (Equations 6.2 and 6.3) and a group of terms accounting the effect of the structural changes which is characterized by a structural parameter,  $\psi$  (Equation 6.4) (Bhatia and Perlmutter, 1980:379; Everson *et al.*, 2008:3403).

$$\frac{dX}{dt} = (1 - X)\sqrt{1 - \psi \ln(1 - X)} \quad (6.1)$$

$$r^L = \frac{r_s S_o}{(1 - \epsilon_o)} \quad (6.2)$$

$$r_s = k_{so} \exp\left(\frac{-E_a}{RT}\right) P_{CO_2}^n \quad (6.3)$$

$$\psi = \frac{4\pi L_o (1 - \epsilon_o)}{S_o^2} \quad (6.4)$$

## CHAPTER 6: GASIFICATION EXPERIMENTS OF CHARs WITH CO<sub>2</sub>

---

By the integration of Equation 6.1, Equation 6.5 for time as a function of conversion is obtained.

$$t = \frac{2}{r^L \psi} \left( \sqrt{1 - \psi \ln(1 - X)} - 1 \right) \quad (6.5)$$

Rearranging Equation 6.5 and expressing the carbon conversion,  $X$ , as a function of time can be obtained (Equation 6.6):

$$X = 1 - \exp \left[ -r^L t \left( 1 + \frac{r^L t \psi}{4} \right) \right] \quad (6.6)$$

In order to evaluate the structural parameter,  $\psi$ , Everson *et al.* (Everson *et al.*, 2008:3403) proposed the use of the reduced time,  $(t/t_{0.9})$ , which can be derived from Equation 6.5 to give Equation 6.7.

$$\frac{t}{t_{0.9}} = \frac{\sqrt{1 - \psi \ln(1 - X)} - 1}{\sqrt{1 - \psi \ln(1 - 0.9)} - 1} \quad (6.7)$$

It can be seen that the ratio  $t/t_{0.9}$  is only dependent on the dimensionless structural parameter,  $\psi$ , and the conversion  $X$ . Thus, a plot of conversion  $X$  versus  $t/t_{0.9}$  can conveniently be used to determine the structural parameter for chemical reaction controlled reactions only.

### 6.2.3 Evaluation procedure

The evaluation procedure adopted for the validation of the random pore model and the determination of the associated parameter consisted of a stage-wise method involving the following: (1) the assessment of the structural parameter according to Equation (6.7) (2) the determination of the lumped reaction rate according to Equation (6.6), and (3) the determination of the activation energy and pre-exponential constant according to Equations (6.3) (Everson *et al.*, 2008:3403). The structural parameter was obtained by

## CHAPTER 6: GASIFICATION EXPERIMENTS OF CHARs WITH CO<sub>2</sub>

---

non-linear regression with the following objective function involving all experimental results obtained at the different temperatures, using Equation (6.7).

$$ESS = \left[ \left( \frac{t}{t_{0.9}} \right)_{Exp} - \left( \frac{\sqrt{1 - \psi \ln(1 - X)} - 1}{\sqrt{1 - \psi \ln(1 - 0.9)} - 1} \right)_{Cal} \right]^2 \quad (6.8)$$

where the subscripts *Exp* and *Cal*, refer to the reduced time determined from the experimental results and the calculated values according to Equation (6.7), respectively.

The lumped reaction rate,  $r^L$ , was also calculated by non-linear regression with known values of the structural parameter involving conversion versus time plots and Equation (6.6). These results were accordingly used to validate the random pore model by comparison of experimental and model results.

With the calculated values of the lumped reaction rates the intrinsic reaction rate parameters in Equation 6.6 were calculated from the following equations derived from Equations (6.2) and (6.3).

$$r^L = k'_{s_0} \exp\left(\frac{-E_a}{RT}\right) \cdot P_{CO_2}^n \quad (6.9)$$

with,

$$k'_{s_0} = \frac{k_{s_0} S_0}{(1 - \varepsilon_0)} \quad (6.10)$$

In order to evaluate the respective reaction rate constants, the well-known procedure involving the logarithmic equivalent of Equation (6.9) and a linear regression calculation was used.

$$\ln(r^L) = -\frac{E_a}{RT} + n \ln(P_{CO_2}) + \ln(k'_{s_0}) \quad (6.11)$$

## CHAPTER 6: GASIFICATION EXPERIMENTS OF CHARs WITH CO<sub>2</sub>

---

The slope of the linear relation obtained was used for the calculation of the  $E_a$ . The lumped pre-exponential factor was calculated from the re-arrangement of Equation (6.11), using the partial pressure of the reactant gas, CO<sub>2</sub>, as 87.5 kPa and assuming that  $n$  is equivalent to 0.6 as determined from previous investigations on similar chars (Everson *et al.*, 2008:3403; Everson *et al.*, 2013:148).

### 6.3 Experimental

Different laboratory reactors have been used for determination of the reaction rates for combustion and gasification of chars consisting of mainly differential reactors and thermogravimetric analysers. In this study, the TGA was used to investigate the char-CO<sub>2</sub> gasification reactivity of the samples. Other investigators have successfully used thermogravimetric analysers in the study of gas-solid reaction kinetics (Dutta *et al.*, 1977:20; Mühlen *et al.*, 1985:944; Matsui *et al.*, 1987:91; Kajitani *et al.*, 2006:163; Mühlen and Sulimma, 1987:145; Everson *et al.*, 2006:418; Everson *et al.*, 2008:3403; Everson *et al.*, 2013:148).

#### 6.3.1 Thermogravimetric analyser

The char-CO<sub>2</sub> gasification experiments were carried out on a TA instruments' SDT Q600 TGA supplied by ALS, South Africa, using the de-ashed chars derived from inertinite-rich and vitrinite-rich South African coals. The SDT Q600 TGA is a versatile equipment that can work within the temperature control range of ambient +5 to 1500 °C with a platinum-rhodium Type R thermocouple; with a temperature accuracy, temperature precision and DTA sensitivity of ± 1 °C, ± 0.5 °C and 0.001 °C, respectively. The TGA is supplied with a very sensitive alumina horizontal beam null balance with a weight sensitivity of 0.1 µg, weight accuracy of ± 0.1% and a repeatability of 99.999%. The controlled temperature zone of the furnace is 50 mm. Gas flow through the TGA furnace is uni-directional over the horizontal balance, thus, a purge gas counter-flow is

## CHAPTER 6: GASIFICATION EXPERIMENTS OF CHARs WITH CO<sub>2</sub>

---

not needed during experiments. The TGA system is equipped with two in-built mass flow controllers for the gas flow control. The results from the experiments, which include weight, temperature, gas flow rates, heat flow and their derivatives, are automatically logged by the TA Advantage™ software that controls the TGA and can be downloaded to other formats for processing.

### 6.3.2 Experimental procedure

The gasification experiments were carried out with CO<sub>2</sub> gas (technical grade) at atmospheric pressure, in the isothermal temperature range of 900 to 980 °C. Sample mass of 10 ± 1 mg of -75 µm particle size was used for each of the experiments on the TGA. The sample was loaded into a 90 µL porous alumina sample holder, carefully placed on the balance pan, and the furnace closed. The equipment (furnace and sample) was flushed with nitrogen gas at a flow rate of 100 cm<sup>3</sup> min<sup>-1</sup> for 25 min; firstly to evacuate any oxidising species in the furnace and secondly to stabilise the balance. After this, the equipment was heated non-isothermally at a heating rate of 30 °C min<sup>-1</sup> in a continuous N<sub>2</sub> gas flow of 100 cm<sup>3</sup> min<sup>-1</sup> to the required isothermal temperature (900-980 °C). As soon as the required isothermal reaction temperature was reached, the N<sub>2</sub> gas flow was automatically turned off and the reaction gas, CO<sub>2</sub>, was turned on. The CO<sub>2</sub> flow rate of 45 cm<sup>3</sup> min<sup>-1</sup> was used for the isothermal gasification experiments.

### 6.3.3 Reaction conditions

Reaction conditions were chosen in order to ensure reaction rate controlling conditions (regime I kinetics) and at temperatures suitable for determination of activation energies and pre-exponential factors according to the Arrhenius equation. A summary of the experimental design and reaction conditions for the experiments is given in Table 6-1. Detailed characteristics of the chars are given in Roberts *et al.* (Roberts *et al.*, 2015:9) and Chapters 3, and 5.

## CHAPTER 6: GASIFICATION EXPERIMENTS OF CHARs WITH CO<sub>2</sub>

---

Table 6-1. Reaction conditions for char-CO<sub>2</sub> gasification experiments.

Variable	Ranges and compositions
Reaction	Gasification of char with CO <sub>2</sub>
Char samples	char IR, and char VR
Char production temperature	1000 °C
Char sample mass	10 ± 1 mg
Char particle diameter	-75 µm
Initial ramp (in N <sub>2</sub> atmosphere)	30 °C·min <sup>-1</sup>
Isothermal reaction temperatures	900, 920, 940, 960 and 980 °C
Reaction gas (CO <sub>2</sub> ) flow rate	45 cm <sup>3</sup> ·min <sup>-1</sup>
Reaction gas concentration	100 % CO <sub>2</sub>
Reaction pressure	Ambient (87.5 kPa in Potchefstroom)

### 6.4 Results and Discussion

The results obtained from the TGA for the two chars at 900 °C are presented in Figure 6-1 showing the mass loss percent as a function of time. The gasification reactions are characterised by a rapid consumption of the carbon in the char during the initial stage followed by a slower rate of consumption and eventually with an asymptotic behaviour until complete gasification of the combustible carbon initially present in the char. Since the chars were de-ashed, the final amounts obtained are very small corresponding to the ash contents of the chars (<1.7 %, db). Reproducibility of the experimental results is discussed in Appendix E.

## CHAPTER 6: GASIFICATION EXPERIMENTS OF CHARs WITH CO<sub>2</sub>

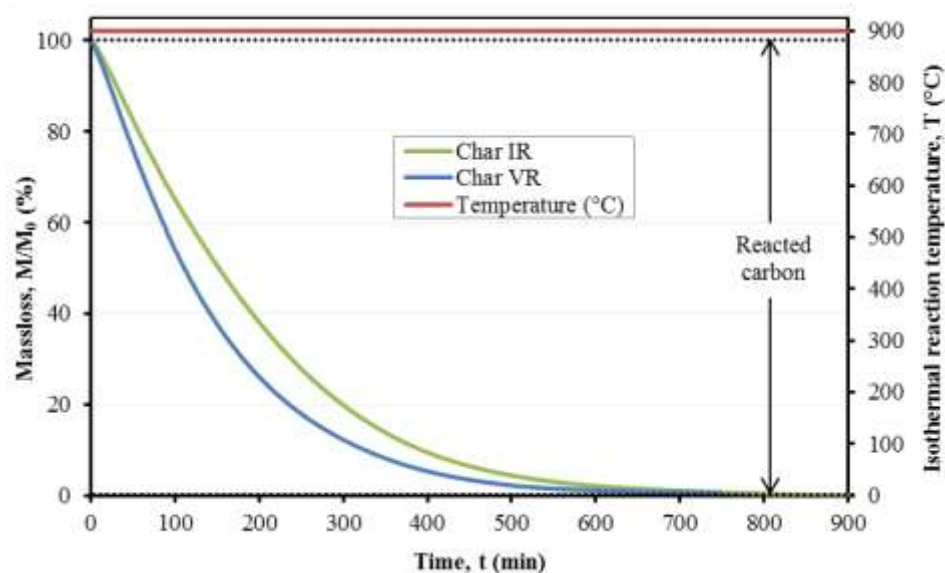


Figure 6-1. Raw TGA results of the isothermal char-CO<sub>2</sub> gasification at 900 °C.

The corresponding conversions,  $X$ , on an ash free basis which were calculated using Equation 6.12 (Dutta *et al.*, 1977:20; Everson *et al.*, 2008:3403; Everson *et al.*, 2006:1076; Everson *et al.*, 2013:148; Hattingh *et al.*, 2011:2048; Umemoto *et al.*, 2013:14) are shown in Figure 6-2 for the respective chars at different temperatures.

$$X = \frac{m_o - m_t}{m_o - m_{ash}} \quad (6.12)$$

The results are consistent with increasing reactivity with temperature as expected, which is controlled by chemical reaction and particle structural changes, such as surface area (Dutta *et al.*, 1977:20; Everson *et al.*, 2008:3403; Everson *et al.*, 2006:1076; Everson *et al.*, 2013:148; Hattingh *et al.*, 2011:2048; Umemoto *et al.*, 2013:14; Kajitani *et al.*, 2006:163; Senneca *et al.*, 1997:141; Wu *et al.*, 2007:199; Zhang *et al.*, 2010:152). The conditions for experimentation were designed to ensure absence of diffusional effects.

## CHAPTER 6: GASIFICATION EXPERIMENTS OF CHARs WITH CO<sub>2</sub>

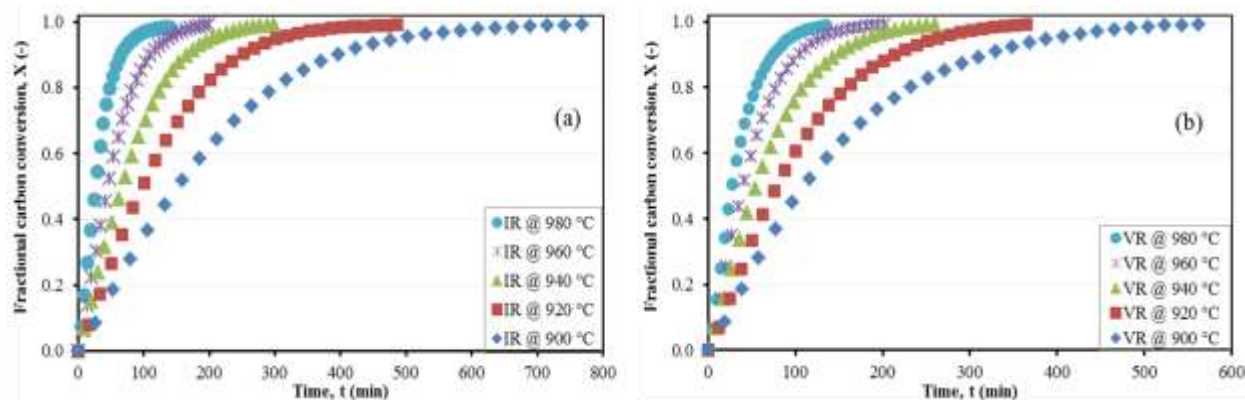


Figure 6-2. Influence of isothermal gasification reaction temperature on the reactivity of the (a) IR (left-hand side) and (b) VR chars (right-hand side).

A comparison of the conversions obtained for the chars at 900 and 980 °C is shown in Figure 6-3. The results indicate that vitrinite-rich char was slightly more reactive than the inertinite-rich char, which, according to Equations (6.1)-(6.4), may be attributed to classical particle kinetics: (1) Structural effects involving essentially char surface area available for reaction, which changes during the reaction, as well as the different initial values. The vitrinite-rich char has a larger initial surface area (Table 6-2); and (2) Chemical reaction, which is the relative intrinsic reactivity of the active surfaces. According to the atomistic reactivity analysis given in Chapter 5, the Fukui function theory also indicated a higher reactivity for the vitrinite-rich char as a result of presence of more smaller molecules (VR char modal value = 21.0Å compared with 36.8Å for IR char). This correlation, however, needs to be examined further in greater detail and was considered beyond the scope of this investigation.

## CHAPTER 6: GASIFICATION EXPERIMENTS OF CHARs WITH CO<sub>2</sub>

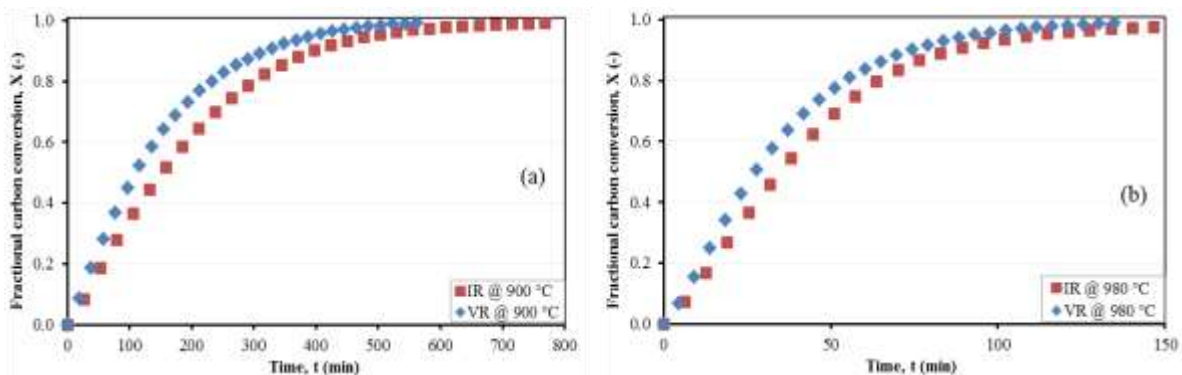


Figure 6-3. Comparison of the CO<sub>2</sub> gasification reactivity of the IR and VR chars. Conversion-time plot at 900 °C (a), left-hand side and 980 °C (b), right-hand side, respectively.

### 6.5 Modelling and evaluation of associated parameters

#### 6.5.1 Model evaluation

The parameters for the random pore model in Equations (6.2) and (6.4) were determined sequentially involving the parameters  $\psi$  and  $t^*$ . This was achieved by regression with the conversion-time results reported above involving one unknown for each calculation.

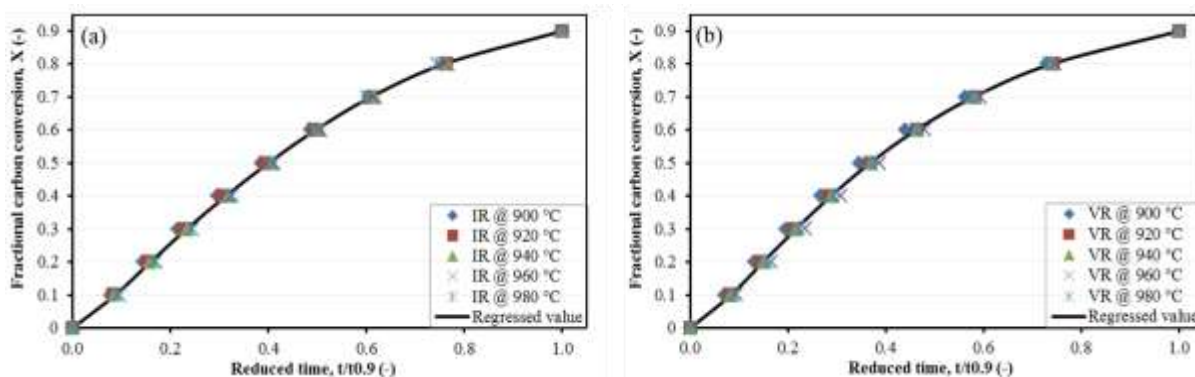


Figure 6-4. Fractional carbon conversion vs reduced time plots of (a) Char IR; and (b) Char VR; at all the isothermal reaction temperatures.

## CHAPTER 6: GASIFICATION EXPERIMENTS OF CHARs WITH CO<sub>2</sub>

---

The results for the determination of the structural parameters are presented for the chars in Figure 6-4, which consists of plots of fractional carbon conversion against reduced time according to Equation (6.7). The resultant structural parameters are shown in Table 6-2. The results (unified plots) confirm the assumption of reaction controlled conditions and was suitable for further analysis (Everson *et al.*, 2008:3403; Everson *et al.*, 2013:148; Bhatia and Perlmutter, 1980:379). The values of the structural parameters of the chars are very different with the inertinite-rich char (IR char) characterised with a  $\psi$  value just greater than two, which indicate that the char is at the limit for initial pore growth to occur during the initial stages of the gasification reaction; whereas for the vitrinite-rich char (VR char) with  $\psi$  value much less than two, which indicates clearly that only pore coalescence occurs (Bhatia and Perlmutter, 1980:379). The lumped reaction rates determined with Equation (6.6) using the experimental results and the respective regressed structural parameters are shown in Table 6-2 for the different temperatures. The results are consistent and it should be noted that, these results includes the effects of porosity and surface area. The corresponding agreement of experimental results and the random pore model results (with  $r^*$  and  $\psi$ ) are shown in Figures 6-5a and b which is considered very good and acceptable for further processing to evaluate the Arrhenius parameters.

### 6.5.2 Reaction rate parameters (intrinsic reaction rate parameters)

The activation energy and the lumped pre-exponential constant were determined using Equation (6.11) according to conventional method described in Section 6.2.3. The results are presented in Figure 6-6 and Table 6-2.

## CHAPTER 6: GASIFICATION EXPERIMENTS OF CHARs WITH CO<sub>2</sub>

Table 6-2. Model parameters.

Properties / Sample ID	Inertinite-rich Char IR	Vitrinite-rich Char VR	Relative rate, $R_{VR}/R_{IR} (R_{rel}) (-)$
Structural Parameters			
RPM Structural parameter, $\psi (-)$	2.08	1.02	-
Surface area (BET), $S_0 (m^2 g^{-1})$	58.4	117.2	-
Initial porosity, $\varepsilon_0 (%)$	3.13	7.83	-
Lumped reaction rates, $r^L (min^{-1})$ Equation (6.13)			
900 °C	3.78E-03	5.60E-03	1.48
920 °C	5.56E-03	7.38E-03	1.33
940 °C	7.77E-03	1.04E-02	1.34
960 °C	1.10E-02	1.31E-02	1.19
980 °C	1.48E-02	2.05E-02	1.39
Reaction rate parameters			
Activation Energy, $E_a (kJ mol^{-1})$	$210 \pm 8$	$191 \pm 25$	-
Lumped pre-exponential factor ( $m Pa^{-n} s^{-1}$ )	$1.3E+05$	$9.7E+04$	-

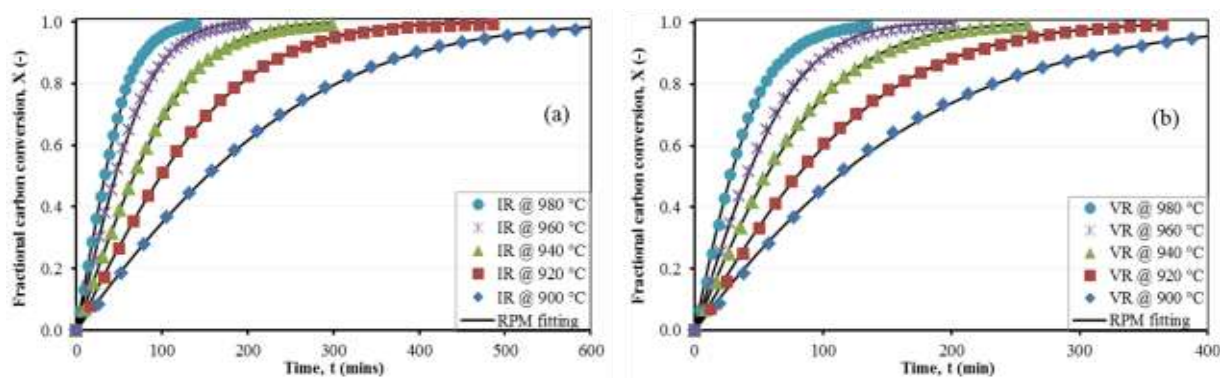


Figure 6-5. RPM fitting to the experimental data of (a) char IR, and (b) VR.

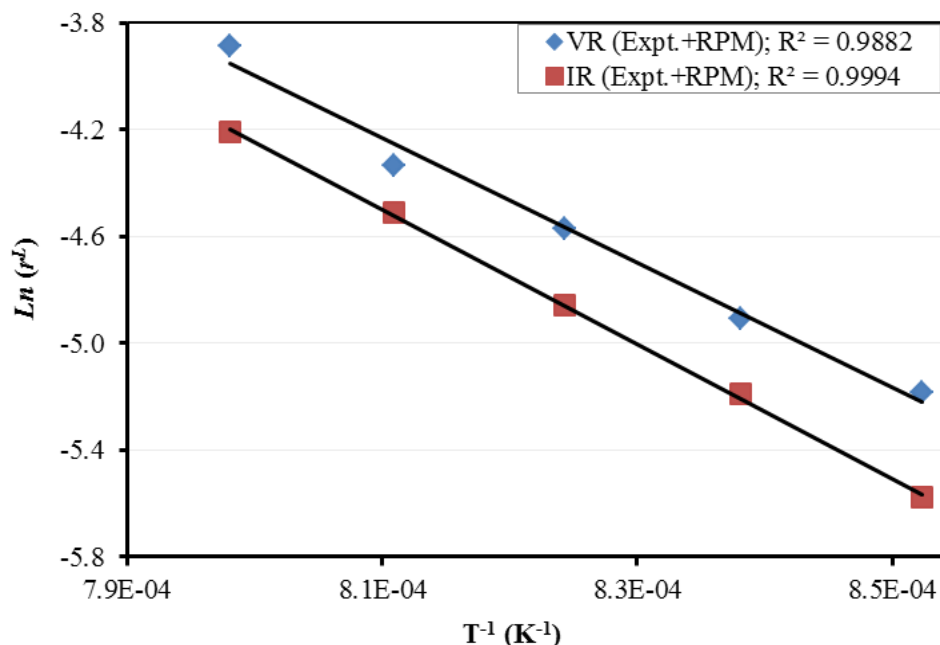


Figure 6-6. Arrhenius plots of the char-CO<sub>2</sub> gasification reactions of chars IR and VR from RPM data.

The estimated activation energies were found to be  $210 \pm 8$  and  $191 \pm 25$  kJ mol<sup>-1</sup> for inertinite-rich and vitrinite-rich chars, respectively, which were considered to be very similar within the limits of the accuracy of the experimentation and regression calculations. The uncertainty calculations associated with these results at 95% confidence interval are shown in Appendix F.

The values of  $E_a$  for the two chars agree well with published results on chars derived from South African coals (Everson *et al.*, 2008:3403), and compares well with published data on coal chars by other investigators (Harris and Smith, 1991:1185; Murillo *et al.*, 2006:11; Ochoa *et al.*, 2001:161; Radovic *et al.*, 1985:311). A comparison of the structural and kinetic parameters from this investigation with reported data from other studies are summarised in Table 6-3 with specific reference to charring temperature and maceral content.

## CHAPTER 6: GASIFICATION EXPERIMENTS OF CHARs WITH CO<sub>2</sub>

Table 6-3. Models used, structural parameter, and kinetic parameters obtained for char-CO<sub>2</sub> gasification reaction by other investigators.

Parent coal type	Maceral abundance <sup>a</sup>	Reactor used	Pyrolysis Temperature range (°C)	Char residence time (min)	Gasification Temperature range (°C)	Model used	RPM $\psi$ (-)	$E_a$ (kJ·mol <sup>-1</sup> )	$k_{s_0}^*$ (mol·min <sup>-1</sup> ·bar <sup>-1</sup> )	Reference
Bituminous	IR	TGA	1000	60	900-980	RPM	2.26	210 ± 8	1.3·10 <sup>5</sup>	IR: This study
Bituminous	VR	TGA	1000	60	900-980	RPM	1.38	191 ± 25	9.7·10 <sup>4</sup>	VR: This study
Bituminous	Inertinite-rich	TGA	900	70	900-950	RPM	1.11-2.58	163-236	2.69·10 <sup>5</sup> -5.22·10 <sup>8</sup>	(Okolo, 2010)
Coal discard	Inertinite-rich	HPTGA	700-900	60	850-900	RPM	1.04	192-266	9.60·10 <sup>8</sup>	(Kaitano, 2007)
Coal discard	IR	TGA	700-900	60	850-900	RPM	1.04	192-247	8.69·10 <sup>7</sup> -1.03·10 <sup>8</sup>	(Everson <i>et al.</i> , 2008:3403)

<sup>a</sup>- Maceral abundance defined by: > 50 vol.%, mmb of inertinite maceral- Inertinite-rich; > 50 vol.%, mmb of vitrinite maceral- Vitrinite-rich.

### 6.6 Conclusions

The random pore model was found to describe the reaction kinetics for the chars very well with results obtained from experimentation with carbon dioxide in a thermogravimetric analyser. The isothermal temperature range (900-980 °C) and reaction gas flow rate were such that the reaction occurred under reaction controlled conditions (regime I). This enabled the determination of the relative activation energies required for the validation of results from the atomistic reactivity studies in Chapter 5. The structural parameters and the lumped reaction rates were very different which influenced the conversions obtained. It was found that the vitrinite-rich char was slightly more reactive than the inertinite-rich char, which can be attributed to the different molecular properties such as the distribution of molecular species with different site activities. In order to fully explain and quantify this effect a more detailed investigation of the molecular structure of the reaction surface would be required.

The activation energy,  $E_a$ , determined using the random pore model to account essentially for the pore variation in addition to the chemical reaction were found to be very similar (210 ± 8 kJ mol<sup>-1</sup> for inertinite-rich char and 191 ± 25 kJ mol<sup>-1</sup> for vitrinite-

## CHAPTER 6: GASIFICATION EXPERIMENTS OF CHARS WITH CO<sub>2</sub>

---

rich char). This result was also found to agree with published results consisting mostly of chars derived from inertinite-rich coals.

## CHAPTER 6: GASIFICATION EXPERIMENTS OF CHARs WITH CO<sub>2</sub>

### Nomenclature

Symbol	Definition	Units
$E_a$	Activation energy	$\text{kJ mol}^{-1}$
$k'_{s0}$	Lumped pre-exponential factor	$\text{m Pa}^{-n} \text{s}^{-1}$
$k_{s0}$	Pre-exponential factor	$\text{m min}^{-1} \text{bar}^{-m}$
$L_0$	Total pore length per unit volume	$\text{m m}^{-3}$
$m_{ash}$	Mass of ash	Mg
$m_o$	Initial mass of char	Mg
$m_t$	Mass of char at time t	Mg
$n$	Reaction order	-
$P_{CO_2}$	Partial pressure of carbon dioxide gas	Pa
$R$	Ideal gas constant	$\text{J K mol}^{-1}$
$r^l$	Lumped reaction rate	$\text{m s}^{-1}$
$r_s$	Intrinsic reaction rate	$\text{m s}^{-1}$
$S_0$	initial surface area	$\text{m}^2 \text{m}^{-3}$
$t$	time	s
$T$	temperature	K
$t/t_{0.9}$	ratio of the experimental real time and time for $X = 0.9$ .	-
$t_{0.9}$	Time for fractional carbon conversion of 90%	Min
$X$	Fractional conversion of carbon	-

### Greek symbols

Symbol	Definition	Units
$\epsilon_0$	Initial porosity of char samples	%
$\psi$	Dimensionless structural parameter for char pores	-

## CHAPTER 6: GASIFICATION EXPERIMENTS OF CHARs WITH CO<sub>2</sub>

---

### Abbreviations

Acronym	Definition
<i>ALS</i>	Advanced laboratory solutions (Supplier)
<i>DTA</i>	Differential thermal analyser
<i>ESS</i>	Error sum of squares
<i>IR</i>	Inertinite-rich
<i>VR</i>	Vitrinite-rich
PBR	Pebble bed reactor
<i>RPM</i>	Random pore model
<i>TGA</i>	Thermogravimetric analyser

---

## CHAPTER 6: GASIFICATION EXPERIMENTS OF CHARs WITH CO<sub>2</sub>

---

### 6.7 References

- BHATIA, S. and PERLMUTTER, D. 1980. A random pore model for fluid-solid reactions: I. Isothermal, kinetic control. *AIChE Journal*, 26, 379.
- DUTTA, S.; WEN, C. Y. and BELT, R. J. 1977. Reactivity of coal and char in carbon dioxide atmosphere. *Industrial & Engineering Chemistry Process Design and Development*, 16, 20.
- EVERSON, R. C.; NEOMAGUS, H. W.; KAITANO, R.; FALCON, R. and DU CANN, V. M. 2008. Properties of high ash coal-char particles derived from inertinite-rich coal: II. Gasification kinetics with carbon dioxide. *Fuel*, 87, 3403.
- EVERSON, R. C.; NEOMAGUS, H. W. and NJAPHA, D. 2006. Kinetic analysis of non-isothermal thermogravimetric analyser results using a new method for the evaluation of the temperature integral and multi-heating rates. *Fuel*, 85, 418.
- EVERSON, R. C.; NEOMAGUS, H. W. J. P.; KASAINI, H. and NJAPHA, D. 2006. Reaction kinetics of pulverized coal chars derived from inertinite-rich coal discards: Gasification with carbon dioxide and steam. *Fuel*, 85, 1076.
- EVERSON, R. C.; OKOLO, G. N.; NEOMAGUS, H. W. J. P. and DOS SANTOS, J.-M. 2013. X-ray diffraction parameters and reaction rate modeling for gasification and combustion of chars derived from inertinite-rich coals. *Fuel*, 109, 148.
- GAVALS, G. R. 1980. A random capillary model with application to char gasification at chemically controlled rates. *AIChE Journal*, 26, 577.
- HARRIS, D. J. and SMITH, I. W. Intrinsic reactivity of petroleum coke and brown coal char to carbon dioxide, steam and oxygen. Symposium (International) on Combustion, 1991. Elsevier, 1185.
- HATTINGH, B. B.; EVERSON, R. C.; NEOMAGUS, H. W. J. P. and BUNT, J. R. 2011. Assessing the catalytic effect of coal ash constituents on the CO<sub>2</sub> gasification rate of high ash, South African coal. *Fuel Processing Technology*, 92, 2048.
- KAITANO, R. 2007. *Characterisation and reaction kinetics of high ash chars derived from inertinite-rich coal discards. Thesis*. North-West University.
- KAJITANI, S.; SUZUKI, N.; ASHIZAWA, M. and HARA, S. 2006. CO<sub>2</sub> gasification rate analysis of coal char in entrained flow coal gasifier. *Fuel*, 85, 163.
- LU, G. and DO, D. 1992. A kinetic study of coal reject-derived char activation with CO<sub>2</sub>, H<sub>2</sub>O and air. *Carbon*, 30, 21.
- MATSUI, I.; KUNII, D. and FURUSAWA, T. 1987. Study of char gasification by carbon dioxide. 1. Kinetic study by thermogravimetric analysis. *Industrial & Engineering Chemistry Research*, 26, 91.
- MIURA, K.; MAKINO, M. and SILVESTON, P. L. 1990. Correlation of gasification reactivities with char properties and pyrolysis conditions using low rank Canadian coals. *Fuel*, 69, 580.
- MÜHLEN, H.-J. and SULIMMA, A. 1987. Thermogravimetric apparatus for characterization of coal with regard to pyrolysis and gasification under pressures up to 100 bar. *Fuel processing technology*, 15, 145.
- MÜHLEN, H.-J.; VAN HECK, K. H. and JÜNTGEN, H. 1985. Kinetic studies of steam gasification of char in the presence of H<sub>2</sub>, CO<sub>2</sub> and CO. *Fuel*, 64, 944.
- MURILLO, R.; NAVARRO, M.; LÓPEZ, J.; GARCÍA, T.; CALLÉN, M.; AYLÓN, E. and MASTRAL, A. 2006. Activation of pyrolytic lignite char with CO<sub>2</sub>. Kinetic study. *Energy & fuels*, 20, 11.
- OCHOA, J.; CASSANELLO, M.; BONELLI, P. and CUKIERMAN, A. 2001. CO<sub>2</sub> gasification of Argentinean coal chars: a kinetic characterization. *Fuel Processing Technology*, 74, 161.
- OKOLO, G. N. 2010. *The effects of chemical and physical properties of chars derived from inertinite-rich, high ash coals on gasification reaction kinetics. Dissertation*. North-West University, South Africa.

## CHAPTER 6: GASIFICATION EXPERIMENTS OF CHARS WITH CO<sub>2</sub>

---

- RADOVIC, L. R.; STECZKO, K.; WALKER JR, P. L. and JENKINS, R. G. 1985. Combined effects of inorganic constituents and pyrolysis conditions on the gasification reactivity of coal chars. *Fuel Processing Technology*, 10, 311.
- ROBERTS, M. J.; EVERSON, R. C.; NEOMAGUS, H. W. J. P.; VAN NIEKERK, D.; MATHEWS, J. P. and BRANKEN, D. J. 2015. Influence of maceral composition on the structure, properties and behaviour of chars derived from South African coals. *Fuel*, 142, 9.
- SENNECA, O.; RUSSO, P.; SALATINO, P. and MASI, S. 1997. The relevance of thermal annealing to the evolution of coal char gasification reactivity. *Carbon*, 35, 141.
- UMEMOTO, S.; KAJITANI, S. and HARA, S. 2013. Modeling of coal char gasification in coexistence of CO<sub>2</sub> and H<sub>2</sub>O considering sharing of active sites. *Fuel*, 103, 14.
- WU, S.; GU, J.; ZHANG, X.; WU, Y. and GAO, J. 2007. Variation of carbon crystalline structures and CO<sub>2</sub> gasification reactivity of Shenfu coal chars at elevated temperatures. *Energy & Fuels*, 22, 199.
- ZHANG, Y.; HARA, S.; KAJITANI, S. and ASHIZAWA, M. 2010. Modeling of catalytic gasification kinetics of coal char and carbon. *Fuel*, 89, 152.

## CHAPTER 7: GENERAL CONCLUSIONS

---

### Chapter 7: General conclusions

#### 7.1 General conclusions

Conclusions are presented from the characterisation results of density separated coals of bituminous medium rank C from Witbank #4 and Waterberg Upper Ecca seams; and their corresponding chars generated at 450, 700 and 1000 °C. The maceral contents of the two coal samples used in this investigation were 85% inertinite and 93% vitrinite by volume, respectively; while the mean random vitrinite reflectance of the respective coals was 0.79 and 0.69%. The characterisation data of the 1000 °C chars were used to construct large-scale atomistic models. Subsequent to this, simplified, single molecule char models without functional atoms were constructed using the data from the HRTEM and XRD techniques. The purpose was to use a high accuracy modelling technique, DFT, to simulate molecular gasification reactions with CO<sub>2</sub>. Gasification experiments were conducted on the 1000 °C chars and compared with the molecular gasification results. The following are the conclusions.

1. The inertinite- and vitrinite-rich chars became similar at 700-1000 °C. The H/C ratios 0.12-0.10 and 0.14-0.12, respectively, compared with 0.68 and 0.80 of the inertinite- and vitrinite-rich coals. The aromaticity values for the two sets of chars were 0.94-0.93 and 0.98-0.96 at 700-1000 °C, respectively, from 0.77 and 0.69 of the respective coals. However, the 1000 °C inertinite- and vitrinite-rich chars were significantly different in respect with Dubinin-Radushkevich surface area (90 and 181 m<sup>2</sup> g<sup>-1</sup>, respectively), CO<sub>2</sub> porosity (3 and 8 Å, respectively) and average crystallite diameter,  $L_a(10)$  (38 and 31 Å, respectively).
2. The coal macerals (inertinite, vitrinite and liptinite) virtually transformed completely into indistinguishable collective at 700-1000 °C, but the char forms significantly distinguished the chars. Greater transition occurred with vitrinite-rich coals, thus highlighting thermal instability of this coal. Changes in the inertinite-group macerals yielded higher proportions of denser chars (60-65%), while char

## CHAPTER 7: GENERAL CONCLUSIONS

---

forms conforming to thick walled coke were predominantly produced by the vitrinite-group macerals.

3. Generally, the chars were similar at chemical level and distinctly different at physical level. The results from the XRD and HRTEM techniques showed a reasonable agreement. The crystallite diameter,  $L_a$  (10), of 37.6Å for the 1000 °C inertinite-rich chars, fell within the range of minimum-maximum length of the 11x11 aromatic fringes (27-45Å). The  $L_a$  (10) of 30.7Å for the vitrinite-rich chars fell closely to minimum-maximum length range of 17-28Å.

4. The characterisation data for the 1000 °C inertinite- and vitrinite-rich chars produced almost similar large-scale atomistic models distinguished specifically by the number and size of molecules. The inertinite-rich char model comprised 106 molecules constructed from a total of 42929 atoms, while the vitrinite-rich char model was made up of 185 molecules consisting of a total of 44315 atoms. The difference between the number of molecules was due to the inertinite-rich char model comprising a higher distribution of larger molecules compared with the vitrinite-rich char model, in agreement with the XRD and HRTEM results.

5. An attempt was made to assess the behaviour of the char models on the basis of gasification reactivity with carbon dioxide gas, by adapting the parallelogram shaped 11x11 and 7x7 PAH molecules (equivalent to modal values) to sizes commensurate with computational abilities of high accuracy, the density functional theory (DFT). Methods from the transition state theory and the Fukui function property gave atomistic reactivity results in fairly good agreement with the experimental data.

6. The average atomistic reactivity using the nucleophilic Fukui function decreased with increasing size of the parallelogram-shaped char models (PAH) and reactivity of PAH edge carbons decreased according to the sequence zigzag > armchair > tip active carbon sites.

## CHAPTER 7: GENERAL CONCLUSIONS

---

7. The Fukui function  $f^+(r)$  was a useful reactivity indicator of the preferred site for the chemisorption of  $\text{CO}_2$ , where the function  $f^+(r)$  is a measure of reactivity toward a donor reagent (nucleophilic attack)
  
8. The  $\text{CO}_2$ -char gasification reaction mechanism using the DFT approach showed that breakdown of the C-H bonds at high temperatures to free the active carbon sites was associated with large enthalpies and activation energies. The subsequent reactive edge had the following  $\text{CO}_2$ -char chemisorption reactivity sequence:  $C_{zi} > C_{r1} > C_t > C_{r2} > C_z$ .
  
9. The experimental activation energies of  $191 \pm 25 \text{ kJ mol}^{-1}$  and  $210 \pm 8 \text{ kJ mol}^{-1}$  using the random pore model for the de-ashed vitrinite- and inertinite-rich chars with  $\text{CO}_2$ , respectively, were found to be similar and compared well with the mean atomistic activation energy for the formation of second CO gas molecule, of  $233 \text{ kJ mol}^{-1}$  using the DFT technique.

## CHAPTER 7: GENERAL CONCLUSIONS

---

### 7.2 Contributions to the knowledge base of coal science and technology

The contribution made to the coal science and technology is summarised as follows:

1. The characterisation of slow-heated South African inertinite- and vitrinite-rich chars of high temperature range, 700-1000 °C, showed that the chars were chemically similar but with different physical structural parameters.
2. Molecular modelling techniques yielded large-scale atomistic representations of coal chars, information of which is scarce. These molecular structures complemented the only two models on Permian-aged coal.
3. The DFT reactivity simulations successfully used very uncommon reactivity indicator in coal science and technology: the Fukui function. The Fukui function is usually given as the change in the density function of the molecule as a consequence of changing the number of electrons in the molecule and allows a chemical reaction to be understood in terms of the HOMO and LUMO. The function  $f^+(r)$  is a measure of reactivity toward a donor reagent (nucleophilic attack),  $f(r)$  values measure reactivity toward an acceptor reagent (electrophilic attack) and an average value of both may be taken as a measure of reactivity toward a radical  $f^\rho(r)$ .
4. The char models used in the DFT reactivity simulations were derived from coal and excluded the functional atoms, therefore, contributing significantly to the utility of molecular models of coal/char using techniques of high accuracy, such as the density functional theory).
5. The atomistic activation energy of 233 kJ mol<sup>-1</sup> using the high-accuracy DFT technique for the formation of second CO gas molecule, derived from the gasification reaction mechanism studied in this thesis, was validated by the

## CHAPTER 7: GENERAL CONCLUSIONS

---

experimental relative activation energies of  $191 \pm 25 \text{ kJ mol}^{-1}$  and  $210 \pm 8 \text{ kJ mol}^{-1}$  using the random pore model.

6. This work established a valuable abilities to use local high performance computing facilities in South African coal chars and provided a good guideline to expand research in this area, and amplifying the South African coal science.

7. It is widely recognised that coal gasification is likely to be part of the spectrum of energy production techniques, especially in countries with low sustainable resources. This is the area that this thesis sought to inform and consequently makes a clear long-term contribution to energy security.

8. The techniques used in this thesis have a substantive potential to be applicable to the global carbon-based resources, in particular to the clean coal science and technology.

## CHAPTER 7: GENERAL CONCLUSIONS

---

### 7.3 Recommendations and future work

1. It is recommended that the atomistic CO<sub>2</sub>-char reactivity modelling should involve larger char models to balance between accuracy and representativeness (e.g. semi-empirical and molecular dynamics modelling techniques).
2. The studies of coal chars generated at 1000 °C may be supplemented by molecular models of chars from lower and higher pyrolysis temperatures. This will give a good visualisation and molecular behaviour of structural evolution, especially for the 700-900 °C chars.
3. It is recommended that DFT modeling technique using the Fukui function be explored on char models with functional atoms and ash to compare with experimental results.
4. It is recommended that DFT modelling efforts be conducted on char models with defects in the basal plane.
5. A follow up research on the Fukui function reactivity indicator and its experimental validation is recommended, since this index is uncommon in coal/char reactivity measurements.
6. It is necessary to give account of occurrences after the formation of a five-membered carbon ring until the whole char molecule has reacted.

## APPENDIX: APPENDIX A: PETROGRAPHIC ANALYSES

---

Appendix

Appendix A: Petrographic analyses

A1. Blocks and macerals. (See figure captions for details)



Figure A-1. Blocks prepared for petrographic analysis.

## APPENDIX A: PETROGRAPHIC ANALYSES

---

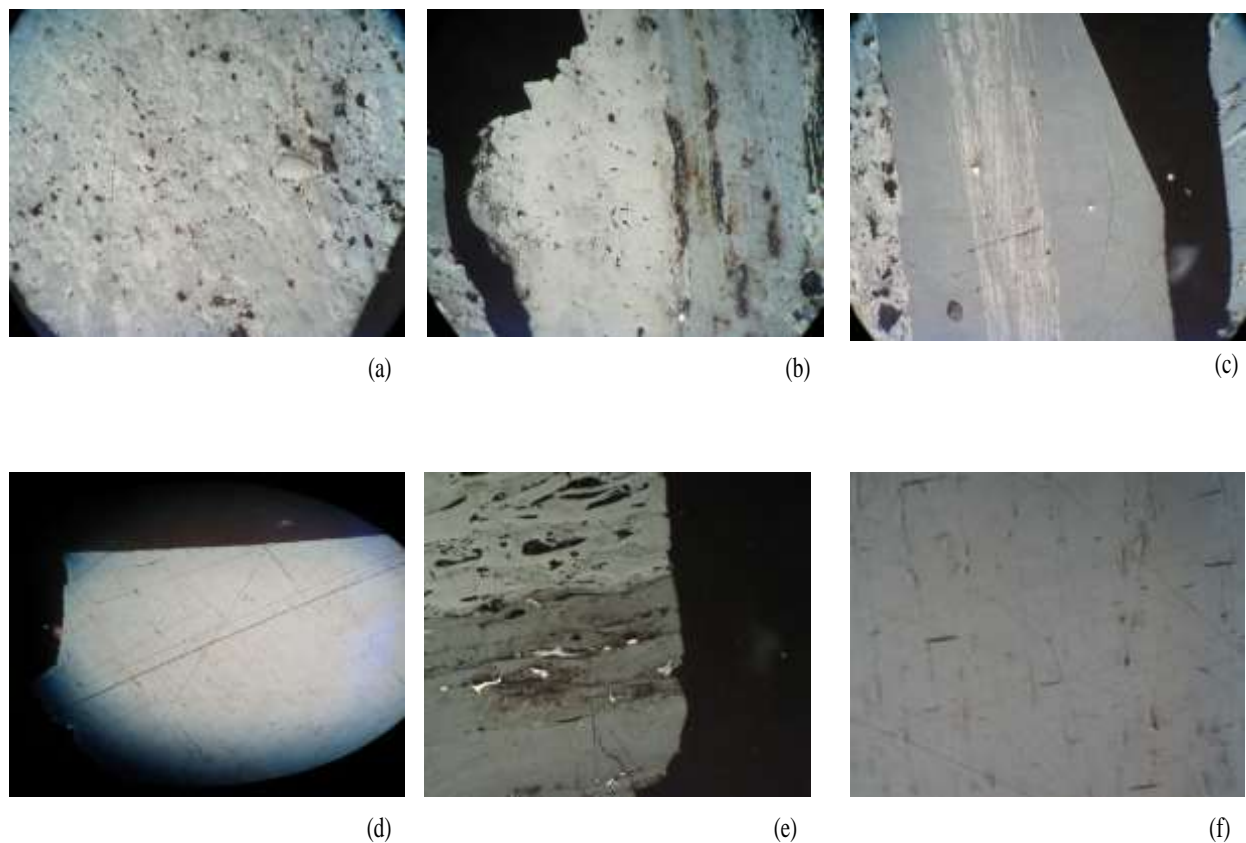


Figure A-2. Major macerals found during petrographic analysis. Inertodetrinite with semifusinite ((a), top row left). Semifusinite ((b) top row middle). Micrinite and pyrite in colotellinite ((c), top row right). Colotellinite ((d), bottom row left). Copotellinite between inertinites ((e), bottom row middle). Pseudovitrinite ((f), bottom row right).

### A2 Repeatability of maceral counting

The repeatability is illustrated in Table A-1, where, for an example, if the volume percentage of vitrinite in a sample were 80%, then the analyst can expect to obtain two results differing by less than 5.1% percentage points (i.e., 76 or 84%) in 19 cases out of 20. The theoretical standard deviation,  $\sigma$ , and repeatability limit of the percentage of a maceral component is an important ingredient in both manual and automated point count systems (Cloke *et al.*, 1995:654). The repeatability of the determination of the abundance of a phase can be defined as 'that value of the difference between two

## APPENDIX A: PETROGRAPHIC ANALYSES

---

single determinations, each based on the same number of point counts carried out by the same operator on the same block using the same apparatus, below which 95% of such differences are expected to lie' (Cloke *et al.*, 1995:654). The repeatability of a result for a given phase is approximately three times the theoretical standard deviation for that phase (Cloke *et al.*, 1995:654). Assuming that the operator makes negligible errors in the identification of individual phases the repeatability is given by Equation (A2.1) (Cloke *et al.*, 1995:654):

$$\text{Repeatability} = (2\sqrt{2})\sigma \quad (\text{A2.1})$$

Table A-1. Theoretical standard deviation and repeatability limit of the percentage of a component, based on counts of 500 points.

---

Volume %	Standard Deviation	Coefficient of Variation	Repeatability Limit
5	1	20	2.8
20	1.8	9	5.1
50	2.2	4.4	6.3
80	1.8	2.3	5.1
95	1	1.1	2.8

---

## APPENDIX A: PETROGRAPHIC ANALYSES

---

### A3. Classification system for the coal chars

The microscopic constituents of the samples were assessed by virtue of their colour, reflectance, and degree of anisotropy, size, morphology and extent of devolatilisation. The relative proportions of the carbon-rich constituents/inorganic materials in each case were established on the basis of a 500 point-count according to the method set out in the ISO Standard 7404 – 3 (1994). The following system of main groups and categories was used:

Table A-2. Classification system used in the petrographic analyses of chars.

Group A	
The components included in this group all showed relatively very high reflectances in normal white light. Oxidation effects were minimal or absent.	
Category 1: Relatively dense char	Category 2 and 3: Networks
<p>Char largely retaining original coal maceral structure.</p> <p><u>From coal vitrinites.</u> These carbon forms sometimes exhibited relatively small gas pores but no well-developed substantially larger devolatilization vesicles.</p> <p><u>From coal inertinites.</u> These carbon forms were derived from inertinites in the parent coal which had not softened, expanded and “opened up” to any very appreciable extent on charring, largely retaining their original coal maceral shape and form. These carbons were of relatively low</p>	<p>Mainly formed from bi- and tri-macerite, the reactive macerals having devolatilized and “plastified” leaving a network of very highly reflecting material.</p> <p><u>Fine walled.</u> High porosity</p> <p><u>Thick walled.</u> Medium porosity</p>

## APPENDIX A: PETROGRAPHIC ANALYSES

porosity.		
Group B		
These components could be classified as “Coke”, i.e. continuous carbon matrices formed from vitrinites and reactive inertinites. The particles were highly reflecting. Oxidation features were minimal or absent.		
Category 4 and 5: Circular anisotropic	Category 6: Incipient anisotropic	Category 7: Isotropic
Carbon textures exhibiting approximately circular regions of distinctly marked anisotropy.  <u>Fine circular anisotropic.</u> Anisotropy in the 0.5 to 1.0 micron size category.  <u>Medium Circular Anisotropic.</u> Anisotropy in the 1.0 to 1.5 micron size category.	Anisotropic forms showing less well-developed textures with domain size of less than 0.5 microns.	Derived from vitrinite in the original coal; porous but no developed texture.
Group C		
These constituents all exhibited relatively lower reflectances and marked oxidation features, in most cases very distinct oxidation rims.		
Category 8: Oxidised	Category 9: Oxidised	Category 10: Oxidised
Mainly from vitrinite.	Mainly from inertinite.	Mainly from network.

## APPENDIX A: PETROGRAPHIC ANALYSES

---

Group D	
Original coal macerals which have been little affected by the process.	
Category 11: Original coal	Category 12: Original coal
Unaffected.	Partially affected.
Group E	
Category 13: Inorganic matter	Category 14: Inorganic matter
Apparently derived from the minerals in the parent.	Apparently additive to the original coal.
Group F	
Category 15. Process-derived depositional carbons, including pyrolytic and spherulitic carbons	

### Reference

CLOKE, M.; LESTER, E.; ALLEN, M. and MILES, N. J. 1995. Repeatability of maceral analysis using image analysis systems. *Fuel*, 74, 654.

## APPENDIX B: X-RAY DIFFRACTION

### Appendix B: The XRD analyses

B.1: Changes in diffractogram patterns from parent coals to chars. See figure captions for details.

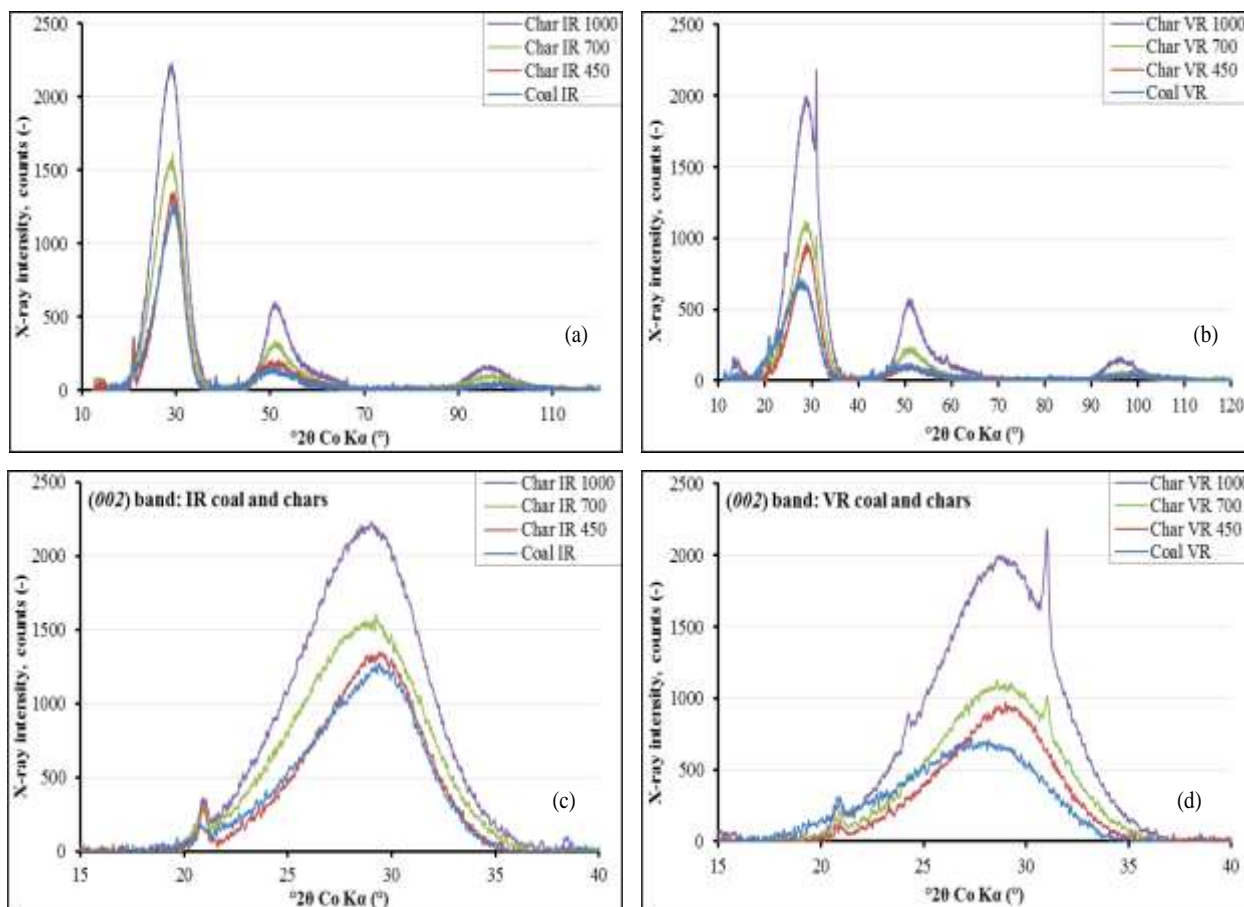


Figure B-1. Diffractograms for inertinite- and vitrinite-rich particles on respective sets of axis. Inertinite-rich particles ((a), top left) and vitrinite-rich particles ((b), top right). Zoomed (002) band for inertinite-rich particles ((c), bottom left) and vitrinite-rich particles ((d), bottom right). IR and VR = inertinite- and vitrinite-rich, respectively.

## APPENDIX B: X-RAY DIFFRACTION

B.2. Comparison of XRD structural parameters. See figure captions for details

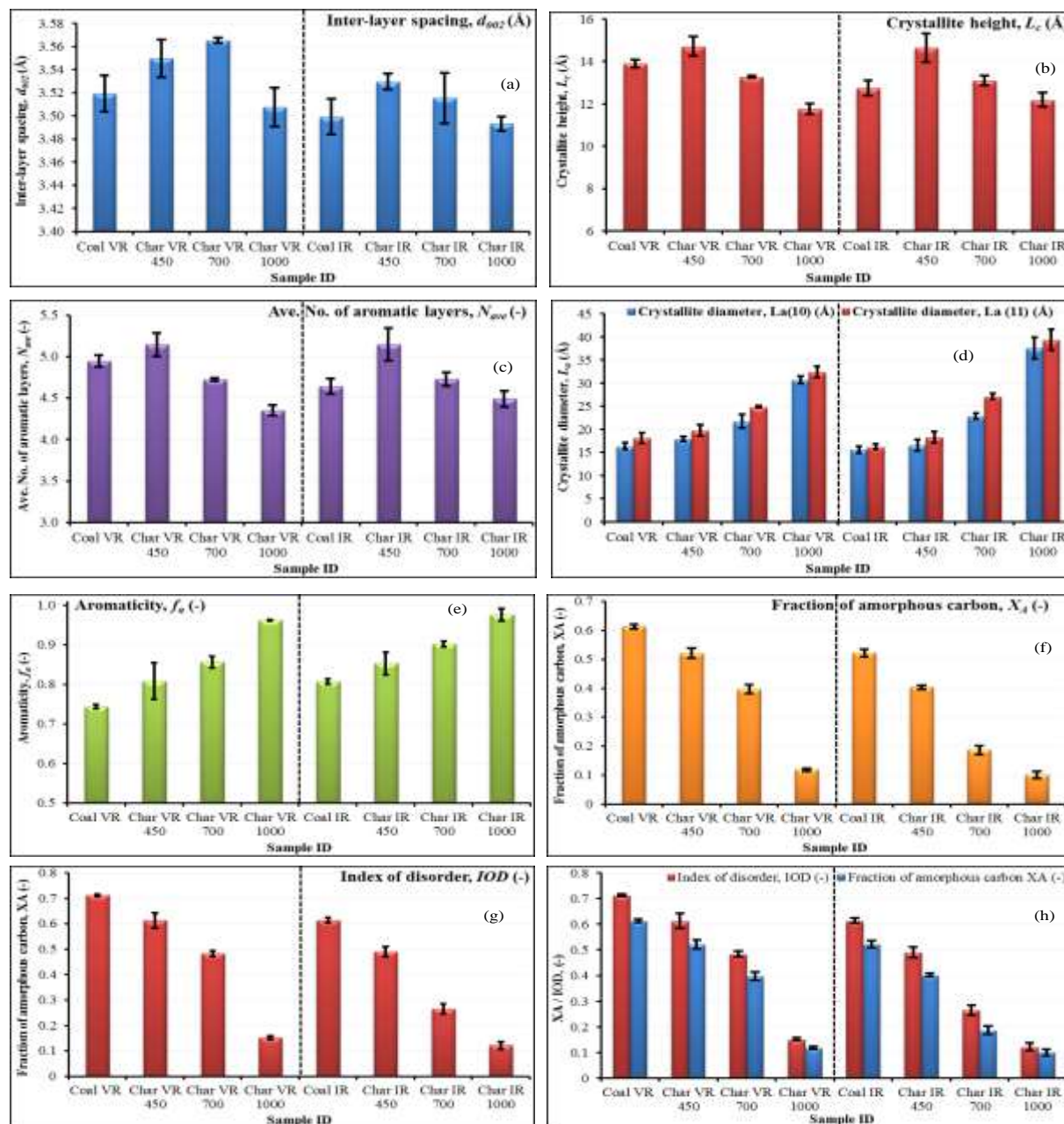


Figure B-2. Comparison of XRD structural parameters. IR and VR = inertinite- and vitrinite-rich, respectively. Numbers = temperature (°C). From top left to bottom right, (a)  $d_{002}$ , (b)  $L_c$ , (c)  $N_{ave}$ , (d)  $L_a$  (10) and  $L_a$  (11), (e)  $f_a$ , (f)  $X_a$ , (g)  $IOD$ , (h)  $IOD$  compared with  $X_a$ .

## APPENDIX B: X-RAY DIFFRACTION

B.3: Comparison and reproducibility of selected diffractogram patterns. See Figure captions for details.

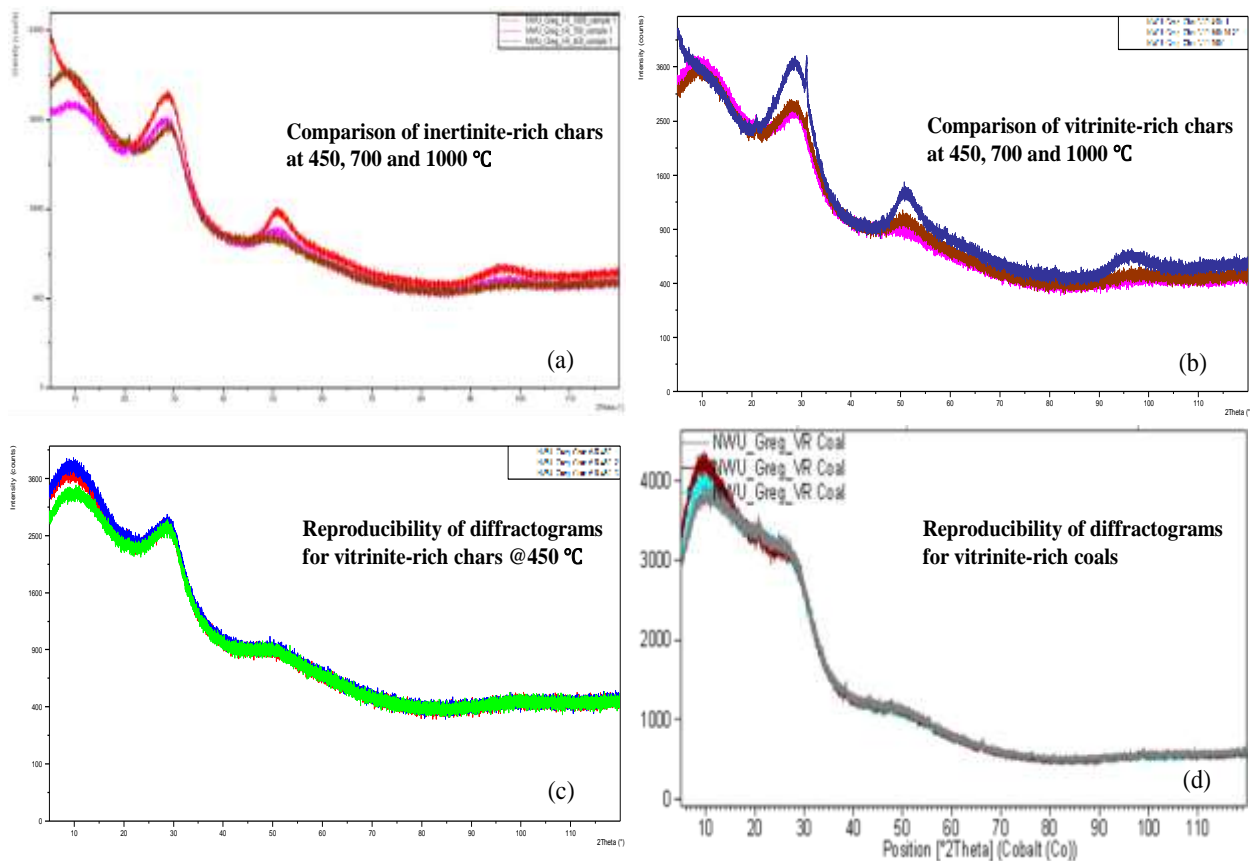


Figure B-3. Selected diffractogram patterns. Inertinite-rich chars ((a), top left) and vitrinite-rich chars ((b), top right) at 450, 700 and 1000 °C. Reproducibility of diffractogram patterns for vitrinite-rich chars at 450 °C ((c), bottom left) and vitrinite-rich coals ((d), bottom right).

## APPENDIX C: HIGH RESOLUTION TRANSMISSION ELECTRON MICROSCOPY

---

### Appendix C: The HRTEM image processing procedure

C1. Steps 1 and 2. Dissect the raw image into suitable areas and start cropping.

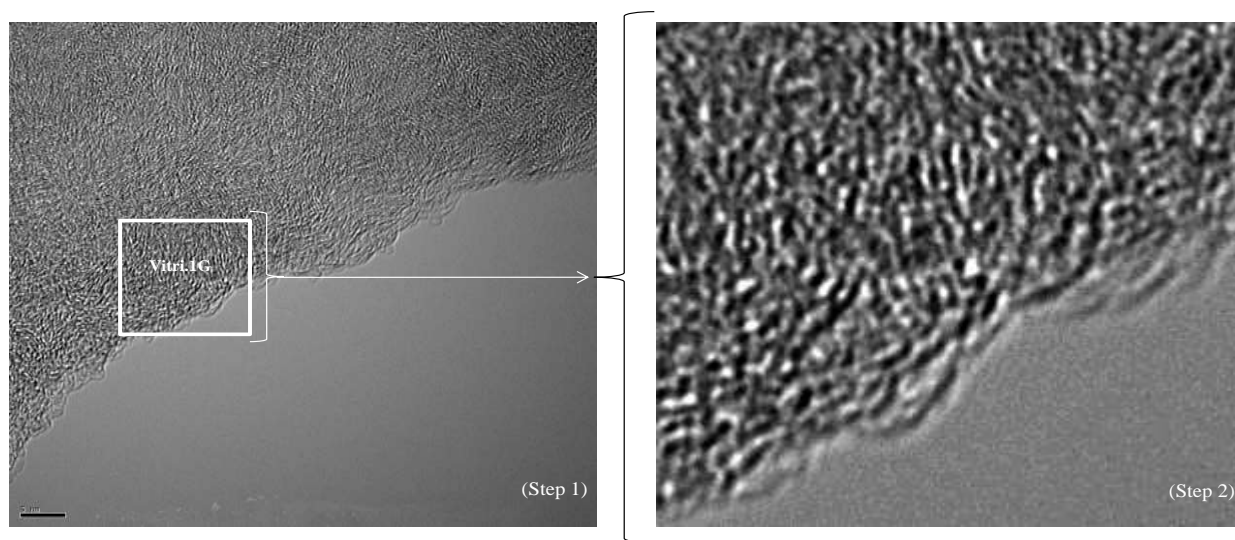


Figure C-1. The HRTEM image for the vitrinite-rich chars generated at 1000 °C. Vitr1.G = area to be cropped ((Step 1), left-hand side) and cropped area ((Step 2), right-hand side).

C2. Steps 3 and 4. Apply fast Fourier transform filter forward followed by general ideal filter.

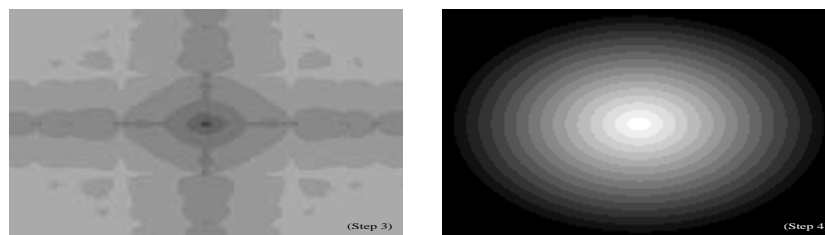


Figure C-2. Fast Fourier transform forward ((Step 3), left-hand side) followed by a general ideal filter ((Step 4), right-hand side).

## APPENDIX C: HIGH RESOLUTION TRANSMISSION ELECTRON MICROSCOPY

---

C3. Steps 5 and 6. Apply inverse fast Fourier transform filter followed by a suitable threshold level.

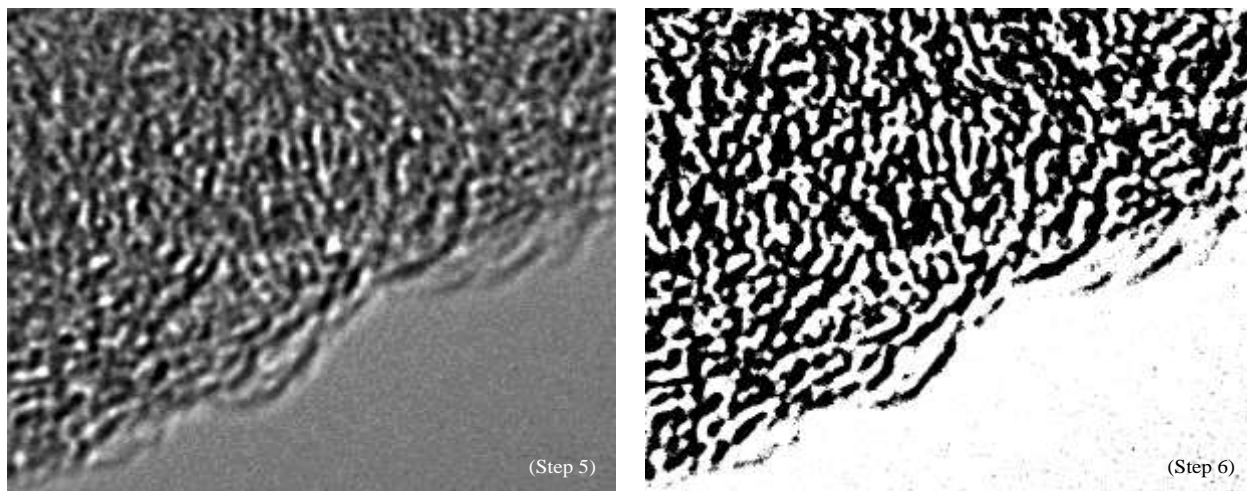


Figure C-3. Inverse fast Fourier transform filter ((Step 5), left-hand side) followed by a suitable threshold level ((Step 6), right-hand side).

C4. Step 7 and 8. Invert binary image and apply conditional smoothing

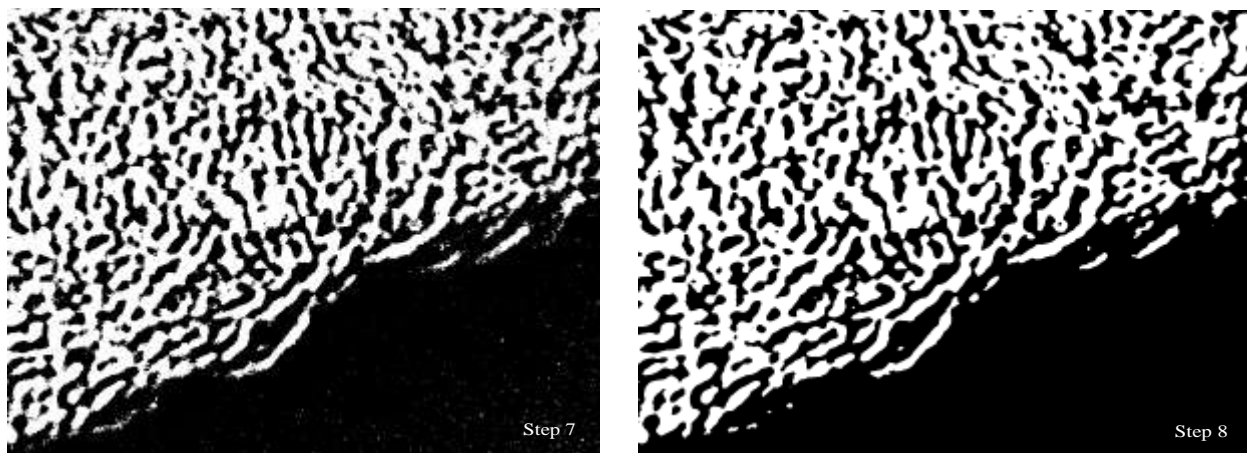


Figure C-4. Binary image inverted ((Step 7, left-hand side) followed by an ideal conditional smoothing five times at high median ((Step 8, right-hand side).

# APPENDIX C: HIGH RESOLUTION TRANSMISSION ELECTRON MICROSCOPY

## C5. Step 9 and 10. Skeletonise and trim

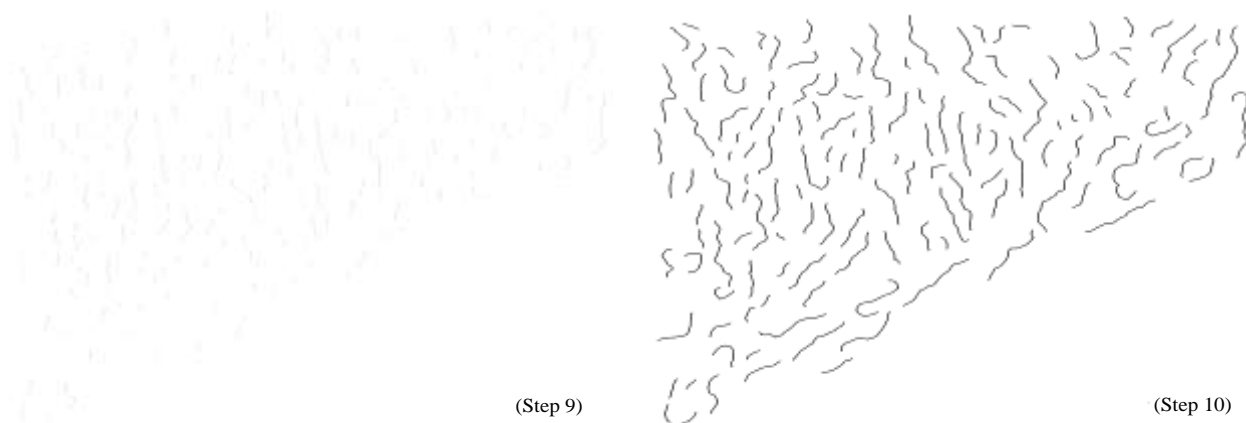


Figure C-5. Skeletonised binary image ((Step 9), left-hand side) followed by trimming ((Step 10, right-hand side).

## C6. Step 11 and 12. Colour by length and calculate all properties of the features (e.g. skeleton length)



Figure C-6. Final results of lattice coloured by length ((Step 11), left-hand side) and representation of all selected features properties after a calculation Step.12 (right-hand side).

## APPENDIX C: HIGH RESOLUTION TRANSMISSION ELECTRON MICROSCOPY

---

C7. Step 13. Conduct scale adjustments by cropping an area containing the scale bar at a size equal to Step 1. Correct the data accordingly.

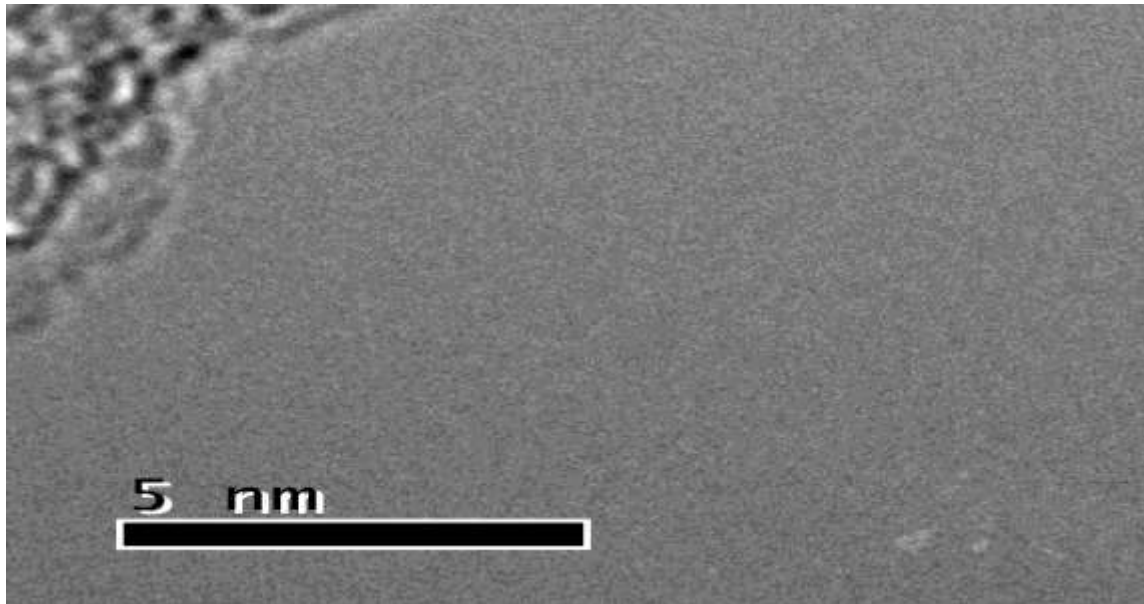


Figure C-7. Scale adjustment.

## APPENDIX C: HIGH RESOLUTION TRANSMISSION ELECTRON MICROSCOPY

---

### C.8 Noise separated during trimming exercises



Figure C-8. Example of unwanted features extracted during trimming process.

## APPENDIX D: SPIN STATES FOR STRUCTURES USED IN CHAPTER 5

### Appendix D: Spin states for the molecular structures used in Chapter 5

Table D-1. Spin states for the molecular structures used in Chapter 5.

Structure	No. of unpaired electrons	Spin state	Spin polarisation (kJ.mol <sup>-1</sup> )
Parallelogram-shaped graphene			
3x3	0	Singlet	6221.4
4x4	0	Singlet	9432.7
5x5	0	Singlet	13252.1
H-loss			
3x3_C <sub>t</sub>	2	Triplet	6221.4
3x3_C <sub>z</sub>	0	Singlet	6221.4
3x3_C <sub>zi</sub>	0	Singlet	6221.4
3x3_C <sub>r1</sub>	0	Singlet	6221.4
3x3_C <sub>r2</sub>	0	Singlet	6221.4
Reactive edge			
3x3	0	Doublet	5628.7
CO <sub>2</sub> Chemisorption			
3x3_C <sub>t</sub>	1	Doublet	6093.4
3x3_C <sub>z</sub>	1	Doublet	6093.4
3x3_C <sub>zi</sub>	1	Doublet	6093.4
3x3_C <sub>r1</sub>	1	Doublet	6093.4
3x3_C <sub>r2</sub>	1	Doublet	6093.4
CO <sub>2</sub> dissociation (Yield of 1 <sup>st</sup> CO gas molecule)			
3x3_C <sub>t</sub>	1	Doublet	6093.4
3x3_C <sub>z</sub>	1	Doublet	6093.4
3x3_C <sub>zi</sub>	1	Doublet	6093.4
3x3_C <sub>r1</sub>	1	Doublet	6093.4
3x3_C <sub>r2</sub>	1	Doublet	6093.4
Char decomposition (Yield of 2 <sup>nd</sup> CO gas molecule)			
3x3_C <sub>t</sub>	1	Doublet	6093.4
3x3_C <sub>z</sub>	1	Doublet	6093.4
3x3_C <sub>zi</sub>	1	Doublet	6093.4
3x3_C <sub>r1</sub>	1	Doublet	6093.4
3x3_C <sub>r2</sub>	1	Doublet	6093.4

## APPENDIX E: REPRODUCIBILITY OF THE TGA RESULTS

---

### Appendix E: Reproducibility of the TGA experimental results

The TGA experimental data were checked for reproducibility. This was done by conducting three independent experiments with each of the chars at the same operating condition. The reproducibility of the conversion time plots of char IR at 960 °C is shown in Figure E-1 from which, it can be seen that the reproducibility of the experimental result is very good. It was also found that calculated results from these data such as times to reach 50% and 90% conversions ( $t_{0.5}$  and  $t_{0.9}$ ) and the lumped reaction rate,  $r^L$ ; exhibited standard deviations, percentage average deviations and percentage uncertainty below 3.5% at 95% confidence interval.

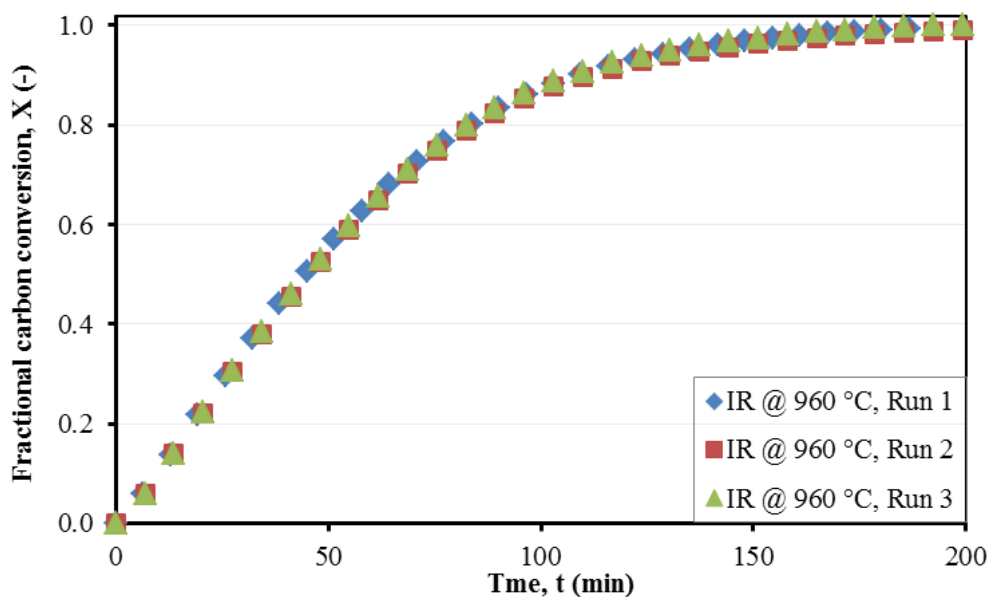


Figure E-1: Reproducibility results for char at 960 °C.

## APPENDIX F: UNCERTAINTY LIMITS ASSOCIATED WITH CALCULATION OF ACTIVATION ENERGIES

Appendix F: Uncertainty limits associated with calculation of activation energies.

The experimental uncertainties associated with the determination of the activation energies of the char-CO<sub>2</sub> gasification reaction of the two char samples were determined from 7 different Arrhenius plots constructed with different sets (7 data sets in total) of four isothermal reaction temperatures from five. The experimental uncertainties were determined at 95% confidence interval. These results are presented in Table F-1, and summarised in Table F-2.

Table F-1. Determination of experimental error from different Arrhenius plots ( $N = 7$ ;  $DF = 14$ ;  $CI = 95\%$ )\*.

Particlars / Sample ID	Char IR	Char VR
	$E_a$	$E_a$
Data set 1	208.9	193.4
Data set 2	207.9	200.3
Data set 3	212.8	174.2
Data set 4	208.9	193.4
Data set 5	210.1	191.6
Data set 6	204.4	204.8
Data set 7	213.6	181.7
Average	210	191
Standard deviation	2.858	9.676
Average deviation.	2.272	7.645
% Experimental uncertainty	3.58	13.269
Experimental uncertainty	8	25

\* $N$  = number of data set;  $DF$  = degree of freedom;  $CI$  = confidence interval

Table F-2. Summary of estimated activation energies from the gasification experiments with uncertainties.

	IR	VR
$E_a$ (kJ/mol)	$210 \pm 8$	$191 \pm 25$